

Studying the effect of non-adiabatic passing electron dynamics on microturbulence self-interaction in fusion plasmas using gyrokinetic simulations

Présentée le 26 novembre 2020

à la Faculté des sciences de base
SPC - Théorie
Programme doctoral en physique

pour l'obtention du grade de Docteur ès Sciences

par

Ajay CHANDRARAJAN JAYALEKSHMI

Acceptée sur proposition du jury

Prof. F. Mila, président du jury
Dr S. Brunner, directeur de thèse
Prof. B. McMillan, rapporteur
Dr Y. Camenen, rapporteur
Dr L. Porte, rapporteur

Put on your 3D glasses now

Abstract

Microturbulence driven by plasma instabilities is in most cases the dominant cause of heat and particle loss from the core of magnetic confinement fusion devices and therefore presents a major challenge in achieving burning plasma conditions. The role of passing electron dynamics in turbulent transport driven by ion-scale microinstabilities, in particular Ion Temperature Gradient (ITG) and Trapped Electron Mode (TEM) instabilities, has been given relatively little attention. In first approximation, these particles, which are highly mobile along the confining magnetic field, are assumed to respond adiabatically to the low frequency ion-scale modes. However, near mode rational surfaces (MRSs), the non-adiabatic response of passing electrons becomes important and can no longer be neglected. This non-adiabatic electron response actually has a destabilising effect and leads to generation of fine-structures located at the MRSs of each eigenmode. This thesis focuses on the effects of non-adiabatic response of passing electrons in tokamak core turbulence.

One such effect of non-adiabatic passing electrons that is of particular interest to this work is the self-interaction mechanism. It is essentially a process by which a microinstability eigenmode that is extended along the direction parallel to the magnetic field interacts non-linearly with itself, in turn generating $E \times B$ zonal flows. Unlike the usual picture of zonal flow drive in which microinstability eigenmodes coherently amplify the flow via modulational instabilities, the self-interaction drive of zonal flows from these eigenmodes are uncorrelated with each other. In the case of ITG driven turbulence, using novel statistical diagnostic methods, it is shown that the associated shearing rate of the fluctuating zonal flows therefore reduces as more toroidal modes are resolved in the simulation. In simulations accounting for the full toroidal domain, such an increase in the density of toroidal modes corresponds in fact to an increase in the system size, leading to a finite system size effect that is distinct from the other better known system size effects such as profile shearing or finite radial extent of the unstable region.

The study of non-adiabatic passing electron dynamics is pursued further to include more reactor relevant conditions such as collisions and background shear flow. It is found that, with increasing collisionality, electrons behave more adiabatic-like, especially the trapped electrons away from MRSs, thereby leading to a decrease in the growth rate of ITG eigenmodes. Furthermore, the shortened electron mean free path in presence of collisions leads to a radial broadening of the fine-structures at the MRS of corresponding

Abstract

eigenmodes. In nonlinear simulations, the turbulent flux levels decrease with increasing collisionality, as a result of the reduced drive from the less unstable ITG eigenmodes. The radial width of the fine structures at MRSs is found to reduce with increasing collisionality as a result of reduced nonlinear modification of the eigenmodes in turbulence simulations. A study of the effect of collisions on the self-interaction mechanism reveals that for physically relevant values of collisionality, the effect of self-interaction is still significant. A preliminary study of the effect of background $E \times B$ flow shear shows that the fine-structures associated with the non-adiabatic passing electron response persist even with finite background flow shearing rates. The turbulent flux-levels decrease with increasing values of background shearing rate, and radially propagating soliton-like structures are seen, similar to the results obtained with adiabatic electrons in previous studies.

Résumé

La micro-turbulence, qui est provoquée par les instabilités dans le plasma, est dans la plupart des cas la cause principale de la perte de chaleur et de particules du centre des dispositifs de fusion par confinement magnétique, et présente donc un défi majeur pour obtenir des conditions de plasma brûlant. Le rôle de la dynamique des électrons passant dans le transport turbulent provoqué par des micro-instabilités à l'échelle ionique - en particulier les instabilités causées par des gradients de température ionique (ITG) et des modes dûs aux électrons piégés (TEM) - a reçu que peu d'attention. En première approximation, les électrons qui sont très mobiles dans la direction le long du champ magnétique de confinement, sont supposés répondre de manière dite adiabatique aux modes de basse fréquence à l'échelle ionique. Cependant, pour les surfaces rationnelles relatif à des modes de bas ordre (MRS), la réponse non-adiabatique des électrons passant devient alors importante et ne peut donc plus être négligée. Cette réponse électronique a en effet un effet déstabilisant et conduit à des structures fines situées au niveau des MRS de chaque mode propre. Cette thèse se concentre sur les effets de la réponse non-adiabatique des électrons passant sur la turbulence dans le centre d'un tokamak.

L'un de ces effets qui présente un intérêt particulier pour cette thèse est le mécanisme d'auto-interaction : un processus par lequel un mode propre de micro-instabilité, allongé le long de la direction du champ magnétique, interagit de manière non-linéaire avec lui-même, générant ainsi, à son tour, un flux zonal de type $E \times B$. Contrairement à l'image habituelle selon laquelle des modes propres de micro-instabilités amplifient de manière cohérente ces flux zonaux à travers les instabilités de modulation, les contributions via l'auto-interaction produisant ces flux zonaux de ces modes propres ne sont pas corrélés les uns aux autres. Dans le cas de la turbulence générée par l'ITG, en utilisant de nouvelles méthodes de diagnostic statistique, il est montré que le taux de cisaillement associé aux flux zonaux fluctuants diminue à mesure que le nombre de modes toroïdaux résolus dans les simulations augmente. Dans les simulations prenant en compte le domaine toroïdal complet, une telle augmentation de la densité des modes toroïdaux correspond à une augmentation de la taille du système, conduisant à un effet de taille de système fini qui est distinct des autres effets mieux connus de ce type, tels que l'effet de cisaillement de profil ou l'extension radiale finie de la région instable.

L'étude de la dynamique des électrons passant non-adiabatiques est poursuivie pour inclure davantage de conditions pertinentes aux conditions d'un réacteur telles que les

Abstract

collisions et les flux de cisaillement macroscopiques. On constate qu'avec l'augmentation de la collisionnalité, les électrons se comportent de manière plus adiabatique, en particulier les électrons piégés loin des MRS, conduisant ainsi à une diminution du taux de croissance des modes propres ITG. De plus, le libre parcours moyen des électrons est raccourci en présence de collisions et conduit à un élargissement radial des structures fines au niveau des MRS correspondantes. Dans les simulations non-linéaires, les niveaux de flux turbulents diminuent avec l'augmentation de la collisionnalité, en raison des modes propres ITG qui sont moins instables. On constate aussi que la largeur radiale des structures fines au niveau des MRS diminue avec l'augmentation de la collisionnalité en raison de la modification non-linéaire réduite des modes propres. Une étude de l'effet des collisions sur le mécanisme d'auto-interaction révèle que, pour les valeurs de collisionnalités pertinentes, l'effet de l'auto-interaction est toujours significatif. Une étude préliminaire de l'effet du cisaillement de flux $E \times B$ macroscopique montre que les structures fines associées à la réponse non-adiabatique des électrons passants persistent même avec des taux de cisaillement fini. Les niveaux de flux turbulents diminuent avec des valeurs croissantes du taux de cisaillement macroscopique, et des structures de type soliton se propageant radialement sont observées, similaires aux résultats obtenus avec des électrons adiabatiques dans des études précédentes.

Contents

Abstract (English/Français)	i
1 Introduction	1
1.1 Nuclear fusion	2
1.2 Magnetic confinement	3
1.2.1 The transport problem	5
1.3 Focus and outline of the Thesis	8
2 Theoretical Background	11
2.1 Magnetic equilibrium	11
2.2 Vlasov-Maxwell system	14
2.3 The gyrokinetic framework	15
2.3.1 The gyrokinetic ordering	16
2.3.2 The modern gyrokinetic derivation	17
2.3.2.1 Particle coordinates - Guiding center transformation . .	17
2.3.2.2 Guiding center - Gyrocenter transformation	19
2.3.2.3 The gyrokinetic equation	21
2.3.3 Background distribution	23
2.3.4 Moments and fluxes	24
2.3.5 Field Equations	25
2.4 Collisions	26
2.4.1 Landau collision operator	27
2.5 Microinstabilities	30
2.5.1 Toroidal ITG instability	31
2.5.2 TEM instability	34
2.5.3 Zonal flows	34
2.5.4 ETG instability	35
2.5.5 Other Instabilities	36
2.6 The GENE code	37
2.6.1 Coordinate system	37
2.6.2 Flux-tube model and boundary conditions	38
2.6.3 Collision frequency	43
2.6.4 Numerical details	44

3	How eigenmode self-interaction affects zonal flows and convergence of turbulence levels with toroidal system size	47
3.1	Introduction	47
3.2	Non-adiabatic passing electron dynamics leading to stationary zonal structures	53
3.3	$k_{y,\min}\rho_i$ scan in ITG-driven turbulence. Role of stationary and fluctuating components of zonal shear flows	56
3.4	Analysing zonal flow drive	65
3.4.1	Reynolds stress as a proxy for the drive of zonal flows	65
3.4.2	Modulational instability in shearless slab system	68
3.4.3	Self-interaction mechanism in sheared toroidal system	71
3.4.4	Evidence of zonal flow drive by modulational instability and self-interaction in reduced simulations	72
3.4.5	Evidence of self-interaction in turbulence simulations	76
3.4.6	Evidence of modulational instability in turbulence simulations. Bicoherence and correlation analysis.	81
3.5	Estimating the reduction in zonal flow drive from self-interaction with decreasing $k_{y,\min}\rho_i$	85
3.6	Conclusions	87
4	Effect of collisions and background shear flows on non-adiabatic passing electron dynamics	91
4.1	Effect of collisions on non-adiabatic passing electron dynamics	91
4.1.1	Effect of collisions in linear simulations	93
4.1.1.1	Decrease in growth rate with increasing collisionality. Adiabatic like electron response away from MRS.	94
4.1.1.2	Increase in radial width of fine structures with increasing collisionality	98
4.1.2	Effect of collisions in nonlinear simulations	100
4.1.2.1	Effect of collisions on heat flux	100
4.1.2.2	Effect of collisions on radial width of fine-structures	103
4.1.2.3	Effect of collisions on parallel correlation	106
4.1.2.4	Effect of collisions on self-interaction mechanism	107
4.1.3	Conclusions	111
4.2	Effect of background shear flow on non-adiabatic passing electron dynamics	112
5	Conclusions	117
5.1	Summary	117
5.2	Outlook	119
A	Local flattening of gradients between lowest order MRSs	121
B	Flux-surface-averaged poloidal momentum conservation equation	125

B.1	Derivation in GENE flux-tube model	125
B.2	Testing validity in linear case: Rosenbluth-Hinton test	131
B.3	Testing validity in non-linear case: Turbulence simulation	131
C	Local linear dispersion relation for analysing effect of collisions on ITG eigenmodes	135
C.1	Testing validity of the BGK-like collision operator	135
C.2	Analysing the effect of collisions on the radial width of fine-structures .	139
	Bibliography	147
	Acknowledgements	159
	Curriculum Vitae	161

1 Introduction

Given the inherent curiosity in us, if not for other reasons, we are a space-faring species by choice. For setting up inter-planetary/galactic journeys, and to establish and sustain human civilisations beyond Earth, it is necessary to have an abundant and robust source of energy. To put the time scales and energy needs being considered into perspective, one can look at the Kardashev scale [Kardashev, 1964] which classifies the advancement of human civilisation based on its energy consumption into three types: The type 1 civilisation uses the equivalent of all the radiant energy falling on a planet from its parent star, which is approximately 1.7×10^{17} watts for the Earth-Sun system. At present (year 2020 in Gregorian calendar), the energy consumption of the world is roughly 2×10^{13} watts. Type 2 civilization uses the equivalent of the total energy radiated by the parent star, which is about 4×10^{26} watts. And type 3 civilisation have access to the power comparable to the luminosity of the host galaxy, about 4×10^{37} watts for the Milky Way.

Let us take a look at the already available technologies that can satisfy our terrestrial and extra-terrestrial energy needs in the future. Combustion of hydrocarbon fuels is not a good option given that they have relatively very low energy densities and are found in limited quantities, that too on very select places such as Earth (for all the fossil fuels), Titan (for methane) etc. Power generation via nuclear fission is a good option but the low availability of heavy fissile elements in the universe [Cameron, 1973] is a reason against it. Harvesting the solar/stellar energy using photovoltaic cells becomes less practical with greater energy needs, as the surface area of the cells will have to increase proportionally. In addition, the radiation flux from the star decreases as one moves farther away from it, as the inverse of the square of distance from the star. A promising alternative is a nuclear fusion based power plant. Hydrogen, the fuel for such a reactor, is the most abundant element in the universe, making up 74% of the baryonic matter. Various designs of possible fusion reactors exist that are inherently safe with no possibility of meltdowns. Furthermore, the fusion process itself involves no radio-active fuel and waste as such; the reactor walls can get activated but the constituent materials have low enough half-lives to be recycled within a hundred years.

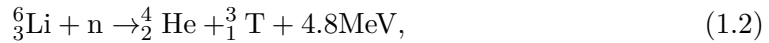
In this thesis, we focus on nuclear fusion as a viable means of energy production. A small summary of the processes involved in typical nuclear fusion reactions of interest are given in section 1.1. There are two broad pathways considered to fusion, either via inertial confinement or via magnetic confinement. The former involves compressing and heating a pellet of fusion fuel via a shock wave produced by multiple high energy laser or ion beams. The latter, of interest to this work, involves confining the fusion fuel in plasma state using magnetic fields. In section 1.2, a description of magnetic confinement is given, wherein the problem of heat and particle leakage from the core of such devices, in particular through turbulence, is introduced. Finally, in section 1.3, the focus and outline of the thesis are presented.

1.1 Nuclear fusion

Nuclear fusion is the process by which two lighter nuclei combine to form a heavier nucleus while releasing energy. The net loss of mass Δm in the reaction is converted to energy following the mass-energy equivalence relation $E = \Delta m c^2$, where c is the speed of light [Einstein, 1905]. It is interesting to note that nuclear fusion is the primary source of power in active stars. For instance, in the Sun, the proton-proton chain reaction which occurs in the solar core at a temperature of 14 million degrees Kelvin involves a net reaction that converts four hydrogen nuclei into one helium nucleus, with the release of two positrons, two neutrinos and energy [Kane, 1987]. The most probable nuclear reaction that can be exploited in a fusion power plant, *i.e.* the one having the highest cross-section to be precise, is the deuterium-tritium fusion, producing a helium nucleus, a neutron and energy [Bosch and Hale, 1992], summarised by:



Following the mass ratio of the products in relation (1.1), $4/5^{th}$ of the energy released, *i.e.* 14.1 MeV, manifests as the kinetic energy of the neutrons, which can be captured by a blanket of lithium surrounding the reactor. Lithium then undergoes the reaction:



producing helium, tritium and more energy. The blanket gets heated up in the process, which can then be used to boil water to produce steam, run turbines and produce electricity. The main purpose of the lithium blanket is to produce tritium which does not occur in nature in quantities that can be considered sufficient for reactor operations [Rubel, 2019]. Note that unlike hydrogen and deuterium, tritium is an unstable isotope, with a half-life of only 12.32 years [Tetsuo, 2017].

Given that the strong force that binds the nucleons together in a nucleus is a short range force acting in distances of the order of a femtometer (10^{-15}m), it is necessary

for the reactants to come within such short distances of each other for fusion to occur. However due to Coulomb repulsion between the two positively charged reactants, which is inversely proportional to the square of the distance between them, they must start with very high kinetic energies to come close enough for fusion to occur. The kinetic energy of the reactants or the associated temperature thus required is well beyond the ionization energy of the corresponding atoms, and hence they exist in the plasma state, as a gas of ions and electrons. A simple estimate for the minimum condition necessary for fusion to be sustained in a reactor with a positive energy balance is given by the so-called Lawson criteria [Lawson, 1957], which states that the triple product of density n , temperature T and the confinement time τ_E (time scale on which energy can be retained within the plasma from being lost to the surrounding) must exceed a critical value:

$$nT\tau_E \geq 3 \times 10^{21} \text{keV s m}^{-3}. \quad (1.3)$$

In magnetic fusion, the typical values of density, temperature and confinement times are of the order of $n \sim 10^{19} \text{m}^{-3}$, $T \sim 10^8 \text{K}$ ($\simeq 10 \text{keV}$) and $\tau_E \sim 10^0 \text{s}$ respectively. Note that the temperature is about 100 times greater than that in the core of the Sun, where the density $n \sim 10^{31} \text{m}^{-3}$ is many orders of magnitude higher, made possible by the immense gravitational force involved. In inertial fusion, densities $n \sim 10^{30} \text{m}^{-3}$ more comparable to that in the core of the Sun are reached by concentrating multiple high power laser beams on a small pellet of fusion fuel for a very short amount of time. In this case, the plasma is confined by the inertia of its own mass, with a confinement time of the order of $\tau_E \sim 10^{-9} \text{s}$. In the following section, magnetic fusion is described in greater details.

1.2 Magnetic confinement

To ensure that a high temperature ($T \sim 10^8 \text{K}$) necessary for fusion is achieved, it is essential for the plasma to be isolated from the walls of the reactor so that heat loss via conduction onto the walls can be minimised. In addition, when coming into contact with plasma, the walls can get damaged and/or release impurities into the plasma, both of which are undesired. Therefore, it is essential for the plasma to be suspended in near vacuum within the reactor walls. Given that the plasma is composed of charged particles, magnetic fields can be used to manipulate them. A particle of mass m and charge q , having a thermal velocity $v_{th} = (T/m)^{1/2}$ [where T is defined in units of energy] in a magnetic field \mathbf{B} (with field strength $B = |\mathbf{B}|$) and zero electric field gyrates around the magnetic field line with a (Larmor/gyro) frequency $\Omega = qB/m$ and a (Larmor/gyro) radius $\rho = v_{th}/\Omega$ according to the equation of motion:

$$m \frac{d\mathbf{v}}{dt} = q \mathbf{v} \times \mathbf{B}. \quad (1.4)$$

By increasing the magnetic field strength, the Larmor radius decreases and the particles adhere more closely to the field lines. Furthermore, in case the particles in a magnetic

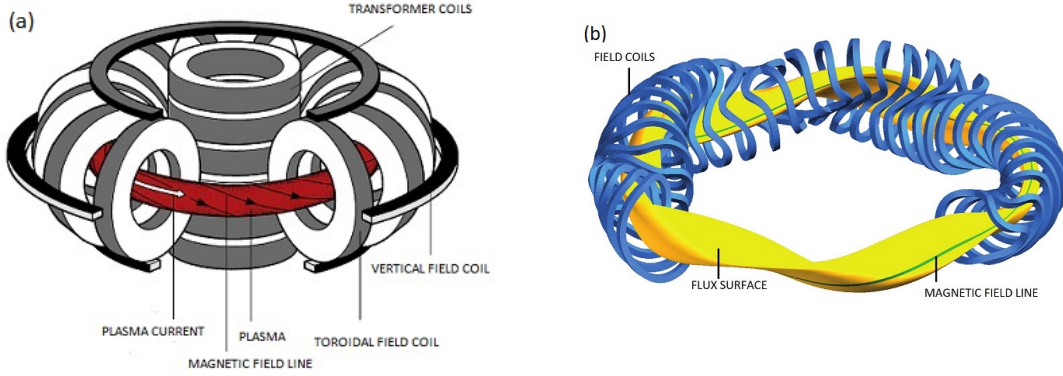


Figure 1.1: Schematic illustration of (a) a tokamak and (b) a stellarator. Source: Max Planck Institute for Plasma Physics.

field \mathbf{B} are subject to an external force \mathbf{F} , it can also undergo drifts in the direction perpendicular to \mathbf{B} , with a drift velocity $\mathbf{v}_F = \mathbf{F} \times \mathbf{B} / qB^2$.

In magnetic fusion reactors where the particles are confined by magnetic fields that touch the reactor walls, the particles having high velocities ($\sim v_{th}$) parallel to the magnetic fields may stream along the field lines and get lost on the walls. In early linear devices, such a loss of particles was minimized by using inhomogeneous magnetic field configurations working as magnetic mirrors. But the confinement offered by these devices were unsatisfactory especially for high energy particles. Hence, toroidal devices were introduced, where the particles are confined to field lines that wrap around toroidally on magnetic surfaces that do not touch the walls. However in such toroidal geometry, the inherent curvature and the inhomogeneity in the magnetic field strength lead respectively to centrifugal force $\mathbf{F}_C = -mv_{\parallel}^2 \mathbf{b} \cdot (\nabla \mathbf{b})$ and force $\mathbf{F}_\mu = -\mu \nabla B$ related to magnetic moment $\mu = mv_{\perp}^2 / 2B$ associated to the gyromotion of the particle; $\mathbf{b} = \mathbf{B} / B$ and, v_{\parallel} and v_{\perp} are particle velocities parallel and perpendicular to the field line respectively. The corresponding drifts ($\mathbf{v}_F = \mathbf{F} \times \mathbf{B} / qB^2$) lead to a curvature drift velocity $\mathbf{v}_C = -mv_{\parallel}^2 (\mathbf{b} \cdot (\nabla \mathbf{b}) \times \mathbf{B}) / qB^2$ and a ∇B drift velocity $\mathbf{v}_{\nabla B} = -mv_{\perp}^2 (\nabla B \times \mathbf{B}) / 2qB^3$. As a rough estimate, one has $|\mathbf{v}_C| \sim v_{th} \rho / R$ and $|\mathbf{v}_{\nabla B}| \sim v_{th} \rho / L_B$, where R is the radius of curvature and L_B is the characteristic gradient length of the background magnetic field. As a result of these drifts, the particles can drift out of the plasma volume. Furthermore, these drift velocities being dependent on the sign of the charge q , lead to a separation of ions and electrons in the plasma. To counter these drifts, a poloidal component of the magnetic field is introduced, resulting in helically twisted field lines. Two such designs of toroidal devices are widely used today: the stellarator and the tokamak. See figure 1.1 for illustration of the magnetic coil geometry, and field directions in a stellarator and a tokamak.

In a stellarator, complex magnetic coils are used to generate the helically twisted field lines. Whereas in a tokamak, the poloidal component of the magnetic field is created

by a toroidal current in the plasma itself, which in turn is induced via the transformer principle, with the plasma being the secondary winding. Note that a stellarator has no plasma current and can be operated continuously, while the tokamak operates a priori in a pulsed mode, limited by the transformer principle. However, with additional current driving mechanisms, such as that via the bootstrap mechanism and neutral beam injection, it is possible to operate tokamaks in a continuous mode as well. While both these designs are being researched upon at the moment, this thesis primarily focuses on tokamaks.

1.2.1 The transport problem

One of the main problems with achieving the Lawson criterion for fusion is the radial transport (loss) of heat and particles from the core of the plasma to the edge. Depending on the origin of such transport processes, they are classified into three, namely *classical*, *neo-classical* and *turbulent/anomalous* transport.

In *classical transport*, collisions between the particles lead to their diffusion across magnetic field lines. Collisions are equally probable in all directions, but given that the plasma density is maximum at the core, a net radial outward diffusive flux is observed. A random walk model given by $D = (\Delta x)^2/\tau$ can be used to estimate the diffusivity D of this process, where Δx is the characteristic step size of a particle over the characteristic time τ . The classical diffusivity takes the form $D_{\text{class}} = \rho^2 \nu_c$, where the step size Δx is of the order of the Larmor radius ρ and $1/\tau$ is of the order of the Coulomb collision frequency ν_c . However experimentally measured diffusivities were found to be about 3 orders of magnitude higher than the classical diffusivity.

Neo-classical transport [Hinton and Hazeltine, 1976, Helander and Sigmar, 2002] results from the toroidicity of the magnetic confinement device. In a circular large aspect ratio ($\epsilon = r_0/R_0 \ll 1$, where r_0 is the minor radius and R_0 is the major radius) tokamak for instance, to first order in ϵ , the magnetic field strength, mostly comprising of its toroidal component, can be expressed as a function of the poloidal angle θ as:

$$B(\theta) \sim \frac{1}{R} = \frac{1}{R_0}(1 - \epsilon \cos\theta), \quad (1.5)$$

where R measures the distance from the center of the torus (see section 2.1 for greater details on the magnetic equilibrium, in particular, figure 2.1). Using conservation of kinetic energy $\mathcal{E} = mv^2/2$ and the adiabatic invariance of the magnetic moment $\mu = mv_{\perp}^2/2B$, one can show that particles starting at any poloidal angle θ with low enough parallel velocities can get reflected as they move towards the inboard side where the magnetic field strength is higher. That is, due to this magnetic mirroring, these particles get trapped on the outboard side of the tokamak, whereas particles with high enough starting parallel velocities can overcome the mirroring effect and complete full

orbits in the poloidal plane. It can be shown that a particle following a given magnetic field line will be trapped if

$$\frac{v_{\parallel}(\theta)}{v_{\perp}(\theta)} < \sqrt{\frac{B_{\max}}{B(\theta)} - 1}, \quad (1.6)$$

where $v_{\parallel}(\theta)$ and $v_{\perp}(\theta)$ are the starting parallel and perpendicular velocities of the particle at any poloidal angle θ where the magnetic field amplitude is $B(\theta)$, and B_{\max} is the maximum magnetic field strength, typically at the inboard midplane $\theta = -\pi$. This is illustrated in figure 1.2(a). The trapped-passing boundary in velocity space specified by the angle ϕ_v is defined such that $\tan(\phi_v) = v_{\parallel}(\theta)/v_{\perp}(\theta)$, as given by equation (1.6). The corresponding fraction α_t of trapped particle for a Maxwellian or any isotropic velocity distribution is given by the relation

$$\alpha_t = \sqrt{1 - \frac{B(\theta)}{B_{\max}}}. \quad (1.7)$$

Note that, as a result of the curvature and ∇B drifts, the orbits of the trapped particles projected on a poloidal plane resemble the shape of a banana as shown in figure 1.2(b). Considering the marginally trapped condition, one can find that the starting velocities $v_{\parallel,0}$ and $v_{\perp,0}$ at the outboard midplane $\theta = 0$ follow the relation $v_{\parallel,0} \sim \sqrt{2\epsilon} v_{\perp,0}$, and for a large aspect ratio, *i.e.* $\epsilon \ll 1$, one thus obtains $v_{\parallel,0} \sim \sqrt{\epsilon} v_{th}$ for trapped particles. The time to complete half an orbit can thus be estimated as $t_b \sim Rq_s/v_{\parallel,0} \sim Rq_s/\sqrt{\epsilon}v_{th}$, where q_s is the safety factor measuring the pitch of the magnetic field. Furthermore, the width of the banana orbit can be estimated as $\delta_b \sim |\mathbf{v}_d|t_b \sim q_s\rho/\sqrt{\epsilon}$, where $\mathbf{v}_d = \mathbf{v}_{\nabla B} + \mathbf{v}_C$, $|\mathbf{v}_d| \sim v_{th}\rho/L_{\perp}$ and $L_{\perp} (\simeq R \simeq L_B)$ is the characteristic gradient length of equilibrium quantities. One can see that, as a result of a collision kicking a particle from one trapped trajectory to another, the particle can radially migrate by a distance $\sim \delta_b$. This is the fundamental process behind neo-classical transport. Moreover, while in classical diffusion, collision frequencies are computed for 90° scattering events, in neo-classical diffusion much smaller scattering angles ($\phi_v \sim \tan\phi_v \sim \sqrt{\epsilon}$) in velocity space can lead to significant changes in the trajectory. Therefore an effective collision frequency defined as $\nu_{\text{eff}} = \nu/\epsilon$ is introduced. One can now estimate the neo-classical diffusion as $D_{\text{neo-class}} = \alpha_t(\delta_b)^2\nu_{\text{eff}}$, which is greater than D_{class} by up to two orders of magnitude. However it is typically still one or two orders of magnitudes less than most experimentally observed diffusivities.

Turbulent transport (also referred to as anomalous transport), resulting from plasma microturbulence, explains the high diffusivities observed in experiments. The large radial gradients in density and temperature necessary to maintain fusion conditions in the core act a source of free energy to various small scale instabilities on scales of the Larmor radius. For example, instabilities such as Ion Temperature Gradient (ITG) or the Trapped Electron Mode (TEM) appear at ion-scales, while Electron Temperature Gradient (ETG) mode appear at electron-scales. In this thesis, particular focus is given to ITG driven turbulence. These microinstability modes compete and interact with each

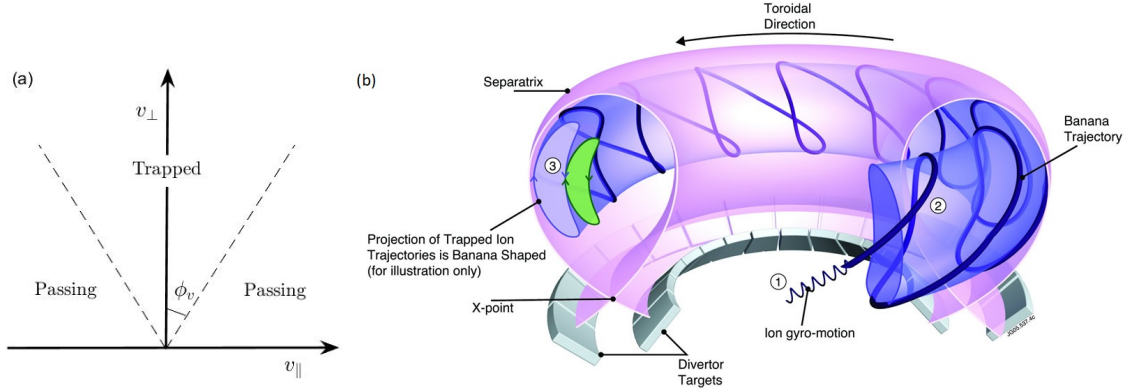


Figure 1.2: (a) Illustration of the trapped-passing boundary in $v_{\perp} - v_{\parallel}$ velocity space. (b) Illustration of a banana orbit in a tokamak. ① The gyro-motion of an ion around the magnetic field line ② The banana orbit in 3D ③ Banana orbit of an ion [blue] and an electron [green] projected on the poloidal plane. Also shown is the separatrix referring to the boundary between closed and open field lines, the x-point and the divertor plates. Source: Euro-Fusion

other, leading to small scale fluctuations in density, temperature and electromagnetic fields, which in turn lead to radial drifts that carry heat and particles from the core of the device towards the walls. The statistically steady-state level of this turbulent transport depends not only on its drive from the various instabilities but also on the turbulence saturation mechanism such as that via the zonal flow shearing mechanism [Diamond et al., 2005], via damped modes [Hatch et al., 2011], perpendicular particle diffusion [Merz and Jenko, 2008], etc. Zonal flows, which result from electrostatic field perturbations that are constant on the magnetic surface but vary in the radial direction, is studied in greater detail in this thesis as it is a dominant saturation mechanism in the considered ITG turbulence regime.

One can obtain a rough estimate of the turbulent diffusivity D_{turb} using the so-called mixing length estimate, which in turn is based on the random walk model. Given that the typical length of turbulent eddies perpendicular to the magnetic field line is of the order of Larmor radius, and considering the characteristic frequency in the random walk model to be the frequency of the instability mode ω_d , one obtains $D_{\text{turb}} \sim \rho^2 \omega_d$. An approximate estimate for the frequency of the instability modes is given by $\omega_d \sim |\mathbf{v}_d| k_{\perp} \sim v_{th} \rho k_{\perp} / L_{\perp}$, where $k_{\perp} \sim 1/\rho$ is the perpendicular wavenumber associated to the instability mode. One thus obtains $D_{\text{turb}} \sim \rho^2 v_{th} / L_{\perp}$. This $D_{\text{turb}} \propto \rho^*$ scaling, where $\rho^* = \rho / L_{\perp}$ measures the system size, is called gyro-Bohm scaling [Cowley et al., 1991]. Note that this is only a very rough estimate, one of the many scaling laws that have been observed in experiments and simulations [Garbet and Waltz, 1996, Petty et al., 1995, Shirai et al., 1995, Lin et al., 2002].

In the next subsection, the subjects of particular focus of this thesis are introduced, along with an outline of how the thesis is organised.

1.3 Focus and outline of the Thesis

Exploiting the difference in time scales between the fast gyromotion of particles and the time scale associated with typical microinstability modes, gyrokinetic simulations that model the particle trajectories averaged over the gyromotion are widely used to study microturbulence. In such simulations, the 6 dimensional phase space is effectively reduced to 5 dimensions and furthermore, the fast cyclotron time scale does not have to be evolved, thereby reducing the computational costs to levels that can be handled by present day supercomputers. The two main numerical methods used in gyrokinetics are the Particle In Cell (PIC) method and the Eulerian method. In the former, a Lagrangian description of the plasma is considered, and a statistical sampling of the particles distribution in phase space is performed, whose trajectories are then evolved in time. In the latter method, the gyrokinetic equation is discretized on a fixed grid in phase space and the resulting system of ordinary differential equations are solved numerically. Each method has its own advantages and disadvantages.

In this thesis, an Eulerian gyrokinetic code called GENE [Jenko et al., 2000, Merz, 2008, Görler et al., 2011] is used to study the role of passing electron dynamics in turbulent transport driven by ion-scale microinstabilities, in particular Ion Temperature Gradient (ITG) instability. In first approximation, these particles, which are highly mobile along the confining magnetic field, are assumed to respond adiabatically to the low frequency ion-scale modes. However, near mode rational surfaces (MRSs), non-adiabatic response of passing electrons becomes important and can no longer be neglected. One such effect of non-adiabatic passing electrons that is of particular interest to this work is the self-interaction mechanism, which is essentially a process by which a microturbulence eigenmode that is extended along the direction parallel to the magnetic field interacts with itself non-linearly. This process is known to drive zonal flows, in particular generate stationary zonal flow shear layers at radial locations near low order mode rational surfaces [Waltz et al., 2006, Dominski et al., 2015, Weikl et al., 2018].

The work done as part of this thesis can be broadly classified into two parts:

1. Effect of self-interaction on zonal flows and convergence of tokamak core turbulence with toroidal system size.

In this part, the self-interaction mechanism is studied in detail. The self-interaction mechanism is found to also play a significant role in generating fluctuating zonal flows, which is critical to regulating transport throughout the radial extent. Using novel statistical diagnostic methods, it is found that, unlike the usual picture of zonal flow drive where the various microturbulence eigenmodes coherently amplify

the flow via the modulational instability mechanism, the self-interaction drive of zonal flows from each of these eigenmodes are uncorrelated with each other in time. The associated shearing rate of the fluctuating zonal flows therefore reduces as more toroidal modes are resolved in the simulation. In flux-tube simulations accounting for the full toroidal domain, such an increase in the density of toroidal modes corresponds to an increase in the system size, leading to a finite system size effect that is distinct from the well-known profile shearing effects [Waltz et al., 1998, Waltz et al., 2002, McMillan et al., 2010].

2. Effect of collisions and background shear flow on the non-adiabatic passing electron dynamics.

In this part, the study of non-adiabatic passing electrons dynamics is pursued further to include more reactor relevant conditions. In particular, the effects of collisions and background shear flow are studied, since a priori, they were considered as potential factors might disrupt the self-interaction mechanism. It is found that, with increasing collisionality, electrons behave more adiabatic-like, especially the trapped electrons away from MRSs, thereby leading to a decrease in the growth rate of ITG eigenmodes. The shortened electron mean free path in presence of collisions also leads to a radial broadening of the fine-structures at the MRSs of corresponding linear eigenmodes. In nonlinear simulations, the turbulent flux levels decrease with increasing collisionality, as a result of the reduced drive from the less unstable ITG eigenmodes. Furthermore, the radial width of the fine structures at MRSs is found to reduce with increasing collisionality as a result of reduced nonlinear modification of the eigenmodes. A study of the effect of collisions on the self-interaction mechanism reveals that for physically relevant values of collisionality, the effect of self-interaction is still significant. A preliminary study on the effect of background $E \times B$ flow shear shows that the fine-structures associated with the non-adiabatic passing electron response persist even with finite background flow shearing rates. The turbulent flux-levels decrease with increasing values of background shearing rate, and radially propagating soliton-like structures are seen, similar to the results obtained with adiabatic electrons in previous studies.

The rest of the thesis is organised as follows. First, a brief theoretical background on simulating microturbulence using gyrokinetic codes is provided in chapter 2, including discussions on the magnetic equilibrium, the gyrokinetic framework, the physics behind the various instabilities and the relevant details of the GENE code. In chapter 3, the effect of self-interaction on zonal flows and convergence of tokamak core turbulence with toroidal system size is discussed. In chapter 4, the effect of collisions and background shear flow on the non-adiabatic passing electron dynamics in Ion Temperature Gradient driven microturbulence is discussed. The conclusions are presented in chapter 5.

2 Theoretical Background

In this chapter, the basic theoretical background necessary for modelling microturbulence in a tokamak is discussed.

This chapter is organised as follows. In section 2.1, a brief description of the magnetic equilibrium in a tokamak is given. In particular, the ad-hoc circular geometry considered in the simulations studied in later chapters is presented. In section 2.2, the most general set of equations modelling plasma, namely the Vlasov-Maxwell system of equations is presented. Given that modelling the full Vlasov-Maxwell system in a magnetic fusion device is computationally very costly, various reduced models such as the fluid, drift kinetic, gyrokinetic etc. are widely used depending on the physics of interest. In this thesis, the gyrokinetic model is used to simulate microturbulence. In section 2.3, the gyrokinetic model is presented including an outline of the derivation of gyrokinetic equations. This is followed by a brief description of collision operators in section 2.4. In section 2.5, the basic mechanisms behind the various microinstabilities such as Ion Temperature Gradient (ITG), Trapped Electron Mode (TEM) etc. are introduced. And finally, in section 2.6, the relevant details of the GENE code used to simulate microturbulence in this thesis are given.

2.1 Magnetic equilibrium

In cylindrical coordinates (R, Z, φ) , illustrated in figure 2.1, the magnetic field can be written as $\mathbf{B} = \mathbf{B}_p + \mathbf{B}_\varphi$, where $\mathbf{B}_p = B_R \mathbf{e}_R + B_Z \mathbf{e}_Z$ and $\mathbf{B}_\varphi = B_\varphi \mathbf{e}_\varphi$ are the poloidal and toroidal components of the magnetic field respectively. Given the toroidal axisymmetry of any equilibrium quantity A in a tokamak, which implies that $\partial A / \partial \varphi = 0$, one can write $\nabla \cdot \mathbf{B} = 0$ as

$$\frac{1}{R} \frac{\partial(RB_R)}{\partial R} + \frac{\partial B_Z}{\partial Z} + \frac{1}{R} \frac{\partial B_\varphi}{\partial \varphi} \overset{0}{=} 0. \quad (2.1)$$

Chapter 2. Theoretical Background

Defining

$$B_z = \frac{1}{R} \frac{\partial \psi}{\partial R} \quad \text{and} \quad B_R = -\frac{1}{R} \frac{\partial \psi}{\partial Z}, \quad (2.2)$$

lets one express the poloidal magnetic field as $\mathbf{B}_p = \nabla \varphi \times \nabla \psi = \nabla \times (\psi \nabla \varphi)$, where ψ is called the stream function. Since $\nabla \psi \cdot \mathbf{B} = 0$, $\psi = \text{const}$ represent magnetic surfaces on which magnetic field lines lie. The magnetic equilibrium in a tokamak is characterised by these magnetic flux surfaces, the inner-most of which reduces to a toroidal line called the magnetic axis. ψ is also a measure of the poloidal magnetic flux $\Phi = \int_S \mathbf{B}_p \cdot d\bar{S}$ through a surface S that takes the form of a ribbon enclosed by two toroidal lines, one of which is on the magnetic surface of interest and the other chosen to be the magnetic axis:

$$\Phi = \int_S \mathbf{B}_p \cdot d\bar{S} = \int_l \psi \nabla \varphi \cdot d\bar{l} = 2\pi\psi \quad (2.3)$$

having made use of the Stoke's theorem, $d\bar{l} = \nabla \varphi / |\nabla \varphi|$, $|\nabla \varphi| = 1/R$ and the fact that poloidal magnetic flux on the magnetic axis is zero. Hence, ψ is also called the poloidal flux function.

The plasma equilibrium in a tokamak is described by the pressure P , current \mathbf{J} and magnetic field \mathbf{B} profiles. Given the equilibrium pressure and current profiles, the corresponding magnetic profile can be found using the Grad-Shafranov equation. One can derive the Grad-Shafranov equation using the ideal Magnetohydrodynamics (MHD) equations which at equilibrium become

$$\nabla P = \mathbf{J} \times \mathbf{B} \quad [\text{force balance}], \quad (2.4)$$

$$\nabla \times \mathbf{B} = \mu_0 \mathbf{J} \quad [\text{Ampère's law}], \quad (2.5)$$

$$\nabla \cdot \mathbf{B} = 0. \quad (2.6)$$

Defining $F(\psi) = RB_\varphi$, one can express the magnetic field as

$$\mathbf{B} = \nabla \varphi \times \nabla \psi + F \nabla \varphi. \quad (2.7)$$

Similarly, one can also express current as

$$\mathbf{J} = \frac{1}{\mu_0} \nabla \varphi \times \nabla F + J_\varphi \nabla \varphi, \quad (2.8)$$

where $\mathbf{J}_p = \mu_0^{-1} \nabla \varphi \times \nabla F$ is the poloidal current. One can in fact show that the function $F(\psi)$ measures the total poloidal current flowing through a surface S extending between the magnetic axis and the magnetic surface labelled by ψ , *i.e.* $\int_S \mathbf{J}_p \cdot d\bar{S} = 2\pi F(\psi)$. Combining equations (2.7) and (2.8) with (2.4) and projecting the resulting equation in the direction normal to the magnetic surface, one obtains the Grad-Shafranov equation:

$$\Delta^* \psi \equiv R^2 \nabla \cdot \left(\frac{1}{R^2} \nabla \psi \right) = -\mu_0 R^2 \frac{\partial P}{\partial \psi} - F \frac{\partial F}{\partial \psi}. \quad (2.9)$$

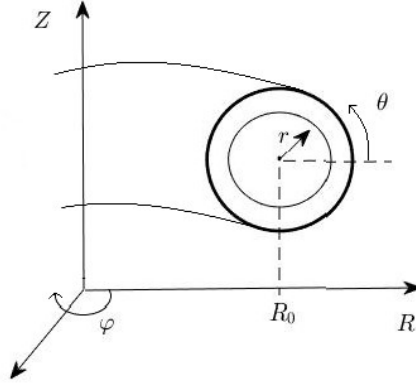


Figure 2.1: Schematic representation of the cylindrical (R, Z, φ) and toroidal (r, θ, φ) coordinates.

Provided the pressure P and current F profiles, the solution to the Grad-Shafranov equation gives the magnetic field equilibrium in a tokamak. Equilibrium codes such as CHEASE [Lütjens et al., 1996] solve the Grad-Shafranov equation and outputs all the magnetic field quantities including the safety factor profile, Jacobian, metric coefficients etc. which are then used as inputs by microturbulence simulations.

Note that the safety factor $q_s(\psi)$ measures the number of toroidal turns taken by a magnetic field line to cover one poloidal turn on the magnetic surface labelled by ψ . More specifically, it is defined as

$$q(\psi) = \frac{1}{2\pi} \int_0^{2\pi} \frac{d\varphi}{d\theta} \Big|_{\text{along } B_0} = \frac{1}{2\pi} \int_0^{2\pi} \frac{\mathbf{B} \cdot \nabla \varphi}{\mathbf{B} \cdot \nabla \theta} d\theta, \quad (2.10)$$

where θ is the geometric poloidal angle (see figure 2.1).

For many applications, it proves useful to consider simple analytic models such as the so-called circular ad-hoc, $s - \alpha$ model, etc., to set the equilibrium magnetic configuration. In the following, a brief description of the circular ad-hoc model is provided. This analytic model is used in the simulations that are studied in this thesis.

Circular ad-hoc geometry

Circular ad-hoc geometry [Lapillonne et al., 2009] represents circular concentric flux-surfaces centered at the magnetic axis. The poloidal flux function $\psi = \psi(r)$ is therefore only a function of r , which is the radial coordinate in the toroidal coordinate system

Chapter 2. Theoretical Background

(r, θ, φ) [see figure 2.1]. The following equation defines the circular ad-hoc geometry:

$$\frac{d\psi}{dr} = \frac{rB_0}{\bar{q}_s(r)}, \quad (2.11)$$

where $\bar{q}_s(r)$ is a pseudo-safety factor related to the true safety factor $q_s(r)$ as shown in equation (2.12). Note that this is only an approximate solution to the Grad-Shafranov equation. The magnetic field can now be expressed as $\mathbf{B} = R_0 B_0 / R [\mathbf{e}_\varphi + r/(R_0 \bar{q}(r)) \mathbf{e}_\theta]$ and the safety factor $q_s(r)$ defined in equation (2.10) becomes

$$\begin{aligned} q_s(r) &= \frac{1}{2\pi} \bar{q}_s(r) \int_0^{2\pi} \frac{1}{1 + \epsilon \cos \theta'} d\theta' \\ &= \frac{\bar{q}_s}{\sqrt{1 - \epsilon^2}}, \end{aligned} \quad (2.12)$$

having used the relation $R = R_0(1 + \epsilon \cos \theta)$, where $\epsilon = r/R_0$ is the inverse aspect ratio of the magnetic surface being considered.

The straight field line poloidal angle χ is defined such that $(\mathbf{B} \cdot \nabla \varphi) / (\mathbf{B} \cdot \nabla \chi) = q(r)$, leading to the relation $d\chi/d\theta = \mathbf{B} \cdot \nabla \varphi / (q(r) \mathbf{B} \cdot \nabla \theta)$. Integrating along θ , one obtains

$$\chi(r, \theta) = \frac{1}{q(r)} \int_0^\theta \frac{\mathbf{B} \cdot \nabla \varphi}{\mathbf{B} \cdot \nabla \theta'} d\theta' = 2 \tan^{-1} \left[\sqrt{\frac{1 - \epsilon}{1 + \epsilon}} \tan \left(\frac{\theta}{2} \right) \right]. \quad (2.13)$$

The corresponding metric tensors $g^{\nu\mu} = \nabla \nu \cdot \nabla \mu$ for $\nu, \mu \in \{\psi, \chi, \varphi\}$ are

$$\begin{aligned} g^{\psi\psi} &= \frac{B_0^2 r^2}{\bar{q}^2}, & g^{\psi\chi} &= -\frac{B_0 \epsilon}{\bar{q}} \frac{\sin \chi}{(1 - \epsilon^2)}, & g^{\psi, \varphi} &= 0, \\ g^{\chi\chi} &= \frac{1}{r^2} \left[\frac{R_0^2 \bar{q}^2}{R^2 q^2} + \frac{\epsilon^2 \sin^2 \chi}{(1 - \epsilon^2)^2} \right], & g^{\chi\varphi} &= 0, & g^{\varphi\varphi} &= \frac{1}{R^2}. \end{aligned} \quad (2.14)$$

2.2 Vlasov-Maxwell system

While it is possible to evolve individual motion of each plasma particle using the Lorentz equation of motion, it proves advantageous in many cases to treat the plasma as a continuous distribution $f_s(\mathbf{x}, \mathbf{v}, t)$ in phase space and then evolve f_s using the Vlasov equation. Physically, $f_s(\mathbf{x}, \mathbf{v}, t)$ measures the number of particles of species s in the infinitesimally small phase space volume $d^3\mathbf{x}, d^3\mathbf{v}$ at the position (\mathbf{x}, \mathbf{v}) , at time t . The corresponding Vlasov equation is:

$$\frac{df_s}{dt} = \frac{\partial f_s}{\partial t} + \dot{\mathbf{x}} \cdot \frac{\partial f_s}{\partial \mathbf{x}} + \dot{\mathbf{v}} \cdot \frac{\partial f_s}{\partial \mathbf{v}} = 0, \quad (2.15)$$

where $\dot{\mathbf{x}} = \mathbf{v}$ and $\dot{\mathbf{v}} = (q_s/m_s)[\mathbf{E}(\mathbf{x}, t) + \mathbf{v} \times \mathbf{B}(\mathbf{x}, t)]$. The operator d/dt in equation (2.15) represents the total time derivative along the unperturbed trajectories in phase space.

The electric and magnetic fields can be obtained from Maxwell's equations:

$$\begin{aligned}\nabla \cdot \mathbf{E} &= \frac{1}{\epsilon_0} \sum_s \varrho_s, & \nabla \times \mathbf{E} &= -\frac{\partial \mathbf{B}}{\partial t}, \\ \nabla \cdot \mathbf{B} &= 0, & \nabla \times \mathbf{B} &= \mu_0 \sum_s \mathbf{J}_s + \mu_0 \epsilon_0 \frac{\partial \mathbf{E}}{\partial t},\end{aligned}\tag{2.16}$$

where the self-consistent charge density is given by $\varrho_s = q_s \int f_s d\mathbf{v} + \varrho_{s,\text{ext}}$ and the current density by $\mathbf{J}_s = q_s \int f_s \mathbf{v} d\mathbf{v} + \mathbf{J}_{s,\text{ext}}$, with $\varrho_{s,\text{ext}}$ and $\mathbf{J}_{s,\text{ext}}$ being the possible external density and current sources respectively.

Equation (2.15) along with (2.16), solved self-consistently, is called the Vlasov-Maxwell system of equations and is one of the most fundamental descriptions of plasma. Note that this system of nonlinear integro-differential equations in 6-dimensional phase space cannot be solved analytically except for some simplified cases, and in general will require numerical computation to solve them. Since tokamak plasma dynamics contain vastly different time scales from the fast electron gyromotion ($\sim 10^{-11}\text{s}$) to confinement times $\sim 10^0\text{s}$ and vastly different spatial scales from the Debye length ($\sim 10^{-4}\text{m}$) to machine size ($\sim 10^0\text{m}$), it is computationally too costly to resolve all these scales. Hence, based on the physical phenomenon of interest, various approximations are made to the Vlasov-Maxwell system of equations. The fluid description is one of the most widely used approaches where the velocity moments of the Vlasov equation leads to time evolution equations for a finite number of moments (such as density, average velocity, pressure and possibly more depending on the considered approximations), essentially reducing the Vlasov-Maxwell system in 6-dimensional phase space to a problem in 3-dimensional configuration space, while ignoring the 'kinetic' dynamics in the velocity space. In cases where the plasma collisionality (more on collisionality discussed in section 2.4) is high, the fluid description proves to be a good model (*e.g.* the set of Braginskii equations [Braginskii, 1965]). However to model microturbulence in a tokamak core where the collisionality is very low and the kinetic effects are relevant, the gyrokinetic model is the most appropriate. In simple terms, this model involves an average over the fast gyromotion of the particles, eliminating the gyroangle dependence and reducing the problem to an effective 5-dimensional phase space. In the next section, an outline of the approximations and the derivation involved in the gyrokinetic model are discussed.

2.3 The gyrokinetic framework

The aim of gyrokinetics is to reduce the dimensionality of the Vlasov-Maxwell system from 6 to 5 by averaging out the fast gyromotion of particles. As a result, the fast cyclotron time scale is also removed. Therefore, gyrokinetic equations are appropriate for representing the low frequency microinstabilities and associated turbulence. In this section, an outline of the modern gyrokinetic theory is given, based on the main original

references [Littlejohn, 1982, Hahm, 1988, Brizard and Hahm, 2007, Cary and Brizard, 2009] and the citations therein. The theses [Görler, 2009, Lapillone, 2010, Dominski, 2016, Merlo, 2016] have been used as immediate references for writing this section.

2.3.1 The gyrokinetic ordering

In the gyrokinetic formalism, the high frequency cyclotron time scales associated with the fast gyromotion is eliminated, *i.e.* the phase of the gyromotion is not resolved, while retaining only the motion of the center of the gyromotion (called the guiding center) along with its finite Larmor radius effect. An essential factor that enables such an approach is the scale separation between Larmor radius (\sim perpendicular scale length of fluctuations) and the background equilibrium scale lengths. In fact all the scale separations that motivate/justify the gyrokinetic approach have been experimentally observed in magnetically confined high temperature plasma in the tokamak core, and are listed below.

1. Spatial scale separation between fluctuations and equilibrium quantities: In the direction perpendicular to the magnetic field, the spatial extension of the fluctuations is typically of the order of the Larmor radius ρ_i . Whereas, the characteristic gradient lengths L_N and L_T of the equilibrium density and temperature profiles respectively are of the order of the minor radius a , which is typically much larger than the Larmor radius of any species. Furthermore, the characteristic gradient length L_B of the background magnetic field strength is of the order of the major radius R . Since $a \sim R$, with the inverse aspect ratio often $\epsilon = a/R \sim 0.2 - 0.4$, one has $\rho_i \ll L_g$, where $L_g (\simeq L_N \simeq L_T \simeq L_B)$ is any characteristic equilibrium length scale.
2. Time-scale separation: The small scale fluctuations in the plasma, typically resulting from drift-wave type instabilities have a characteristic frequency ω of the order of the diamagnetic frequency $\omega_D \simeq Tk_\perp/qB_0L_N$, where L_N is the characteristic length scale of equilibrium density gradient. These frequencies are much smaller than the gyro-frequency Ω associated to the fast gyromotion of the particles, *i.e.* $\omega \ll \Omega$.
3. Anisotropy of the fluctuations: As already mentioned in the previous point, the fluctuations are constrained in the perpendicular direction by the Larmor radius and the corresponding wavenumber follows $k_\perp \rho_i \sim 1$. Whereas no such constraint is observed in the parallel direction. The fluctuations therefore extend significantly more along the direction parallel to the magnetic field as compared to the perpendicular direction, *i.e.* $k_\parallel/k_\perp \ll 1$.
4. Small relative fluctuation levels: $\delta f/f_0 \ll 1$, where δf and f_0 are the fluctuating and equilibrium parts of distribution function respectively. The same ordering

holds for the field quantities, *i.e.* $e\Phi_1/T_0 \ll 1$ and $\delta B/B_0 \ll 1$, where Φ_1 and δB are the fluctuating scalar potential and magnetic field respectively.

In the gyrokinetic framework, all the above mentioned scale-separations are assumed to follow the ordering:

$$\frac{\rho_i}{L_g} \sim \frac{\omega}{\Omega} \sim \frac{k_{\parallel}}{k_{\perp}} \sim \frac{\delta f}{f_0} \sim \frac{e\Phi_1}{T_0} \sim \frac{\delta B}{B_0} \sim \epsilon, \quad (2.17)$$

where $\epsilon \ll 1$ is a small parameter.

2.3.2 The modern gyrokinetic derivation

The modern derivation of the gyrokinetic model can be broadly divided into two steps. Using the gyrokinetic ordering mentioned in the previous subsection and the scale separations involved, one can change the coordinate system from the original particle phase space variables to a new coordinate system called the guiding center coordinate system where it is possible to easily average out the gyroangle dependence from the Vlasov equation in the absence of fluctuations. This change of coordinates from the particle to guiding center variables is essentially the first step in the gyrokinetic derivation. However it turns out that the gyroangle dependence in the Vlasov equation accounting for fluctuations cannot be removed as easily. Hence, towards this goal, in the second step, a further change of coordinates to the so-called gyrocenter coordinates is carried out using Lie transformations. These two steps have been illustrated in subsections 2.3.2.1 and 2.3.2.2, followed by obtaining the final form of the gyrocenter equation in subsection 2.3.2.3.

2.3.2.1 Particle coordinates - Guiding center transformation

For a charged particle in electromagnetic field, the Lagrangian in the particle coordinates (\mathbf{x}, \mathbf{v}) is given by $\mathcal{L} = \mathbf{p} \cdot \mathbf{v} - \left[\frac{1}{2}mv^2 + q\Phi(\mathbf{x}, t) \right]$, where $\mathbf{p} = m\mathbf{v} + q\mathbf{A}(\mathbf{x}, t)$ is the canonical momentum. The corresponding one-form γ is then defined as

$$\gamma \equiv \mathcal{L}dt = [m\mathbf{v} + q\mathbf{A}(\mathbf{x}, t)] \cdot d\mathbf{x} - \left[\frac{1}{2}mv^2 + q\Phi(\mathbf{x}, t) \right] dt. \quad (2.18)$$

Let, $\mathbf{A}(\mathbf{x}, t) = \mathbf{A}_0(\mathbf{x}, t) + \mathbf{A}_1(\mathbf{x}, t)$ and $\Phi(\mathbf{x}, t) = \Phi_1(\mathbf{x}, t)$, where fields have been split into the equilibrium and perturbed parts, with $\mathbf{B}_0 = \nabla \times \mathbf{A}_0$ and assuming that the equilibrium electrostatic field $\Phi_0(\mathbf{x}, t) \equiv 0$. The one-form can be similarly split into the

Chapter 2. Theoretical Background

equilibrium and perturbed part as

$$\gamma = \gamma_0 + \gamma_1 \quad \text{where} \quad (2.19)$$

$$\gamma_0 = [m\mathbf{v} + q\mathbf{A}_0(\mathbf{x})] \cdot d\mathbf{x} - \frac{1}{2}mv^2 dt \quad \text{and} \quad (2.20)$$

$$\gamma_1 = q\mathbf{A}(\mathbf{x}, t) \cdot d\mathbf{x} - q\Phi_1(\mathbf{x}, t)dt. \quad (2.21)$$

As mentioned earlier, the objective of the first step in the gyrokinetic derivation is the transformation from the particle to the guiding center coordinate system where the fast gyromotion can be averaged out for the equilibrium dynamics. The guiding center coordinates are defined by the variables $(\mathbf{X}_g, v_{\parallel,g}, \mu_g, \alpha_g)$, where \mathbf{X}_g is the guiding center position, $v_{\parallel,g} = \mathbf{v} \cdot \mathbf{b}_0$ is the velocity parallel to the equilibrium magnetic field, $\mu_g = (mv_{\perp,g}^2)/(2B_0)$ is the magnetic moment and α_g is the gyroangle. $\mathbf{v}_{\perp,g} = \mathbf{v} - v_{\parallel,g}\mathbf{b}_0$, $\mathbf{b}_0 = \mathbf{B}_0/B_0$ and $B_0 = |\mathbf{B}_0|$. Based on the gyrokinetic ordering, in particular that the magnetic field varies slowly over spatial distances of the order of Larmor radius ($\rho_i/L_B \sim \epsilon \ll 1$), one can approximate the fast gyromotion of the particles as a circle in the plane perpendicular to the magnetic field to zeroth order in ϵ . The transformation from particles to guiding center coordinates can then be expressed as

$$\mathbf{x} = \mathbf{X}_g + \mathbf{r} \quad \text{and} \quad \mathbf{v} = v_{\parallel,g}\mathbf{b}_0 + v_{\perp,g}\mathbf{c}(\alpha_g), \quad (2.22)$$

where

$$\mathbf{r} = \frac{v_{\perp,g}}{\Omega(\mathbf{X}_g)}\mathbf{a}(\alpha_g), \quad (2.23)$$

and $\mathbf{a}(\alpha_g) = \cos \alpha_g \mathbf{e}_1 + \sin \alpha_g \mathbf{e}_2$ and $\mathbf{c}(\alpha_g) = -\sin \alpha_g \mathbf{e}_1 + \cos \alpha_g \mathbf{e}_2$ are unit vectors along the radial and tangential directions to a (gyro)circle in the local Cartesian coordinate system spanned by $(\mathbf{e}_1, \mathbf{e}_2, \mathbf{b}_0)$.

Now in order to express the one-form in guiding center coordinates, one can make use of the following relation. Under a coordinate transformation $(z) \rightarrow (Z)$, the one-form Γ in the new coordinates (Z) can be expressed in terms of the one-form γ in the old coordinates (z) as

$$\gamma_\mu dz^\mu = \gamma_\nu \frac{\partial z^\nu}{\partial Z^\mu} dZ^\mu = \Gamma_\mu dZ^\mu, \quad (2.24)$$

where $z^\mu = (z, t)$, $Z^\mu = (Z, t)$ and Einstein's summation convention is implied. Furthermore, using the first order expansion $\mathbf{A}_0(\mathbf{X}_g + \mathbf{r}) \simeq \mathbf{A}_0(\mathbf{X}_g) + \mathbf{r} \cdot \nabla \mathbf{A}_0|_{\mathbf{X}_g}$, and performing an appropriate phase space gauge transformation (equivalent to applying the gyroaverage operator $\mathcal{G} = \frac{1}{2\pi} \int d\alpha_g$), the unperturbed one-form in guiding center coordinates to zeroth

order in ϵ becomes

$$\Gamma_{0,g}(\mathbf{X}_g, v_{\parallel,g}, \mu_g) = \left[m v_{\parallel,g} \mathbf{b}_0(\mathbf{X}_g) + q \mathbf{A}_0(\mathbf{X}_g) \right] \cdot d\mathbf{X}_g + \frac{m}{q} \mu_g d\alpha_g - \left[\frac{1}{2} m v_{\parallel,g}^2 + \mu_g B_0(\mathbf{X}_g) \right] dt. \quad (2.25)$$

Note that $\Gamma_{0,g}$ is independent of α_g , implying that α_g is a cyclic variable. Furthermore, the associated canonical momentum is the magnetic moment μ_g which is therefore an invariant of motion of the unperturbed trajectories.

Similarly, the perturbed part of the one-form to first order in ϵ can be obtained as

$$\begin{aligned} \Gamma_{1,g}(\mathbf{X}_g, v_{\parallel,g}, \mu_g, \alpha_g) = \\ q \mathbf{A}_1(\mathbf{X}_g + \mathbf{r}, t) \cdot \left[d\mathbf{X}_g + \frac{1}{q v_{\perp}(\mathbf{X}_g)} \mathbf{a}(\alpha_g) d\mu_g + \frac{m v_{\perp}(\mathbf{X}_g)}{q B_0(\mathbf{X}_g)} \mathbf{c}(\alpha_g) d\alpha_g \right] - q \Phi_1(\mathbf{X}_g + \mathbf{r}, t) dt. \end{aligned} \quad (2.26)$$

Note that the dependence of \mathbf{r} , \mathbf{a} and \mathbf{c} on α_g in the above equation reflects that α_g is not a cyclic variable in presence of fluctuations. Since the fluctuating fields vary strongly with spatial distances of the order of $|\mathbf{r}|$ (\sim gyroradius ρ), a simple gyroaveraging is not applicable. Hence another coordinate change to the gyro-center coordinates is required to systematically eliminate the gyroangle dependence.

2.3.2.2 Guiding center - Gyrocenter transformation

The guiding center $Z_g = (\mathbf{X}_g, v_{\parallel,g}, \mu_g, \alpha_g)$ to gyrocenter $Z = (\mathbf{X}, v_{\parallel}, \mu, \alpha)$ coordinate transformation is done via Lie transforms which is a continuous, near identity coordinate transformation:

$$Z(Z_g, \epsilon) = T^{-1} Z_g, \quad (2.27)$$

where $Z(Z_g, 0) = Z_g$ and the Lie transform can be expressed as

$$T = e^{-\epsilon L}. \quad (2.28)$$

L is the Lie derivative operator which acts on a scalar function \mathcal{F}_g as

$$L \mathcal{F}_g = g^\nu \frac{\partial \mathcal{F}_g}{\partial Z_g^\nu}, \quad (2.29)$$

and on the one-form $\Gamma_g = \Gamma_{g,\mu} dZ_g^\mu$ as

$$(L \Gamma_g)_\mu = g^\nu \left(\frac{\partial \Gamma_{g,\mu}}{\partial Z_g^\nu} - \frac{\partial \Gamma_{g,\nu}}{\partial Z_g^\mu} \right), \quad (2.30)$$

Chapter 2. Theoretical Background

with the indices μ, ν running over all the coordinates in (Z_g, t) , and the sum over ν is implied following Einstein's convention. The generators g^ν associated to the Lie transform are defined by

$$g^\nu = \frac{\partial Z_g}{\partial \epsilon}. \quad (2.31)$$

A general coordinate transformation can now be expressed as

$$\Gamma = T\Gamma_g + dS, \quad (2.32)$$

where S represents a possible phase space gauge and the overall transform T is composed of individual Lie transforms as

$$T = \dots T_2 \cdot T_1 \quad (2.33)$$

with each transform $T_n = e^{-\epsilon^n L_n}$. Expanding each term in equation (2.32) in terms of ϵ , the one-form can be written as $\Gamma = \Gamma_0 + \Gamma_1 + \dots$, with

$$\Gamma_0 = \Gamma_{g,0} + dS_0, \quad (2.34)$$

$$\Gamma_1 = \Gamma_{g,1} - L_1\Gamma_{g,0} + dS_1 \quad (2.35)$$

Now, by specifying appropriate generators and phase space gauge terms at each order in ϵ , the gyroangle dependence can be removed from Γ , thus ensuring that the transformed gyroangle α remains cyclic in presence of fluctuations. Since, we are interested in a transformation to first order in ϵ , the corresponding generators (see reference [Dannert, 2005] for details) are

$$\begin{aligned} g_1^{\mathbf{x}} &= \tilde{\mathbf{A}}_1 \times \frac{\mathbf{b}_0}{B_{0,\parallel}^*} - \frac{1}{m} \frac{\mathbf{B}_{0,\parallel}^*}{B_{0,\parallel}^*} \frac{\partial S_1}{\partial v_{\parallel}} + \frac{1}{q} \nabla S_1 \times \frac{\mathbf{b}_0}{B_{0,\parallel}^*}, \\ g_1^{v_{\parallel}} &= \frac{1}{m} \frac{\mathbf{B}_{0,\parallel}^*}{B_{0,\parallel}^*} \cdot (q\tilde{\mathbf{A}}_1 + \nabla S_1), \\ g_1^\mu &= q \frac{v_{\perp}}{B_0} \mathbf{A}_1 \cdot \mathbf{c} + \frac{q}{m} \frac{\partial S_1}{\partial \alpha}, \\ g_1^\alpha &= -\frac{q}{m} \left(\frac{1}{v_{\perp}} \mathbf{A}_1 \cdot \mathbf{a} + \frac{\partial S_1}{\partial \mu} \right), \\ g_1^t &= 0, \end{aligned} \quad (2.36)$$

and the corresponding gauge S_1 is

$$S_1 = \frac{1}{\Omega} \int^\alpha \left(q\tilde{\Phi}_1 + \frac{1}{B_{0,\parallel}^*} (\mathbf{b}_0 \times \tilde{\mathbf{A}}_1) \cdot \mu \nabla B_0 - qv_{\parallel} \frac{\mathbf{B}_0^*}{B_{0,\parallel}^*} \cdot \tilde{\mathbf{A}}_1 - qv_{\perp} \widetilde{\mathbf{A} \cdot \mathbf{c}} \right) d\alpha', \quad (2.37)$$

where $\mathbf{B}_0^* = \mathbf{B}_0 + (m/q)v_{\parallel} \nabla \times \mathbf{b}_0$ and $\tilde{\mathcal{F}}(\mathbf{X}, \mu, \alpha) = \mathcal{F}(\mathbf{X} + \mathbf{r}) - \bar{\mathcal{F}}(\mathbf{X}, \mu)$, with $\bar{\mathcal{F}}(\mathbf{X}, \mu)$

denoting the gyroaverage of the quantity \mathcal{F} as:

$$\bar{\mathcal{F}}(\mathbf{X}, \mu) = \frac{1}{2\pi} \int \mathcal{F}(\mathbf{X} + \mathbf{r}(\mathbf{X}, \mu, \alpha)) d\alpha. \quad (2.38)$$

The one-form in gyrocenter coordinates now becomes

$$\begin{aligned} \Gamma &= \Gamma_0 + \Gamma_1, \\ &= \left(mv_{\parallel} \mathbf{b}_0 + q \mathbf{A}_0 + q \bar{A}_{1,\parallel} \mathbf{b}_0 \right) \cdot d\mathbf{X} + \frac{m}{q} \mu d\alpha - \left(\frac{1}{2} mv_{\parallel}^2 + q \bar{\Phi}_1 + \mu (B_0 + \bar{B}_{1,\parallel}) \right) dt. \end{aligned} \quad (2.39)$$

Note that in the above equations, the equilibrium quantities have been evaluated at the gyrocenter \mathbf{X} . The perturbed fields are evaluated at the particle position $\mathbf{x} = \mathbf{X} + \mathbf{r}$ and furthermore gyroaveraged, so that Γ is independent of the gyroangle α , which is therefore cyclic as intended.

The particle distribution function in gyrocenter variables $f(Z)$ can be expressed in guiding center variables $f_g(Z_g)$ using the operator T^{-1} as:

$$f_g(Z_g) = (T^{-1}f)(Z_g), \quad (2.40)$$

where T^{-1} is now also called the pull-back operator.

Note that, from this point on in this chapter, only the magnetic fluctuations related to $A_{1,\parallel}$ are considered while the parallel magnetic fluctuations $B_{1,\parallel}$ are neglected.

Using equations (2.28), (2.29), (2.33) and (2.40), the perturbed part of the distribution function for a species denoted by index j in guiding center variables can be expressed in terms of gyrocenter variables as

$$f_{g,1,j} = f_{1,j} + \frac{1}{B_0} \left[\left(\Omega_j \frac{\partial f_{0,j}}{\partial v_{\parallel}} - q_j v_{\parallel} \frac{\partial f_{0,j}}{\partial \mu} \right) \bar{A}_{1,\parallel} + q_j \bar{\Phi}_1 \frac{\partial f_{0,j}}{\partial \mu} \right]. \quad (2.41)$$

2.3.2.3 The gyrokinetic equation

For a given one-form Γ in coordinates (Z, t) , the corresponding Euler-Lagrange equations of motion are given by:

$$\omega_{\mu\nu} \frac{dZ^\nu}{dt} = 0, \quad \text{where} \quad \omega_{\mu\nu} = \frac{\partial \Gamma_\nu}{\partial Z^\mu} - \frac{\partial \Gamma_\mu}{\partial Z^\nu}. \quad (2.42)$$

Using the above relation for the one-form in gyrocenter coordinates obtained in equation (2.39), and the approximation $\nabla(\bar{A}_{1,\parallel} \mathbf{b}_0) \simeq \nabla \bar{A}_{1,\parallel} \times \mathbf{b}_0 + O(\epsilon)$, the corresponding

Chapter 2. Theoretical Background

equations of motion reduce to:

$$\dot{\mathbf{X}} = v_{\parallel} \mathbf{b}_0 + \frac{B_0}{B_{0,\parallel}^*} (\mathbf{v}_E + \mathbf{v}_{\nabla B} + \mathbf{v}_C), \quad (2.43a)$$

$$\dot{v}_{\parallel} = -\frac{1}{m_j v_{\parallel}} \dot{\mathbf{X}} \cdot (q_j \nabla \bar{\Phi}_1 + q_j \mathbf{b}_0 \dot{\bar{A}}_{1,\parallel} + \mu \nabla B_0), \quad (2.43b)$$

$$\dot{\mu} = 0, \quad (2.43c)$$

$$\dot{\alpha} = \Omega_j + \frac{q_j^2}{m_j} \left(\frac{\partial \bar{\Phi}_1}{\partial \mu} - v_{\parallel} \frac{\partial \bar{A}_{1,\parallel}}{\partial \mu} \right), \quad (2.43d)$$

where the generalised $E \times B$ velocity is given by

$$\mathbf{v}_E = -\frac{\nabla(\bar{\Phi}_1 - v_{\parallel} \bar{A}_{1,\parallel}) \times \mathbf{B}_0}{B_0^2}, \quad (2.44)$$

the grad-B drift velocity by

$$\mathbf{v}_{\nabla B} = \frac{\mu}{m_j \Omega_j B_0} \mathbf{B}_0 \times \nabla B_0, \quad (2.45)$$

and the curvature drift velocity by

$$\mathbf{v}_C = \frac{v_{\parallel}^2}{\Omega_j} (\nabla \times \mathbf{b}_0) = \frac{\mu_0 v_{\parallel}^2}{\Omega_j B_0^2} \mathbf{b}_0 \times \nabla \left(P_0 + \frac{B_0^2}{2\mu_0} \right), \quad (2.46)$$

having used the equilibrium ideal MHD equations (2.4) and (2.5).

Now, the Vlasov equation (2.15) in gyrocenter coordinates can be written as:

$$\frac{df_j}{dt} = \frac{\partial f_j}{\partial t} + \dot{\mathbf{X}} \cdot \frac{\partial f_j}{\partial \mathbf{X}} + \dot{v}_{\parallel} \frac{\partial f_j}{\partial v_{\parallel}} + \dot{\mu} \frac{\partial f_j}{\partial \mu} + \dot{\alpha} \frac{\partial f_j}{\partial \alpha} = 0. \quad (2.47)$$

Given the invariance of μ in equation (2.43c), the fourth term in the above equation vanishes. Furthermore, given that the gyroangle α is now a cyclic variable, gyroaveraging the above equation (the term $\dot{\alpha} \partial f_j / \partial \alpha$ which averages out to zero given that f_j is 2π periodic in α) leads to the gyrokinetic equation

$$\frac{\partial \bar{f}_j}{\partial t} + \dot{\mathbf{X}} \cdot \frac{\partial \bar{f}_j}{\partial \mathbf{X}} + \dot{v}_{\parallel} \frac{\partial \bar{f}_j}{\partial v_{\parallel}} = 0, \quad (2.48)$$

also called specifically the 'full-f' gyrokinetic equation. In the rest of this chapter, one reassigns $\bar{f} \rightarrow f$.

Now, the gyrokinetic equation can be split into an equilibrium and a perturbed (to first

order in ϵ) part as

$$f_j = f_{0,j} + f_{1,j}. \quad (2.49)$$

This is also called the 'delta-f' splitting. One of the advantages of performing this splitting is that it enables one to obtain a linearized Vlasov-Maxwell system for the perturbed part, which can then be conveniently used for basic stability analysis. Using equations (2.47), (2.49), (2.43a) and (2.43b), the unperturbed part of the gyrokinetic equation becomes:

$$\left. \frac{df_{0,j}}{dt} \right|_{u.t.} = \left[v_{\parallel} \mathbf{b}_0 + \frac{B_0}{B_{0,\parallel}^*} (\mathbf{v}_{\nabla B} + \mathbf{v}_C) \right] \cdot \left(\nabla f_{0,j} - \frac{1}{m_j v_{\parallel}} \mu \nabla B_0 \frac{\partial f_{0,j}}{\partial v_{\parallel}} \right) = 0, \quad (2.50)$$

where $d/dt|_{u.t.}$ stands for the total time derivative along the unperturbed trajectories and the equilibrium part $f_{0,j}$ of the distribution function is assumed to be a stationary solution, *i.e.* $f_{0,j} = f_{0,j}(\mathbf{X}, v_{\parallel}, \mu) \neq \text{fct}(t)$. Now, the gyrokinetic equation of the perturbed part becomes:

$$\begin{aligned} & \frac{\partial g_{1,j}}{\partial t} + \frac{B_0}{B_{0,\parallel}^*} \mathbf{v}_E \cdot \left(\nabla f_{0,j} - \frac{\mu}{m_j v_{\parallel}} \nabla B_0 \frac{\partial f_{0,j}}{\partial v_{\parallel}} \right) \\ & + \frac{B_0}{B_{0,\parallel}^*} (\mathbf{v}_E + \mathbf{v}_{\nabla B} + \mathbf{v}_C) \cdot \left(\nabla f_{1,j} - \frac{q_j}{m_j v_{\parallel}} \nabla \bar{\Phi}_1 \frac{\partial f_{0,j}}{\partial v_{\parallel}} \right) + v_{\parallel} \mathbf{b}_0 \cdot \left(\nabla f_{1,j} - \frac{q_j}{m_j v_{\parallel}} \nabla \bar{\Phi}_1 \frac{\partial f_{0,j}}{\partial v_{\parallel}} \right) \\ & - \frac{\mu}{m_j} \left(\mathbf{b}_0 + \frac{B_0}{v_{\parallel} B_{0,\parallel}^*} \mathbf{v}_C \right) \cdot \nabla B_0 \frac{\partial f_{1,j}}{\partial v_{\parallel}} = 0, \end{aligned} \quad (2.51)$$

having defined

$$g_{1,j} = f_{1,j} - \frac{q_j}{m_j} \bar{A}_{1,\parallel} \frac{\partial f_{0,j}}{\partial v_{\parallel}}. \quad (2.52)$$

Note that, consistent with the GENE code used in this work, the parallel non-linearity $[\propto \dot{\mathbf{X}} \cdot \nabla \Phi_1 \partial f_{1,j} / \partial v_{\parallel}]$ has been neglected. In general, the parallel nonlinearity is necessary for phase space volume conservation (of particle number), and its effect could be particularly significant in 'full-f' codes with evolving backgrounds [Idomura et al., 2007]. However in reference [Candy et al., 2006], it is shown that for 'delta-f' codes (such as GENE) where only the perturbation [*i.e.* equation (2.51)] is evolved in time, the effect of parallel nonlinearity is negligible.

2.3.3 Background distribution

The background distribution $f_{0,j}$ can in general be any function of the constants of motion of the unperturbed gyrokinetic equation (2.50), namely the kinetic energy $\mathcal{E} = mv_{\parallel}^2/2 + \mu B_0$, magnetic moment μ and the toroidal canonical momentum $\psi_0 = \psi + v_{\parallel} m R B_{\varphi} / B$.

Chapter 2. Theoretical Background

Usually one assumes a Maxwellian distribution of the form [Angelino et al., 2006]:

$$f_{0,CM}(\mathcal{E}, \mu, \Psi) = \frac{N_{eq}(\Psi)}{[2\pi T_0(\Psi)/m]^{3/2}} e^{-\mathcal{E}/T_0(\Psi)}, \quad (2.53)$$

where $\Psi(\psi_0, \mathcal{E}, \mu) = \psi_0 + \psi_{0\text{corr}}$ and

$$\psi_{0\text{corr}} = -\text{sign}(v_{\parallel}) \frac{q}{m} R_0 \sqrt{2(\mathcal{E} - \mu B_{\text{max}})} \mathcal{H}(\mathcal{E} - \mu B_{\text{max}}), \quad (2.54)$$

with \mathcal{H} being the heaviside function.

Another common choice for the background distribution is the so-called local Maxwellian

$$f_{0,LM}(\mathcal{E}, \mu, \psi) = \frac{N_{eq}(\psi)}{[2\pi T_0(\psi)/m]^{3/2}} e^{-\mathcal{E}/T_0(\psi)}, \quad (2.55)$$

which is a function of the magnetic flux-surface label ψ . Note that $f_{0,LM}$ is not an exact solution of the unperturbed gyrokinetic equation. It in fact becomes a solution if the curvature and grad-B drifts are neglected in equation (2.50), and therefore can be considered as a canonical Maxwellian in the limit of zero finite orbit width. A study on the consequence of choosing local Maxwellian over the canonical Maxwellian can be found in reference [Angelino et al., 2006]. Note that, in the flux-tube model (discussed in section 2.6.2) used in simulations studied in this thesis, the perturbed gyrokinetic equation (2.51) is solved with the local Maxwellian $f_{0,LM}$ as the background distribution function.

2.3.4 Moments and fluxes

Macroscopic observables such as density, temperature, heat and particle fluxes etc. involve taking the velocity moments of the distribution function. One is usually interested in obtaining these physical quantities at fixed particle position \mathbf{x} . Therefore, it is necessary to first transform the distribution function from gyrocenter to particle coordinates. This is done in two steps: First, the transformation from gyrocenter coordinates to guiding center coordinates is done using the pull back operator T^{-1} , done in equations (2.40) and (2.41), followed by the transformation from guiding center to particle coordinates using an appropriate delta function, as shown below:

$$\mathcal{A}[a](\mathbf{x}) = \int d\mathbf{X} dv_{\parallel} d\mu d\alpha \frac{B_{0,\parallel}^*}{m_j} \delta(\mathbf{X} + \mathbf{r} - \mathbf{x}) a(\mathbf{X}, v_{\parallel}, \mu) T^{-1} f_{1,j}(\mathbf{X}, v_{\parallel}, \mu), \quad (2.56)$$

where $\mathcal{A}[a](\mathbf{x})$ is the perturbed part of an observable in particle coordinates \mathbf{x} , which, depending on the choice of a , gives different physical quantities of interest, some of which are listed below:

1. Density, $n_{1,j} = \mathcal{A}[1]$
2. Parallel fluid velocity, $u_{1,\parallel,j} = \mathcal{A}[v_{\parallel}]/n_{0,j}$
3. Parallel temperature, $T_{1,\parallel,j} = \mathcal{A}[(v_{\parallel} - u_{1,\parallel,j})^2] - T_{0,j}n_{1,j}/n_{0,j}$
4. Perpendicular temperature, $T_{1,\perp,j} = \mathcal{A}[v_{\perp}^2/2] - T_{0,j}n_{1,j}/n_{0,j}$
5. Turbulent particle flux, $\Gamma_j = \mathcal{A}[\mathbf{v}_E]$
6. Turbulent heat flux, $Q_j = \mathcal{A}[\mathbf{v}_E m_j v^2/2]$

As a result of the coordinate transformation from gyrocenter to guiding center [essentially equation (2.41) for $f_{1,j}$], each of these quantities can in fact be split into two parts, one containing the perturbed distribution function $f_{1,j}$, and the second one referred to as the polarisation term, containing Φ_1 but not $f_{1,j}$. For instance, the perturbed density can be expressed as:

$$n_{1,j}(\mathbf{x}) = \underbrace{\frac{2\pi}{m_j} \int B_{0,\parallel}^* \bar{f}_{1,j} dv_{\parallel} d\mu}_{n_{1gj}} - \underbrace{\frac{q_j n_{0,j}}{T_{0,j}} \left[\Phi_1 - \frac{B_0}{T_{0,j}} \int \bar{\bar{\Phi}}_1 e^{-\mu B_0/T_{0,j}} d\mu \right]}_{n_{1pj}}, \quad (2.57)$$

where the first term n_{1gj} is the so-called gyro-density and the second term n_{1pj} is the polarisation density. $\bar{\bar{\mathcal{F}}}$ represents the double gyroaverage of any scalar quantity \mathcal{F} , defined as

$$\bar{\bar{\mathcal{F}}} = \frac{1}{(2\pi)^2} \int d\alpha d\alpha' \mathcal{F}(\mathbf{X} - \mathbf{r} - \mathbf{r}'). \quad (2.58)$$

Similarly, the parallel fluid velocity can be expressed as:

$$u_{1,\parallel,j}(\mathbf{x}) = \frac{2\pi}{m_j} \int B_{0,\parallel}^* v_{\parallel} \bar{f}_{1,j} dv_{\parallel} d\mu - \frac{n_{0,j} \mu_0 j_{0,\parallel}}{B_0^2} \left[\Phi_1 - \frac{B_0}{T_{0,j}} \int \bar{\bar{\Phi}}_1 e^{-\mu B_0/T_{0,j}} d\mu \right] \quad (2.59)$$

where $j_{0,\parallel} = \mathbf{j}_0 \cdot \mathbf{b}_0 = (\nabla \times \mathbf{B}_0/\mu_0) \cdot \mathbf{b}_0$.

2.3.5 Field Equations

Using Maxwell's equations (2.16), one can relate the scalar and vector potentials Φ and \mathbf{A} of the self-consistent electromagnetic fields with moments of the distribution function, which can then be used to solve the gyrokinetic equation. To solve the perturbed part of the gyrokinetic equation (2.51) in particular, one needs to evaluate Φ_1 and $A_{1,\parallel}$ using the Poisson equation and Ampere's law respectively, as illustrated below.

Poisson equation

Noting that the unperturbed scalar potential Φ_0 is assumed to be zero, the Poisson equation becomes:

$$\nabla^2 \Phi_1(\mathbf{x}) = -\frac{1}{\epsilon_0} \sum_j \varrho_{1,j}(\mathbf{x}) \quad (2.60)$$

where the perturbed charge density $\varrho_{1,j}(\mathbf{x}) = q_j \int f_{1,j}(\mathbf{x}) d\mathbf{v} = q_j n_{1,j}(\mathbf{x})$. Using the assumption of anisotropy of fluctuations ($k_{\parallel}/k_{\perp} \ll 1$) in the gyrokinetic ordering, one can already express $\nabla^2 \simeq \nabla_{\perp}^2$. Furthermore, in ion scale turbulence, the Debye length $\lambda_{D,i}$ of ions is much smaller than the perpendicular scale length $\lambda_{\perp} \sim 1/k_{\perp}$ of fluctuations, *i.e.* $\lambda_{D,i} \ll \lambda_{\perp}$, and in this limit, the Poisson equation reduces to the quasi-neutrality equation:

$$\sum_j q_j n_{1,j}(\mathbf{x}) = 0. \quad (2.61)$$

Using the above quasi-neutrality equation, and with $n_{1,j}(\mathbf{x})$ already found in equation (2.57), one can now express the field Φ_1 in terms of $f_{1,j}$.

Ampere's law

Using the same assumption as has been made to evaluate the Poisson equation and neglecting the displacement current, the Ampere's law provides an equation for the perturbed parallel component $A_{1,\parallel}$ of the vector potential:

$$\nabla_{\perp}^2 A_{1,\parallel}(\mathbf{x}) = -\mu_0 \sum_j j_{1,\parallel}(\mathbf{x}). \quad (2.62)$$

Given that the perturbed parallel current component is defined by $j_{1,\parallel}(\mathbf{x}) = q_j u_{1,\parallel,j}(\mathbf{x})$ where $u_{1,\parallel,j}(\mathbf{x})$ has already been defined in equation (2.59), one can now express $A_{1,\parallel}$ in terms of $f_{1,j}$.

2.4 Collisions

Collisions provide the physical link between macroscopic plasma heating and microturbulence, through dissipation of small-scale structures, thereby enabling the system to reach a statistical steady state [Abel et al., 2008]. Note that in collisionless simulations, numerical dissipation such as hyperdiffusion is essential towards achieving a steady state [Krommes, 1999], however these effects are not physical in the true sense. Therefore, to realistically model the plasma behaviour, proper treatment of the discrete particle interactions via collisions is required. Furthermore, collisions can stabilise microinstability

modes such as ITG [Mikkelsen and Dorland, 2008] and TEM [Connor et al., 2006], and also play a crucial role in zonal flow damping [Hinton and Rosenbluth, 1999].

Note that the Vlasov equation and the gyrokinetic equation derived from it consider the collisionless limit. Collisions can be modelled via an additional term $C(f_j)$ in the Vlasov equation (2.15), called the collision operator, as given by the Fokker-Planck Equation:

$$\frac{df_j}{dt} = \frac{\partial f_j}{\partial t} + \dot{\mathbf{x}} \cdot \frac{\partial f_j}{\partial \mathbf{x}} + \dot{\mathbf{v}} \cdot \frac{\partial f_j}{\partial \mathbf{v}} = C(f_j), \quad (2.63)$$

A typical form of collision operator that is used in gyrokinetic codes is the Landau collision operator, which in turn is based on the Fokker-Planck collision model. Either linear or nonlinear versions of the Landau collision operator are used, depending on the type of the code and the plasma conditions being simulated. For instance, in full-f codes such as XGC [Ku et al., 2009] which aims to simulate turbulence in the edge of plasmas, the full nonlinear Landau operator is used [Hager et al., 2016]. In the edge of tokamak plasma, the length scale of variation of the plasma background is comparable to the ion Larmor radius and turbulence correlation widths. Furthermore, in the scrape-off layer region and around the magnetic separatrix surface, there is particle loss to the material wall, radiative energy loss, charge-exchange processes, etc. These lead to the perturbation f_1 being comparable to the background distribution f_0 , making the assumptions for linearising the collision operator invalid. However, in the plasma core where $f_1 \ll f_0$, it is justified to use linearised collision operators which are also computationally less costly. In delta-f codes such as GENE, the linearised Landau collision operator can be used, taking the form of the perturbed distribution scattering off the background, and a back reaction term that is used to conserve momentum and energy.

In the following, a summary of the Fokker-Planck collision model and the Landau form of the collision operator is presented.

2.4.1 Landau collision operator

In typical tokamak plasmas, which are weakly coupled, small angle scattering of a charged particle off the Debye spheres of other charge particles dominate the collision processes. Fokker-Planck collision operators can be used to model such small angle collisions.

An outline of the derivation of the Fokker-Planck collision operator is provided here, following references [Rosenbluth et al., 1957, Hazeltine and Waelbroeck, 1998]. The collision process is assumed to be such that the time-scale t_{coll} associated with a collisional event is much less than the time-scale t associated with other collisionless dynamics in the plasma. This lets one model the effect of collisions of species a off of species b by a

Chapter 2. Theoretical Background

probability distribution such that:

$$f_a(\mathbf{x}, \mathbf{v}, t) = \int f_a(\mathbf{x}, \mathbf{v} - \Delta\mathbf{v}, t - \Delta t) P(\mathbf{v} - \Delta\mathbf{v}, \Delta\mathbf{v}, \Delta t) d^3\Delta\mathbf{v} \quad (2.64)$$

where f_a is the distribution function of a species a and $P(\mathbf{v} - \Delta\mathbf{v}, \Delta\mathbf{v}, \Delta t)$ is the probability, that in time Δt , a particle will change its velocity from $\mathbf{v} - \Delta\mathbf{v}$ by $\Delta\mathbf{v}$. Now assuming that Δt is small with respect to collisionless plasma dynamics (but still larger than t_{coll}), one can Taylor expand equation (2.64) to first order in Δt . Further, since Δt is small and only small angle collisions are being modelled, one can also perform a Taylor expansion in Δv , but now to second order. This gives

$$\begin{aligned} f_a(\mathbf{x}, \mathbf{v}, t) = & \int \{ f_a(\mathbf{x}, \mathbf{v}, t) P(\mathbf{v}, \Delta\mathbf{v}, \Delta t) - \frac{\partial f_a}{\partial t} \Delta t P(\mathbf{v}, \Delta\mathbf{v}, \Delta t) \\ & - \Delta\mathbf{v} \cdot \frac{\partial}{\partial \mathbf{v}} (P(\mathbf{v}, \Delta\mathbf{v}, \Delta t) f_a(\mathbf{x}, \mathbf{v}, t)) \\ & + \frac{1}{2} \Delta\mathbf{v} \cdot \frac{\partial^2}{\partial \mathbf{v} \partial \mathbf{v}} (P(\mathbf{v}, \Delta\mathbf{v}, \Delta t) f_a(\mathbf{x}, \mathbf{v}, t)) \cdot \Delta\mathbf{v} \} d^3\Delta\mathbf{v} \end{aligned}$$

Since, $\int d^3\Delta v P(\mathbf{v}, \Delta\mathbf{v}, \Delta t) = 1$, the term on the LHS and the first term on the RHS in the above equation cancels out. Further, since only collisions are considered here, one can identify the term $\partial f_a / \partial t$ as the collision operator $C_{ab}(f_a, f_b)$, giving

$$C_{ab}(f_a, f_b) = -\frac{\partial}{\partial \mathbf{v}} \cdot (\mathbf{\Gamma}_{ab} f_a) + \frac{\partial^2}{\partial \mathbf{v} \partial \mathbf{v}} \cdot (\underline{D}_{ab} f_a) \quad (2.65)$$

where

$$\begin{aligned} \mathbf{\Gamma}_{ab} &= \frac{1}{\Delta t} \int d^3\Delta v P(\mathbf{v}, \Delta\mathbf{v}, \Delta t) \Delta\mathbf{v}, \\ \underline{D}_{ab} &= \frac{1}{2\Delta t} \int d^3\Delta v P(\mathbf{v}, \Delta\mathbf{v}, \Delta t) \Delta\mathbf{v} \Delta\mathbf{v}, \end{aligned}$$

stand for the drag term and diffusion tensor respectively.

The particular case of the Landau operator is discussed in the following. See reference [Rosenbluth et al., 1957] for a detailed derivation. The drag and diffusion coefficients in the Landau form can be written in terms of the distribution function f_b as:

$$\mathbf{\Gamma}_{ab} = \frac{q_a^2 q_b^2 \ln \Lambda}{8\pi \epsilon_0^2 m_a \mu_{ab}} \int \underline{U}(\mathbf{u}) \cdot \frac{\partial f_b}{\partial \mathbf{v}_b} d^3 v_b, \quad (2.66)$$

$$\underline{D}_{ab} = \frac{q_a^2 q_b^2 \ln \Lambda}{8\pi \epsilon_0^2 m_a^2} \int \underline{U}(\mathbf{u}) f_b d^3 v_b. \quad (2.67)$$

$\ln\Lambda$ is the Coulomb logarithm, ϵ_0 is the permittivity of free space, $\mu_{ab} = m_a m_b / (m_a + m_b)$ is the reduced mass, $\mathbf{u} = \mathbf{v}_a - \mathbf{v}_b$ is the relative velocity of collision, and tensor $\underline{U}(\mathbf{u}) = (\mathbf{I} - \hat{u}\hat{u})/u$, where $\hat{u} = \mathbf{u}/u$. At this point, one can note that the collision operator $C_{ab}(f_a, f_b)$ is a nonlinear (quadratic) operator in the distribution functions.

The drag vector can also be written as

$$\mathbf{\Gamma}_{ab} = -\frac{q_a^2 q_b^2 \ln\Lambda}{4\pi\epsilon_0^2 m_a \mu_{ab}} \int f_b \frac{\mathbf{u}}{u^3} d^3 v_b \quad .$$

having used the relation

$$\frac{\partial}{\partial \mathbf{v}_b} \cdot \underline{U}(\mathbf{u}) = 2 \frac{\mathbf{u}}{u^3}.$$

Now, the drag vector and diffusion tensor can be expressed in terms of the Rosenbluth potentials h_b and g_b , where

$$h_b(\mathbf{v}_a) = \int f_b \frac{1}{u} d^3 v_b \quad \text{and} \quad g_b(\mathbf{v}_a) = \int f_b u d^3 v_b. \quad (2.68)$$

Using the relations $\int (\mathbf{u} f_b / u^3) d^3 v_b = -\partial h_b / \partial \mathbf{u} = -\partial h_b / \partial \mathbf{v}_a$, $\underline{U}(\mathbf{u}) = \partial^2 u / \partial \mathbf{u} \partial \mathbf{u}$ and $\int \underline{U}(\mathbf{u}) f_b d^3 v_b = \int (\partial^2 u / \partial \mathbf{u} \partial \mathbf{u} f_b) d^3 v_b = \partial^2 g_b / \partial \mathbf{v}_a \partial \mathbf{v}_a$, one obtains

$$\mathbf{\Gamma}_{ab} = \frac{q_a^2 q_b^2 \ln\Lambda}{4\pi\epsilon_0^2 m_a \mu_{ab}} \frac{\partial h_b}{\partial \mathbf{v}_a}, \quad (2.69)$$

$$\underline{D}_{ab} = \frac{q_a^2 q_b^2 \ln\Lambda}{8\pi\epsilon_0^2 m_a^2} \frac{\partial^2 g_b}{\partial \mathbf{v}_a \partial \mathbf{v}_a}. \quad (2.70)$$

Note that so far the collision operator has been expressed in particle coordinates and cannot as such be added to the RHS of the gyrokinetic equation (2.48) which is expressed in gyrocenter variables. Hence, similar to the transformation of the Vlasov equation in particle coordinates to the gyrokinetic equation in gyrocenter coordinates, the collision operator should also undergo the same transformation so as to systematically eliminate its gyroangle dependence. For instance in the Landau collision operator, the velocity gradient $\partial/\partial \mathbf{v}$ evaluated at a fixed particle position should now be evaluated at a fixed gyrocenter position. This leads to additional Finite Larmor Radius (FLR) terms [and polarization terms, which are neglected by almost all gyrokinetic codes at the level of collision dynamics] in the collision operator, with the FLR correction appearing as spatial diffusion terms in gyrocenter coordinates [Abel et al., 2008].

Linearising the collision operator

For use in a delta-f code, one typically linearises the collision operator. Making use of the gyrokinetic ordering $|f_1/f_0| \ll 1$, one can write using the bi-linearity of the collision operator:

$$\begin{aligned} C_{ab}(f_a, f_b) = & C_{ab}(f_{0,a}, f_{0,b}) + C_{ab}(f_{1,a}, f_{0,b}) + C_{ab}(f_{0,a}, f_{1,b}) + C_{ab}(f_{1,a}, f_{1,b}) \\ & \simeq C_{ab}(f_{1,a}, f_{0,b}) + C_{ab}(f_{0,a}, f_{1,b}). \end{aligned} \quad (2.71)$$

The term $C_{ab}(f_{0,a}, f_{0,b})$ denotes the thermalisation of the background distribution functions which happens at much longer time-scales as compared to microturbulence timescales, and hence can be ignored. Furthermore, the nonlinear term $C_{ab}(f_{1,a}, f_{1,b})$ denotes the scattering of the perturbed distribution functions of species a and b off of each other, and can be neglected since being of order ϵ^2 . One thus obtains the collision operator correct to order ϵ .

The (non-linear and linearised) collision operator should follow certain local conservation laws, namely the conservation of particles, momentum, energy and the H-theorem for entropy production [Brunner et al., 2010]. However, the linearised Landau operator, or any linearised Fokker Planck operator in general, does not satisfy the H-theorem for non-isothermal ($T_{0,a} \neq T_{0,b}$) cases. This problem has been corrected in the so-called Sugama collision operator [Sugama et al., 2009].

2.5 Microinstabilities

Microinstabilities are characterised by fluctuations having perpendicular length scales of the order of Larmor radius, that grow exponentially in time (initially, and later saturating to quasi-stationary amplitudes as a result of various saturation mechanisms). The associated radial drifts carry heat and particles from the core to the edge of the plasma, thereby limiting the ability of a tokamak to reach confinement conditions necessary for ignition. These instabilities can be driven by a variety of factors. For instance, the equilibrium radial pressure gradients can lead to instabilities such as the drift wave, Ion Temperature Gradient (ITG), Electron Temperature Gradient (ETG) instability etc. The presence of trapped particles in a tokamak and their particular dynamics can lead to associated instabilities such as the Trapped Electron Mode (TEM) instability. While all the examples mentioned so far are electrostatic instabilities, having a higher beta (=pressure/magnetic pressure) can lead to electromagnetic instabilities such as for example, the Kinetic Ballooning Modes (KBM) and the microtearing mode instabilities. Furthermore, depending on the length scale of the fluctuations, the various instabilities can be classified into ion-scale or electron-scale instabilities. For instance, while the ETG instability is an electron-scale instability leading to fluctuations that have a perpendicular length scale of the order of the electron Larmor radius, ITG and TEM are ion-scale

instabilities having perpendicular length scales of the order of the ion Larmor radius.

In this thesis, a turbulence regime dominated by ITG instability is studied. Hence in section 2.5.1, a brief review of the ITG instability is provided. While the basic ITG instability already exists in slab geometry, here the interchange-like toroidal ITG instability is considered. In addition, short descriptions of ETG, TEM and some other common instabilities are provided in subsections 2.5.4, 2.5.2 and 2.5.5 respectively.

2.5.1 Toroidal ITG instability

The toroidal ITG instability, first identified in reference [Horton et al., 1981], is an interchange instability driven by the combined effect of equilibrium ion temperature gradient as well as grad-B and curvature drifts. It is one of the most common instability driving turbulent transport in the core of most of today's tokamaks.

The essential physical mechanisms behind the toroidal ITG instability can be explained as follows, with the help of figure 2.2. First, one can look at the outboard side of the tokamak, where the gradient of the equilibrium magnetic field ∇B and pressure ∇P ($\simeq n\nabla T + T\nabla n$) are both pointed in the same direction. Assuming an initial pressure perturbation δP , a charge separation develops as a result of the curvature and grad-B drifts in the vertical direction [both these drifts are charge dependent velocities, see equations (2.45) and (2.46)]. At the outer midplane, the resulting electric field in turn leads to an $E \times B$ drift with velocity v_E [charge independent, see equation (2.44)] that amplifies the initial perturbation, thereby leading to an instability. However, at the inboard midplane, where ∇B and ∇P are pointed in opposite directions, the resulting $E \times B$ drift is such that it negates any initial perturbation and charge separations. ITG is therefore an 'interchange instability', meaning that it is unstable on the outboard side but stable on the inboard side of the tokamak.

As already mentioned in section 2.3.5, under the subsection on the Poisson equation, quasi-neutrality is a good approximation for studying ion-scale microturbulence. However in reality, a slight deviation from quasi-neutrality exists, leading to a small charge separation and the consequent generation of an electric field, as explained in the physical picture of the ITG instability presented above.

A local dispersion relation for the ITG instability can be obtained from the gyrokinetic equation (2.51) together with the quasi-neutrality equation (2.61). In the linear, electrostatic limit, assuming a local Maxwellian background distribution function [$f_0 = f_{0,LM}$,

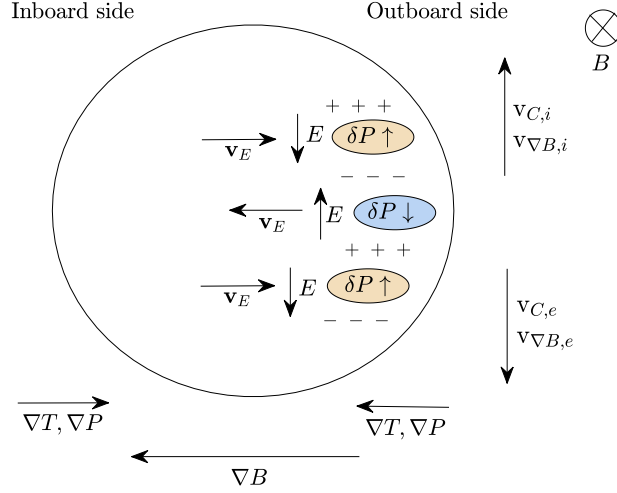


Figure 2.2: Illustration of a toroidal ITG instability mechanism on the outboard side of a tokamak. $\delta P \uparrow$ and $\delta P \downarrow$ denote respectively regions with higher and lower pressure. The grad-B and curvature drifts lead to charge separations that then result in generation of electric fields. The associated $E \times B$ drift velocity \mathbf{v}_E then reinforces the initial pressure perturbation, by bringing high pressure plasma from the center of the tokamak to the $\delta P \uparrow$ regions, and by taking low pressure plasma from the edge to $\delta P \downarrow$ regions.

see equation (2.55)], one obtains:

$$\left. \frac{dh_{1,i}}{dt} \right|_{\text{u.t.}} = \frac{\nabla \bar{\Phi} \times \mathbf{b}_0}{B_{0,\parallel}^*} \cdot \nabla \psi \left[\frac{\partial}{\partial \psi} \log(n_{0,i}) + \frac{\partial}{\partial \psi} \log(T_{0,i}) \left(\frac{\mathcal{E}}{T_{0,i}} - \frac{3}{2} \right) \right] f_{0,i} + \frac{q_j f_{0,i}}{T_{0,i}} \frac{\partial \bar{\Phi}}{\partial t}, \quad (2.72)$$

where $d/dt|_{\text{u.t.}}$ represents the total derivative along the unperturbed trajectory and $h_{1,j} = f_{1,j} - q_j \bar{\Phi} f_{0,j}/T_{0,j}$ is the non-adiabatic part of the perturbed ion distribution function.

Assuming a response of the form $h_{1,j} = \sum_{\omega, \mathbf{k}} \hat{h}_{1,j}(\omega, \mathbf{k}) e^{-i(\omega t - \mathbf{k} \cdot \mathbf{X})}$ and $\Phi = \sum_{\omega, \mathbf{k}} \hat{\Phi}(\omega, \mathbf{k}) e^{-i(\omega t - \mathbf{k} \cdot \mathbf{X})}$, and integrating along the unperturbed trajectory, one finds:

$$\hat{h}_{1,i}(\omega, \mathbf{k}) = \frac{q_i}{T_{0,i}} \hat{\Phi} J_0 \left(\frac{k_{\perp} v_{\perp}}{\Omega_i} \right) \frac{\omega - \omega_i^*}{\omega - k_{\parallel} v_{\parallel} - \omega_{D,i}} f_{0,i}, \quad (2.73)$$

where

$$\omega_i^* = \omega_{N,i} [1 + \eta_i T_i (\partial / \partial T_{0,i})] \quad (2.74)$$

is an operator acting on $f_{0,i}$, with $\omega_{N,i} = -k_y T_{0,i} / q_i B_0 L_N$ being the drift frequency related to the density gradient. $L_N = 1/|\nabla \log n_{0,i}|$ and $L_{T,i} = 1/|\nabla \log T_{0,i}|$ are the characteristic gradient lengths related to density and temperature respectively. $\eta_i = L_N / L_{T,i}$, $\omega_{D,i} = -k_y (v_{\parallel}^2 + v_{\perp}^2 / 2) / \Omega B_0 L_B$ is the drift frequency related to curvature

and grad-B drifts, $L_B = 1/|\nabla \log B_0|$, k_y is the wavenumber in the binormal direction $\mathbf{y} = \mathbf{b}_0 \times \nabla \psi / |\nabla \psi|$ and J_0 is the zeroth order Bessel function of the first kind accounting for FLR effects. More details on the derivation can be found in reference [Brunner, 2014].

Assuming adiabatic electrons, the quasi-neutrality equation ($n_{0,e} = Z_i n_{0,i}$) leads to the following dispersion relation

$$\epsilon(\mathbf{k}, \omega) = \frac{1}{(k\lambda_{D,e})^2} + \frac{1}{(k\lambda_{D,i})^2} \left[1 - \int d^3v J_0^2 \left(\frac{k_\perp v_\perp}{\Omega_i} \right) \frac{\omega - \omega_i^*}{\omega - k_\parallel v_\parallel - \omega_{D,i}} \frac{f_{0,i}}{n_{0,i}} \right] = 0, \quad (2.75)$$

where $\epsilon(\omega, \mathbf{k})$ is the plasma dielectric function, $\lambda_{D,e/i}$ are the electron or ion Debye lengths and $k = |\mathbf{k}|$. By ignoring the term $\omega_{D,i}$, the effects of toroidicity can be removed, and one can obtain the dispersion relation for the slab ITG instability.

Making certain approximations and assumptions on the above dispersion relation, it is possible to find that ITG modes are essentially ion acoustic like waves, and show the interchange nature of the mode [Brunner, 2014]. In the fluid limit $|\omega/(k_\parallel v_{th,i})| \ll 1$, assuming slow guiding center drifts $|\omega/\omega_{D,i}| \simeq |\omega^*/\omega_{D,i}| \gg 1$, and keeping the FLR effects to second order $J_0(k_\perp v_\perp/\Omega_i) \simeq 1 - (k_\perp v_\perp/\Omega_i)^2/2$, one obtains

$$\frac{T_{0,i}}{T_{0,e}Z_i} + \frac{\omega_{N,i}}{\omega} + \left[1 - \frac{\omega_N}{\omega}(1 + \eta_i) \right] \left[(k_\perp \rho_i)^2 - \frac{\langle \omega_{D,i} \rangle}{\omega} - \left(\frac{k_\parallel v_{th,i}}{\omega} \right)^2 \right] = 0, \quad (2.76)$$

where $\langle \omega_{D,i} \rangle = \int d^3v \omega_{D,i} f_{0,i}/n_{0,i} = -2T_{0,i}k_\perp/q_i B_0 L_B$. In the case of homogeneous equilibrium where $\omega^* = 0$, and $\omega_{D,i} = 0$, the dispersion relation reduces to

$$\omega^2 = \frac{(k_\parallel c_s)^2}{1 + (k_\perp \rho_s)^2}, \quad (2.77)$$

where $c_s = \sqrt{Z_i T_{0,e}/m_i}$ is the ion sound speed, essentially showing the ion-acoustic like wave nature of ITG modes. To show the interchange nature of the mode, one can consider the case of field aligned fluctuation $k_\parallel \simeq 0$, toroidal geometry $\omega_{D,i} \neq 0$, no density gradient $\omega_{N,i} = 0$ and identify $\omega_{T,i} = \omega_{N,i}\eta_i = -k_y T_{0,i}/q_i B_0 L_{T,i}$. In these limits, one obtains

$$\omega^2 \left(1 + \frac{T_{0,i}}{T_{0,e}Z_i} \right) - \omega(\omega_{T,i} k_\perp^2 \rho_i^2 - \langle \omega_{D,i} \rangle) + \omega_{T,i} \omega_{D,i} = 0. \quad (2.78)$$

For the above dispersion relation, which is quadratic in ω , to have an unstable branch (to have solutions with $\text{Im}[\omega] > 0$), a necessary condition is to have a negative discriminant, *i.e.* $\omega_{T,i} \langle \omega_{D,i} \rangle > 0$. Since $\omega_{T,i} \langle \omega_{D,i} \rangle \sim \nabla B \cdot \nabla T_i$, this demonstrates the interchange nature of the mode.

2.5.2 TEM instability

The Trapped Electron Mode (TEM) instability arises from the resonance between the slow (as compared to fast bounce motion along the banana trajectory) precessional drift of trapped electrons and electrostatic perturbations. Apart from ITG, TEM is another one of the most common instabilities in present day tokamaks.

In order to obtain a local dispersion relation for TEM instability, following reference [Brunner, 1997], one can consider an adiabatic response for passing electrons and a bounce averaged kinetic description for the trapped electrons as given below:

$$\frac{n_{1,e,trap}}{n_{0,e}} = \alpha_t \frac{e\Phi}{T_{0,e}} \left[1 + \left(1 - \frac{\omega_e^*}{\omega} \right) z_{be}^2 W(z_{be}) \right], \quad (2.79)$$

where α_t is the fraction of trapped electrons, ω_e^* is the electron equivalent of equation (2.74), $z_{be} = \text{sign}(\omega_{\varphi e}) \sqrt{2\omega/\omega_{\varphi e}}$, $\omega_{\varphi e} = n\langle\dot{\varphi}\rangle v_{th,e}^2/\mathcal{E} \simeq 1$, $\mathcal{E} = (v_\perp^2 + v_\parallel^2)/2$ is the kinetic energy, $n\langle\dot{\varphi}\rangle$ is the toroidal precession drift frequency and $W(z) = (2\pi)^{-1} \int dx e^{-x^2/2} x/(x - z)$ is the dispersion function.

Considering the same kinetic ion response as for the toroidal ITG case [see equation (2.75)], the local dispersion relation can be obtained from the quasi-neutrality equation:

$$Z_i \frac{T_{0,i}}{T_{0,e}} - Z_i \frac{T_{0,i}}{T_{0,e}} \int d^3v J_0^2 \frac{\omega - \omega_i^*}{\omega - k_\parallel v_\parallel - \omega_{D,i}} \frac{f_{0,i}}{n_{0,i}} + 1 + \left(1 - \frac{\omega_e^*}{\omega} \right) \alpha_t z_{be}^2 W(z_{be}) = 0. \quad (2.80)$$

TEM instability can be driven by a gradient in either the background electron temperature or density. Typically, the TEM growth rate $\gamma \sim \omega_e^*$ and the real frequency range is similar to that of ITG, but with an opposite sign. Also, the TEM perpendicular wavelength is approximately the same as that of typical ITG perpendicular wavelengths, and hence TEM instability is often coupled with ITG instability [Romanelli and Briguglio, 1990]. Furthermore, TEM instability can be strongly stabilised by collisions [Connor et al., 2006, Camenen et al., 2007] and therefore increasing collisionality often leads to a transition from TEM to ITG dominant turbulence [Ryter et al., 2005]. It is worth noting that, while ITG is mainly responsible for ion heat transport, TEM mainly gives rise to electron heat and particle transport.

2.5.3 Zonal flows

Zonal flows are toroidally symmetric electrostatic potential fluctuations with finite radial wavenumber. The resulting radial electric field consequently leads to an $E \times B$ rotation of the plasma. In tokamaks, zonal flows are ubiquitous features in all geometries, present both in the core and edge.

The shearing of turbulent eddies by zonal flows is one of the primary mechanisms by which microturbulence saturates [Diamond et al., 2005]. Zonal flows are not driven linearly, but nonlinearly by the unstable drift waves, for example via secondary instabilities such as modulational instability [Hasegawa and Mima, 1978, Hasegawa et al., 1979, Chen et al., 2000], as well as the self-interaction mechanism [Weikl et al., 2018] (described in detail in chapter 3). Once zonal flows grow beyond a critical level, it can then damp via tertiary instabilities such as Kelvin-Helmholtz instability [Rogers et al., 2000, Idomura et al., 2000]. The self-regulation of turbulence by zonal flows therefore can be explained via a predator-prey model [Diamond et al., 2005].

The efficacy of the zonal flow turbulence saturation mechanism depends in general on the type of the dominant instability. For instance, while it is one of the primary saturation mechanisms in ITG turbulence [Lin et al., 1998], in TEM turbulence, it is dominant only in certain parameter regimes [Lang et al., 2008].

As is most frequently done, poloidal $E \times B$ zonal flow is studied in this thesis. Given the toroidicity of a tokamak, this flow gets compressed as it moves from the outboard side to the inboard side. For stationary zonal flows, a flow v_{\parallel} parallel to the magnetic field can compensate this compression without any density oscillations, as can be seen in the continuity equation $\partial n / \partial t = -\nabla \cdot (n\mathbf{v}) \simeq -\nabla \cdot (n\mathbf{v}_{E \times B}) - \nabla_{\parallel}(nv_{\parallel})$, assumed to have no source terms. In cases the parallel flow is not able to cancel the divergence of $n\mathbf{v}_{E \times B}$, a pressure perturbation builds up, that eventually leads to an inversion of the flow which then becomes oscillatory. Such finite frequency zonal flows having an associated oscillating density perturbation with an $m = 1$ poloidal (and $n = 0$ toroidal) dependence are called Geodesic Acoustic Modes (GAMs) [Winsor et al., 1968]. Given that the frequency of the GAMs and the residual level of zero frequency zonal flows can be analytically obtained [Rosenbluth and Hinton, 1998], these results (referred to as the Rosenbluth-Hinton test) are often used to validate gyrokinetic codes, as discussed in more detail in section B.2.

2.5.4 ETG instability

The mechanism behind Electron Temperature Gradient (ETG) instability is essentially the same as that of ITG but with the electrons playing the role of ions. ETG turbulent eddies, also called ETG streamers, have been observed to be significantly elongated in the radial direction, allowing for significant transport of heat radially out of the plasma [Dorland et al., 2000]. Compared to ion-scale turbulence, it is more difficult to measure these fluctuations in experiments [Mazzucato et al., 2008, Smith et al., 2009]. Hence, studies of ETG turbulence have largely been restricted to numerical simulations.

Given that ions over their gyromotion perpendicular to the magnetic field can respond rapidly to any perturbations at the small electron Larmor scale length, their response can

be considered to be adiabatic-like, allowing one in first approximation to perform purely electron scale simulations to obtain the ETG turbulent flux levels. Making use of this scale separation between electron and ion scale turbulence, the sum of the fluxes from two separate single scale simulations, one for electron and the other for ion scale turbulence, provides an estimate for the total flux level. However various recent works [Görler and Jenko, 2008, Maeyama et al., 2015, Howard et al., 2016] show that such a simple superposition of fluxes is flawed and that various cross-scale effects play a dominant role. For instance, the long wavelength eddies generated by ion scale turbulence have been shown to shear the ETG streamers and suppress the electron scale turbulence. Studies such as [Maeyama et al., 2017] also show that short wavelength zonal flows produced by non-adiabatic passing electron dynamics (including possibly the fine-structures at low order mode rational surfaces [Dominski et al., 2015], which is the main focus of this thesis), which play a role in reducing ion-scale turbulence, can be affected by electron scale turbulence.

It is also worth noting that the ITG turbulence is more efficient in driving zonal flows as compared to ETG turbulence, and moreover, the saturation via the zonal flow shearing mechanism is much more significant in ITG turbulence than in ETG turbulence [Dorland et al., 2000].

2.5.5 Other Instabilities

Among the many different types of microinstabilities, the two most common electromagnetic instabilities are the Kinetic Ballooning Mode (KBM) and microtearing modes. Given the topic of this thesis, it is interesting to note that fine radial structures on the field profiles are present at MRSs of KBM eigenmodes as well [Falchetto et al., 2003], similar to that observed in ITG and TEM eigenmodes. Microtearing modes, driven mainly by electron temperature gradient, lead to small-scale magnetic islands that ‘stochasticize’ the magnetic field [Doerk et al., 2011]. They are essentially the gyrokinetic equivalent to MHD tearing modes. These modes are particularly unstable at very low wavenumbers $k_y \rho_i \sim 0.1$. A feature of electromagnetic simulations in general is the so-called non-zonal transition limit, a limit on β beyond which the simulations tend not to converge [Pueschel et al., 2013]. This is explained to result from the suppression of $E \times B$ zonal flows by the currents generated by electrons that ‘peel off’ radially from the flux surface as they travel along the magnetic field lines perturbed by the electromagnetic fluctuations. Furthermore, in reference [Pueschel and Jenko, 2010], it has been shown that finite β can lead to a critical gradient upshift of ITG turbulence. Resistive Ballooning modes [Bourdelle et al., 2012], Parallel Velocity Gradient (PVG) [Barnes et al., 2011, Ball et al., 2019] modes etc. are further examples of other types of microinstabilities.

2.6 The GENE code

GENE (Gyrokinetic Electromagnetic Numerical Experiment) is an Eulerian gyrokinetic code that solves the time evolution of the perturbed (delta-f) part of the distribution function on a fixed phase space grid [Jenko et al., 2000, Görler et al., 2011]. It has the ability to handle electromagnetic fluctuations, multiple species, collisions with different collision operators [Merz, 2008, Goerk, 2012, Crandall, 2019], background shear flow [Told, 2012, McMillan et al., 2019, Ball et al., 2019] etc. While a global version of the code [Görler, 2009, Lapillone, 2010] is available, in this thesis, the local (flux-tube) version is used.

In this section, first the field aligned coordinate system used in GENE is described in subsection 2.6.1, followed by a detailed description of the flux-tube model and the boundary conditions involved in subsection 2.6.2. The numerical schemes employed in GENE are then briefly discussed in subsection 2.6.4.

2.6.1 Coordinate system

GENE uses a non-orthogonal, curvilinear, field-aligned coordinate system (x, y, z) defined in terms of the magnetic coordinates (ψ, χ, φ) as follows [Beer et al., 1995] :

$$x = x(\psi) : \text{radial coordinate}, \quad (2.81)$$

$$y = C_y[q_s(\psi)\chi - \varphi] : \text{binormal coordinate}, \quad (2.82)$$

$$z = \chi : \text{parallel coordinate}. \quad (2.83)$$

ψ, χ and φ represent the poloidal magnetic flux, straight field line poloidal angle [defined by equation (2.13] for the case of circular geometry) and the toroidal angle, respectively. The function $x(\psi)$ is a function of ψ with units of length. $C_y = r_0/q_0$ is a constant defined such that y also has units of length, where q_0 is the safety factor at $r = r_0$ denoting the radial position of the flux-tube; $r(\psi)$ is in general an estimate of the (average) geometric minor radius of the magnetic surface labelled by ψ . The inverse aspect ratio of the flux-tube is defined as $\epsilon = r_0/R$, where R is the major radius of the tokamak.

In these coordinates, the magnetic field [defined by equation (2.7)] can be expressed as:

$$\mathbf{B} = \mathcal{C} \nabla x \times \nabla y, \quad (2.84)$$

where $\mathcal{C} = 1/[(d x(\psi)/d\psi)C_y]$. One can note that on a given flux surface defined by $x = \text{const.}$, the coordinate y is essentially a magnetic field line label. Furthermore, for a given magnetic field line labelled by $(x = \text{const.}, y = \text{const.})$, one moves along the field line as the coordinate z is varied, explaining why it is called the parallel coordinate.

While the radial x coordinate is treated in real space in the global version of GENE, in

the flux-tube model, a Fourier representation is used, as will be discussed in detail in the next subsection. The binormal y and parallel z coordinates are treated in Fourier and real space respectively, in both versions of the code.

The discretisation of the coordinates is discussed in the following. In real space, the simulation volume $L_x \times L_y \times L_z$ is discretised by $N_x \times N_y \times N_z$ equidistant grid points. In the k_y Fourier space related to the y direction, one considers N_{k_y} Fourier modes such that $N_y = 2N_{k_y} - 1$. Note that by invoking the reality condition, only modes $k_y \geq 0$ are evolved in GENE. The parallel coordinate extends over $z \in [-L_z/2, +L_z/2[$. For the parallel velocity coordinate one considers $v_{\parallel} \in [-v_{\parallel, \max}, +v_{\parallel, \max}]$ with a discretisation involving $N_{v_{\parallel}}$ equidistant grid points, while for the μ coordinate one considers $\mu \in [0, \mu_{\max}]$ with a discretisation involving N_{μ} grid points following the Gauss-Laguerre integration scheme.

2.6.2 Flux-tube model and boundary conditions

In the flux-tube model, the simulation domain is assumed to be a box spanning a tiny radial extent of the plasma volume and extending along the magnetic field line. See figure 2.3 where an illustration of the flux-tube box is shown. It assumes a scale separation between the radial correlation length of turbulent eddies ($\sim 10\rho_i$) and the radial length scale of variation of equilibrium ($\sim a$), thus corresponding to the limit $\rho^* = \rho_i/a \ll 1$. Consistent with this scale separation, the background density and temperature profiles and their gradients, as well as the magnetic equilibrium quantities, are considered constant across the radial extension L_x of the flux-tube, and are evaluated at r_0 . An exception is the safety factor appearing in the parallel boundary condition, discussed in detail later in this section. The background density and temperature of a species j are, respectively, $n_{j,0} = n_{j,0}(r_0)$ and $T_{j,0} = T_{j,0}(r_0)$ and their inverse radial gradients lengths are $1/L_{Nj} = -d \log n_{j,0}/dr|_{r=r_0}$ and $1/L_{Tj} = -d \log T_{j,0}/dr|_{r=r_0}$. The magnetic field amplitude $B_0 = B_0(z)$, Jacobian $\mathcal{J}^{xyz} = \mathcal{J}^{xyz}(z)$ and the metric coefficients $g^{\mu\nu}(z) = \nabla\mu \cdot \nabla\nu$ where μ and ν stand for the flux-tube coordinates (x, y, z) , depend only on the parallel coordinate. Furthermore, given the toroidal axisymmetry, the equilibrium quantities are independent of the coordinate y .

The flux-tube coordinates (x, y, z) satisfy the double periodic boundary condition in a tokamak as follows. The $\Delta\varphi$ -periodicity of any physical quantity \mathcal{A} , in particular fluctuations, along the toroidal direction φ reads:

$$\mathcal{A}(\psi, \chi, \varphi + \Delta\varphi) = \mathcal{A}(\psi, \chi, \varphi),$$

and translates in (x, y, z) coordinates to an L_y -periodicity along y :

$$\mathcal{A}(x, y + L_y, z) = \mathcal{A}(x, y, z). \quad (2.85)$$

where $L_y = C_y \Delta\varphi$. If the flux-tube covers the full flux-surface, $\Delta\varphi = 2\pi$, else $\Delta\varphi$ is only

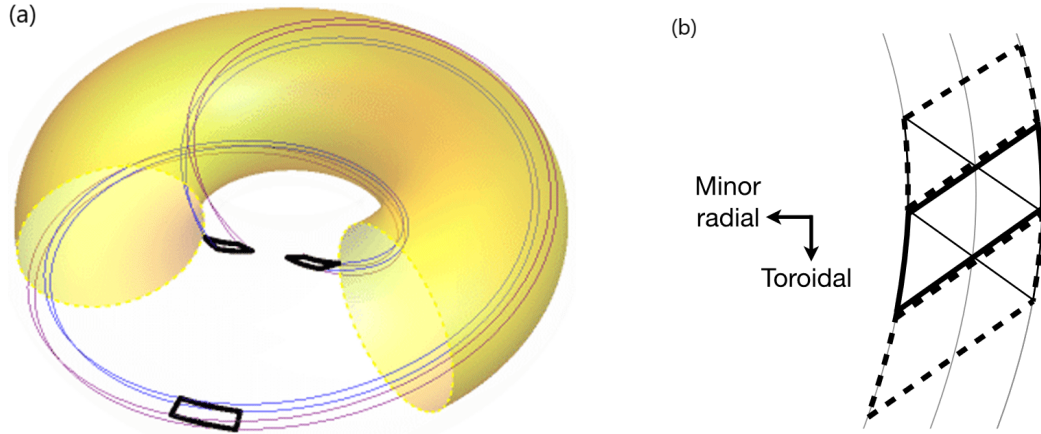


Figure 2.3: (a) An illustration of a flux-tube box (blue and purple lines) that is one poloidal turn long. The black rectangle indicates the cross-sectional shape of the flux-tube at the outboard midplane and the black parallelograms indicate the cross-sections at the inboard midplane. The transparent yellow surface indicates the central flux-surface with a toroidal wedge removed for visual clarity. (b) The toroidal cross-section of the flux-tubes at the inboard midplane, illustrating the "twist and shift" parallel boundary condition. The solid thin parallelogram represents one end of the flux-tube shown in the subfigure (a) on the left. The parallel boundary condition involves shifting the other end of the flux-tube (represented by thick solid parallelogram in this plot) toroidally until it is centred on the other end, and then making periodic copies offset in the toroidal direction (as shown by two thick dashed parallelograms). The flux-surfaces are shown with thin solid grey lines. Source: [Ball et al., 2020]

Chapter 2. Theoretical Background

a fraction of 2π . The 2π -periodicity in the poloidal direction χ reads:

$$\mathcal{A}(\psi, \chi + 2\pi, \varphi) = \mathcal{A}(\psi, \chi, \varphi),$$

and translates in (x, y, z) coordinates to a pseudo-periodic condition (also called the "twist and shift" method [Scott, 1998]) along z :

$$\mathcal{A}(x, y + C_y q_s(x) 2\pi, z + 2\pi) = \mathcal{A}(x, y, z). \quad (2.86)$$

This boundary condition is referred to as the parallel boundary condition [Scott, 1998].

The effect of these boundary conditions on the flux-tube simulation box can be seen in figure 2.3(a). The flux-tube box follows the background magnetic field lines. The cross-section is a rectangle at the outboard midplane (at $z = 0$) which then twists as a result of finite shear, becoming parallelograms at the inboard midplane. The "twist and shift" parallel boundary condition essentially involves shifting one end of the flux-tube at the inboard midplane toroidally until it is centred on the other end, and then making periodic copies offset in the toroidal direction, as shown in figure 2.3(b). For a more detailed explanation with illustrations, see [Ball et al., 2020]. Note that in the flux-tube model in general, one can consider a periodicity in z that is larger than 2π as well [Beer et al., 1995, Ball et al., 2020]. However, typically the 2π -periodicity is considered, as in this work.

Furthermore, the radial scale separation $\rho^* \ll 1$ justifies periodic boundary conditions along x :

$$\mathcal{A}(x + L_x, y, z) = \mathcal{A}(x, y, z). \quad (2.87)$$

Given the periodicity along x and y expressed by equations (2.87) and (2.85), a Fourier series decomposition in these directions is a practical representation of fluctuation fields as it naturally satisfies these boundary conditions. Such a Fourier representation reads:

$$\mathcal{A}(x, y, z) = \sum_{k_x, k_y} \hat{\mathcal{A}}_{k_x, k_y}(z) \exp[i(k_x x + k_y y)], \quad (2.88)$$

with k_x and k_y spanning in general all harmonics of the minimum wave numbers $k_{x, \min} = 2\pi/L_x$ and $k_{y, \min} = 2\pi/L_y$, respectively.

The underlying axisymmetry of a tokamak corresponds to an invariance of the unperturbed system with respect to φ in (ψ, χ, φ) coordinates. This translates to an invariance with respect to y in (x, y, z) coordinates. Consequently, any fluctuating field related to a *linear* eigenmode of the toroidal system is thus composed of a single k_y Fourier mode. Note that a given k_y wave number is equivalent to a toroidal wave number n according to the relation

$$n = -k_y C_y. \quad (2.89)$$

The pseudo-periodic boundary condition (2.86) remains to be expressed in the Fourier representation (2.88). In doing so, one considers the x -dependence of the safety factor profile $q_s(x)$. This is essential to ensure that the flux-tube model contains the information on the radial position of MRSs related to a k_y mode and thus accounts for the particular dynamics, in particular resonances, that can take place at such surfaces. This is of key importance to the study carried out in this thesis. Accounting for the x -dependence of the safety factor in these boundary conditions is thus an exception in the flux-tube framework, as all other background and magnetic geometry coefficients, as already mentioned, are assumed x -independent. Only a *linearised* safety factor profile of the form:

$$q_s(x) = q_0[1 + \hat{s}(x - x_0)/r_0], \quad (2.90)$$

is in fact compatible with the Fourier representation along x . \hat{s} is the magnetic shear at the center of the flux-tube, defined as

$$\hat{s} = \frac{r}{q_s} \frac{dq_s}{dr} \Big|_{r_0}.$$

For a given k_y Fourier mode, inserting (2.88) and (2.90) into (2.86) leads to

$$\sum_{k_x} \hat{\mathcal{A}}_{k_x, k_y}(z + 2\pi) \exp[2\pi i k_y C_y q_s(x = 0)] \exp[i(k_x + 2\pi k_y \hat{s})x] = \sum_{k_x} \hat{\mathcal{A}}_{k_x, k_y}(z) \exp(ik_x x). \quad (2.91)$$

For convenience and without further loss of generality, one assumes here that the origin of the x coordinate corresponds to the lowest order MRS (LMRS), *i.e.* a MRS related to $k_{y, \min}$. This condition reads:

$$k_{y, \min} C_y q_s(x = 0) = n_{\min} q_s(x = 0) = n_{\min} q_0(1 - \hat{s}x_0/r_0) \in \mathbb{Z},$$

with n_{\min} the toroidal wave number associated to $k_{y, \min}$ according to equation (2.89). Note that this relation provides an equation for the shift in x_0 and ensures that the phase factor $\exp[2\pi i k_y C_y q_s(x = 0)] = 1$ for all k_y modes. Also note that such a shift in x_0 is valid only in the case of finite magnetic shear. Based on (2.91), the boundary condition in z then finally translates for a given k_y Fourier mode to the following coupling between k_x Fourier modes:

$$\hat{\mathcal{A}}_{k_x, k_y}(z + 2\pi) = \hat{\mathcal{A}}_{k_x + 2\pi k_y \hat{s}, k_y}(z). \quad (2.92)$$

The coupling between k_x Fourier modes can also be understood as follows. In a sheared toroidal system, the wave vector associated to a Fourier mode (k_x, k_y) is given by

$$\vec{k} = k_x \nabla x + k_y \nabla y = (k_x + k_y \hat{s} z) \nabla x - n q_s \nabla \chi + n \nabla \varphi, \quad (2.93)$$

having used relations (2.82) and (2.89). After one poloidal turn ($z \rightarrow z + 2\pi$), the wave vector (2.93) obviously becomes the one associated to the Fourier mode $(k_x + 2\pi k_y \hat{s}, k_y)$,

Chapter 2. Theoretical Background

thus explaining the coupling of k_x modes.

One should emphasize that this coupling resulting from the parallel boundary condition applies to any fluctuating field and in particular already to linear eigenmodes of the system and is thus of different physical nature than the three Fourier mode (~ 3 -wave) interaction discussed later on in sections 3.4.2 and 3.4.3, resulting from non-linear dynamics.

A linear eigenmode with fixed k_y thus couples to a set of $k_x = k_{x0} + p 2\pi k_y \hat{s}$, $p \in \mathbb{Z}$, modes and is of the form:

$$\mathcal{A}(x, y, z) = \exp(ik_y y) \sum_{p=-\infty}^{+\infty} \hat{\mathcal{A}}_{k_{x0}+p2\pi k_y \hat{s}, k_y}(z) \exp[i(k_{x0} + p 2\pi k_y \hat{s})x]. \quad (2.94)$$

One can show that this form is equivalent to the so-called ballooning representation [Connor et al., 1978, Hazeltine and Newcomb, 1990]:

$$\mathcal{A}(\psi, \chi, \varphi) = \sum_{p=-\infty}^{+\infty} \hat{\mathcal{A}}_b(\chi + p 2\pi) \exp[in(\varphi - q_s(\psi)(\chi + p 2\pi - \chi_0))], \quad (2.95)$$

noting in this relation the ballooning envelope $\hat{\mathcal{A}}_b(\chi)$, defined over the extended ballooning space $\chi \in]-\infty, +\infty[$, as well as the field-aligned phase factor including the ballooning angle χ_0 . The relation between the two representations (2.94) and (2.95), for $\chi \in [-\pi, \pi[$, is given by [Merlo et al., 2016]

$$\hat{\mathcal{A}}_b(\chi + p 2\pi) = \hat{\mathcal{A}}_{k_{x0}+p2\pi k_y \hat{s}, k_y}(\chi) \quad (2.96)$$

$$\chi_0 = -k_{x0}/(k_y \hat{s}), \quad (2.97)$$

In a flux-tube of radial extension L_x , all coupled Fourier modes $k_x + p 2\pi k_y \hat{s}$ relative to this direction must be harmonics of $k_{x,\min}$. This must hold for all k_y and in particular for the lowest harmonic $k_{y,\min}$:

$$2\pi k_{y,\min} \hat{s} = M k_{x,\min} = M \frac{2\pi}{L_x},$$

with $M \in \mathbb{N}^*$ a strictly positive integer. This relation can be rewritten:

$$L_x = \frac{M}{k_{y,\min} \hat{s}} = M \Delta x_{\text{LMRS}} = \frac{M}{2\pi \hat{s}} L_y, \quad (2.98)$$

thus imposing a constraint between the extensions L_x and L_y of the flux tube along the directions x and y respectively. In practice, the integer M must be chosen such that L_x is larger then the radial correlation length of turbulent eddies.

Relation (2.98) also implies that L_x must be an integer multiple of $\Delta x_{\text{LMRS}} = 1/(k_{y,\min}\hat{s})$, identified as the distance between lowest order MRSs. Indeed, considering the linearised safety factor profile (2.90), the distance Δx_{MRS} between MRSs corresponding to a given $k_y \neq 0$ mode is constant and given by

$$1 = \Delta[nq_s(x)] = k_y \hat{s} \Delta x_{\text{MRS}} \implies \Delta x_{\text{MRS}}(k_y) = 1/(k_y \hat{s}),$$

having invoked (2.89). One thus in particular has $\Delta x_{\text{LMRS}} = \Delta x_{\text{MRS}}(k_{y,\min}) = 1/(k_{y,\min}\hat{s})$. For a given $k_y \neq 0$ mode, the radial positions of corresponding MRSs are thus

$$x_{\text{MRS}} = m \Delta x_{\text{MRS}} = m \frac{k_{y,\min}}{k_y} \Delta x_{\text{LMRS}}, \quad m \in \mathbb{Z}.$$

Note that the positions of lowest order MRSs, $x_{\text{LMRS}} = m \Delta x_{\text{LMRS}}$, are MRSs to *all* $k_y \neq 0$ modes. More generally, there tends to be an alignment of the radial positions of MRSs corresponding to the different k_y around the lower order MRSs (second order MRSs are common to every second k_y , third order MRSs to every third k_y , etc.) and a misalignment around the higher order MRSs, as shown in figure 3.4(a). This level of (mis)alignment of MRSs can be measured by their radial density, as shown in figure 12 in [Dominski et al., 2017].

2.6.3 Collision frequency

In GENE, collision frequency is set via the normalised quantity ν_c defined as

$$\nu_c = \frac{\pi \ln \Lambda e^4 n_{\text{ref}} L_{\text{ref}}}{2^{3/2} T_{\text{ref}}^2}, \quad (2.99)$$

where n_{ref} , L_{ref} and T_{ref} are the reference density, length and temperature respectively. For the simulations considered in this thesis, one has $n_{\text{ref}} = n_{0,i} = n_{0,e}$, $L_{\text{ref}} = R$ and $T_{\text{ref}} = T_{0,i} = T_{0,e}$. ν_c is related to the electron-ion collision rate ν_{ei} [Hinton and Hazeltine, 1976] as

$$\nu_{ei}(v) = \frac{\sqrt{2} \pi Z^2 e^4 n_{0,i} \ln \Lambda}{\sqrt{m_e} T_{0,e}^{3/2}} \frac{v_{T,e}^3}{v^3} = 4 Z^2 \frac{n_{0,i}}{n_{\text{ref}}} \frac{T_{\text{ref}}^2}{T_{0,e}^2} \frac{v_{T,e}^3}{v^3} \frac{v_{th,e}}{L_{\text{ref}}} \nu_c, \quad (2.100)$$

where $v_{T,e} = \sqrt{2T_{0,e}/m_e}$. A physically more illustrative measure of collision frequency is the normalised collisionality ν_e^* , which estimates the average number of times a trapped electron is scattered to become passing before completing a banana orbit. Naturally, the banana regime for electrons is therefore characterised by $\nu_e^* < 1$ [Hinton and Hazeltine, 1976]. For a general geometry, ν_e^* is defined as

$$\nu_e^* = \frac{\sqrt{2} a B_0}{B_{p0} v_{T,e} \epsilon^{3/2} \tau_e}, \quad (2.101)$$

where B_{p0} is the poloidal component of the background magnetic field strength and $\tau_e = 3m_e^2 v_{T,e}^2 / 16\sqrt{\pi} Z^2 e^4 n_{0,i} \ln \Lambda$ is the electron-ion momentum exchange time, also called the electron collision time. For the circular ad-hoc geometry considered in this thesis, one has

$$\nu_e^* = \frac{16}{3\sqrt{\pi}} \frac{q_0 Z^2}{\epsilon^{3/2}} \frac{R}{L_{\text{ref}}} \frac{n_i}{n_{\text{ref}}} \frac{T_{\text{ref}}^2}{T_{0,e}^2} \nu_c. \quad (2.102)$$

The corresponding ion collisionality ν_i^* is given by

$$\nu_i^* = \frac{8}{3\sqrt{\pi}} \frac{q_0 Z^2}{\epsilon^{3/2}} \frac{R}{L_{\text{ref}}} \frac{n_i}{n_{\text{ref}}} \frac{T_{\text{ref}}^2}{T_{0,i}^2} \nu_c. \quad (2.103)$$

2.6.4 Numerical details

The gyrokinetic equation for the perturbed part of the distribution function can be expressed as

$$\frac{df_1}{dt} = L[f_1] + N[f_1],$$

where L and N represent the linear and non-linear operators respectively. GENE discretisation of the gyrokinetic equation is based on the method of lines, *i.e.* one starts discretising the phase space, leading (after solving the Maxwell's equations for Φ_1 and $A_{1,\parallel}$ in terms of f_1 and inserting in the gyrokinetic equation) to a system of ordinary differential equations for the perturbed distribution.

Time evolution and time step adaptation

In linear simulations, the linearised gyrokinetic equation can be solved either by using an eigenvalue solver to obtain a spectrum of eigenvalues (whose real and imaginary parts gives the growth rate and real frequency of the linear modes respectively) or by using an initial value solver to obtain the most unstable mode asymptotically in time. In turbulence simulations, the nonlinear gyrokinetic equation is evolved using the initial value solver. An explicit time stepping scheme, typically the Runge-Kutta scheme of order 4, is used in the initial value solver for the time evolution, which in turn needs to obey the Courant-Friedrich-Lewy (CFL) condition. The CFL condition demands that the time step Δt must be less than a certain limit to ensure the numerical stability of the scheme. In linear simulations using an initial value solver, the maximum time step Δt_{lin} is set such that $\omega_{\text{max}} \Delta t_{\text{lin}} < \alpha$, with $\alpha \simeq 1$; the eigenvalue solver is used to find for the considered phase space grid, the discretized eigenmode with the highest real frequency ω_{max} . In nonlinear simulations, the $E \times B$ advection velocity evolves in time and hence the time step needs to be periodically adapted such that it is less than both Δt_{lin} and

Δt_{nl} where Δt_{nl} is the maximum possible time step associated with the $E \times B$ velocity [Dannert, 2005].

Derivatives, numerical hyperdiffusion and anti-aliasing

In case the Fourier representation is used for any coordinate u (always true for the binormal coordinate y , and only true for the radial coordinate x in the flux-tube version), the derivatives can be obtained by $\partial f / \partial u \rightarrow i k_u \hat{f}_{k_u}$ without any loss of accuracy. For other coordinates, mostly the fourth-order centered finite difference scheme is used:

$$\left. \frac{\partial f}{\partial x} \right|_{x=x_i} \rightarrow \frac{f_{i-2} - 8f_{i-1} + 8f_{i+1} - f_{i+2}}{12\Delta x}. \quad (2.104)$$

A drawback associated with this particular scheme is that it tends to decouple the neighbouring gridpoints, *i.e.* between the gridpoints having odd and even indices. This can further lead to a divergence of the two subsets. To avoid this, *i.e.* to couple the odd and even gridpoint subsets, a fourth order hyperdiffusion term is added to the right hand side of the gyrokinetic equation (2.51), as given by:

$$-\nu_x \left. \frac{\partial^4 f}{\partial x^4} \right|_{x=x_i} \rightarrow h_x \frac{-f_{i-2} + 4f_{i-1} - 6f_i + 4f_{i+1} - f_{i+2}}{16}, \quad (2.105)$$

where $h_x = \nu_x / \Delta x^4$ is the damping coefficient [Püschel, 2009].

The quadratic $E \times B$ term in the gyrokinetic equation will lead to coupling of the two Fourier modes with wavenumber k_1 and k_2 to a third Fourier mode $k_3 = k_1 + k_2$ (and also $k_3 = k_1 - k_2$). In case k_3 is such that it lies outside the Nyquist limit, *i.e.* $k_3 > N/2$ where N is the number of gridpoints, then aliasing takes place, leading to the generation of unphysical mode couplings in the system. To avoid this, the so-called 3/2 rule is used, whereby a buffer of $N/4$ Fourier gridpoints are added to either side of the spectrum before the nonlinear term is evaluated, and once the nonlinear term is evaluated, the buffer is simply removed.

3 How eigenmode self-interaction affects zonal flows and convergence of turbulence levels with toroidal system size

3.1 Introduction

The role of passing electron dynamics in turbulent transport driven by ion-scale microinstabilities, in particular Ion Temperature Gradient (ITG) and Trapped Electron Mode (TEM) instabilities, has been given relatively little attention. In first approximation, these particles, which are highly mobile along the confining magnetic field, are assumed to respond adiabatically to the low frequency ion-scale modes. However, in a tokamak geometry, the phase velocity parallel to the magnetic field of a perturbation with fixed mode numbers m and n in the poloidal and toroidal directions, respectively, becomes infinite at the radial position $r_{m,n}$ of the corresponding Mode Rational Surface (MRS), where the magnetic safety factor profile $q_s(r)$ is such that $q_s(r_{m,n}) = m/n$. Consequently, on these surfaces, the condition for passing electrons to respond adiabatically gets violated and their non-adiabatic response becomes important. One notes that, given the toroidal axisymmetry of a tokamak, each linear microturbulence eigenmode has a fixed toroidal mode number n , but is in general a superposition of many poloidal Fourier modes m , so that associated MRSs are the positions $r_{m,n}$ for the different values of m .

In fact, as a result of the non-adiabatic passing electron dynamics, linear ITG and TEM eigenmodes can become significantly extended along the magnetic field lines [Hallatschek and Dorland, 2005], producing fine radial structures at corresponding MRSs [Falchetto et al., 2003, Chowdhury et al., 2008]. These fine structures on the eigenmodes persist in corresponding turbulence simulations, and via non-linear couplings lead to stationary corrugations on the radial profiles of density, temperature and in particular $E \times B$ zonal shear flows, aligned with low order MRSs, which effectively appear as fine-scale transport barriers [Waltz et al., 2006, Dominski et al., 2015, Dominski et al., 2017]. Given that

Chapter 3. How eigenmode self-interaction affects zonal flows and convergence of turbulence levels with toroidal system size

shearing and decorrelation of turbulent eddies by zonal flows is a primary mechanism by which turbulence saturates [Biglari et al., 1990, Waltz et al., 1994, Rosenbluth and Hinton, 1998, Lin et al., 1998], it is clearly of interest to understand the generation of these fine scale zonal flow structures in detail.

The generation of the fine zonal flow structures at low order MRSs, via a process called self-interaction, has in fact already been discussed to some length in the work by [Weikl et al., 2018]. The general motivation for the work presented in this chapter has been to further investigate the properties of zonal flow drive from this self-interaction mechanism. This process essentially involves each individual microturbulence eigenmode interacting non-linearly with itself to produce a Reynolds stress contribution to the zonal flow drive, which turns out to be located around its corresponding MRSs. Key to this self-interaction is the fact that an eigenmode which is significantly extended along the magnetic field line ‘bites its tail’ after one poloidal turn. For each eigenmode, self-interaction will therefore be particularly significant at its MRSs, given that the radially fine structures located at these positions, resulting from the non-adiabatic passing electron response, are elongated along the magnetic field lines. At low order MRSs (in practice implying mainly integer and half-integer q_s -surfaces), these self-interaction contributions to Reynolds stress from the different eigenmodes radially align and add up constructively to drive the stationary $E \times B$ zonal shear flows. Clear illustrations of these fine stationary zonal flow structures can be seen for example in figure 2 of Ref. [Waltz et al., 2006], figure 12 of Ref. [Dominski et al., 2017], figure 3 of Ref. [Weikl et al., 2018], and figure 3.4 of this chapter.

It is important to point out that in the core of a tokamak, low order MRSs are in fact few and far apart, whereas the radial domains between them occupy the majority of the plasma volume. Therefore, at least as important as understanding how self-interaction generates the above-mentioned stationary structures at lowest order MRSs, clearly visible on any flux surface-averaged field, is to address how the same self-interaction mechanism might affect zonal flow drive and therefore turbulent transport in the radial regions *between* low order MRSs. Addressing this question is the main focus of this chapter.

While lowest order MRSs are common to all eigenmodes, between them, the MRSs related to the various microturbulence modes tend to be radially misaligned. Hence, in these radial regions, the self-interaction contributions to Reynolds stress from these modes tend to cancel each other out when averaged over time, thus resulting in a nearly *zero stationary* component of the zonal flows. But, given that in the turbulent phase amplitudes of the various microinstability eigenmodes vary in time and furthermore are decorrelated with each other, this cancellation is not ensured at each time instant but only on average over time. As a result, self-interaction drives a *non-zero fluctuating* zonal flow component between low order MRSs.

An important observation resulting from our study is that in simulations accounting for non-adiabatic passing electron dynamics, self-interaction contributions to Reynolds stress

from the various microturbulence modes can indeed be significant in the radial regions between lowest order MRSs and in fact act as *random decorrelated kicks* that can in some cases actually disrupt what is usually considered the main drive mechanism of zonal flows - modulational instability [Hasegawa and Mima, 1978, Hasegawa et al., 1979, Chen et al., 2000]. The modulational instability mechanism involves the resonant decays of microinstability modes into zonal modes via secondary microinstability daughter modes. Unlike self-interaction, it is a *coherent* process, leading to a *correlated* contribution from the various microinstability modes to the Reynolds stress drive of zonal modes.

In order to quantify the relative importance of these two alternative, possibly competing mechanisms driving zonal flows, *i.e.* self-interaction and modulational instability, we have studied the statistical properties of the Reynolds stress contributions from the various microturbulence modes. Given the different nature of the two driving processes, one can identify high correlation levels between the mode contributions to conditions where modulational instability drive dominates, while lower correlation levels are characteristic of a significant effect from self-interaction. Central to this statistical analysis has been a series of gyrokinetic simulations obtained for identical driving conditions but varying the number of significant toroidal modes participating in the turbulence. Varying the number of toroidal modes changes in particular the number of associated random kicks from self-interaction to the zonal flow drive at each radial position.

Varying the number of significant toroidal modes is in fact related to varying the system size, typically measured by $\rho^* = \rho_i/a$, *i.e.* the ratio of the thermal ion Larmor radius ρ_i to the minor radius a of the tokamak. Indeed, invoking the fact that the unstable modes driving ion-scale microturbulence are such that $k_\perp \rho_i \lesssim 1$, where k_\perp is the wave vector component perpendicular to the magnetic field, and furthermore noticing that for a given eigenmode with toroidal mode number n an estimate for k_\perp is given by the poloidal wave vector component, which in turn can be evaluated as $k_\chi \simeq m/r_0 \simeq nq_s(r_0)/r_0$ [r_0 is the average radial position of the eigenmode and m its characteristic poloidal mode number estimated as $m \simeq nq_s(r_0)$, given that fluctuations are nearly field-aligned], one obtains that $k_\perp \rho_i \simeq nq_s(r_0)\rho_i/r_0 = (q_s a/r_0)n\rho^* \sim n\rho^*$, so that the number N_φ of toroidal modes contributing to the turbulence scales as $N_\varphi \sim 1/\rho^*$.

In view of what has just been said, it may at first sight appear surprising that the study presented in this chapter is in fact based on simulations carried out in the framework of the flux-tube model [Beer et al., 1995], whose underlying assumption is the scale separation between the characteristic length of microturbulence (\sim Larmor radius ρ) and the characteristic length of equilibrium (\sim minor radius a), hence *a priori* achieved by taking the strict limit $\rho^* \rightarrow 0$ of the gyrokinetic equations. In this limit, the radial dependence of all equilibrium profiles and their gradients appearing in the gyrokinetic equations are constant over the flux-tube volume. There is however one exception to this in the standard flux tube model [Scott, 1998]: a linearised radial dependence of the safety factor profile $q_s(r)$ (\sim constant magnetic shear approximation) is kept in the twist and

Chapter 3. How eigenmode self-interaction affects zonal flows and convergence of turbulence levels with toroidal system size

shift boundary condition applied after usually following the magnetic field line a single turn in the poloidal direction. Through this parallel boundary condition, an eigenmode ‘bites its tail’ and in particular correctly accounts for the possible resonances that may develop at its associated MRSs. The fact that the eigenmodes correctly “feel” their associated MRSs is obviously key to the development of the fine radial structures and related non-linear self-interaction which is the focus of our study. Also, close agreement between flux-tube [Dominski et al., 2015] and global [Dominski et al., 2017] gyrokinetic simulations regarding the characteristics of the fine stationary zonal flow structures at lowest order MRSs clearly confirm that the dynamics of the self-interaction mechanism can indeed be correctly accounted for using such a local model.

Let us already briefly provide here some further insight into how the toroidal spectral density is varied in a flux-tube code (all details are given in §2.6). The flux-tube version of the GENE code [Jenko et al., 2000, Merz, 2008] which we have applied for the present study, considers the field aligned coordinate system defined [in equations (2.81-2.83)] by the variables (x, y, z) which are respectively the radial, binormal and parallel coordinates. Note that the binormal coordinate y is the only one of the three coordinates (x, y, z) which actually depends on the toroidal angle φ . The length L_y of the flux-tube in this direction can thus be associated with its angular extent $\Delta\varphi$ along φ : $L_y = C_y \Delta\varphi$, where the constant $C_y = r_0/q_0$ ensures that y has units of length, r_0 being the radial position at which the flux-tube is positioned and $q_0 = q_s(r_0)$. Also, as a linear eigenmode has a fixed toroidal mode number n , it consequently has a fixed Fourier mode number k_y with respect to y when represented in field-aligned coordinates, given by $k_y = n/C_y = nq_0/r_0$, *i.e.* k_y is actually equivalent to the previously mentioned poloidal mode number estimate k_χ . The significant k_y modes contributing to ion-scale turbulence are therefore such that $k_y \rho_i \lesssim 1$, and given that the minimum mode number for a flux-tube box with length L_y is given by $k_{y,\min} = 2\pi/L_y$, the number of toroidal modes contributing to the turbulence is estimated as $N_\varphi \simeq 1/k_{y,\min}\rho_i = (1/2\pi)L_y/\rho_i$. Hence, when studying microturbulence using flux-tube simulations, carrying out a scan in $k_{y,\min}\rho_i$ (or equivalently L_y/ρ_i) corresponds to varying the toroidal spectral density.

In view of the above, it is therefore possible to realistically study the importance of the self-interaction mechanism via a flux-tube simulation for a given size tokamak, characterized by a finite ρ^* value, by considering the appropriate toroidal spectral density, *i.e.* by setting $k_{y,\min}\rho_i = \rho_i/C_y = (q_0 a/r_0)\rho^*$ corresponding to the toroidal mode number $n = 1$ (one naturally recovers here that the number of modes contributing to turbulence scales as $N_\varphi \simeq 1/k_{y,\min}\rho_i \sim 1/\rho^*$). This is clearly equivalent to setting $L_y = 2\pi C_y$, *i.e.* $\Delta\varphi = 2\pi$, which along with parallel box length $L_z = 2\pi$ implies having the flux-tube cover the *full* magnetic surface once. Therefore, considering a finite $k_{y,\min}\rho_i$ value in a flux-tube simulation effectively corresponds to accounting for a finite ρ^* effect. All other finite ρ^* effects such as profile shearing [Waltz et al., 1998, Waltz et al., 2002], or finite radial extent of the unstable region [McMillan et al., 2010], are however obviously absent in a flux-tube.

Given that $k_{y,\min}\rho_i \sim \rho^*$, the true flux-tube model would require considering the limit of $k_{y,\min}\rho_i \rightarrow 0$. In numerical simulations however, for obvious practical reasons, $k_{y,\min}\rho_i \sim \rho_i/L_y$ is always finite, so that if turbulence actually converges for $k_{y,\min}\rho_i \rightarrow 0$, this limit can at best be approximately approached in the limit of large box length L_y/ρ_i , which may become numerically prohibitive. Thus, carrying out the above mentioned $k_{y,\min}\rho_i$ scan also enables us to investigate whether/how the flux-tube simulation results converge as $k_{y,\min}\rho_i \rightarrow 0$, a problem that was already addressed in [Ball et al., 2020]. It is remarkable that, to our knowledge, the convergence of flux-tube gyrokinetic turbulence simulations with respect to $k_{y,\min}\rho_i$ seems not to have been given more attention in the literature, at least not considering fully kinetic electron dynamics. Our simulations of ITG-driven turbulence indeed illustrate that for practical values of $k_{y,\min}\rho_i$, typically chosen in the range $10^{-2} - 10^{-1}$, convergence of turbulent fluxes is in many cases not yet reached. Particularly in the case of strong background temperature gradients, *i.e.* away from marginal stability, the gyro-Bohm normalised ion heat flux Q_i keeps on increasing with a nearly algebraic scaling $Q_i \sim (k_{y,\min}\rho_i)^{-\alpha}$, $\alpha > 0$, when decreasing $k_{y,\min}\rho_i$, thus showing no apparent sign of convergence within this range of values. In the particular strong gradient case considered, corresponding to parameters near to the Cyclone Base Case (CBC) [Dimits et al., 2000], one has $\alpha \simeq 0.45$ (see Fig. 3.7 in this chapter), so that Q_i increases by nearly a factor of 3 over the range $k_{y,\min}\rho_i = 10^{-2} - 10^{-1}$. In agreement with related work by one of our co-authors [Ball et al., 2020], for sufficiently small values of $k_{y,\min}\rho_i$, the algebraic scaling is ultimately broken and convergence of the fluxes is finally approached within $\sim 5\%$ for $k_{y,\min}\rho_i \simeq 5 \cdot 10^{-3}$ (see Fig. 3.19). But this corresponds to a value of $k_{y,\min}\rho_i$ one order of magnitude smaller than usually considered. For gradients closer to marginal stability, this dependence of Q_i on $k_{y,\min}\rho_i$ appears to be weakened and convergence approached already for somewhat larger, numerically more affordable values. This can be seen as good news, as gradients near marginal stability may be considered as the physically most relevant cases. It nonetheless appears essential that one keeps in mind this potentially significant dependence of the fluxes on $k_{y,\min}\rho_i$ in the range of typically considered values, which seems to have very often been overlooked or at least not been given sufficient attention in past studies.

In conjunction with the observed increase in fluxes with system size over the considered range of $k_{y,\min}\rho_i = 10^{-2} - 10^{-1}$, a decrease in the shearing rate associated with fluctuating zonal flows is also observed [see Fig. 3.6(c)]. Via a simple “back-of-the-envelope” estimate, this decrease in the shearing rate associated with fluctuating zonal flows is shown to result from the fact that the self-interaction drive of zonal flows from the various microturbulence modes are decorrelated with each other.

The remainder of this chapter is organized as follows.

A brief summary of a set of previous studies [Dominski et al., 2015, Dominski et al., 2017], addressing the role of non-adiabatic passing electron dynamics and which provided the starting point for the main work presented in this chapter, is given in §3.2. The same

Chapter 3. How eigenmode self-interaction affects zonal flows and convergence of turbulence levels with toroidal system size

ITG-driven turbulence case as in [Dominski et al., 2015] will in fact also be considered as a reference case here. Its parameters are recalled as well as the linear frequency and growth rate spectra. Also pointed out are the fine radial structures that develop on the linear eigenmodes as a result of the non-adiabatic passing electron dynamics. Furthermore summarized is how these fine structures on the eigenmodes act as channels for electron heat and particle transport, and, through non-linear coupling, are observed to lead to corrugations at low order MRSs of the time-averaged density and temperature profiles as well as $E \times B$ zonal flow shear layers.

The main results for the present study, consisting of non-linear flux-tube simulations of ITG-driven turbulence are presented in §3.3. Sets of simulations have been obtained by scanning $k_{y,\min}\rho_i$ over the typical range of values considered in practice, *i.e.* $k_{y,\min}\rho_i = 10^{-2} - 10^{-1}$. These scans were repeated considering ion temperature gradients both near and far from marginal stability. Furthermore, to clearly illustrate how the fine radial structures resulting from the non-adiabatic passing electron dynamics lead to particularly strong contributions to zonal flow drive from the self-interaction mechanism, simulations with two different electron models were carried out: either considering fully kinetic electron dynamics or enforcing their fully adiabatic response (fine radial structures being absent with the latter model). First analysis of results are carried out in this same section, showing that especially in the case of fully kinetic electrons and far from marginal stability, heat fluxes Q_i have not yet converged over the considered range of typical $k_{y,\min}\rho_i$ values. Given its key role in saturating ITG-driven turbulence, the level of zonal flow shearing rate, $\omega_{E \times B}$, is carefully diagnosed. It is shown how in all cases this shearing rate decreases with decreasing $k_{y,\min}\rho_i$ (see figure 3.6). Also analysed is the radial correlation length of the turbulence. An important observation is that for sufficiently small $k_{y,\min}\rho_i$, the radial extent of turbulent eddies presents a clearly shorter scale length than the distance between lowest order MRSs (figure 3.8). From this one concludes that, for these lower values of $k_{y,\min}\rho_i$, the turbulence is mostly sheared by the zonal flows between lowest order MRSs, where $\omega_{E \times B}$ is essentially composed of its fluctuating component, rather than sheared by the stationary component of $\omega_{E \times B}$ located at the lowest order MRSs.

Section 3.4 is dedicated to understanding why fluctuating zonal shear flow level decreases with $k_{y,\min}\rho_i$. To this end, the different zonal flow driving mechanisms are analysed in detail. After showing in §3.4.1 that Reynolds stress can be considered as a proxy for measuring the drive of zonal flows, we review the two basic zonal flow driving mechanisms: modulational instability in §3.4.2 and self-interaction in §3.4.3. To illustrate these two basic mechanisms, reduced non-linear simulations are presented in §3.4.4, where the drive of zonal modes via the decay of an initially single finite amplitude ITG eigenmode is studied. These simulations are carried out with both adiabatic and kinetic electrons to demonstrate the dominant role of modulational instability in the former case and the significant role of self-interaction in the latter.

3.2. Non-adiabatic passing electron dynamics leading to stationary zonal structures

Evidence of the self-interaction and the modulational instability mechanisms in fully developed turbulence is then addressed in §3.4.5 and §3.4.6, respectively. A comparison between simulations with adiabatic and kinetic electrons is done here as well. It is shown that the self-interaction mechanism is persistent in the turbulence simulations accounting for fully kinetic electrons, while it is weak in simulations with adiabatic electrons, consistent with the reduced nonlinear simulations. Using statistical methods such as bicoherence and Reynolds stress correlation analysis diagnostics, we show that the self-interaction contributions to Reynolds stress from the various microturbulence modes are decorrelated in time, and essentially act as random kicks on the zonal modes, while the contributions from modulational instability, which is a coherent process, are correlated with each other. In the case of adiabatic electron simulations, strong correlation between Reynolds stress contributions from different modes as well as large bicoherence levels are measured, reflecting that self-interaction is indeed weak and zonal flow drive is dominated by the modulational instability. In the case of kinetic electrons however, self-interaction may disrupt the zonal flow drive from modulational instability and, consequently, correlation between Reynolds stress contributions as well as bicoherence levels are found to be relatively weak (see figures 3.16 and 3.17).

Based on the study carried out in §3.4, providing evidence of the decorrelated nature of the self-interaction contributions to zonal flow drive from the various microturbulence modes, we carry out a “back-of-the-envelope” derivation, using simple statistical arguments, to predict the scaling observed in simulations with kinetic electrons of the zonal flow shearing rate $\omega_{E \times B}$ with $k_{y,\min}\rho_i$. This derivation is presented in §3.5.

Final discussion and conclusions are provided in §3.6.

Two appendices are also part of this chapter. In appendix A, the possibility of local flattening of effective gradients between Lowest order Mode Rational Surfaces (LMRSs) as a means to explain the increase in flux levels with decreasing $k_{y,\min}\rho_i$ observed for the kinetic electron runs (see figure 3.7), is explored. In appendix B, an approximate evolution equation for the shearing rate $\omega_{E \times B}$ associated with $E \times B$ zonal flows is derived so as to identify the nonlinear driving terms, and in particular justify Reynolds stress as a proxy for the zonal flow drive.

3.2 Non-adiabatic passing electron dynamics leading to stationary zonal structures

This section presents a summary of relevant results from the articles [Dominski et al., 2015, Dominski et al., 2017], which addressed certain effects of non-adiabatic passing electron dynamics on turbulent transport.

Non-adiabatic passing electron response leads to generation of fine-structures at MRSs

Chapter 3. How eigenmode self-interaction affects zonal flows and convergence of turbulence levels with toroidal system size

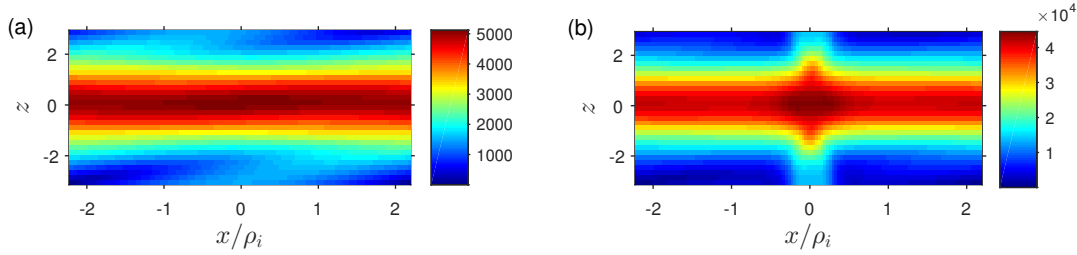


Figure 3.1: Linear eigenmode with $k_{x0} = 0$ and $k_y \rho_i = 0.28$, in the case of (a) adiabatic, (b) kinetic electron response. Shown is the (x, z) -dependence of the electrostatic potential Φ in absolute value, weighted by the Jacobian, $J|\Phi|$.

which can be first studied in linear simulations. Figure 3.1 shows the envelope in the (x, z) plane of the electrostatic potential Φ of the unstable linear ITG eigenmode with $k_y \rho_i = 0.28$, considering either adiabatic or kinetic electron response, and for the set of physical parameters given in Table 3.1. This is the same ITG case as considered in reference [Dominski et al., 2015] and same numerical grid resolutions have been used here. While in both cases the modes are ballooned at $z = 0$, one observes a fine radial structure at the corresponding MRS (positioned at the center $x = 0$ of the radial domain) only in the latter case. This is the result of the non-adiabatic passing electron response taking place at MRSs where the parallel wavenumber $k_{\parallel} \rightarrow 0$ [Chowdhury et al., 2008, Dominski et al., 2015]. In the vicinity of MRSs, the condition for adiabatic electron response is violated as the phase velocity of the eigenmode parallel to the magnetic field becomes greater than the electron thermal velocity: $|\omega/k_{\parallel}| > v_{th,e}$. These fine structures along the x direction translate to a broad range of significant k_x Fourier modes, *i.e.* to a broad ballooning structure according to equation (2.96), which is referred to as the “giant electron tails” in [Hallatschek and Dorland, 2005]; see figure 3.2. No such broad tails in the ballooning structure are observed with adiabatic electrons. Figure 3.3 plots the k_y spectrum of linear growth rates γ and real frequencies ω_R of most unstable eigenmodes for the cases considered here. Note that $\omega_R > 0$ corresponds in GENE convention to a mode propagating in the ion-diamagnetic direction, as expected for ITG instabilities.

The radial structures related to the non-adiabatic passing electron dynamics have been shown to persist in the non-linear turbulent regime, as discussed in references [Waltz et al., 2006, Dominski et al., 2015, Dominski et al., 2017]. Studies by [Dominski et al., 2015, Dominski et al., 2017], based on both local (flux-tube) and global gyrokinetic simulations, have furthermore shown that, for each fluctuation mode with mode number k_y , the corresponding MRSs act as radially localized transport channels. This is illustrated in figures 3.4(a,b). Radial regions with high (resp. low) density of MRSs thus tend to lead to high (resp. low) particle and heat diffusivities. Consequently, to ensure radially constant time-averaged total particle and heat fluxes, density and temperature gradients (driving the turbulence) become corrugated, steepening in regions with low density of MRSs and flattening in regions with high density of MRSs. See figures 3.4(c,d) where

3.2. Non-adiabatic passing electron dynamics leading to stationary zonal structures

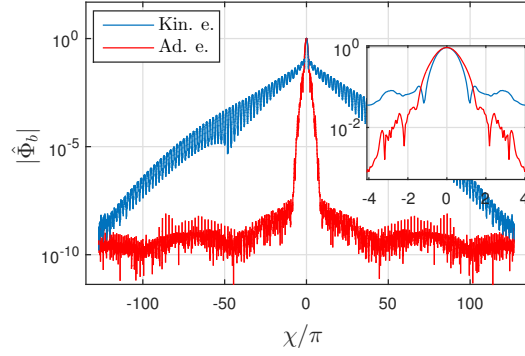


Figure 3.2: Ballooning representation $|\hat{\Phi}_b(\chi)|$ of the electrostatic potential Φ for the same linear eigenmode as in figure 3.1, showing both the case of kinetic (blue) and adiabatic (red) electrons. Inset figure shows the zoom near $\chi = 0$.

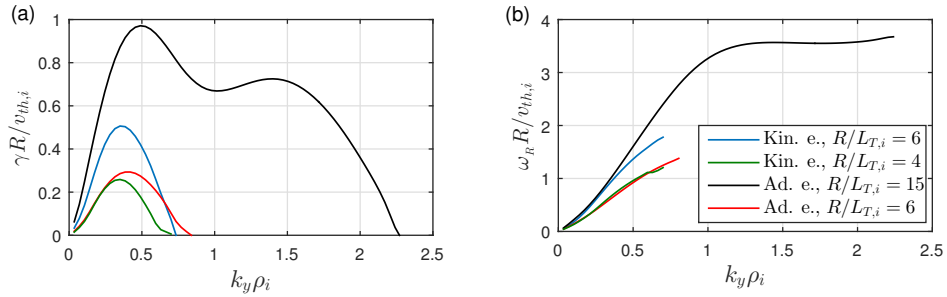


Figure 3.3: (a) Linear growth rate γ and (b) real frequency ω_R in units of $v_{th,i}/R$ as a function of $k_y \rho_i$. Adiabatic electron simulations with $R/L_{T,i} = 6$ and 15 are plotted in red and black respectively. Kinetic electron simulations with $R/L_{T,i} = 4$ and 6 are plotted in green and blue respectively.

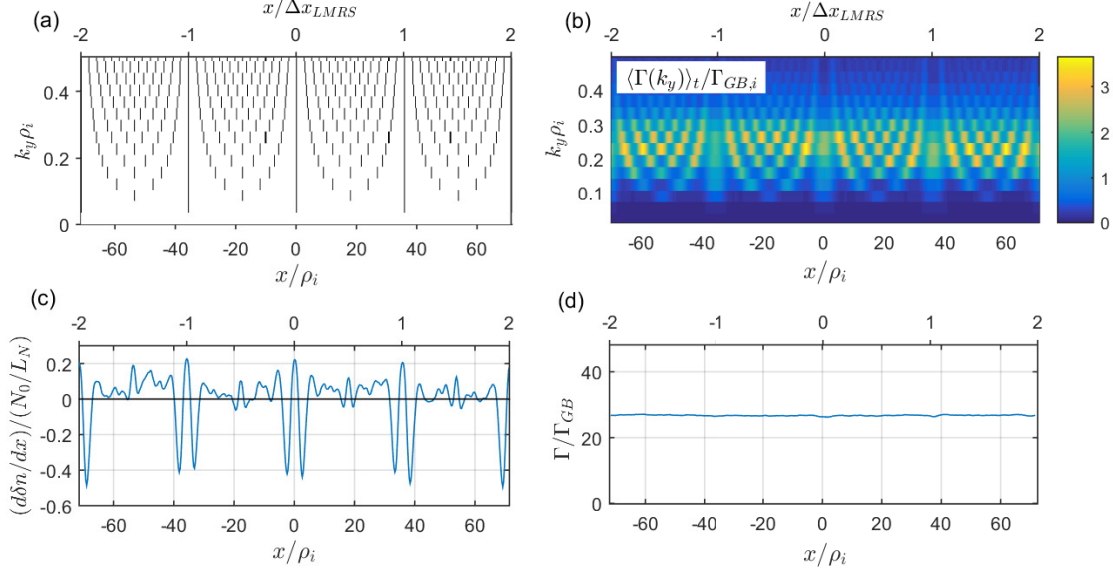


Figure 3.4: (a) Radial position of MRSs for each k_y mode, (b) radial dependence of contribution to time-averaged particle flux Γ in gyro-Bohm units $\Gamma_{GB} = N_0 v_{th,i} (\rho_i/R)^2$ from each k_y mode, (c) radial gradient of flux-surface and time-averaged density fluctuation δn normalised with respect to N_0/L_N (positive/negative values correspond respectively to flattening/steepening of profiles), and (d) radial profile of time-averaged total particle flux (summed over all k_y). All subplots correspond to kinetic electron simulation for the parameter set given in table 3.1, with $k_{y,min}\rho_i = 0.035$ and $R/L_{T,i} = 6$. Ticks $x/\Delta x_{LMRS} = \{-2, -1, 0, 1, 2\}$ on the top axes denote the lowest order MRSs (LMRSs).

the time-averaged density gradient and particle flux are shown as a function x .

Stationary $E \times B$ shear flow layers associated with the time-averaged radial electric field are also observed (see figure 3.5 where the corresponding effective shearing rate as defined in (3.2) is plotted). This electric field component ensures the radial force balance with the pressure gradients related to the corrugation of density and temperature profiles [Waltz et al., 2006]. In sections 3.4.3 - 3.4.5, it is shown that these stationary shear structures are actually driven by a contribution to the Reynolds Stress coming from the so-called self-interaction mechanism [Weikl et al., 2018].

3.3 $k_{y,min}\rho_i$ scan in ITG-driven turbulence. Role of stationary and fluctuating components of zonal shear flows

Non-linear simulations have been carried out considering conditions of ITG-driven turbulence. Reference physical and numerical parameters for these simulations are summarized in table 3.1. The physical parameters are close to the Cyclone Base Case (CBC) [Dimits et al., 2000], with background gradients slightly modified to eliminate

3.3. $k_{y,\min}\rho_i$ scan in ITG-driven turbulence. Role of stationary and fluctuating components of zonal shear flows

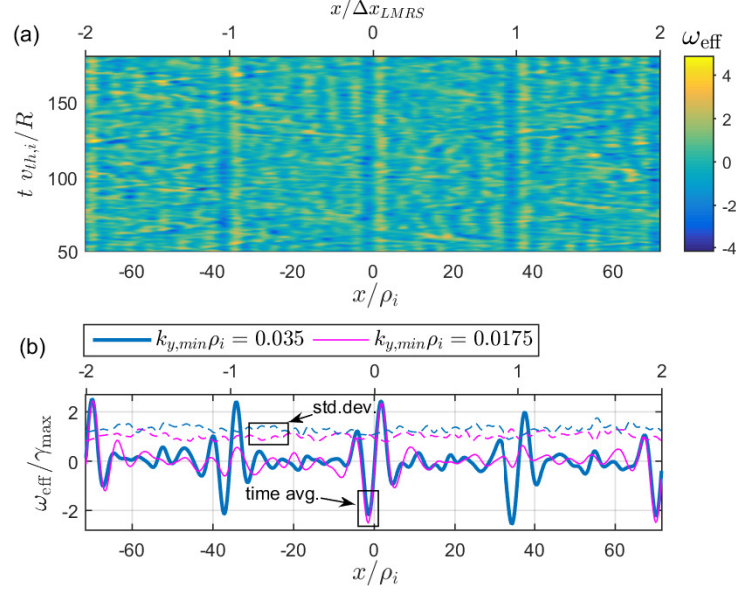


Figure 3.5: (a) Effective shearing rate $\omega_{\text{eff}}(x, t)$ plotted as a function of the radial position x and time t , for the kinetic electron simulation with parameters as given in table 3.1, $k_{y,\min}\rho_i = 0.035$ and $R/L_{T,i} = 6$. (b) Solid blue line indicates the associated time-averaged component $\langle \omega_{\text{eff}} \rangle_t$, normalised by the corresponding maximum linear growth rate γ_{max} , at each radial position x . Dashed blue line indicates the standard deviation $\text{SD}_t(\omega_{\text{eff}})(x) = \left[\langle (\omega_{\text{eff}} - \langle \omega_{\text{eff}} \rangle_t)^2 \rangle_t \right]^{1/2}$ in time, normalised by γ_{max} . For comparison, results for $k_{y,\min}\rho_i = 0.0175$ have been added in magenta.

Chapter 3. How eigenmode self-interaction affects zonal flows and convergence of turbulence levels with toroidal system size

Geometry: Ad-hoc concentric circular geometry[Lapillonne et al., 2009]

$\epsilon = 0.18$	$q_0 = 1.4$	$\hat{s} = 0.8$	$\beta = 0.001$	
$m_i/m_e = 400$	$T_e/T_i = 1.0$	$R/L_N = 2.0$	$R/L_{T_i} = 6.0$	$R/L_{T_e} = 2.0$
$L_x = 142.9 \rho_i$	$L_y^* = 179.5 \rho_i$	$L_z = 2\pi$	$v_{\parallel, \max} = 3\sqrt{2} v_{th, i}$	$\mu_{\max} = 9 T_{0, i} / B_{0, \text{axis}}$
$M^* = 4$	$N_{k_x} \times N_{k_y}^* \times N_z \times N_{v_{\parallel}} \times N_{\mu} = 512 \times 128 \times 16 \times 64 \times 9$			

Table 3.1: Parameter set for non-linear simulations. The parameter $k_{y, \min} = 2\pi/L_y$ is scanned and takes the values $k_{y, \min} \rho_i \in \{0.14, 0.07, 0.035, 0.0175\}$, while $k_{y, \max} = k_{y, \min} N_y / 2$ and $L_x = M / \hat{s} k_{y, \min}$ are kept constant. The values indicated in the table correspond to the particular case $k_{y, \min} \rho_i = 0.035$. Asterisks indicate variables which vary during the $k_{y, \min} \rho_i$ scan. $v_{th, i} = \sqrt{T_i / m_i}$ stands for the ion thermal velocity and $B_{0, \text{axis}}$ for the magnetic field on axis.

unstable TEM and ETG modes. Compared to typical flux-tube runs, a high radial resolution is chosen (with radial grid-points $N_x = 512$) in order to ensure that the dynamics at MRSs (separated by a radial distance $\Delta x_{MRS} = 1 / \hat{s} k_y$ for a given k_y) is very well resolved, as discussed in detail in Ref. [Dominski et al., 2015]. In our work, this high x -resolution is all the more critical since the fine-structures forming at the MRSs play an important role in the self-interaction mechanism, which is crucial to our study.

A scan in $k_{y, \min} \rho_i$ is performed while keeping both $k_{y, \max} \rho_i$ and L_x / ρ_i fixed. Successively halving $k_{y, \min} \rho_i$, the values $k_{y, \min} \rho_i = 0.14, 0.07, 0.035$, and 0.0175 have been considered. Note that these values for $k_{y, \min} \rho_i$ span the typical range $10^{-2} - 10^{-1}$ considered in practice when carrying out ion-scale flux-tube simulations. To keep $k_{y, \max} \rho_i$ fixed, the total number N_y of k_y modes must thus be doubled between consecutive runs, whereas to keep L_x / ρ_i fixed, the number M of lowest order MRSs contained in the simulation box is halved. The parameter M thus takes on the respective values $M = 16, 8, 4$ and 2 . The case $k_{y, \min} \rho_i = 0.07$ is in fact equivalent to the ITG case already studied by [Dominski et al., 2015].

Based on the relation $k_{y, \min} \rho_i = (q_0 a / r_0) \rho^*$ (assuming that all toroidal modes are accounted for, so that $n_{\min} = 1$) and for the typical mid-radius value $r_0 / a = 0.5$ and here considered $q_0 = 1.4$, one obtains $\rho^* = 5.0 \cdot 10^{-2}, 2.5 \cdot 10^{-2}, 1.25 \cdot 10^{-2}, 6.25 \cdot 10^{-3}$. Note for reference that typical values for this parameter are $\rho^* \simeq 1 \cdot 10^{-2}$ in a smaller-size machine such as the TCV tokamak, $\rho^* \simeq 3 \cdot 10^{-3}$ in the DIII-D tokamak[Waltz, 2005], while the projected values for ITER are still an order of magnitude smaller.

In order to address how the results from the $k_{y, \min} \rho_i$ scan depend on whether one is near or far from marginal stability, the scan was repeated for a second ion temperature gradient in both the adiabatic and kinetic electron cases. To this end, carrying out preliminary R/L_{T_i} scans for $k_{y, \min} \rho_i = 0.035$, the non-linear (Dimits-shifted) critical temperature gradients $R/L_{T_i, \text{crit}}$ were first identified. For adiabatic electrons, $R/L_{T_i, \text{crit}} = 5.5$ was found, so that the reference case temperature gradient $R/L_{T_i} = 6$ ($Q_i / Q_{GB, i} = 28.8$) is

3.3. $k_{y,\min}\rho_i$ scan in ITG-driven turbulence. Role of stationary and fluctuating components of zonal shear flows

relatively *near* marginal stability and the second $k_{y,\min}\rho_i$ scan was therefore performed for $R/L_{Ti} = 15$ ($Q_i/Q_{GB,i} = 258.9$) in this case, *i.e.* *farther* from marginal stability. For kinetic electrons, $R/L_{T_{i,\text{crit}}} = 3.5$, so that the reference case temperature gradient $R/L_{Ti} = 6$ ($Q_i/Q_{GB,i} = 262.4$) is relatively *far* from marginal stability and the second $k_{y,\min}\rho_i$ scan was therefore performed for $R/L_{Ti} = 4$ ($Q_i/Q_{GB,i} = 87.1$) in this case, *i.e.* *nearer* marginal stability.

To ensure that the simulations results are sound, convergence tests with respect to radial box size L_x and the numerical resolutions N_z , $N_{v_{\parallel}}$ and N_{μ} were carried out. Convergence test on N_x had already been addressed in [Dominski et al., 2015]. Based on these tests, the turbulent heat and particle fluxes, as well as statistical properties of $E \times B$ shearing rates are estimated to be within $\sim 10\%$ of their converged value. Benchmarking of the GENE results with the gyrokinetic code GS2 [Dorland et al., 2000] was furthermore performed for a limited number of simulations. Although a reduced mass ratio is considered here, similar results have been obtained with the physical mass ratio of hydrogen $m_i/m_e = 1836$.

First results from the $k_{y,\min}\rho_i$ scan will now be discussed. Given their importance in saturating ITG turbulence, particular attention will be given to the statistical properties of the shearing rate $\omega_{E \times B}$ associated with the zonal $E \times B$ flows. We will in fact consider the effective shearing rate ω_{eff} , inspired by the definitions in [Dominski et al., 2015]. This rate is estimated as follows. One first defines the zonal $E \times B$ shearing rate experienced by the ions, which are the dominant instability drivers in the case of ITG turbulence considered here:

$$\omega_{E \times B, \text{ion}}(x, t) = \frac{1}{B_0} \frac{\partial^2 \langle \bar{\Phi} \rangle_{y,z}}{\partial x^2}, \quad (3.1)$$

where the flux-surface average $\langle \bar{\Phi} \rangle_{y,z}$ provides the zonal component of $\bar{\Phi}$ and involves both an average over y , $\langle \cdot \rangle_y = (1/L_y) \int_0^{L_y} \cdot dy$, and an average over z , $\langle \cdot \rangle_z = \int_{-\pi}^{+\pi} \cdot J^{xyz} dz / \int_{-\pi}^{+\pi} J^{xyz} dz$. $\bar{\Phi}$ is the scalar potential gyroaveraged over the Maxwellian ion background velocity distribution, *i.e.* $\bar{\Phi} = \mathcal{G}_i \Phi$ where the gyroaveraging operator \mathcal{G}_i itself involves averaging over the Maxwellian background distribution, given in Fourier space by

$$\hat{\mathcal{G}} = \frac{B_0}{T_{0,i}} \int_0^\infty d\mu \exp\left(\frac{\mu B_0}{T_{0,i}}\right) J_0\left(\frac{k_{\perp} v_{\perp}}{\Omega_i}\right) = e^{-(k_{\perp} v_{\perp})^2/4}.$$

Since the effective electric field felt by the ions is a gyro-averaged one, it is justified to consider the gyro-average of the scalar potential. It also helps to eliminate the non-vanishing tail in the k_x -spectra of $\omega_{E \times B}$ at large when a non-gyroaveraged scalar potential is considered.

The shearing rate $\omega_{E \times B, \text{ion}}$ is then furthermore averaged over a small time window of width τ , given that fluctuations that are very short-lived in time do not contribute effectively towards the zonal flow saturation mechanism [Hahm et al., 1999], thus providing the

Chapter 3. How eigenmode self-interaction affects zonal flows and convergence of turbulence levels with toroidal system size

effective shearing rate:

$$\omega_{\text{eff}}(x, t) = \frac{1}{\tau} \int_{t-\tau/2}^{t+\tau/2} \omega_{E \times B, \text{ion}}(x, t') dt'. \quad (3.2)$$

Here, $\tau = 1/\gamma_{\text{max}}$ is considered, where γ_{max} is the growth rate of the most unstable linear mode.

As an illustration, the effective shearing $\omega_{\text{eff}}(x, t)$ has been plotted in figure 3.5(a) as a function of x over the full flux-tube width L_x and as a function of t over the simulation time slice $50 < t v_{\text{th},i}/R < 180$. Shown is the case with kinetic electrons, $R/L_{T_i} = 6$ and $k_{y,\text{min}}\rho_i = 0.035$. The radial profile for the time-averaged component $\langle \omega_{\text{eff}} \rangle_t(x)$, is shown in figure 3.5(b). For comparison, the same profile is also shown for the same physical parameters except for $k_{y,\text{min}}\rho_i = 0.0175$.

The system average of the *total* effective shearing rate is plotted in figure 3.6(a) as a function of $k_{y,\text{min}}\rho_i$, considering a log-log scale. This average value is provided by the Root Mean Square (RMS) estimate:

$$\text{RMS}_{x,t}(\omega_{\text{eff}}) = \left(\langle \omega_{\text{eff}}^2 \rangle_{x,t} \right)^{1/2}, \quad (3.3)$$

involving both a radial average, $\langle \cdot \rangle_x = (1/L_x) \int_0^{L_x} \cdot dx$, and an average over the whole simulation time t_{sim} , $\langle \cdot \rangle_t = (1/t_{\text{sim}}) \int_0^{t_{\text{sim}}} \cdot dt$. Figure 3.6(a) shows results for the scans carried out for the two respective temperature gradients R/L_{T_i} considered for both adiabatic and kinetic electrons. The shearing rates have been normalised with respect to the value of γ_{max} , which takes on different values for the four considered datasets (see figure 3.3). Normalised shearing values $\omega_{\text{eff}}/\gamma_{\text{max}} \gtrsim 1$ can be considered as significant for saturating ITG-driven turbulence. Note that a straight system average $\langle \omega_{\text{eff}}(x, t) \rangle_{x,t}$ of the shearing rate would converge to zero over sufficiently long simulation time, which is why the RMS estimate (3.3) is considered. One notes that, over the considered range $10^{-2} - 10^{-1}$ in $k_{y,\text{min}}\rho_i$ values, the total effective shearing rate $\text{RMS}_{x,t}(\omega_{\text{eff}})$ decreases in all cases with decreasing $k_{y,\text{min}}\rho_i$, *i.e.* with increasing machine size. However, significantly stronger scaling is observed for the scans with kinetic compared to adiabatic electrons. As can be seen from the log-log plot, the shearing rate appears to roughly scale as $\sim (k_{y,\text{min}}\rho_i)^\alpha$, $\alpha > 0$. This scaling is particularly evident for the kinetic electron case far from marginal stability ($R/L_{T_i} = 6$), for which $\alpha \simeq 0.34$. Similar scaling is observed nearer marginal stability ($R/L_{T_i} = 4$) as well. The adiabatic electron scans however show a weaker scaling with $\alpha \simeq 0.08$ for both $R/L_{T_i} = 6$ and $R/L_{T_i} = 15$.

Figure 3.7(a) plots in log-log scale, the time and flux-tube -averaged radial ion heat flux Q_i as a function of $k_{y,\text{min}}\rho_i$. Heat fluxes have been normalised to gyro-Bohm units $Q_{GB,i} = n_{0,i} T_i v_{\text{th},i} (\rho_i/R)^2$. Results for all four considered datasets are again presented. Over the considered range of $k_{y,\text{min}}\rho_i$, fluxes appear not to be converged with respect

3.3. $k_{y,\min}\rho_i$ scan in ITG-driven turbulence. Role of stationary and fluctuating components of zonal shear flows

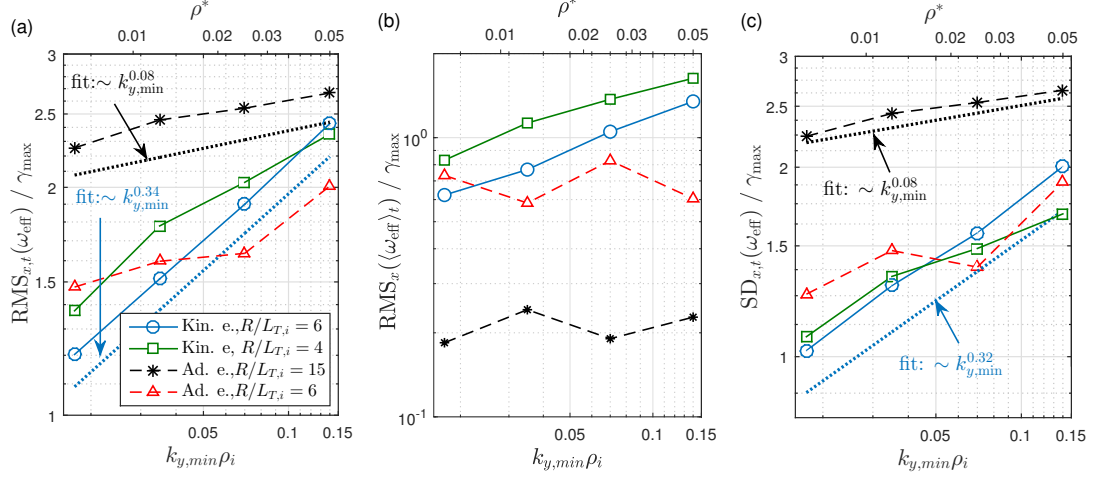


Figure 3.6: Effective shearing rate ω_{eff} associated with the zonal $E \times B$ flows, normalised to corresponding maximum linear growth rate γ_{\max} , as a function of $k_{y,\min}\rho_i$. Solid lines denote kinetic electron simulations for $R/L_{T,i} = 4$ (green squares) and 6 (blue circles) respectively. Dashed lines denote adiabatic electron simulations for $R/L_{T,i} = 6$ (red triangles) and 15 (black stars) respectively. Other parameters remain the same as in table 3.1. (a) System average of total shearing rate $\text{RMS}_{x,t}(\omega_{\text{eff}}) = (\langle \omega_{\text{eff}}^2 \rangle_{x,t})^{1/2}$. (b) Contribution from the stationary component, $\text{RMS}_x(\langle \omega_{\text{eff}} \rangle_t) = [\langle (\langle \omega_{\text{eff}} \rangle_t)^2 \rangle_x]^{1/2}$. (c) Contribution from fluctuation component, $\text{SD}_{x,t}(\omega_{\text{eff}}) = [\langle (\omega_{\text{eff}} - \langle \omega_{\text{eff}} \rangle_t)^2 \rangle_{x,t}]^{1/2}$. All plots in log-log scale.

Chapter 3. How eigenmode self-interaction affects zonal flows and convergence of turbulence levels with toroidal system size

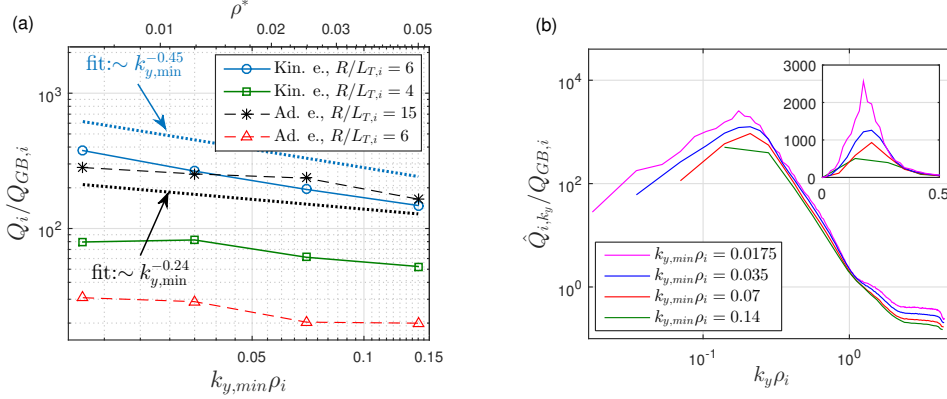


Figure 3.7: (a) Log-log plot of the time-averaged and gyro-Bohm normalised ion heat flux Q_i as a function of $k_{y,min}\rho_i$. Same cases as considered in figure 3.6. (b) Log-log plot of k_y spectra of ion heat flux Q_i for the kinetic electron runs with $R/L_{T,i} = 6$ and $k_{y,min}\rho_i = 0.0175$ (magenta), 0.035 (blue), 0.07 (red) and 0.14 (green). Inset figure shows lin-lin plot of the zoom near the peaks.

to this parameter. This non-convergence is particularly striking for both adiabatic and kinetic electron simulations for the respective ion temperature gradients far from marginal stability. As can be seen from the log-log plot, in these cases one observes a scaling $Q_i/Q_{GB,i} \sim (k_{y,min}\rho_i)^{-\alpha}$, $\alpha > 0$, with $\alpha = 0.45$ (kin.e., $R/L_{T,i} = 6$) and 0.24 (ad.e., $R/L_{T,i} = 15$).

To provide insight into which wavelengths mainly contribute to the increasing heat flux as $k_{y,min}\rho_i$ decreases, the heat flux k_y -spectra is plotted in figure 3.7(b) for the set of simulations corresponding to the $k_{y,min}\rho_i$ scan with kinetic electrons and $R/L_{T,i} = 6$. Q_{i,k_y} is defined such that total heat flux $Q_i = \sum_{k_y} Q_{i,k_y} dk_y$, where $dk_y = k_{y,min}$. One observes that all spectra present a peak at $k_y\rho_i \simeq 0.2$ and that the increase in heat flux as $k_{y,min}\rho_i \rightarrow 0$ is not carried by the ever smaller minimum wavenumbers but by the contributions of modes $0.07 \leq k_y\rho_i \leq 0.35$ in the vicinity of the peak (contributing to at least 90% of the heat flux), range fully covered by all simulations, except for the largest considered $k_{y,min}\rho_i = 0.14$. Note that the inertial range ($k_y\rho_i \gtrsim 0.35$) remains essentially identical over all runs.

In appendix A, the possibility of $E \times B$ zonal shear flows acting as mini transport barriers at LMRSs, leading to local flattening of effective gradients between LMRSs, is explored. For simulations with lower $k_{y,min}\rho_i$, the density of these mini transport barriers would decrease, and potentially explain the increase in flux levels with decreasing $k_{y,min}\rho_i$ observed in kinetic electron runs. However this analysis concludes that the local flattening of effective gradients between LMRSs at most plays a minor role in explaining the observed increase in flux levels.

A priori, a straightforward explanation for the decreasing $E \times B$ shearing rate leading

3.3. $k_{y,\min}\rho_i$ scan in ITG-driven turbulence. Role of stationary and fluctuating components of zonal shear flows

to increased heat fluxes as $k_{y,\min}\rho_i$ decreases, is the reduction in the radial density of stationary shear layers at LMRSs. Let us indeed recall that the distance between LMRSs is given by $\Delta x_{\text{LMRS}} = 1/(k_{y,\min}\hat{s})$. Note as well the remarkable fact that the radial width and amplitude of the shear layers at LMRSs remains essentially invariant when varying $k_{y,\min}\rho_i$, as illustrated in figure 3.5(b). The contribution to the total shearing rate estimate (3.3) from the stationary component of the shearing rate profile $\langle\omega_{\text{eff}}\rangle_t(x)$ can be calculated by:

$$\text{RMS}_x(\langle\omega_{\text{eff}}\rangle_t) = \left[\langle (\langle\omega_{\text{eff}}\rangle_t)^2 \rangle_x \right]^{1/2}, \quad (3.4)$$

and has been plotted in log-log scale as a function of $k_{y,\min}\rho_i$ in figure 3.6(b). As expected, this system average of the stationary shearing rate profile decreases algebraically for kinetic electron simulations with decreasing $k_{y,\min}$, while for the adiabatic electron simulations there is no obvious dependence on $k_{y,\min}\rho_i$ as the mechanism developing the prominent fine stationary structures on $\langle\omega_{\text{eff}}\rangle_t(x)$ is absent in this case.

This explanation for the increase of turbulent fluxes as a result of the decrease in the radial density of stationary zonal $E \times B$ shear layers is however not satisfactory at closer scrutiny. This is made clear by the results presented in figure 3.8, where the radial correlation length of turbulent eddies λ_x is plotted as a function of $k_{y,\min}\rho_i$ for the case with kinetic electrons and $R/L_{Ti} = 6$. The radial correlation length is defined as $\lambda_x = \langle\lambda_x(y)\rangle_y$, with $\lambda_x(y)$ estimated as that smallest value of Δx for which the auto-correlation function $R(\Delta x, y) = \int \Phi^*(x - \Delta x, y)\Phi'(x, y)dx$ is $1/e$ times its maximum value (this maximum is reached for $\Delta x = 0$ and e is the base of the natural logarithm). $\Phi'(x, y)$ is the scalar potential evaluated at the outboard midplane, with the zonal ($k_y = 0$) component removed: $\Phi'(x, y) = \Phi(x, y, z = 0) - \langle\Phi(x, y, z = 0)\rangle_y$. This radial correlation length increases as $k_{y,\min}\rho_i$ decreases, but with a much weaker scaling (fit provides $\lambda_x/\rho_i \sim k_{y,\min}\rho_i^{-0.27}$ over the considered range $k_{y,\min}\rho_i = 10^{-2} - 10^{-1}$) than the increase of the distance $\Delta x_{\text{LMRS}}/\rho_i \sim (k_{y,\min}\rho_i)^{-1}$ between the main stationary shear layers located at LMRSs. Below a sufficiently small value of $k_{y,\min}\rho_i$, one thus clearly has $\lambda_x \ll \Delta x_{\text{LMRS}}$. That is, the turbulent eddies are getting actively sheared and broken *in between* low order MRSs where the stationary zonal shear flows are insignificant. The stationary shear layers are therefore not expected to play a major role in the saturation of turbulence as $k_{y,\min}\rho_i \rightarrow 0$. We therefore conclude that as $k_{y,\min}\rho_i \rightarrow 0$, the saturation of turbulence through the break-up of turbulent eddies is mainly to be attributed to the *fluctuating* component of zonal flows. This is discussed in detail in the following.

The time dependent component (as opposed to the stationary component) of the $E \times B$ zonal flow and associated shearing rate thus appears to control the saturation of turbulence and related flux levels *between* LMRSs. An estimate for the amplitude of this fluctuating part of the shearing rate is provided by computing the radial profile of the Standard

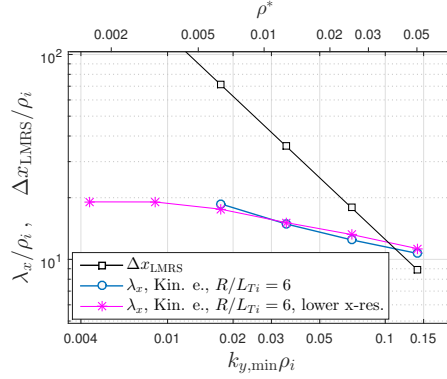


Figure 3.8: Blue circles denote the radial correlation length λ_x of turbulent eddies in units of ρ_i as a function of $k_{y,min} \rho_i$ for kinetic electron simulations and $R/L_{Ti} = 6$ (all parameters as given in table 3.1). Magenta asterisks correspond to results obtained with the same parameters except for a decreased radial resolution (by a factor 4), which enabled to carry out runs with $k_{y,min} \rho_i$ values as low as $\sim 5 \cdot 10^{-3}$ (these simulations are discussed in more detail in relation with Fig. 3.19). Distance $\Delta x_{LMRS} = 1/(k_{y,min} \hat{s})$ between LMRSs is plotted with black squares.

Deviation $SD_t(\omega_{eff})$ of ω_{eff} around the stationary component $\langle \omega_{eff} \rangle_t$:

$$SD_t(\omega_{eff})(x) = \left[\langle (\omega_{eff} - \langle \omega_{eff} \rangle_t)^2 \rangle_t \right]^{1/2}$$

The radial dependence of $SD_t(\omega_{eff})$ has been added to figure 3.5(b) for the cases with kinetic electrons, $R/L_{Ti} = 6$ and both $k_{y,min} \rho_i = 0.035$ and $k_{y,min} \rho_i = 0.0175$. Based on figure 3.5(b), it appears that the fluctuating part of the shearing rate remains essentially constant across the radial extent of the system. Furthermore, its amplitude for the considered values of $k_{y,min} \rho_i$ still remains significant, *i.e.* larger than γ_{max} , and of the same order as the maximum amplitude of the time-averaged $\langle \omega_{E \times B} \rangle_t$ structures. A decrease of the fluctuating component with decreasing $k_{y,min} \rho_i$ is also observed. This is summarized in figure 3.6(c), where the radial average of the fluctuating component, estimated by

$$SD_{x,t}(\omega_{eff}) = \left[\langle (\omega_{eff} - \langle \omega_{eff} \rangle_t)^2 \rangle_{x,t} \right]^{1/2}, \quad (3.5)$$

has been plotted. While $SD_{x,t}(\omega_{eff})$ decreases with $k_{y,min} \rho_i$ in both adiabatic and kinetic electron simulations, the scaling is much stronger in the latter case. For instance, in the considered range of $k_{y,min} \rho_i$, $SD_{x,t}(\omega_{eff}) \sim (k_{y,min} \rho_i)^\alpha$, where $\alpha = 0.08$ for the case with adiabatic electrons at $R/L_{Ti} = 15$ while $\alpha = 0.32$ for the case with kinetic electrons at $R/L_{Ti} = 6$.

Note that according to the definitions (3.3), (3.4) and (3.5), one has

$$[RMS_{x,t}(\omega_{eff})]^2 = [RMS_x(\langle \omega_{eff} \rangle_t)]^2 + [SD_{x,t}(\omega_{eff})]^2. \quad (3.6)$$

The decrease of both the fluctuation level of the shearing rate, shown in figure 3.6(c), along with the decrease in the density of stationary shearing layers at LMRSs, reflected by figure 3.6(b), thus provides a more complete picture of the decrease in the total system average of the shearing rate ω_{eff} as $k_{y,\text{min}}\rho_i$ decreases, shown in figure 3.6(a). While the reason for the decrease in the contribution to the shearing rate from stationary zonal flows has already been discussed and is relatively obvious, the reason for the decrease of the contribution from fluctuating zonal flows is not. To explain the latter, it is necessary to understand and analyse the different mechanisms driving the zonal flows. This is done in the following section.

3.4 Analysing zonal flow drive

In this section, the drive of zonal flows via the two main mechanisms, the modulational instability and self-interaction, are studied. In particular, the statistical properties of these different zonal flow drives are analysed using various diagnostics techniques, with the primary objective of understanding why the fluctuating zonal flow levels decrease with decreasing $k_{y,\text{min}}\rho_i$ as seen in figure 3.6(c).

In order to ensure a systematic study, this section has been organised as follows. To start, it is essential to identify the physical quantity(ies) representing the drive of zonal flows (\sim modes $k_y\rho_i = 0$) by the microinstability modes (\sim modes $k_y\rho_i \neq 0$). In § 3.4.1, it is found that Reynolds stress can be used as a convenient proxy for quantifying the drive of zonal flows. The two main mechanisms driving zonal flows are then discussed in the following two subsections: a summary of the well known modulational instability mechanism is given in § 3.4.2, followed by a detailed description of the self-interaction mechanism in § 3.4.3. These two mechanisms and the nature of their drives are illustrated first in a simple nonlinear set-up, referred to as the “reduced simulations”, in § 3.4.4.

This is followed by providing the evidence for self-interaction and modulational instability in full turbulence simulations, discussed in § 3.4.5 and § 3.4.6 respectively. In the latter subsection, using a bicoherence-like analysis and an estimate of the correlation between the different k_y contributions to Reynolds stress, it is shown that the drive of zonal flows via self-interaction from each k_y are essentially incoherent and decorrelated, unlike that via modulational instability. This result will then be used in the following § 3.5, to show how such a decorrelated drive could explain the observed decrease in fluctuating zonal flow levels with decreasing $k_{y,\text{min}}\rho_i$.

3.4.1 Reynolds stress as a proxy for the drive of zonal flows

Zonal flows are linearly stable and are driven by turbulence through the quadratic $\mathbf{E} \times \mathbf{B}$ non-linearity appearing in the gyrokinetic equation. To better understand their evolution,

Chapter 3. How eigenmode self-interaction affects zonal flows and convergence of turbulence levels with toroidal system size

we will analyse the properties of Reynolds stress [Diamond et al., 2005], more exactly the off-diagonal component $\langle \tilde{V}_x \tilde{V}_\chi \rangle$ of the Reynolds stress tensor resulting from the combination of fluctuating $E \times B$ flow components in the radial and poloidal directions. We will justify in the following that this Reynolds stress can be considered as a valid proxy of the zonal flow drive [Weigl et al., 2018]. By analyzing Reynolds stress we will be able to identify the different possible mechanisms driving zonal flows, their statistical properties, and relative importance.

We start by considering an approximate evolution equation for the shearing rate $\omega_{E \times B}$ associated with the $E \times B$ zonal flows. As shown in references [Parra and Catto, 2009, Abiteboul et al., 2011, Abiteboul, 2012], such an equation can be obtained from the radial conservation equation for the total gyrocenter charge density, which in turn is derived by taking the appropriate velocity moment and flux-surface -average of the gyrokinetic equation. The approach in reference [Abiteboul, 2012] has been considered here, but starting from the gyrokinetic equation in the limit of the local (flux-tube) delta-f model rather than the global full-f model considered by [Abiteboul, 2012]. Furthermore, assuming the electrostatic limit, invoking $m_e/m_i \ll 1$, and making use of the quasi-neutrality equation in the long wavelength approximation (final result thus valid only to second order in $k_\perp \rho_i$), leads to a relation that can be interpreted as a generalized vorticity equation:

$$\frac{\partial}{\partial t}(\Omega + \Pi) = \frac{\partial^2}{\partial x^2}(\mathcal{R} + \mathcal{P}) + \frac{\partial}{\partial x}\mathcal{N}. \quad (3.7)$$

See appendix B for the full derivation. One identifies on the left hand side of equation (3.7) the generalized vorticity term $\Omega + \Pi$, composed of the actual vorticity associated with zonal flows and closely related to the zonal flow shearing rate $\omega_{E \times B}$ (by neglecting the z dependence of B_0 and $g^{xx} \simeq 1$):

$$\Omega = n_{0,i} m_i \frac{\partial^2}{\partial x^2} \left\langle \frac{g^{xx}}{B_0^2} \Phi \right\rangle_{yz} \simeq \frac{n_{0,i} m_i}{B_0} \omega_{E \times B},$$

as well as a perpendicular pressure term, related to lowest order finite ion Larmor radius effects:

$$\Pi = \frac{m_i}{2q_i} \frac{\partial^2}{\partial x^2} \left\langle \frac{g^{xx}}{B_0^2} P_{\perp,i} \right\rangle_{yz},$$

with the fluctuating part of the perpendicular ion gyrocenter pressure $P_{\perp,i}$ expressed in terms of the corresponding gyrocenter distribution fluctuation δf_i :

$$P_{\perp,i} = \int \mu B_0 \delta f_i d^3v.$$

On the right hand side of equation (3.7) one identifies the second radial derivative of a term $\mathcal{R} = (n_{0,i} m_i / \mathcal{C})$ RS, proportional to the Reynolds stress component RS driving

zonal flows:

$$\text{RS} = \left\langle \frac{1}{B_0^2} \frac{\partial \Phi}{\partial y} \left(g^{xx} \frac{\partial \Phi}{\partial x} + g^{xy} \frac{\partial \Phi}{\partial y} \right) \right\rangle_{yz}. \quad (3.8)$$

This Reynolds stress term also has a finite Larmor radius correction term \mathcal{P} , again expressed in terms of $P_{\perp,i}$:

$$\mathcal{P} = \frac{m_i}{2q_i \mathcal{C}} \left\langle \frac{1}{B_0^2} \left(g^{xx} \frac{\partial \Phi}{\partial x} \frac{\partial P_{\perp,i}}{\partial y} + 2 g^{xy} \frac{\partial \Phi}{\partial y} \frac{\partial P_{\perp,i}}{\partial y} + g^{xx} \frac{\partial \Phi}{\partial y} \frac{\partial P_{\perp,i}}{\partial x} \right) \right\rangle_{yz}.$$

The last contribution on the right hand side of equation (3.7) is the radial derivative of the so-called neoclassical term \mathcal{N} , related to both curvature and ∇B drifts:

$$\mathcal{N} = - \sum_{\text{species}} \frac{2\pi \mathcal{C}}{m} \left\langle \gamma_2 \frac{\partial B_0}{\partial z} \int dv_{\parallel} d\mu \frac{mv_{\parallel}^2 + \mu B_0}{B_0^2} \left(\delta f + \frac{q \bar{\Phi}}{T_0} f_0 \right) \right\rangle_{yz},$$

with f_0 the Maxwellian background distribution, $\gamma_2 = g^{xx} g^{yz} - g^{xy} g^{xz}$ and the constant $\mathcal{C} = B_0 / |\nabla x \times \nabla y|$.

The different terms appearing in (3.7) can be monitored as a diagnostic along a gyrokinetic simulation. For the purpose of verification, this diagnostic was first applied to simple test cases, including the Rosenbluth-Hinton problem [Rosenbluth and Hinton, 1998] addressing the linear dynamics of zonal fluctuations [in this case only the linear neoclassical term contributes on the RHS of (3.7); see section B.2 in appendix B for a detailed analysis], as well as the non-linear decay of an initially single unstable eigenmode (as discussed in §3.4.4). For these simple tests, only longer wavelength modes were considered, so as to stay well within the limit $k_{\perp} \rho_i \ll 1$ assumed for the derivation of relation (3.7).

After this successful initial verification phase, the terms appearing in equation (3.7) were monitored and compared for the fully developed turbulence simulations studied in this chapter, considering the reference gradient case $R/L_{T,i} = 6$. In order to validate Reynolds stress as a good proxy for the drive of zonal flows, the correlation between $\Omega \sim \omega_{E \times B}$ and the two non-linear driving terms $\partial^2 \mathcal{R} / \partial x^2$ and $\partial^2 \mathcal{P} / \partial x^2$ in (3.7) was estimated over these simulations. To this end, the following correlation estimator between two observables a and b , functions of the radial variable x and time t , was applied:

$$\text{Corr}(a, b) = \frac{\sigma_{x,t}(a, b)}{\sigma_{x,t}(a) \sigma_{x,t}(b)} = \frac{\langle (a - \langle a \rangle_{x,t}) (b - \langle b \rangle_{x,t}) \rangle_{x,t}}{\sqrt{\langle (a - \langle a \rangle_{x,t})^2 \rangle_{x,t}} \sqrt{\langle (b - \langle b \rangle_{x,t})^2 \rangle_{x,t}}}. \quad (3.9)$$

Significant correlation estimates were obtained in this way between Ω and the Reynolds stress drive term $\partial^2 \mathcal{R} / \partial x^2$. Correlation values were found to increase further by considering only the longer wavelength contributions, achieved by filtering out $|k_x| \rho_i > 0.5$ and $|k_y| \rho_i > 0.5$ Fourier modes from the signals. This is in agreement with the long wavelength approximation assumed for deriving equation (3.7). The positive correlation values $\text{Corr} = 0.77$ and 0.37 were obtained in this way between Ω and $\partial^2 \mathcal{R} / \partial x^2$ for the

Chapter 3. How eigenmode self-interaction affects zonal flows and convergence of turbulence levels with toroidal system size

adiabatic and kinetic electron turbulence simulations respectively, while the correlation between Ω and $\partial^2 \mathcal{P} / \partial x^2$ provided the values $\text{Corr} = 0.75$ and 0.40 respectively. These results validate considering the Reynolds stress term $\partial^2 \text{RS} / \partial x^2$ as a proxy for the drive of zonal flow shear $\omega_{E \times B}$. A more detailed analysis on this can be found in appendix B, in section B.3.

In the following, it will be insightful to consider the contributions from different k_y Fourier modes components of the fluctuating fields to the Reynolds stress term RS. Relation (3.8) for RS can indeed be written as a sum over k_y :

$$\text{RS}(x, t) = \sum_{k_y > 0} \hat{\text{RS}}_{k_y}(x, t), \quad (3.10)$$

with the contribution from the k_y Fourier mode $\hat{\Phi}_{k_y}(x, z, t) = \frac{1}{L_y} \int_0^{L_y} \Phi \exp(-ik_y y) dy$ given by

$$\hat{\text{RS}}_{k_y}(x, t) = 2 \text{Re} \left[\left\langle \frac{1}{B_0^2} k_y \hat{\Phi}_{k_y} \left(g^{xx} i \frac{\partial \hat{\Phi}_{k_y}^*}{\partial x} + g^{xy} k_y \hat{\Phi}_{k_y}^* \right) \right\rangle_z \right], \quad (3.11)$$

having invoked the reality condition $\hat{\Phi}_{-k_y} = \hat{\Phi}_{k_y}^*$. Considering as well the k_x Fourier mode decomposition of Φ , each of these k_y contributions can also be written as follows:

$$\hat{\text{RS}}_{k_y}(x, t) = 2 \text{Re} \left\{ \sum_{k_x, k_x''} \left\langle \frac{1}{B_0^2} k_y (g^{xx} k_x'' + g^{xy} k_y) \hat{\Phi}_{k_x, k_y} \hat{\Phi}_{k_x'', k_y}^* \right\rangle_z \exp[i(k_x - k_x'')x] \right\}, \quad (3.12)$$

illustrating the drive of zonal modes $(k_x' = k_x - k_x'', 0)$ through non-linear interaction between Fourier modes (k_x, k_y) and (k_x'', k_y) , extensively discussed in sections §3.4.2 and §3.4.3.

For the study carried out in this chapter, it is essential to understand how different drift modes may non-linearly interact to drive zonal flows via Reynolds stress. To start, we recall in the next subsection the basic mechanism underlying the drive of zonal flows in a simple shearless slab system before considering the more complex case of direct interest to us, *i.e.* of a sheared toroidal system.

3.4.2 Modulational instability in shearless slab system

The drive of zonal flows by microturbulence has been extensively studied in the literature considering a simple slab-like plasma confined by a uniform, shearless magnetic field. Such a system was in particular addressed in the original work by [Hasegawa and Mima, 1978], where a cold fluid model was assumed for ions and an adiabatic response for electrons. In this model, choosing an orthogonal Cartesian coordinate system (x, y, z) , the magnetic field is aligned along z , $\mathbf{B} = B \mathbf{e}_z$ and the background density inhomogeneities along x ,

$\nabla n_0 = (dn_0/dx)\mathbf{e}_x$. The corresponding well-known model equation for the non-linear evolution of the electrostatic potential Φ associated with the fluctuating fields describes the essentially two-dimensional drift wave turbulence in the (x, y) plane perpendicular to the magnetic field. This model equation led to a first understanding of the generation of zonal flows along y , *i.e.* in the direction both perpendicular to \mathbf{B} and the direction of inhomogeneity. The emergence of such large scale flows can in particular be explained as the result of an anisotropic inverse cascade of energy related to the conservation of energy and enstrophy in the 2-dimensional turbulence. The emergence of zonal flows can also be understood at the level of elementary non-linear processes as recalled in the following.

In a shearless slab system, the spatial dependence of linear eigenmodes is given by a *single* Fourier mode $\Phi(x, y) \sim \Phi_{\mathbf{k}} \exp(i\mathbf{k} \cdot \mathbf{x})$, with $\mathbf{x} = x\mathbf{e}_x + y\mathbf{e}_y$ and $\mathbf{k} = k_x\mathbf{e}_x + k_y\mathbf{e}_y$. The corresponding time dependence is of the form $\sim \exp(-i\omega_{\mathbf{k}}t)$, with $\omega_{\mathbf{k}}$ the eigenfrequency of the mode. In the simple Hasegawa-Mima model, one has $\omega_{\mathbf{k}} = k_y v_d / (1 + k^2)$, with $\mathbf{v}_d = -(T_e/eB)(d \log n_0/dx)\mathbf{e}_y$ these eigenmodes result from the *quadratic* non-linearity in the Hasegawa-Mima equation, related to the $\mathbf{v}_{E \times B} = (-\nabla\Phi \times \mathbf{B})/B^2$ drift. The elementary non-linear interaction thus involves a *triplet* of Fourier modes \mathbf{k} , \mathbf{k}' , \mathbf{k}'' satisfying the wave vector matching condition $\mathbf{k} = \mathbf{k}' + \mathbf{k}''$, where each of the modes, *e.g.* \mathbf{k} , is coupled to the two others, \mathbf{k}' and \mathbf{k}'' in this case. In case of frequency matching $\omega_{\mathbf{k}} \simeq \omega_{\mathbf{k}'} + \omega_{\mathbf{k}''}$ and under the condition $k' < k < k''$, one can have a resonant decay of mode \mathbf{k} , *i.e.* a transfer of energy from this mode, into the daughter modes \mathbf{k}' and \mathbf{k}'' . This basic process is referred to as the resonant 3-wave interaction mechanism. One can furthermore show that in the case where mode \mathbf{k} represents a drift wave, *i.e.* typically with $|k_y| \gg |k_x|$, the decay happens preferentially (meaning with a higher growth rate of decay) if one of the daughter wave vectors, *e.g.* \mathbf{k}' , is (nearly-) aligned along the x direction, $|k'_x| \gg |k'_y|$ [Hasegawa et al., 1979]. The $E \times B$ flow associated with the daughter mode \mathbf{k}' is then obviously along y , thus explaining the emergence of zonal flows in this direction. Such a mode with vector aligned along the direction of inhomogeneity \mathbf{e}_x is thus referred to as a zonal mode. See figure 3.9 for an illustration of the three Fourier modes involved in such a resonant 3-wave interaction.

Let us still further consider the decay of a pump drift wave $\mathbf{k} = (k_x, k_y)$, $k_y \neq 0$, into a zonal mode $\mathbf{k}' = (k'_x, 0)$ and the second daughter wave $\mathbf{k}'' = \mathbf{k} - \mathbf{k}' = (k_x - k'_x, k_y)$, itself a drift wave. The non-linear interaction between the two drift waves \mathbf{k} and \mathbf{k}'' thus provides the drive to the zonal mode \mathbf{k}' via the Reynolds stress RS discussed in §3.4.1, while the non-linear coupling between the original drift wave \mathbf{k} and zonal mode \mathbf{k}' , leading to the growth of the daughter drift wave \mathbf{k}'' , actually represents the *shearing* of the drift mode \mathbf{k} by the zonal flows associated with \mathbf{k}' .

Variations to the simple Hasegawa-Mima model have been considered in the literature. In particular, the Enhanced Hasegawa-Mima model [Krommes and Kim, 2000, Gallagher et al., 2012] accounts for the fact that the adiabatic electron response is inhibited for

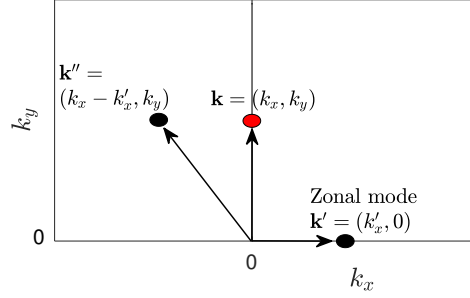


Figure 3.9: Illustration of the 3 Fourier modes involved in resonant 3-wave interaction under wave vector matching condition.

magnetic surface-averaged fluctuations, *i.e.* modes \mathbf{k} with $k_y = 0$, in other words zonal modes, which leads them to having a reduced effective inertia compared to standard drift waves with $k_y \neq 0$. This effect results in an amplification of the decay rates of drift waves into zonal modes and thus to an enhancement of corresponding energy transfer.

A further refinement to the basic driving mechanism of zonal flows is obtained by accounting for the fact that given an initial large amplitude drift mode \mathbf{k} , decaying into a zonal mode \mathbf{k}' , both triplet interactions $[\mathbf{k}, \mathbf{k}', \mathbf{k}'' = \mathbf{k} - \mathbf{k}']$ and $[\mathbf{k}, -\mathbf{k}', \mathbf{k}''' = \mathbf{k} + \mathbf{k}']$ may be simultaneously resonant, *i.e.* $\omega_{\mathbf{k}} \simeq \omega_{\mathbf{k}'} + \omega_{\mathbf{k}''}$ and $\omega_{\mathbf{k}} \simeq -\omega_{\mathbf{k}'} + \omega_{\mathbf{k}'''}$. This coupled pair of 3-wave interactions leads to an effective 4-wave interaction involving modes \mathbf{k} , \mathbf{k}' , \mathbf{k}'' and \mathbf{k}''' , referred to as the modulational instability mechanism [Gallagher et al., 2012].

An important point to emphasize is that, in both the case of the simple resonant 3-wave interaction or the more specific modulational instability, resonant coupling between the initial large amplitude (pump) drift mode $\mathbf{k} = (k_x, k_y \neq 0)$ and a zonal mode $\mathbf{k}' = (k'_x, k'_y = 0)$ is established via either one sideband $\mathbf{k}'' = \mathbf{k} - \mathbf{k}'$, or respectively two sidebands \mathbf{k}'' and $\mathbf{k}''' = \mathbf{k} + \mathbf{k}'$, where all these Fourier modes are *linearly decoupled* from each other. As a result, in the situation where in addition to the pump drift mode \mathbf{k} , the zonal mode \mathbf{k}' itself already has a finite initial amplitude and a well defined phase, the other daughter waves \mathbf{k}'' (and \mathbf{k}''') are *free* to adapt their phases to ensure a resonant interaction and thus an efficient energy transfer from the pump to the zonal mode, resulting in the further amplification of this zonal mode. In fact, a finite amplitude zonal mode can *stimulate* the decay of multiple non-zonal modes, thus leading to *coherent* (as a result of the frequency matching involved) and therefore *correlated* contributions from these non-zonal modes to the Reynolds stress drive of the zonal mode.

One should note here that, while modulational instability leads to an efficient transfer of energy to the zonal modes, in general, any 3-wave interactions involving two Fourier modes having the same $k_y (\neq 0)$ can drive the wave-vector matched zonal mode. Under realistic conditions, multiple such 3-wave interactions happen both simultaneously and

successively in time, leading to an expanding set of Fourier modes, and ultimately to a fully developed turbulent spectrum.

3.4.3 Self-interaction mechanism in sheared toroidal system

As in the shearless slab geometry, in the case of a tokamak system, *i.e.* based on a sheared axisymmetric toroidal magnetic geometry, which is of main interest to our study, the modulational instability involving resonant 3-wave interactions remains an essential driving mechanism of zonal flows [Chen et al., 2000]. In a tokamak however, one must distinguish another form of the non-linear interaction leading to the drive of zonal modes. This mechanism, referred to as self-interaction, is specific to systems presenting magnetic shear and is explained in the following.

As already discussed in §2.6, parallel boundary conditions lead to the linear coupling of k_x Fourier modes. In particular, according to equation (2.94), the electrostatic potential field Φ_L of a linear microinstability eigenmode with fixed k_{x0} and $k_y \neq 0$ is composed of Fourier modes $\hat{\Phi}_{k_{x0}+p2\pi k_y \hat{s}, k_y}$, $p \in \mathbb{Z}$. The spatial dependence of the corresponding eigenmode structure is thus given by:

$$\Phi_L(x, y, z) = \tilde{\Phi}_{k_{x0}, k_y}(x, z) \exp(ik_y y) + \text{c.c.}, \quad (3.13)$$

where c.c. stands for the complex conjugate [considered here to ensure that Φ_L is real-valued, essential for computing the quasi-linear estimate in (3.15)], and with the complex-valued (x, z) -dependent envelope given by:

$$\tilde{\Phi}_{k_{x0}, k_y}(x, z) = \sum_{p=-\infty}^{+\infty} \hat{\Phi}_{k_{x0}+p2\pi k_y \hat{s}, k_y}(z) \exp[i(k_{x0} + p2\pi k_y \hat{s})x]. \quad (3.14)$$

These linearly coupled k_x Fourier modes, all having same k_y , drive the zonal modes $(k'_x, 0)$, with $k'_x = p'2\pi k_y \hat{s}$, $p' \in \mathbb{Z}$, forming a set of harmonics. Indeed, any two Fourier modes $\hat{\Phi}_{k_{x0}+p2\pi k_y \hat{s}, k_y}$ and $\hat{\Phi}_{k_{x0}+p''2\pi k_y \hat{s}, k_y}$ composing the physical eigenmode will drive, via three Fourier mode coupling, the zonal mode $\hat{\Phi}_{p'2\pi k_y \hat{s}, 0}$ with $p' = p - p''$ [see equation (3.12)]. Note that this drive of zonal modes is via the same quadratic non-linearity in the gyrokinetic equation related to $E \times B$ drifts as the one driving zonal modes through the modulational instability, but in this case involving Fourier modes which are already *linearly* coupled to each other.

Assuming that the relative phases between the Fourier modes $\hat{\Phi}_{k_{x0}+p2\pi k_y \hat{s}, k_y}$ remains set by the linear coupling, even during the non-linear turbulent evolution (to what extent this assumption holds is validated in §3.4.5), the phases of the associated contributions to Reynolds stress driving the zonal modes is *fixed*. This translates in direct space to an essentially fixed periodic radial dependence (with period $\Delta x_{\text{MRS}} = 1/k_y \hat{s}$ corresponding to the distance between MRSs) of the contribution to Reynolds stress through this

Chapter 3. How eigenmode self-interaction affects zonal flows and convergence of turbulence levels with toroidal system size

self-interaction mechanism from a given k_y eigenmode. The overall magnitude of this contribution obviously varies in time as the amplitude of the eigenmode evolves. This is a critical difference compared to the drive of zonal modes \mathbf{k}' through the modulational instability discussed in §3.4.2, where the relative phases between the pump mode \mathbf{k} and sidebands \mathbf{k}'' , \mathbf{k}''' are *free* to adapt to enable a coherent (*i.e.* in phase) drive of a given zonal mode.

Figure 3.10 plots the quasi-linear estimates of this self-interaction contribution to the Reynolds stress drive term $\partial^2 \text{RS} / \partial x^2$ from the linear eigenmode with $k_{x0} = 0$, $k_y \rho_i = 0.28$, and $R/L_{T_i} = 6$, whose ballooning structures are given in figure 3.2, considering both the case of kinetic and adiabatic electron response. These results are obtained by inserting the corresponding eigenmode structure (3.13) into relations (3.11) and (3.12), leading to the Reynolds stress contribution denoted $\widetilde{\text{RS}}_{k_{x0}, k_y}(x)$:

$$\begin{aligned} \widetilde{\text{RS}}_{k_{x0}, k_y}(x) &= \text{RS}[\Phi_L] = \hat{\text{RS}}_{k_y}[\tilde{\Phi}_{k_{x0}, k_y}] \\ &= 2 \text{Re} \left[\left\langle \frac{1}{B_0^2} k_y \tilde{\Phi}_{k_{x0}, k_y} \left(g^{xx} i \frac{\partial \tilde{\Phi}_{k_{x0}, k_y}^*}{\partial x} + g^{xy} k_y \tilde{\Phi}_{k_{x0}, k_y}^* \right) \right\rangle_z \right] \\ &= 2 \text{Re} \left[\sum_{p'=-\infty}^{+\infty} e^{ip' 2\pi k_y \hat{s} x} \sum_{p=-\infty}^{+\infty} \left\langle \frac{1}{B_0^2} k_y (g^{xx} k_x'' + g^{xy} k_y) \hat{\Phi}_{k_x, k_y} \hat{\Phi}_{k_x'', k_y}^* \right\rangle_z \right]. \end{aligned} \quad (3.15)$$

In the last equality of relation (3.15), $k_x = k_{x0} + p 2\pi k_y \hat{s}$, $k_x'' = k_{x0} + p'' 2\pi k_y \hat{s}$ and $p'' = p - p'$. This relation also clearly points out how this contribution to Reynolds stress from a given k_y eigenmode through self-interaction is periodic with period $\Delta x_{\text{MRS}} = 1/k_y \hat{s}$.

The overall amplitude of the quasi-linear estimates shown in figure 3.10 are naturally irrelevant. Furthermore, as these contributions to Reynolds stress have period $\Delta x_{\text{MRS}} = 1/k_y \hat{s}$, only one such period is shown. Note how the radial profile of the quasi-linear estimate of $\partial^2 \hat{\text{RS}}_{k_y} / \partial x^2$ is narrow in the case of kinetic electrons and localized around the MRS at $x = 0$, clearly related to the fine structures of the eigenmode at MRSs and the associated broad tail in ballooning representation. As expected, the corresponding radial profile is much broader in the case of adiabatic electrons, as fine structures at MRSs are essentially absent in this case.

3.4.4 Evidence of zonal flow drive by modulational instability and self-interaction in reduced simulations

In this subsection, we consider reduced non-linear simulation setups in tokamak geometry to clearly illustrate the two basic mechanisms driving zonal flows discussed in §3.4.2 and §3.4.3. For these reduced simulations, the same physical parameters as summarized in Table 3.1 is considered, however with particular initial conditions defined as follows:

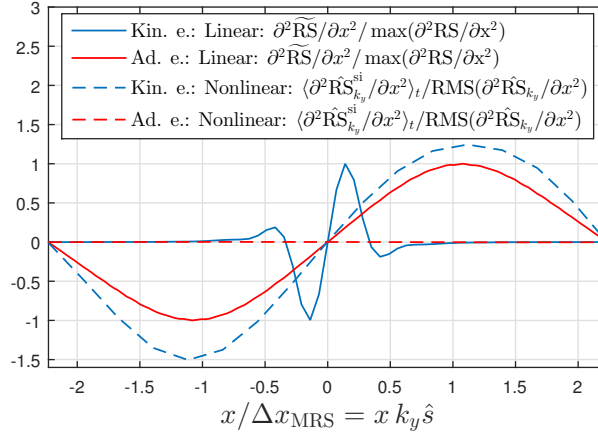


Figure 3.10: Solid lines indicate the quasi-linear estimate of $\partial^2 \widetilde{RS}_{k_{x0}, k_y} / \partial x^2$ normalised to its maximum value as a function of x for the linear eigenmode with $k_{x0} = 0$, $k_y \rho_i = 0.28$ and either kinetic (blue) or adiabatic (red) electrons. Dashed lines denote the time-average $\langle \partial^2 \hat{RS}_{k_y}^{\text{si}} / \partial x^2 \rangle_t$ normalised with respect to the RMS in time of the total contribution $\partial^2 \hat{RS}_{k_y} / \partial x^2$, for $k_y \rho_i = 0.28$, in turbulence simulations considering either kinetic (blue) or adiabatic (red) electrons. $k_{y,\min} \rho_i = 0.035$, $R/L_{Ti} = 6$ and other parameters are given in table 3.1.

An unstable linear eigenmode (hereby called the pump mode with $k_y = k_{y,\text{pump}} \neq 0$) is initialized with an amplitude a few times (~ 5) less than the corresponding one in the fully saturated turbulence simulation discussed in §3.4.5. The purpose of the simulation is to study how this single eigenmode drives zonal modes via either the modulational instability or self-interaction. The eigenmode with $k_{x0} = 0$ and $k_y \rho_i = 0.28$ was chosen for this pump mode, as it is among the most linearly unstable ones and also contributes significantly to the non-linear fluctuation spectra in the fully developed turbulence simulations (see figures 3.3 and 3.7(b)). In addition, zonal Fourier modes (with $k_y = 0$) are initialized to amplitudes 10 – 12 orders of magnitude less than the pump mode to provide a necessary seed for possible modulational instabilities. All Fourier modes not part of the pump and zonal modes are initialized to zero. With this initial setup, only k_y modes which are harmonics of $k_{y,\text{pump}}$ can possibly develop non-linearly ($k_y = p k_{y,\text{pump}}$, $p \in \mathbb{N}$). For these reduced simulations we therefore set $k_{y,\min} = k_{y,\text{pump}}$ and actually only considered $N_{k_y} = 8$ Fourier modes. The flux-tube width in the x direction was set to $L_x = M / \hat{s} k_{y,\min}$ with $M = 32$, so that it remains the same as in full turbulence simulations and the resulting fine k_x -spectrum allows for a detailed analysis of k_x -dependence of zonal mode growth. The remaining numerical resolutions are kept the same as in Table 3.1. This system is then let to evolve until higher k_y Fourier harmonics start to develop amplitudes similar to the fundamental $k_{y,\text{pump}}$. These steps ensure that the dominant non-linear interactions mainly involve only $k_y = 0$ and $k_{y,\text{pump}}$. This reduced non-linear setup thus clearly isolates the contribution to the drive of zonal modes from a single k_y mode, while

Chapter 3. How eigenmode self-interaction affects zonal flows and convergence of turbulence levels with toroidal system size

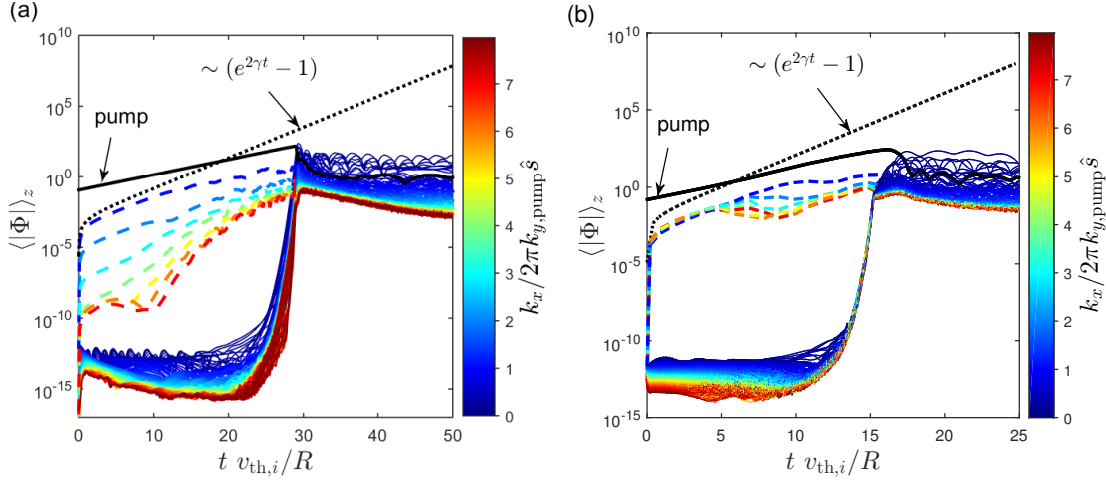


Figure 3.11: Lin-log plots. Coloured lines represent the time evolution of the z -averaged amplitudes $\langle |\hat{\Phi}_{k_x, k_y=0}| \rangle_z$ of zonal modes in reduced non-linear simulations initialized with a single large amplitude $k_{y,pump} \neq 0$ eigenmode, considering either (a) adiabatic or (b) kinetic electrons. The colourbar maps the value of k_x in units of $2\pi k_{y,pump} \hat{s}$. Zonal modes with $k_x = p' 2\pi k_{y,pump} \hat{s}$, $p' \in \mathbb{N}$, are plotted with dashed lines. The solid black line represents the time trace of the pump Fourier mode amplitude $\langle |\hat{\Phi}_{k_x=0, k_{y,pump}}| \rangle_z$. The dotted black line represents an evolution proportional to $(e^{2\gamma t} - 1)$, where γ is the linear growth rate of the pump mode.

in the much more complex case of a standard fully developed turbulence simulation, multiple k_y contributions may act simultaneously.

Figure 3.11 plots the evolution of the pump mode and the zonal modes driven by it. Solid black line represents the time trace of the z -averaged amplitude of the most dominant Fourier mode $\langle |\hat{\Phi}_{k_{x0}, k_{y,pump}}| \rangle_z(t)$ composing the pump mode. Note that the other linearly coupled Fourier modes composing the pump mode are not shown. Coloured lines represent the zonal mode amplitude $\langle |\hat{\Phi}_{k_x, k_y=0}(t)| \rangle_z$ for each k_x . These results are shown for reduced non-linear simulations considering either adiabatic electrons (figure 3.11(a)) or kinetic electrons (figure 3.11(b)).

In the initial stage, the pump eigenmode grows exponentially with corresponding linear growth rates, *i.e.* $\gamma R/v_{th,i} = 0.25$ in the case of adiabatic electrons and $\gamma R/v_{th,i} = 0.47$ in the case of kinetic electrons.

Zonal Fourier modes $\hat{\Phi}_{k'_x, k_y=0}$ with $k'_x = p' 2\pi k_{y,pump} \hat{s}$, $p' \in \mathbb{Z}$, (see dashed coloured time traces in figure 3.11) are driven by the large amplitude pump eigenmode through the self-interaction mechanism, *i.e.* are driven by multiple quadratic non-linearities, each involving two exponentially growing k_x Fourier components of the pump, $\hat{\Phi}_{k_x, k_{y,pump}}(t)$, $\hat{\Phi}_{k''_x, k_{y,pump}}(t) \sim e^{\gamma t}$, where $k_x^{(n)} = k_{x0} + p^{(n)} 2\pi k_{y,pump} \hat{s}$, $p^{(n)} \in \mathbb{Z}$, and $p - p'' = p'$. One

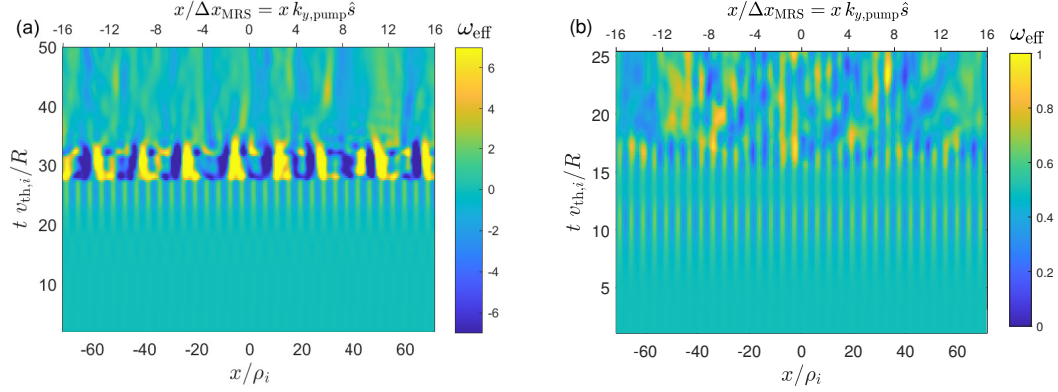


Figure 3.12: Effective zonal flow shearing rate ω_{eff} as a function of radial position x and time t for the same reduced non-linear simulations as in figure 3.11. Cases with either (a) adiabatic or (b) kinetic electrons are shown.

thus has for $k'_x = p' 2\pi k_{y,\text{pump}} \hat{s}$:

$$\begin{aligned} \hat{\Phi}_{k'_x, k_y=0}(t) - \hat{\Phi}_{k'_x, k_y=0}(0) &\sim \int_0^t \hat{\Phi}_{k_x, k_{y,\text{pump}}}(t') \hat{\Phi}_{k'_x, k_{y,\text{pump}}}^*(t') dt' \sim \int_0^t e^{2\gamma t'} dt' \\ &\sim (e^{2\gamma t} - 1). \end{aligned}$$

Note that for $t \ll 1/\gamma$ these modes thus start by growing linearly in time. In the initial stage of the simulations shown in figures 3.11(a) and 3.11(b), *i.e.* for $t \lesssim 28R/v_{\text{th},i}$ and $t \lesssim 15R/v_{\text{th},i}$ in the case of adiabatic and kinetic electrons respectively, the Fourier modes driven by self-interaction, $\hat{\Phi}_{p' 2\pi k_{y,\text{pump}} \hat{s}, k_y=0}$, therefore dominate the zonal k_x -spectrum. Black dotted lines in these figures indicate the time evolution $\sim (e^{2\gamma t} - 1)$, providing a good fit to the initial evolution of these particular zonal modes. As discussed in §3.4.3, these modes are driven by the Reynolds stress resulting from the self-interaction of the eigenmode with $k_y = k_{y,\text{pump}}$, which in direct space is periodic in x with period $\Delta x_{\text{MRS}} = 1/k_{y,\text{pump}} \hat{s}$ and aligned with corresponding MRSs. This is clearly reflected in Figures 3.12(a) and 3.12(b), plotting the effective zonal flow shearing rate ω_{eff} as a function of x and time t , again for simulations with either adiabatic or kinetic electrons. At least in the initial stage of the simulations, these plots indeed present a periodic radial variation of ω_{eff} with period $1/k_{y,\text{pump}} \hat{s}$ and perfectly aligned with the MRSs of the pump mode.

Zonal Fourier modes $\hat{\Phi}_{k'_x, k_y=0}$ with $k'_x \neq p' 2\pi k_{y,\text{pump}} \hat{s}$, $p' \in \mathbb{Z}$, (see solid coloured time traces in figure 3.11) are however driven by the pump eigenmode via the modulational instability mechanism, *i.e.* mainly through the quadratic non-linearities involving the large amplitude Fourier component $\hat{\Phi}_{k_{x0}, k_{y,\text{pump}}}$ of the pump and either one of the initially low amplitude sideband modes $\hat{\Phi}_{k_{x0} \pm k'_x, k_{y,\text{pump}}}$. As a result, these particular zonal modes grow as $\sim e^{\gamma_{\text{mod}} t}$, where γ_{mod} stands for the growth rate of the modulational instability. Given that $\gamma_{\text{mod}} \sim |\Phi_{\text{pump}}|$ [Hasegawa et al., 1979] and that the pump amplitude

Chapter 3. How eigenmode self-interaction affects zonal flows and convergence of turbulence levels with toroidal system size

itself grows exponentially, $|\Phi_{\text{pump}}| \sim e^{\gamma t}$, these zonal modes effectively end up growing super-exponentially.

One can also see in figure 3.11(b) that all plotted zonal modes driven by self-interaction, $\hat{\Phi}_{p'2\pi k_{y,\text{pump}}\hat{s},k_y=0}$, $p' = 1, \dots, 7$, are from the start driven up to similarly large amplitudes in the case of kinetic electrons, as opposed to the adiabatic case in figure 3.11(a), where these same modes are driven more weakly. This is explained by the different eigenmode structures of the pump in the adiabatic and kinetic electron cases (see corresponding ballooning representations in figure 3.2). With kinetic electrons, the Fourier mode components $\hat{\Phi}_{k_x,k_{y,\text{pump}}}(z)$, where $k_x = k_{x0} + p2\pi k_{y,\text{pump}}\hat{s}$ and $p \in \mathbb{Z}^*$ (set of integers excluding 0), which compose the tail of the ballooning representation, have much higher relative amplitudes compared to the main Fourier component $\hat{\Phi}_{k_{x0},k_{y,\text{pump}}}(z)$ than in the case with adiabatic electrons. As a result, the self-interaction drive of a zonal mode $\hat{\Phi}_{p'2\pi k_{y,\text{pump}}\hat{s},k_y=0}$, $p' \in \mathbb{Z}^*$, dominated by the non-linear interaction between $\hat{\Phi}_{k_{x0},k_{y,\text{pump}}}(z)$ and $\hat{\Phi}_{k_{x0}+p'2\pi k_{y,\text{pump}}\hat{s},k_{y,\text{pump}}}(z)$, is stronger with kinetic than with adiabatic electrons.

The weaker drive of the zonal modes by the self-interaction mechanism in the case with adiabatic electrons also explains why these particular zonal modes end up getting overwhelmed by the ones driven by the modulational instability mechanism (reflected by the absence of fine structures at MRSs on ω_{eff} in figure 3.12(a) for $t \gtrsim 28 R/v_{\text{th},i}$), while they remain significant in the case with kinetic electrons even after saturation of the modes driven by the modulational instability (reflected by the persistent fine structures on ω_{eff} in figure 3.12(b) even for $t \gtrsim 15 R/v_{\text{th},i}$).

In the following two subsections, evidence of the self-interaction and modulational instability mechanisms are provided in the case of fully developed turbulence simulations. The relative importance of these two mechanisms is compared between simulations with adiabatic and kinetic electron response. Such simulations involve a fully saturated spectrum of multiple k_y modes, unlike the case in the just considered reduced non-linear simulations. We find that the results obtained in the reduced non-linear simulations follow in general to the full turbulence scenarios, but with certain differences.

3.4.5 Evidence of self-interaction in turbulence simulations

In this subsection, the self-interaction mechanism is analysed in fully developed turbulence simulations with physical and numerical parameters given in Table 3.1. We first test if in this non-linear system, the relative phase differences between the linearly coupled k_x –Fourier modes remain the same as in corresponding linear eigenmode, as was assumed earlier in §3.4.3. It is found that the relative phase difference is only partially preserved, and the consequent effect on the Reynolds stress driving zonal flows via self-interaction is illustrated.

To find the non-linear modification of an eigenmode, first the absolute value of the time-

averaged ballooning structure of the electrostatic potential $|\langle \hat{\Phi}_{b, \text{nl}}(\chi, t) / \hat{\Phi}_{b, \text{nl}}(\chi_0 = 0, t) \rangle_t|$ for an eigenmode with $k_{x0} = 0$ and $k_y \rho_i = 0.28$ in the full turbulence simulation is plotted along with the corresponding linear ballooning structure $|\hat{\Phi}_{b, \text{lin}}(\chi) / \hat{\Phi}_{b, \text{lin}}(\chi_0 = 0)|$, in figure 3.13(a). See equation (2.96) for the definition of the ballooning structure $\hat{\Phi}_b(\chi)$. The non-linear result with kinetic electrons starts significantly deviating from the linear result for $|\chi| \gtrsim \pi$. That is, the 'giant tails' in the ballooning structure are reduced compared to the linear case. Nonetheless, the non-linear ballooning structure with kinetic electrons retain more significant tails compared to the case with adiabatic electrons. One also finds that, with kinetic electrons, the relative phase along the ballooning structure $\delta\phi_{\text{nl}}(\chi, t) = \phi[\hat{\Phi}_{b, \text{nl}}(\chi, t) / \hat{\Phi}_{b, \text{nl}}(\chi_0 = 0, t)]$ remains approximately constant in time (contrary to adiabatic electron results) and equal to its linear value $\delta\phi_{\text{lin}}(\chi) = \phi[\hat{\Phi}_{b, \text{lin}}(\chi) / \hat{\Phi}_{b, \text{lin}}(\chi_0 = 0)]$; Here, $\phi[A] = \arg(A)$ stands for the phase or argument of the complex number A . This is true in particular for $|\chi| \lesssim 4\pi$, as demonstrated by the solid blue line in figure 3.13(b) representing $\Delta\phi(\chi, t) = \delta\phi_{\text{nl}}(\chi, t) - \delta\phi_{\text{lin}}(\chi)$ for $\chi = 2\pi$ in the kinetic electron case. While there are jumps of 2π , the line closely adheres to the linear phase difference. To be quantitative, one considers the estimate $\text{MOD}(\Delta\phi(\chi, t))$, where

$$\text{MOD}(A) = (\langle |\text{mod}_{2\pi}(A)|^2 \rangle_t)^{1/2}, \quad (3.16)$$

$\text{mod}_{2\pi}(A) \equiv A - 2\pi \times \text{round}(A/2\pi)$, $A \in \mathbb{R}$, and the function round provides the nearest integer. One notes that, lower the value of $\text{MOD}(\Delta\phi)$, more strongly is the relative phase fixed by the linear coupling. Further, for uniform random values of $\Delta\phi$ between $-\pi$ and π , one gets $\text{MOD}(\Delta\phi) = 0.58\pi$. It is found that, for the case with kinetic electrons, $\text{MOD}(\Delta\phi(\chi = 2\pi, t)) = 0.34\pi$. At $\chi = 4\pi$, as illustrated by the dotted blue line in figure 3.13(b), the phase imposed by linear coupling appears to be weakened but still present, giving $\text{MOD}(\Delta\phi(\chi, t)) = 0.50\pi$. The corresponding results with adiabatic electrons, denoted by the solid and dashed red lines for $\chi = 2\pi$ and 4π respectively, clearly do not retain constant phase differences. The respective values of $\text{MOD}(\Delta\phi(\chi, t))$ are 0.57π and 0.61π .

In other words, in a full turbulence simulation with adiabatic electrons, for a linearly unstable eigenmode with given k_{x0} and k_y , linear coupling between the Fourier modes $(k_x = k_{x0} + 2\pi p k_y \hat{s}, k_y)$ where $p \in \mathbb{Z}$ have become subdominant compared to non-linear coupling effects. Thus, each (k_x, k_y) Fourier mode can be considered linearly decoupled as in a shearless slab system and hence, modulational instability is the only driving mechanism of zonal flows in turbulent simulations with adiabatic electrons. On the other hand, with kinetic electrons, for a linearly unstable physical mode with given k_{x0} and k_y , linear coupling of Fourier modes is preserved to some extent but reduced to only the three Fourier modes with $k_x = k_{x0} + 2\pi p k_y \hat{s}$ and $|p| = 0, \pm 1$. Only these Fourier modes have their relative phases largely fixed by their linear dynamics (and not for all $p \in \mathbb{Z}$, as assumed in §3.4.3). Hence the self-interaction mechanism is effectively reduced to driving the zonal Fourier modes with $k'_x = \pm 2\pi k_y \hat{s}$. Furthermore, the self-interacting contribution to Reynolds stress $\widetilde{\text{RS}}_{k_{x0}, k_y}(x)$ (defined in equation (3.15)) from

Chapter 3. How eigenmode self-interaction affects zonal flows and convergence of turbulence levels with toroidal system size

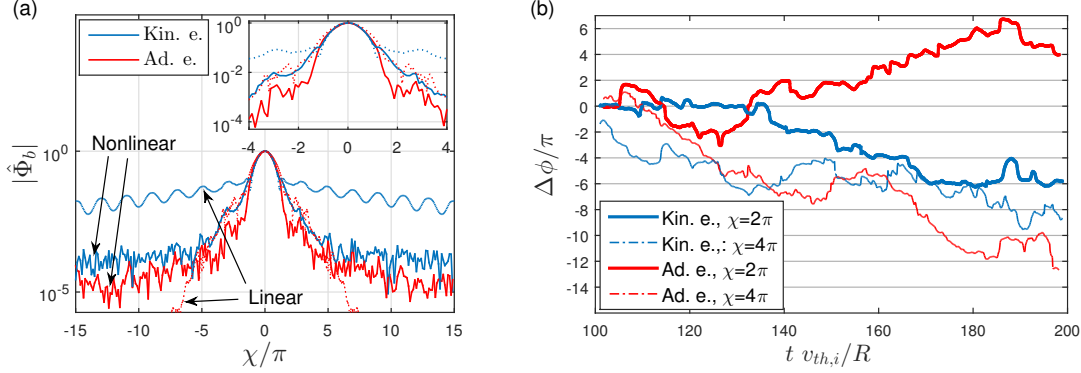


Figure 3.13: (a) Solid lines denote the absolute value of the time-averaged ballooning structure of the electrostatic potential $|\langle \hat{\Phi}_{b,nl}(\chi, t) / \hat{\Phi}_{b,nl}(\chi_0 = 0, t) \rangle_t|$ for $k_{x0} = 0$ and $k_y \rho_i = 0.28$ in the non-linear simulation described in table 3.1, with $k_{y,min} \rho_i = 0.035$ and $R/L_{T,i} = 6$. Dotted lines denote the corresponding ballooning representation in linear simulations (same as in figure 3.2). Inset figure shows the zoom near $\chi = 0$. Red and blue colours represent adiabatic and kinetic electron simulations respectively. (b) Phase difference $\Delta\phi(\chi, t) = (\phi[(\hat{\Phi}_{b,nl}(\chi, t) / \hat{\Phi}_{b,nl}(\chi_0 = 0, t))(\hat{\Phi}_{b,lin}(\chi_0 = 0) / \hat{\Phi}_{b,lin}(\chi))])$ plotted as a function of time. Here, $\hat{\Phi}_{b,nl}$ and $\hat{\Phi}_{b,lin}$ denote the ballooning representation of the electrostatic potential for the same eigenmode considered in subplot (a), in non-linear and linear simulations respectively. Solid and dotted lines represent $\chi = 2\pi$ and 4π respectively.

the particular physical eigenmode, becomes essentially sinusoidal in x , spanning the full distance between corresponding MRSs with a period of $\Delta x_{MRS} = 1/k_y \hat{s}$, and with fixed phase/sign in time. Note that the radial width of the fine-structures do not have a dependence on electron-ion mass ratio in turbulence simulations as they are already broadened to span the distance between MRSs as a result of non-linear coupling effects. This is unlike in linear simulations where such a dependence exists [Dominski et al., 2015].

The net contribution RS^{si} from the self-interaction mechanism to Reynolds stress can be obtained by summing $\widetilde{RS}_{k_{x0}, k_y}(x)$ over all k_y 's and all ballooning angles (measured by k_{x0} ; see (2.97)):

$$RS^{si}(x) = \sum_{k_y > 0} \hat{RS}_{k_y}^{si}(x) \quad (3.17)$$

where

$$\hat{RS}_{k_y}^{si} = \sum_{k_{x0} = -\pi k_y \hat{s}}^{\pi k_y \hat{s}} \widetilde{RS}_{k_{x0}, k_y}(x). \quad (3.18)$$

In figure 3.10, the self-interaction contribution $\partial^2 RS^{si} / \partial x^2$ from a particular k_y in full turbulence simulation is plotted. The dashed lines denote the time average of $\partial^2 \hat{RS}_{k_y}^{si} / \partial x^2$ for $k_y \rho_i = 0.28$, normalised by the RMS in time of total $\partial^2 \hat{RS}_{k_y} / \partial x^2$, in simulations

with kinetic (blue) and adiabatic (red) electrons; the total Reynolds stress contribution $\hat{\text{RS}}_{k_y}$ from a given k_y being defined in (3.12). This diagnostic simultaneously measures the relative importance of self-interaction drive of zonal flows with respect to the total contribution to Reynolds stress drive from the considered k_y , as well as how good its phase/sign is fixed in time. One notes that, since for a given k_y , eigenmode with $k_{x0} = 0$ is the most unstable/dominant, similar results are obtained for $\text{RS}_{k_{x0}=0, k_y}(x)$ as well, instead of $\hat{\text{RS}}_{k_y}^{\text{si}}$ in this diagnostic. From figure 3.10, one can conclude that, in full turbulence simulations with kinetic electrons, each k_y contribution $\partial^2 \hat{\text{RS}}_{k_y}^{\text{si}} / \partial x^2$ from self-interaction is significant. Furthermore, it is a sinusoidal with a period of $1/k_y \hat{s}$ and maintains the same sign at each radial position (although with randomly varying amplitude in time, as will be shown at the end of §3.4.6). In particular, $\partial^2 \hat{\text{RS}}_{k_y}^{\text{si}} / \partial x^2$ is zero at MRSs, negative to the left and positive to the right. Whereas with adiabatic electrons, the self-interaction contribution is weak, does not have a fixed sign, and essentially averages out to zero over time. Further, with kinetic electrons, these significant time-averaged self-interaction contributions, localized at MRSs of each k_y , align at LMRSs, driving time-averaged zonal flows at these radial positions. Whereas, away from LMRSs, the time-averaged self-interaction contributions $\partial^2 \hat{\text{RS}}_{k_y}^{\text{si}} / \partial x^2$ from each k_y are spatially misaligned and cancel each other out, resulting in relatively negligible time averaged zonal flow levels.

In figure 3.14, the time average of the total $\partial^2 \hat{\text{RS}}_{k_y} / \partial x^2$ is plotted as a function of both position x and wavenumber k_y . While between LMRSs, $\partial^2 \hat{\text{RS}}_{k_y} / \partial x^2$ follows essentially the same spatial orientation (phase) as $\partial^2 \hat{\text{RS}}_{k_y}^{\text{si}} / \partial x^2$ in figure 3.10, near LMRSs, there is a reversal of spatial phase. We suspect this to be a result of the back reaction of zonal modes driven by self-interaction on turbulence. At the moment, we postpone further analysis on this to a later time.

Recall from earlier in this subsection that in kinetic electron turbulence simulations, the self-interaction contribution from a given $k_y \neq 0$ is effectively reduced to driving the zonal Fourier modes with $k'_x = \pm 2\pi k_y \hat{s}$. The combined self-interacting contributions from the various k_y 's therefore drive zonal Fourier modes with $k_x = 2\pi p \hat{s} k_{y,\text{min}}$, where $p \in \mathbb{Z}$. This can be seen as peaks in the k_x -spectra of the time-averaged shearing rate $\langle \omega_{\text{eff}} \rangle_t$, shown with blue dashed line in figure 3.15 and correspond to the time-constant structures at LMRSs separated by $\Delta x_{\text{LMRS}} = 1/\hat{s} k_{y,\text{min}}$ in figure 3.5. Given that, in the case of the reference turbulence simulation with kinetic electrons, the highest contribution to heat flux (see figure 3.7(b)) and the $|\Phi|^2$ amplitude spectra is at $k_y \rho_i \sim 0.21$ and that for a given k_y , eigenmodes with $k_{x0} = 0$ are the most dominant, the zonal mode with $k_x \rho_i \sim 2\pi \hat{s} \times 0.21 \sim 1.06$ are driven strongly via the self-interaction mechanism and hence has the highest value in the k_x -spectra of shearing rate. Similarly, those k_y 's with lower heat flux and amplitude contributions, contribute lesser towards the self-interaction mechanism and thereby explains the number and position of peaks in the k_x -spectra of shearing rate with kinetic electrons in figure 3.15.

Chapter 3. How eigenmode self-interaction affects zonal flows and convergence of turbulence levels with toroidal system size

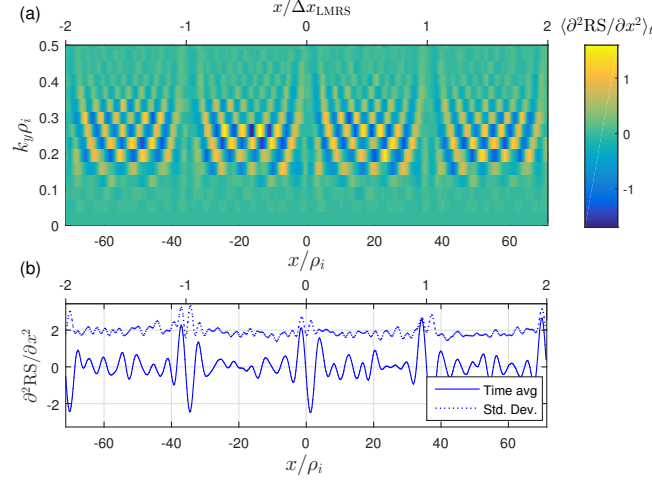


Figure 3.14: (a) Each k_y contribution of $\langle \partial^2 \text{RS} / \partial x^2 \rangle_t$ plotted as a function of the radial coordinate x . (b) Total $\langle \partial^2 \text{RS} / \partial x^2 \rangle_t$ plotted vs x . Dashed line denote the standard deviation. Results correspond to the non-linear simulation described in table 3.1, with $k_{y,\min} \rho_i = 0.035$, $R/L_{T,i} = 6$ and kinetic electrons.

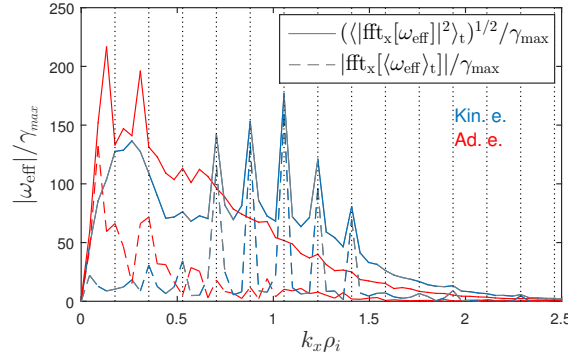


Figure 3.15: k_x spectra of the effective shearing rate ω_{eff} in turbulence simulations with adiabatic (red) and kinetic (blue) electrons. Corresponding parameters are given in table 3.1, with $k_{y,\min} \rho_i = 0.035$ and $R/L_{T,i} = 6$. Solid lines and dashed lines represent time average of the amplitude and amplitude of the time average of ω_{eff} respectively. All traces are normalised by corresponding maximum linear growth rate γ_{max} . Vertical dotted lines indicate positions where $k_x = 2\pi p \hat{s} k_{y,\min}$; $p \in \mathbb{Z}$.

Solid red line in figure 3.15 denotes the k_x -spectra of ω_{eff} in the simulation with adiabatic electron response. These zonal Fourier modes are driven predominantly by modulational instability. In the next subsection, we test, if consequently, as a result of the frequency matching involved in the modulational instability mechanism, those zonal modes having high shearing rate amplitudes end up playing a major role in pacing the dynamics of much of the $(k_x, k_y \neq 0)$ Fourier modes in adiabatic electron simulations.

3.4.6 Evidence of modulational instability in turbulence simulations. Bicoherence and correlation analysis.

In this subsection, we verify in fully developed turbulence simulations, that indeed with adiabatic electron response, zonal flows are driven predominantly via modulational instability, as found in reduced simulations in §3.4.4 and as discussed in §3.4.5. We test this by doing a bicoherence-like analysis. We simultaneously show that, as a consequence, this leads to *correlated* contributions from the various k_y 's to the Reynolds stress drive of zonal modes. We furthermore show that in kinetic electron simulations, the self-interaction contributions to Reynolds stress from the various k_y 's are random in time and *decorrelated* with each other.

As already discussed earlier, modulational instability mechanism involves resonant 3-wave interactions which require frequency matching. The strength of a particular resonant interaction between the 3 Fourier modes, $\mathbf{k} = (k_x, k_y)$, the zonal mode $\mathbf{k}' = (k'_x, 0)$ and daughter mode $\mathbf{k}'' = \mathbf{k} - \mathbf{k}' = (k_x - k'_x, k_y)$, can thus be measured via a bicoherence-type analysis, essentially involving the time-average of the triplet product

$$T(\mathbf{k} ; +\mathbf{k}') = \hat{\Phi}_{\mathbf{k}}(t) \hat{\Phi}_{\mathbf{k}'}^*(t) \hat{\Phi}_{\mathbf{k}''}^*(t) \quad (3.19)$$

where $\hat{\Phi}_{\mathbf{q}}(t) \sim \exp[-i(\omega_{\mathbf{q}}t + \phi_{\mathbf{q}})]$ is the complex time dependent amplitude of the electrostatic field with any Fourier mode \mathbf{q} , having a frequency $\omega_{\mathbf{q}}$, initial phase $\phi_{\mathbf{q}}$, and evaluated at $z=0$. If the Fourier modes $[\mathbf{k}, \mathbf{k}', \mathbf{k}'' = \mathbf{k} - \mathbf{k}']$ are frequency matched in the simulation time, i.e. $\omega_{\mathbf{k}} = \omega_{\mathbf{k}'} + \omega_{\mathbf{k}''}$, then $\langle T(\mathbf{k} ; +\mathbf{k}') \rangle_t \neq 0$, where $\langle \cdot \rangle_t$ stands for the time-average over the simulation time.

Here, we remark that, for a given set of Fourier modes $[\mathbf{k}, \mathbf{k}', \mathbf{k}'' = \mathbf{k} - \mathbf{k}']$ under frequency matching condition, different resonant decay mechanisms could be possible, each with a specific phase difference $\Delta\phi = \phi_{\mathbf{k}} - \phi_{\mathbf{k}'} - \phi_{\mathbf{k}''}$ associated with it. Hence, a non-zero time average $\langle T(\mathbf{k} ; +\mathbf{k}') \rangle_t$ over the simulation time is indicative of a particular resonant decay mechanism being persistent throughout the simulation.

Now, a normalised measure of the strength of the resonant 3-wave interaction can be

Chapter 3. How eigenmode self-interaction affects zonal flows and convergence of turbulence levels with toroidal system size

calculated by the following estimate:

$$b_N(\mathbf{k} ; +\mathbf{k}') = \frac{|\langle T(\mathbf{k} ; +\mathbf{k}') \rangle_t|}{\langle |T(\mathbf{k} ; +\mathbf{k}')| \rangle_t}, \quad (3.20)$$

defined as the bicoherence between the Fourier triplet $[\mathbf{k}, \mathbf{k}', \mathbf{k}'' = \mathbf{k} - \mathbf{k}']$. Note $0 \leq b_N \leq 1$. Further, $b_N(\mathbf{k} ; +\mathbf{k}') \simeq 1$ indicates a fully resonant 3-wave interaction between \mathbf{k} , \mathbf{k}'' and the zonal mode \mathbf{k}' , while $b_N \simeq 0$ indicates a non-resonant process. Since modulational instability is a simultaneous resonant interaction between both triplets $[\mathbf{k}, \mathbf{k}', \mathbf{k}'' = \mathbf{k} - \mathbf{k}']$ and $[\mathbf{k}, -\mathbf{k}', \mathbf{k}''' = \mathbf{k} + \mathbf{k}']$, we define total bicoherence

$$B_N(\mathbf{k} ; \mathbf{k}') = (b_N(\mathbf{k} ; +\mathbf{k}') + b_N(\mathbf{k} ; -\mathbf{k}'))/2, \quad (3.21)$$

such that a value of $B_N \simeq 1$ indicates a fully resonant modulational instability mechanism. In general, values of B_N closer to zero are indicative of non-resonant interactions while larger values of B_N are characteristic of modulational instability mechanisms.

Note that, while the resonant 3-wave interaction is defined for the case of a single pump mode with a well defined frequency decaying into a zonal mode via a daughter mode while ensuring frequency matching, in a turbulent system many such pump modes are present. The frequencies of these pump modes may not be the same as their original linear eigenmodes, especially in the case of strong turbulence where they undergo significant nonlinear frequency shifts. The bicoherence analysis, in the strict sense, therefore measures the level of a more general resonant 3-wave interaction mechanism (or a more general modulational instability mechanism) where frequency matching is satisfied. However, in the analysis presented here, we assume that the frequencies of the pump modes remain the same as their corresponding linear eigenmodes, and hence, the bicoherence analysis can be said to measure the level of modulational instability in the system.

Figure 3.16(a) shows $B_N(\mathbf{k} ; \mathbf{k}')$ as a function of $\mathbf{k} = (k_x, k_y)$, in the reference simulation with adiabatic electrons, for the fixed zonal mode with $\mathbf{k}' = (k'_x = 0.13\rho_i^{-1}, 0)$ which has the highest contribution to the zonal shearing rate k_x -spectra (see solid red line in figure 3.15). One can see that most $\mathbf{k} = (k_x, k_y)$ have high values of $B_N \gtrsim 0.3$, reflecting the dominance of resonant 3-wave interaction processes. Whereas in figure 3.16(b), corresponding kinetic electron simulation result for the zonal mode with $\mathbf{k}' = (k'_x = 0.26\rho_i^{-1}, 0)$ having highest contribution to the shearing rate k_x -spectra shows much smaller values of B_N , indicating much weaker resonant 3-wave interactions. Similar differences are seen between adiabatic and kinetic electron results for other zonal modes $\mathbf{k}' = (k'_x, 0)$ as well.

Note that, for a given zonal mode $\mathbf{k}' = (k'_x, 0)$, under wave vector matching condition, one has the following approximate estimate between associated triple products and the

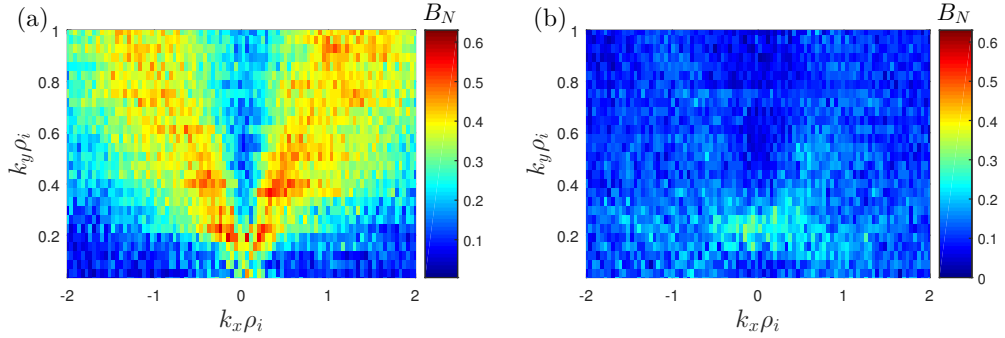


Figure 3.16: The bicoherence level B_N , as defined by equation (3.21), in (a) adiabatic and (b) kinetic electron turbulence simulations, for the zonal modes with $k'_x \rho_i = 0.13$ and 0.26 respectively. Results correspond to simulations with parameters as given in table 3.1, with $k_{y,\min} \rho_i = 0.035$ and $R/LT_i = 6$.

Reynolds stress contributions driving the particular zonal mode:

$$\sum_{k_x} T(\mathbf{k} ; \mathbf{k}') \sim \hat{\Phi}_{\mathbf{k}'}^* \hat{\mathbf{R}}\hat{\mathbf{S}}_{k_y}, \quad (3.22)$$

where $\hat{\mathbf{R}}\hat{\mathbf{S}}_{k_y}$ has been defined in equation (3.12). Now, if $\langle T(\mathbf{k} ; \mathbf{k}') \rangle_t$ (and the corresponding total bicoherence $B_N(\mathbf{k} ; \mathbf{k}')$) for multiple Fourier modes $\mathbf{k} = (k_x, k_y)$ are simultaneously significant for the same dominant zonal mode \mathbf{k}' (as is the case in figure 3.16(a) for adiabatic electron simulation), then based on (3.22) one can conclude that the Reynolds stress contributions $\hat{\mathbf{R}}\hat{\mathbf{S}}_{k_y}$ from the various k_y 's tend to be in phase with the particular zonal mode. This implies a coherent and thus correlated contributions (drives) from these various $\hat{\mathbf{R}}\hat{\mathbf{S}}_{k_y}$ ($\partial^2 \hat{\mathbf{R}}\hat{\mathbf{S}}_{k_y} / \partial x^2$). To verify this explicitly, we define an effective correlation function C_{RS} measuring the average correlation between all pairs of $[\partial^2 \hat{\mathbf{R}}\hat{\mathbf{S}}_{k_{y,1}} / \partial x^2, \partial^2 \hat{\mathbf{R}}\hat{\mathbf{S}}_{k_{y,2}} / \partial x^2]$ for $k_{y,1} \neq k_{y,2}$:

$$C_{\text{RS}}[f] = \sum_{\substack{k_{y,i}, k_{y,j} \\ k_{y,j} > k_{y,i}}} \frac{\text{Cov}[\hat{f}_{k_{y,i}}, \hat{f}_{k_{y,j}}]}{\sigma[\hat{f}_{k_{y,i}}] \sigma[\hat{f}_{k_{y,j}}]} \bigg/ \sum_{\substack{k_{y,i}, k_{y,j} \\ k_{y,j} > k_{y,i}}} 1. \quad (3.23)$$

$f = \partial^2 \text{RS} / \partial x^2$, $\hat{f}_{k_y} = \partial^2 \hat{\mathbf{R}}\hat{\mathbf{S}}_{k_y}(x) / \partial x^2$, covariance $\text{Cov}[a, b] = (\sigma^2[a + b] - \sigma^2[a] - \sigma^2[b]) / 2$, and variance $\sigma^2[a] = \langle |a - \langle a \rangle_t|^2 \rangle_t$, with $\langle \cdot \rangle_t$ representing average over simulation time. Note that $C_{\text{RS}} \in [0, 1]$, with 1 corresponding to perfect correlation between Reynolds stress drive from all k_y 's and 0 corresponding to total decorrelation between them. In figure 3.17, C_{RS} is plotted as a function of the radial position x , for adiabatic and kinetic electron turbulence simulations. We can find that $C_{\text{RS}}[\partial^2 \text{RS} / \partial x^2]$ for adiabatic electron case (solid red line) only shows $\sim 7\%$ correlation. However the important point to note is that this is roughly an order of magnitude higher than that for kinetic electron simulation (solid blue line). Thus, this diagnostic verifies that in adiabatic electron turbulence simulations where modulational instability mechanism is stronger, Reynolds stress drive

Chapter 3. How eigenmode self-interaction affects zonal flows and convergence of turbulence levels with toroidal system size

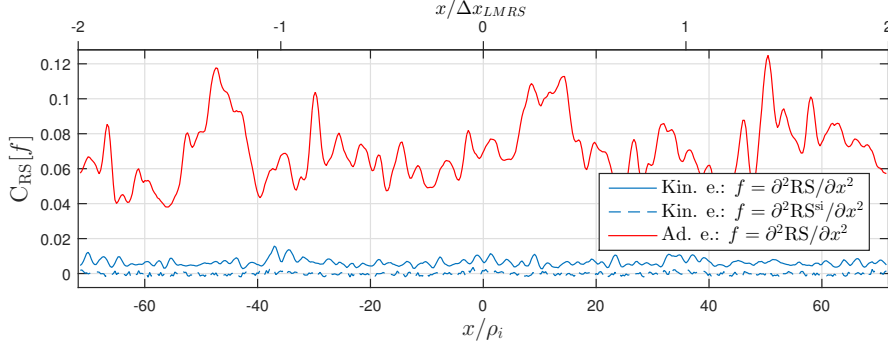


Figure 3.17: Correlation between the k_y modes of $\partial^2 \text{RS} / \partial x^2$, as defined by equation (3.23), as a function of x in turbulence simulations with kinetic (solid blue line) and adiabatic (solid red line) electrons. Corresponding parameters are given in table 3.1, with $k_{y,\min} \rho_i = 0.035$ and $R/L_{T,i} = 6$. Correlation between the k_y modes of self-interacting contribution $\partial^2 \text{RS}^{\text{si}} / \partial x^2$ in the simulation with kinetic electrons is shown with dashed blue line.

$\partial^2 \hat{\text{RS}}_{k_y} / \partial x^2$ from the various k_y 's are indeed more correlated with each other, when compared to kinetic electron simulations where modulational instability mechanism is weaker.

The same correlation diagnostic is now performed on the self-interacting part of Reynolds stress in kinetic electron simulations. In figure 3.17, the correlation between the k_y contributions to $\partial^2 \text{RS}^{\text{si}} / \partial x^2$, measured by $C_{\text{RS}}[\partial^2 \text{RS}^{\text{si}} / \partial x^2]$, is found to be nearly zero. This implies that, each k_y contribution to $\partial^2 \text{RS}^{\text{si}} / \partial x^2$ at a given radial position (while in general having a fixed sign) has an amplitude that is completely independent and uncorrelated with the other k_y contributions. The self-interaction drive of zonal modes from each k_y thus acts like random kicks. Consequently, if the decorrelated (*incoherent*) contributions from the self-interaction mechanism becomes significant, it may disrupt the (*coherent*) modulational instability interactions. We interpret this as being the cause for lower bicoherence values of B_N in figure 3.16(b), as well as the lower level of $C_{\text{RS}}[\partial^2 \text{RS} / \partial x^2]$ in figure 3.17 with kinetic electrons as compared to adiabatic electrons.

To summarise, in this section 3.4, various zonal flow driving mechanisms have been discussed. Given the quadratic $E \times B$ nonlinearity, the zonal modes can in fact be driven via any 3-Fourier mode interaction process verifying the wave-vector matching condition. In this section, the two main such mechanisms have been studied in detail, namely the modulational instability and the self-interaction mechanism. We have shown that, as a result of the stronger linear k_x -couplings within an eigenmode in kinetic electron simulations, the associated drive of zonal flows via self-interaction is much more significant, than in the case of adiabatic electron simulations. This has been illustrated in both reduced and full turbulence simulations. Furthermore, in turbulence simulations,

3.5. Estimating the reduction in zonal flow drive from self-interaction with decreasing $k_{y,\min}\rho_i$

it was shown that the contributions to zonal flow drive from each k_y mode, via the self-interaction mechanism, are random and decorrelated with each other in time. In the next section, we explain how such a decorrelated drive can lead to a decrease in the fluctuating zonal flow levels with decreasing $k_{y,\min}\rho_i$.

3.5 Estimating the reduction in zonal flow drive from self-interaction with decreasing $k_{y,\min}\rho_i$

The low temporal correlation between the various k_y contributions to the Reynolds stress drive $\partial^2 \text{RS} / \partial x^2$ of zonal flows in kinetic electron simulations, which is a result of strong self-interaction mechanism, could explain the decrease in the level of shearing rate ω_{eff} associated with fluctuating $E \times B$ zonal flows with increasing toroidal system size, over the range of $k_{y,\min}\rho_i$ considered in figure 3.6(c). This explanation is based on simple statistical arguments described as follows.

To start with, let us assume that the fluctuation energy density, proportional to amplitude density $|\Phi|^2$ of the fluctuating electrostatic field Φ , remains the same across the simulations with different $k_{y,\min}$ s. Consequently the amplitude $|\hat{\Phi}_{k_y}|^2$ of each k_y Fourier component of the electrostatic field scales as $1/N_y$ where N_y is the number of participating modes, according to the following estimate based on Parseval's identity:

$$\frac{1}{L_y} \int_0^{L_y} |\Phi|^2 dy = \sum_{k_y=0}^{N_y} |\hat{\Phi}_{k_y}|^2 = \text{constant} \implies |\hat{\Phi}_{k_y}|^2 \sim \frac{1}{N_y}. \quad (3.24)$$

Here, $\hat{\Phi}_{k_y}$ is defined as per the relation

$$\Phi(x, y, z) = \sum_{k_y} \hat{\Phi}_{k_y}(x, z) e^{ik_y y}. \quad (3.25)$$

Since Reynolds stress is a quadratic quantity in Φ , the scaling in relation (3.24) also implies that each k_y contribution to the Reynolds stress drive scales as $\partial^2 \hat{\text{RS}}_{k_y} / \partial x^2 \sim |\hat{\Phi}_{k_y}|^2 \sim 1/N_y$. Since $N_y = k_{y,\max}/k_{y,\min}$ and $k_{y,\max}$ remains the same across simulations in the $k_{y,\min}$ scan, one also has $1/N_y \sim k_{y,\min}$.

Now, further assuming the various k_y contributions to Reynolds stress drive $\partial^2 \hat{\text{RS}}_{k_y} / \partial x^2$ to be nearly fully decorrelated (characteristic of kinetic electron simulations; see figure 3.17), the variance of the total Reynolds stress drive $\partial^2 \text{RS} / \partial x^2 = \sum_{k_y} \partial^2 \hat{\text{RS}}_{k_y} / \partial x^2$ becomes the sum of variances of all k_y contributions:

$$\text{Var} \left(\sum_{k_y} \frac{\partial^2}{\partial x^2} \hat{\text{RS}}_{k_y} \right) \simeq \sum_{k_y} \text{Var} \left(\frac{\partial^2}{\partial x^2} \hat{\text{RS}}_{k_y} \right) \sim N_y \frac{1}{N_y^2} \sim \frac{1}{N_y} \sim k_{y,\min}, \quad (3.26)$$

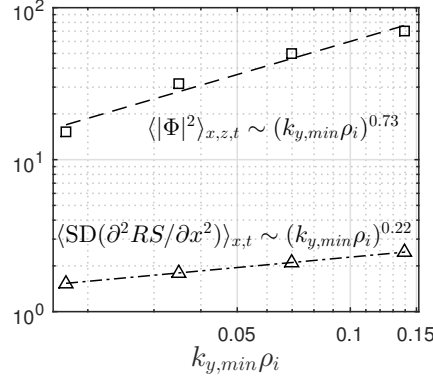


Figure 3.18: Triangles: Standard deviation $\langle \text{SD}(\partial^2 \text{RS} / \partial x^2) \rangle_{x,t}$ of Reynolds stress drive plotted as a function of $k_{y,\min}$ in log-log scale, in turbulence simulations with kinetic electrons. Corresponding parameters are given in table 3.1, with $R/L_{T,i} = 6$. Fit (dashed-dotted line) shows scaling $\sim (k_{y,\min} \rho_i)^{0.22}$. Squares: $\langle |\hat{\Phi}|^2 \rangle_{x,z,t}$ ($k_y \rho_i = 0.28$) plotted as a function of $k_{y,\min}$, in the same set of simulations. Fit (dashed line) shows scaling $\sim (k_{y,\min} \rho_i)^{0.73}$.

having made use of $\text{Var}(\partial^2 \hat{\text{RS}}_{k_y} / \partial x^2) \sim 1/N_y^2$, given that $\partial^2 \hat{\text{RS}}_{k_y} / \partial x^2 \sim 1/N_y$. We therefore expect the standard deviation SD of the Reynolds stress drive $\partial^2 \text{RS} / \partial x^2$ to scale as $\text{SD} = \text{Var}^{0.5} \sim k_{y,\min}^{0.5}$. Further, since $\partial^2 \text{RS} / \partial x^2$ is a proxy for the drive of zonal flows, this explains a decrease in the standard deviation of ω_{eff} with decreasing $k_{y,\min}$.

From the $k_{y,\min}$ scan performed with kinetic electrons, $R/L_{T,i} = 6$ and other parameters as given in Table 3.1, we find that the x and time-averaged standard deviation $\langle \text{SD}(\partial^2 \text{RS} / \partial x^2) \rangle_{x,t}$ of the Reynolds stress drive actually scales as $k_{y,\min}^{0.22}$, as shown in figure 3.18. This mismatch between the expected and observed scalings pushes us to reconsider the assumptions made that led to the estimate $\text{SD} \sim k_{y,\min}^{0.5}$.

The small but non-zero value of the correlation between the k_y contributions of $\partial^2 \text{RS} / \partial x^2$ in these simulations (see solid blue line in figure 3.17) may account for a small part of the discrepancy. However, the primary cause seems to arise from the faulty assumption of constant fluctuation energy density across simulations with different $k_{y,\min}$ s. As the zonal flow shearing rate decreases with decreasing $k_{y,\min}$, the energy density in the system tends to increase, so that the estimate made in relation (3.24) has to be reconsidered. This is confirmed in figure 3.18 where the same set of simulations show $\langle |\hat{\Phi}_{k_y}|^2 \rangle_{x,z,t} \sim k_{y,\min}^{0.73}$, for $k_y \rho_i = 0.28$ having a significant amplitude in the k_y -spectra of $|\Phi|^2$ and heat flux. Using this scaling $\partial^2 \hat{\text{RS}}_{k_y} / \partial x^2 \sim |\hat{\Phi}_{k_y}|^2 \sim k_{y,\min}^{0.73}$ in place of $\sim k_{y,\min}^1$ in (3.26), we get

$$\text{Var} \left(\sum_{k_y} \frac{\partial^2}{\partial x^2} \hat{\text{RS}}_{k_y} \right) \simeq \sum_{k_y} \text{Var} \left(\frac{\partial^2}{\partial x^2} \hat{\text{RS}}_{k_y} \right) \sim \frac{1}{k_{y,\min}} (k_{y,\min}^{0.73})^2 \sim k_{y,\min}^{0.46}, \quad (3.27)$$

i.e. the standard deviation of $\partial^2 \text{RS} / \partial x^2$ scales as $\text{SD} = \text{Var}^{0.5} \sim k_{y,\min}^{0.23}$, which is very close to the observed trend of $\langle \text{SD}(\partial^2 \text{RS} / \partial x^2) \rangle_{x,t} \sim k_{y,\min}^{0.22}$.

3.6 Conclusions

In this chapter, we have addressed the self-interaction mechanism and how it affects the drive of zonal flows in ion-scale gyrokinetic turbulence simulations. The basic mechanism of self-interaction is the process by which a microinstability eigenmode nonlinearly interacts with itself, generating a Reynolds stress contribution localised at its corresponding MRS (figure 3.10). Compared to adiabatic electron simulations, this effect is more prominent in kinetic electron simulations. The origin of this increased self-interaction in kinetic electron simulations is the result of the non-adiabatic passing electron response at MRSs leading to fine slab-like structures at these radial positions, reflected as well by broadened ballooning structures of the eigenmodes (figure 3.2).

These self-interacting contributions from various eigenmodes to Reynolds stress radially align at low order MRSs to generate significant stationary zonal flow shear layers at these positions. However, given that low order MRSs occupy only a tiny radial fraction of core tokamak plasmas, we have focused primarily on how self-interaction affects the drive of zonal flows between the low order MRSs. We have found that self-interaction plays an important role in generating fluctuating zonal flows, in fact *throughout* the full radial extent. These fluctuating components of zonal flows are furthermore found to be critical to regulating transport levels.

These findings were obtained by studying the self-interaction contributions to Reynolds stress drive from the various microturbulence modes by focusing on their statistical properties. Critical to this approach has been to vary the number of significant toroidal modes participating in our turbulence simulations by performing scans over $k_{y,\min} \rho_i$.

In these turbulence simulations, using correlation analysis (see figure 3.17), we have in particular shown that the amplitude of the Reynolds stress contributions from self-interaction of each microturbulence mode are essentially random and decorrelated with each other. In the case of kinetic electron simulations, the significant self-interaction mechanism can in this way disrupt the coherent contributions from the alternative zonal flow drive process provided by the modulational instability mechanism, as reflected by the corresponding weak bicoherence analysis estimates presented in figure 3.16. In simulations with adiabatic electrons however, for which self-interaction is weak, bicoherence estimates reflect strong resonant 3 wave interactions, characteristic of the modulational instability process being dominant in this case.

Using simple statistical scaling arguments we have then demonstrated how such a decorrelated drive from the self-interaction of various microturbulence modes could in

Chapter 3. How eigenmode self-interaction affects zonal flows and convergence of turbulence levels with toroidal system size

turn lead to a decrease in shearing rate associated with fluctuating zonal flows with decreasing $k_{y,\min}\rho_i$ [see kinetic electron results in figure 3.6(c)]. Assuming that the zonal flow shearing mechanism is the dominant saturation mechanism at play, this in turn would lead to an increase in gyro-Bohm normalised heat and particle flux levels as $k_{y,\min}\rho_i$ decreases.

For the range $k_{y,\min}\rho_i = 10^{-2} - 10^{-1}$ considered in section 3.3, the kinetic electron simulations far from marginal stability [blue circles in figure 3.7(a)] indeed show such an increase in ion heat flux, presenting a power law scaling of the form $(k_{y,\min}\rho_i)^\alpha$, with $\alpha < 0$. It is important to note that, as one continues to decrease $k_{y,\min}\rho_i$, this scaling ultimately breaks and the simulation results do finally converge; in other words, the true $\rho^* \rightarrow 0$ limit of the flux-tube model can be reached, as already reported in the work by [Ball et al., 2020]. To demonstrate this for the particular case far from marginal stability ($R/L_{T,i} = 6$), the original scan was extended to lower values of $k_{y,\min}\rho_i$, but with a quarter of the resolution in the radial direction to make the runs computationally feasible. The corresponding ion heat flux plot is shown in figure 3.19(a), where the power law scaling finally breaks for $k_{y,\min}\rho_i \lesssim 10^{-2}$, and a convergence within 5% is observed at $k_{y,\min}\rho_i \sim 5 \times 10^{-3}$. The corresponding estimates of the effective shearing rate, namely $\text{RMS}_{x,t}(\omega_{\text{eff}})$, $\text{SD}_{x,t}(\omega_{\text{eff}})$ and $\text{RMS}_x(\langle\omega_{\text{eff}}\rangle_t)$, are plotted in figure 3.19(b). As had been discussed in §3.3, the most interesting quantity to us is the shearing rate of fluctuating zonal flows measured by $\text{SD}_{x,t}(\omega_{\text{eff}})$, which is also seen to deviate from its the power law scaling for values of $k_{y,\min}\rho_i \lesssim 10^{-2}$, hinting towards a near convergence for $k_{y,\min}\rho_i \sim 5 \times 10^{-3}$. Furthermore, in figure 3.8, corresponding results of the radial correlation length of turbulent eddies is given, also showing a convergence for $k_{y,\min}\rho_i \sim 5 \times 10^{-3}$.

Closer to marginal stability [green line in figure 3.7(a)], the gyro-Bohm normalised flux levels in kinetic electrons simulations appear to be already essentially converged for $k_{y,\min}\rho_i \sim 10^{-2}$. The convergence of fluxes observed for this particular case is despite a decrease in the shearing rate associated with zonal flows (seen in $\text{RMS}_{x,t}(\omega_{\text{eff}})$, $\text{SD}_{x,t}(\omega_{\text{eff}})$ and $\text{RMS}_x(\langle\omega_{\text{eff}}\rangle_t)$, shown with green lines in figure 3.6(a-c)). One possible explanation for this could be that, as the various estimates of normalised shearing rate decrease below $\omega_{\text{eff}}/\gamma_{\text{max}} \simeq 1$, the zonal flow saturation mechanism becomes less effective in regulating flux levels. Other saturation mechanisms such as that via damped eigenmodes [Hatch et al., 2011] could then be taking over.

Since $k_{y,\min}\rho_i \sim \rho^*$, one can interpret the decrease in zonal flow shearing rates and the possible associated increase in heat and particle flux levels in any particular range in $k_{y,\min}\rho_i$ as a finite toroidal system size effect still present in the flux-tube simulations. One may deal in practice with this system size dependence of flux-tube simulations in two ways:

1. One approach has the intent of correctly resolving this physical finite ρ^* effect,

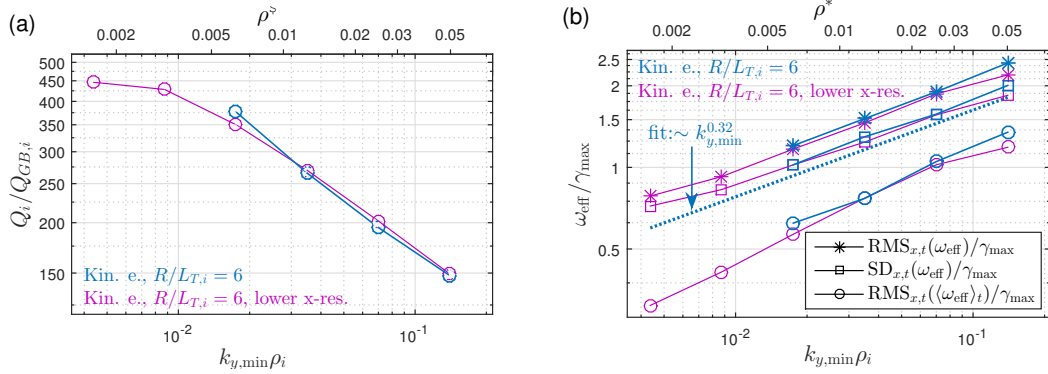


Figure 3.19: (a) Ion heat flux plotted as a function of $k_{y,min} \rho_i$. (b) Asterisks, squares and circles represent $\text{RMS}_{x,t}(\omega_{eff})$, $\text{SD}_{x,t}(\omega_{eff})$ and $\text{RMS}_x(\langle \omega_{eff} \rangle_t)$ respectively, plotted as a function of $k_{y,min} \rho_i$. In both sub-plots, blue colour represents the kinetic electron reference simulations whose parameters are given in table 3.1 [the case far from marginal stability ($R/L_{T,i} = 6$)]; these are the same plots as those shown with blue colour in figure 3.7(a) and figure 3.6. Magenta colour represent simulations with a quarter of the resolution in the radial coordinate.

but to be accurate, this requires considering the physical $k_{y,min} \rho_i = n_{min}(q_0 a / r_0) \rho^*$ value of the tokamak plasma conditions one is studying, which corresponds to the flux-tube covering the *full* reference flux-surface in both the poloidal (with $L_z = 2\pi$) and toroidal (with $n_{min} = 1$) directions. In this chapter, only this approach has been considered.

This can however be quite challenging in practice, even for flux-tube simulations relevant for a medium-sized tokamak. A scan in $k_{y,min}$, even when limited to ion scale turbulence, is numerically quite costly, as it involves computations of larger and larger systems along y as $k_{y,min}$ is decreased. For DIII-D for example, with $\rho^* \simeq 1/300$, for a full flux-surface located at mid-radius of the plasma ($r_0/a = 0.5$), for $q_0 = 1.4$ considered here, the value of $k_{y,min} \rho_i = (q_0 a / r_0) \rho^* \simeq 1.4 \cdot 10^{-2}$ is approximately equal to the value $k_{y,min} \rho_i = 0.0175$ considered in our scan. Large machines such as JET ($\rho^* \simeq 1/600$) and ITER ($\rho^* \simeq 1/1000$) has corresponding values of $k_{y,min} \rho_i \simeq 4.7 \cdot 10^{-3}$ and $2.8 \cdot 10^{-3}$ respectively.

Therefore in practice, if the simulation results (including heat and particle fluxes, shearing rate associated with zonal flows, radial correlation length of turbulent eddies etc.) are found to be converged for values of $k_{y,min} \rho_i$ larger than that corresponding to the machine one is interested in, then one obviously does not need to simulate the full physical flux-surface, as the system size effect of self-interaction has also saturated. However, if no such convergence is observed as $k_{y,min} \rho_i$ approaches the physical value corresponding to the machine, then one should use that physical $k_{y,min} \rho_i$ and correctly account for the effect of self-interaction [Ball et al., 2020].

Note that, with this approach of using flux-tube simulations to physically resolve

Chapter 3. How eigenmode self-interaction affects zonal flows and convergence of turbulence levels with toroidal system size

the particular finite system size effect resulting from the self-interaction mechanism, the other finite ρ^* effects, such as profile shearing [Waltz et al., 1998, Waltz et al., 2002], effect of finite radial extent of the unstable region [McMillan et al., 2010] etc., are missing. Therefore, if one wants to study how self-interaction competes with other finite ρ^* effects, either *global* simulations should be used, or local simulations that treat these other finite ρ^* effects explicitly such as [Candy et al., 2020]. Note that even in global simulations, the full flux-surface will have to be modelled to accurately account for self-interaction, in the sense that a simulation volume covering only a toroidal wedge, corresponding to considering $n_{\min} > 1$, is in general insufficient.

2. As a second approach, one can deliberately remove the effects of self-interaction, as suggested by [Beer et al., 1995, Faber et al., 2018, Ball et al., 2020], by increasing the parallel length of the simulation volume along the magnetic field until convergence is observed. In practice, this is achieved by having the flux-tube undergo multiple poloidal turns before it connects back onto itself, *i.e.* by increasing $L_z = N_{pol} \cdot 2\pi$ with $N_{pol} > 1$, instead of $L_z = 2\pi$ usually considered. Given that self-interaction is a result of microinstability eigenmodes ‘biting their tails’ after one poloidal turn at corresponding MRSs, this approach weakens the self-interaction mechanism.

4 Effect of collisions and background shear flows on non-adiabatic passing electron dynamics

In this chapter, the study of non-adiabatic passing electrons dynamics is pursued further to include more reactor relevant conditions. In particular, the effects of collisions and background shear flows are studied in sections 4.1 and 4.2 respectively.

4.1 Effect of collisions on non-adiabatic passing electron dynamics

The temperatures and densities typical of tokamak cores lead to plasmas with very low collisionalities, with collision frequencies lower than that of typical frequencies of microinstabilities. Hence these plasmas are often approximated as collisionless and modelled without collisions in gyrokinetic simulations. However, it is important to model collisions properly for various reasons. For instance, collisions are necessary to smoothen the small-scale structures in velocity space, which have been observed in gyrokinetic simulations [Watanabe and Sugama, 2004, Tatsuno et al., 2009], and playing an important role in the energy transfer mechanism [Schekochihin et al., 2008]. In fact collisions provide the physical link between macroscopic plasma heating and microturbulence, through dissipation of small-scale structures in both position and velocity space, thereby enabling the system to reach the right statistical steady state [Krommes, 1999, Abel et al., 2008]. Collisions can affect the steady-state turbulence levels either by affecting the linear microinstability drive of turbulence or by affecting the saturation mechanism. An example of the former case is the collisional stabilisation of TEM microinstability, which in experiments has been shown to lead to the transition of TEM dominant turbulence to ITG dominant one with increasing collisionality [Ryter et al., 2005, Camenen et al., 2007]. And an example of collisions affecting turbulence saturation is the collisional damping

Chapter 4. Effect of collisions and background shear flows on non-adiabatic passing electron dynamics

of zonal flows which in turn can lead to larger heat and particle steady-state flux levels [Hinton and Rosenbluth, 1999].

In this section, the effect of collisions on ITG driven turbulence is studied using gyrokinetic simulations. In linear simulations with adiabatic electrons, collisions (*i.e.* ion-ion collisions) do not significantly alter ITG linear eigenmodes [Kauffmann et al., 2010, Vernay, 2013]. However this is not found to be true when non-adiabatic passing electron response is considered [Mikkelsen and Dorland, 2008]. This study is followed up by exploring the effects of collisions, in particular on the fine-structures associated to non-adiabatic passing electrons and the self-interaction mechanism discussed in chapter 3.

Using *linear* simulations, through a scan in collisionality, two preliminary results are obtained: One, growth rate of ITG eigenmode decreases with increasing collisionality in collisionality regimes typical of the core, and two, the radial width of fine-structure associated to non-adiabatic passing electron response broadens with increasing collisionality. While the first result has already been reported in reference [Mikkelsen and Dorland, 2008], its fundamental reason has not been illustrated in detail. Through a detailed velocity space analysis of the distribution function, in this chapter, it is shown that collisions lead to a more adiabatic-like response of electrons away from MRS, which in turn explains the decrease in growth rates with increasing collisionality. Furthermore it is shown that collisionality sets the characteristic parallel length scale associated to the ballooning envelope tail of eigenmodes, which in turn explains the radial broadening of the fine-structures.

In *turbulence* simulations, the eigenmodes can get deformed by the various nonlinear mechanisms [C.J.,Ajay et al., 2020]. Furthermore, as already mentioned, collisions can affect the nonlinear turbulence saturation mechanism through damping of zonal flows. Of particular interest to this work is investigating how collisions affect the nonlinear drive of zonal flows via the self-interaction mechanism. Therefore it is important to study the effects of collisions in nonlinear simulations as well. In this chapter, it is found that the steady-state heat flux decreases with increasing collisionality which is then illustrated to be the consequence of the corresponding decrease in the growth rate of linear eigenmodes. The width of the fine-structures in nonlinear simulations is not found to show an increase with increasing collisionality. This is because of the nonlinear broadening of these fine structures, discussed in section 3.4.5. Motivated by the finding in the linear simulations study, that the parallel length scale of eigenmodes associated to their ballooning representation tails are determined by collisionality, the effect of collisions on the parallel correlation length of turbulent eddies is explored. No obvious dependence of parallel correlation length on collisionality is found, possibly again due to nonlinear effects. Finally the effect of collisions on the self-interaction mechanism is studied using some of the diagnostics already presented in chapter 3, more specifically, by computing the normalised self-interaction contribution to Reynolds stress, the bicoherence estimate and the correlation between the various k_y contributions to Reynolds stress.

4.1. Effect of collisions on non-adiabatic passing electron dynamics

These studies are organised in this section as follows. In section 4.1.1, the linear simulation study is presented, in two parts: in section 4.1.1.1, the analysis on the dependence of growth rate on collisionality is discussed, and in section 4.1.1.2 the analysis on the increase in the radial width of fine-structures with collisionality is discussed. The results on the effect of collisions in nonlinear simulations is presented in four subsections which are as follows. The effect of collisions on the heat flux and the shearing rate associated to zonal flows is discussed in section 4.1.2.1, followed by its effect on the radial width of fine-structures in section 4.1.2.2. In section 4.1.2.3, the effect of collisions on the parallel correlation length of turbulent eddies is shown, and in section 4.1.2.4, the effect of collisions on the self-interaction mechanism is studied using the diagnostic methods already mentioned in the previous paragraph. The conclusions are presented in section 4.1.3.

Furthermore, in appendix C, an analysis based on a local dispersion relation is presented, studying the effects of collisions. This study extends the analysis presented in reference [Dominski et al., 2015] to include the effects of collisions, using a BGK-like collision operator [Bhatnagar et al., 1954, Angus and Krasheninnikov, 2012].

4.1.1 Effect of collisions in linear simulations

In this subsection, the effects of collisions on ITG eigenmodes with kinetic electrons are explored by analysing linear simulation results with different collisionalities. The parameters of simulations performed here are given in table 4.1. The physical and geometric parameters remain the same as in the case considered in chapter 3, with the exceptions of a larger logarithmic ion temperature gradient ($R/L_{T,i} = 8$) and an electron-ion mass ratio ($m_e/m_i = 1/1836$) corresponding to hydrogen. With $R/L_{T,i} = 6$ (considered in chapter 3), corresponding nonlinear simulation with adiabatic electrons is found to be very close to marginal stability and tends to show very long intermittency intervals. Hence, a steeper logarithmic temperature gradient of $R/L_{T,i} = 8$ is chosen for both linear and nonlinear runs. However, note that the results discussed in the following qualitatively remain the same for both cases, near and far from marginal stability. The numerical resolutions N_z , $N_{v_{\parallel}}$ and N_{μ} along the coordinates z , v_{\parallel} and μ respectively have been chosen after performing convergence scans on these parameters.

Collisions are modelled with the Landau collision operator, and a scan in collisionality is carried out over the range $0 \leq \nu_e^* \leq 2.758$. Note that the background densities n_0 and temperatures T_0 typical of tokamak cores lead to collisionalities ($\nu^* \propto n_0/T_0^2$) that fall within the banana regime characterised by $\nu^* < 1$, while those at the plasma edge can extend towards the plateau regime characterised by $1 < \nu^* < \epsilon^{-3/2}$ [Hinton and Hazeltine, 1976]. The FLR corrections to the collision operator appearing as spatial diffusion terms in gyrocenter coordinates [Abel et al., 2008] (as already mentioned in section 2.4.1) are absent in the standard 'Landau' collision operator available in GENE,

Chapter 4. Effect of collisions and background shear flows on non-adiabatic passing electron dynamics

Geometry: Ad-hoc concentric circular geometry [Lapillonne et al., 2009]

$\epsilon = 0.18$	$q_0 = 1.4$	$\hat{s} = 0.8$	$\beta = 0.001$	
$m_i/m_e = 1836$	$T_e/T_i = 1.0$	$R/L_N = 2.0$	$R/L_{T_i} = 8.0$	$R/L_{T_e} = 2.0$
$L_x = 142.9 \rho_i$	$L_y = 17.95 \rho_i$ (179.5 ρ_i)	$L_z = 2\pi$	$v_{\parallel, \max} = 3\sqrt{2} v_{th,i}$	$\mu_{\max} = 9 T_{0i}/B_{0, \text{axis}}$
$M = 1$ (4)	$N_{k_x} \times N_{k_y}^* \times N_z \times N_{v_{\parallel}} \times N_{\mu} = 96$ (256) $\times 1$ (64) $\times 24 \times 48 \times 16$			$k_{y, \min} \rho_i = 0.35$ (0.035)

Table 4.1: Parameter set for linear simulations. In parenthesis, parameters for non-linear simulations are given if they differ from those in the linear case.

which has been used in the simulations shown in this chapter. However, in the most recent version of GENE, the option to account for the FLR correction terms has been implemented. Using this option, it has been verified that the FLR terms in the collision operator leads to an insignificant change in the results shown for the linear simulations in this section, for the considered range of collisionality.

4.1.1.1 Decrease in growth rate with increasing collisionality. Adiabatic like electron response away from MRS.

In the collisionless case, non-adiabatic electron dynamics is known to strengthen the ITG instability drive [Rewoldt and Tang, 1990, Mikkelsen and Dorland, 2008, Dominski et al., 2015]. With the introduction of collisions, the instability drive is found to weaken. In figure 4.1, the growth rate of ITG microinstability with kinetic electrons and $k_y \rho_i = 0.35$ (most unstable) is shown to decrease with increasing collisionality for $\nu_e^* < 1$, and approaching the growth rate of the modes with adiabatic electrons for $\nu_e^* \sim 1$. The growth rate of the eigenmode with adiabatic electrons, by itself, presents a weak increase as collisionality is increased. In this subsection, a velocity space analysis of the electron distribution function is done to explain the weakening of the non-adiabatic electron instability drive with collisions. In appendix C (see figure C.6), the local dispersion relation based analysis is found to lead to a decrease in the growth rate of ITG eigenmodes with increasing collisionality. However these results do not match quantitatively with the results obtained with linear GENE simulations.

In figure 4.2, the real value of the perturbed electron distribution function $f_{1,e}$ at the outboard midplane ($z = 0$) for radial locations at ($x = 0$) and away ($x = -L_x/2$) from MRS is plotted as a function of (v_{\parallel}, μ) for three cases, with collisionalities $\nu_e^* = 0, 0.276$ and 2.758 . v_{\parallel} in these plots is normalised by $v_{T,e} = \sqrt{2T_{0,e}/m_e}$ (not to be confused with $v_{th,e} = \sqrt{T_{0,e}/m_e}$). Magenta circles in the plots represent the boundary between the trapped and passing electron velocity space domains, defined by the relation $v_{\parallel}^2 = (2/m_e)[B_0(z = -\pi) - B_0(z = 0)]\mu$. Recollect from section 2.6.2, that in the flux-tube model, B_0 represents the equilibrium magnetic field strength on the flux-surface considered, and is independent of the radial coordinate x . Furthermore, $z = -\pi$ and $z = 0$ denote the inboard midplane and outboard midplane where the magnetic field strength

4.1. Effect of collisions on non-adiabatic passing electron dynamics

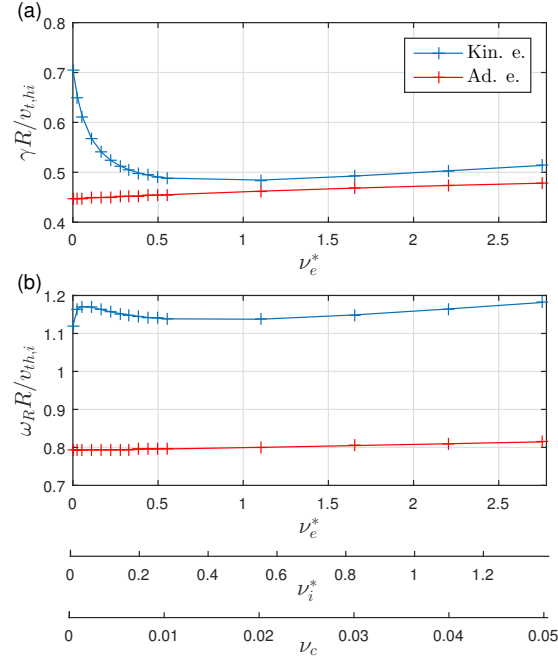


Figure 4.1: (a) Growth rate γ and (b) real frequency ω_R , both in units of $v_{th,i}/R$, of ITG eigenmodes obtained for $k_y \rho_i = 0.35$, plotted as a function of effective electron collisionality ν_e^* in linear simulations with either adiabatic (red) or kinetic (blue) electrons. Other simulation parameters are given in table 4.1. Axes with corresponding ion collisionality ν_i^* and GENE collisionality ν_c are also shown for comparison.

Chapter 4. Effect of collisions and background shear flows on non-adiabatic passing electron dynamics

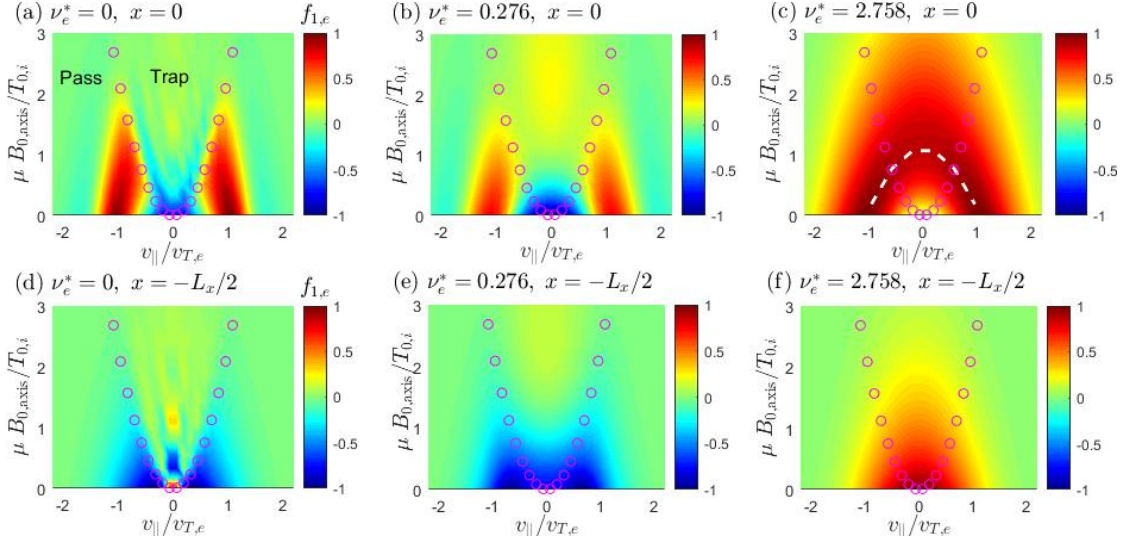


Figure 4.2: $(v_{||}, \mu)$ velocity space colour plot of the real value of the perturbed electron distribution function $f_{1,e}$ of the eigenmodes in linear simulations with three different collisionalities $\nu_e^* = 0, 0.276$ and 2.758 (from left to right). The distribution function at the outboard mid-plane $z = 0$ is plotted for all the subfigures, with those at the top corresponding to radial location $x = 0$, *i.e.* at the corresponding MRS, and those at the bottom corresponding to $x = -L_x/2$, *i.e.* mid-point between MRSs. Magenta circles indicate the boundary between trapped and passing regions. White dashed line indicate the constant energy curve $m_e v_{||}^2 + B_0 \mu = \text{const}$.

is maximum and minimum respectively, in the considered circular ad-hoc equilibrium.

In the collisionless case, using local dispersion relation, trapped electron response can be shown to have little effect on the growth rate of ITG eigenmodes, and hence the trapped electron response is considered to be passive [Dominski et al., 2015]. This is illustrated in appendix C as well, in particular in figure C.4 where it is shown that the simplified slab like passing electron kinetic response *SimPassKinE* result closely matches that including kinetic trapped electron response *SimPassKinE + TrapKinE*. In figure 4.2(a,d), while there is a non-negligible contribution to the electron distribution function in the trapped region, much of the contribution is indeed localised in the passing electron velocity space, verifying that the passive response of trapped electrons in the collisionless case is partly true. One may also note here that, in linear simulations, in absence of collisions, passing and trapped electrons do not mix with each other. With collisions, *i.e.* in figures 4.2(b,c,e,f), the contribution to the electron distribution function in the trapped region can be found to increase. This is a result of the collisional trapping-detraping of electrons.

At MRS, in the collisionless case, *i.e.* in figure 4.2(a), one can observe large relative amplitude of the perturbed electron distribution function at $v_{||} \simeq \pm v_{T,e}$ in the passing electron domain of the velocity space. These structures are in fact characteristic of the

4.1. Effect of collisions on non-adiabatic passing electron dynamics

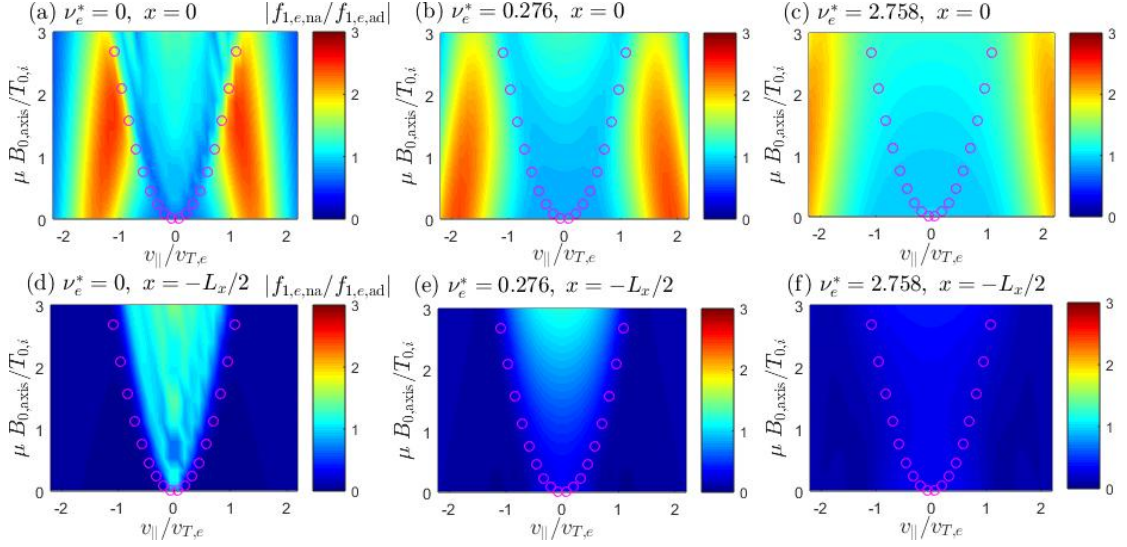


Figure 4.3: $(v_{||}, \mu)$ velocity space contour plot of the non-adiabatic part of the perturbed electron distribution function $f_{1,e,na} = f_{1,e} - f_{1,e,ad}$ normalised by the adiabatic part $f_{1,e,ad}$, in absolute value, *i.e.* $|f_{1,e,na}/f_{1,e,ad}|$, of the eigenmodes in linear simulations presented in figures 4.5 and 4.2. Cases with three different collisionalities $\nu_e^* = 0, 0.276$ and 2.758 are shown, from left to right. The outboard mid-plane $z = 0$ slice is plotted for all the subfigures, with those at the top corresponding to radial location $x = 0$, *i.e.* at the corresponding MRS, and those at the bottom corresponding to $x = -L_x/2$, *i.e.* mid-point between MRSs. Magenta circles indicate the boundary between trapped and passing regions.

non-adiabatic passing electron dynamics, as evident from the corresponding dominant structures in figure 4.3(a), where the non-adiabatic part of the perturbed electron distribution function $f_{1,e,na} = f - f_{1,e,ad}$ normalised by the adiabatic part $f_{1,e,ad} = e\Phi f_{0,e}/T_0$ is plotted. Recollect that $f_{0,e}$ is the local Maxwellian already defined in equation (2.55). With collisions, the passing electrons get trapped and vice-versa, leading to a 'smearing' of these structures associated to non-adiabatic passing electrons in figure 4.2(a) into the trapped electron domain of the velocity space as seen more so in figure 4.2(c). In fact in figure 4.2(c), one could clearly observe that the 'smeared' velocity space distribution of the electron distribution function follows the constant energy curve ($m_e v_{||}^2 + B_0 \mu = \text{const.}$, denoted by the dashed white line), indicating that electron-ion pitch angle-scattering is the dominant collision mechanism at play.

Away from MRS, in the collisionless case, passing electrons behave adiabatically, as evident in figure 4.3(d). As collisionality increases, the collisional trapping-detrapping of electrons becomes more frequent and as one moves away from the banana regime there is less distinction between trapped and passing electrons. The trapped electrons as well therefore begin to respond adiabatically as can be seen in figure 4.3(e,f). The more adiabatic-like electron response away from MRS with increasing collisionality is also evident in figure 4.4 which plots the $v_{||}$ and μ profiles of the perturbed electron distribution

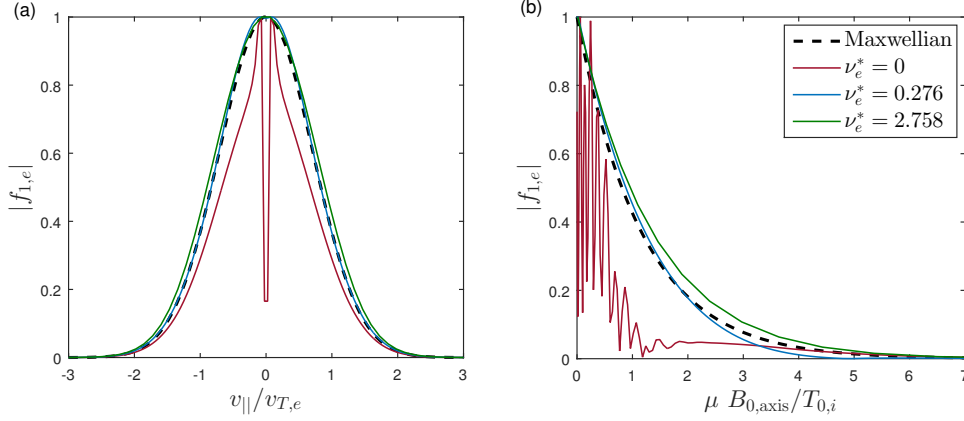


Figure 4.4: Velocity space profiles of the real value of the perturbed electron distribution function $f_{1,e}$, normalised by its max value, of the eigenmodes in the same set of linear simulations presented in figure 4.2, with collisionality $\nu_e^* = 0$ (brown), 0.278 (blue) and 2.758 (green). In (a), the $v_{||}$ profile is shown at $\mu = 0$ and in (b), the μ velocity profile is shown at $v_{||} = 0$, both at the outboard midplane $z = 0$ and at the radial position $x = -L_x/2$ away from MRS. Dashed black line represent the normalised Maxwellian distribution.

function $f_{1,e}$ normalised by its maximum value, at $\mu = 0$ and $v_{||} = 0$ respectively, at $x = -L_x/2$, at the outboard midplane. That is, with collisions, the distribution function becomes proportional to a Maxwellian, characteristic of adiabatic electron response. This is observed to a lesser extent at MRS as well. Naturally with increasing collisionality, as a greater fraction of electrons behave adiabatic-like, the growth rate decreases and approaches that for the fully adiabatic electron model.

4.1.1.2 Increase in radial width of fine structures with increasing collisionality

With non-adiabatic passing electron dynamics, ITG (and TEM) linear eigenmodes can become significantly extended along the magnetic field lines [Hallatschek and Dorland, 2005], producing fine radial structures at corresponding MRSs [Waltz et al., 2006, Chowdhury et al., 2008, Dominski et al., 2015, Dominski et al., 2017, C.J., Ajay et al., 2020]. Collisions are found to increase the radial width of these fine-structures. This is evident in figure 4.5(a-c) which shows the (x, z) dependence of the absolute value of the electrostatic potential $|\Phi|$ for the same eigenmodes considered in figures 4.2, with different collisionalities. The corresponding z -averaged electrostatic potential subtracted by its minimum value, *i.e.* $\langle |\Phi| \rangle_z - \min[\langle |\Phi| \rangle_z]$ is also plotted as a function of x in figures 4.5(d-f). To quantify the radial broadening of the fine-structures, the full width at half maximum FWHM of $\langle |\Phi| \rangle_z$ is plotted as a function of collisionality in figure 4.6. In appendix C (see figure C.7), the local dispersion relation based analysis shows an increase

4.1. Effect of collisions on non-adiabatic passing electron dynamics

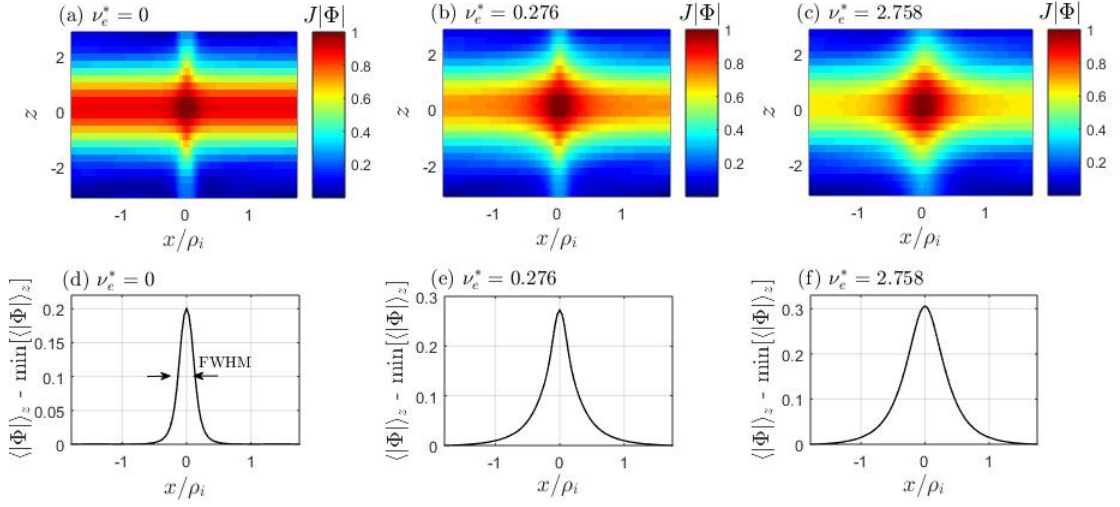


Figure 4.5: Top: (x, z) colour plot of the absolute value of the electrostatic potential, (normalised by its maximum value and) weighted by the Jacobian, *i.e.* $J|\Phi|$, for the eigenmodes in the same set of linear simulations in figure 4.2, with collisionalities (a) $\nu_e^* = 0$, (b) $\nu_e^* = 0.276$ and (c) $\nu_e^* = 2.758$. Bottom: The corresponding z -average of the absolute value of the electrostatic potential, subtracted by its minimum value, *i.e.* $\langle |\Phi| \rangle_z - \min[\langle |\Phi| \rangle_z]$, plotted as a function of x .

in the radial width of fine-structures at the MRS of corresponding ITG eigenmodes, with increasing collisionality. However these results do not match quantitatively with the results obtained with linear GENE simulations. In the following, this radial broadening of fine-structures is explained as the consequence of a decrease in the characteristic parallel length associated to the tail of ballooning representation of the eigenmodes with increasing collisionality.

In the ballooning representation, the radial Fourier (k_x) and the parallel (z) dependence of the linear mode profile is mapped to a purely parallel (extended ballooning space χ) dependence. See section 2.6.2 for a detailed review of the ballooning space representation. In figure 4.7(a), the ballooning representation of the electrostatic potential $|\hat{\Phi}_b|$ is plotted as a function of the extended ballooning space angle χ , for ITG eigenmodes with different collisionalities. It can be seen that, the tail of each of these ballooning structures presents essentially an exponential decay. A fit of the form $\mathcal{A}e^{-\chi/\Delta\chi}$ is therefore made, as indicated by the thicker lines in figure 4.7(a); \mathcal{A} is a constant and $\Delta\chi$ measures a characteristic parallel 'angular' extension of the mode in the extended ballooning space χ . The angular width $\Delta\chi$ can be related to a characteristic length scale $\lambda_{||}$, in the considered circular ad-hoc geometry, by the relation $\lambda_{||} = Rq_0\Delta\chi$. In figure 4.7(b), the characteristic parallel length $\lambda_{||}$ is shown to scale linearly with the electron-ion mean free path $\lambda_{\text{mfp}}^{e/i} = v_{th,e}/\nu_{ei}$, where ν_{ei} is the electron-ion collision frequency [relation between ν_{ei} and ν_e^* can be obtained from equations (2.100) and (2.101)]. That is, the electron-ion

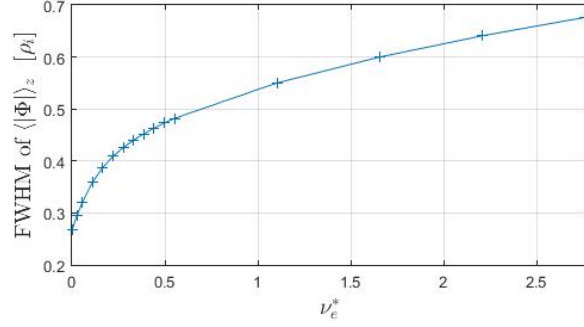


Figure 4.6: Full radial width at half maximum FWHM of the z-averaged electrostatic potential $\langle |\Phi| \rangle_z$ of the eigenmodes for the same set of linear simulations with kinetic electrons presented in figure 4.1.

mean free path $\lambda_{\text{mfp}}^{e/i}$ (or collisionality $\nu_e^* \propto 1/\lambda_{\text{mfp}}^{e/i}$) sets the characteristic parallel length λ_{\parallel} of the eigenmodes.

To summarize, increasing collisionality leads to an increasing exponential decay rate $1/\Delta\chi$ ($\propto 1/\lambda_{\parallel}$) of the tail of the ballooning envelope. Given that a narrower tail, *i.e.* with larger decay rate, is associated to broader radial fine-structures, one can therefore see how collisions lead to broadening of the fine-structures in real space.

4.1.2 Effect of collisions in nonlinear simulations

In this subsection, the effects of collisions in nonlinear turbulence ITG simulations are studied, in particular on the fine-structures associated to non-adiabatic passing electrons and the self-interaction mechanism which are the primary interests of this work. Towards this goal, a scan in collisionality $\nu_e^* \in \{0, 0.028, 0.276, 2.758\}$ is performed, with the physical parameters as given in table 4.1, modelling the same ITG dominant turbulent regime as considered for the linear study. In this table, numerical parameters wherever different from that in linear simulations have been given within parenthesis. The results are presented in the following four subsections.

4.1.2.1 Effect of collisions on heat flux

In this subsection, the dependence of ion heat flux on collisionality, in nonlinear simulations with kinetic and adiabatic electron response, is discussed.

In simulations with *kinetic* electrons, the gyro-Bohm normalised ion heat flux is found to decrease with increasing collisionality, as shown in figure 4.8. In reference [Mikkelsen and Dorland, 2008], this drop in heat flux with collisionality is attributed to the corresponding reduction in the linear growth rates (discussed in section 4.1.1.1, see figure 4.1). In the

4.1. Effect of collisions on non-adiabatic passing electron dynamics

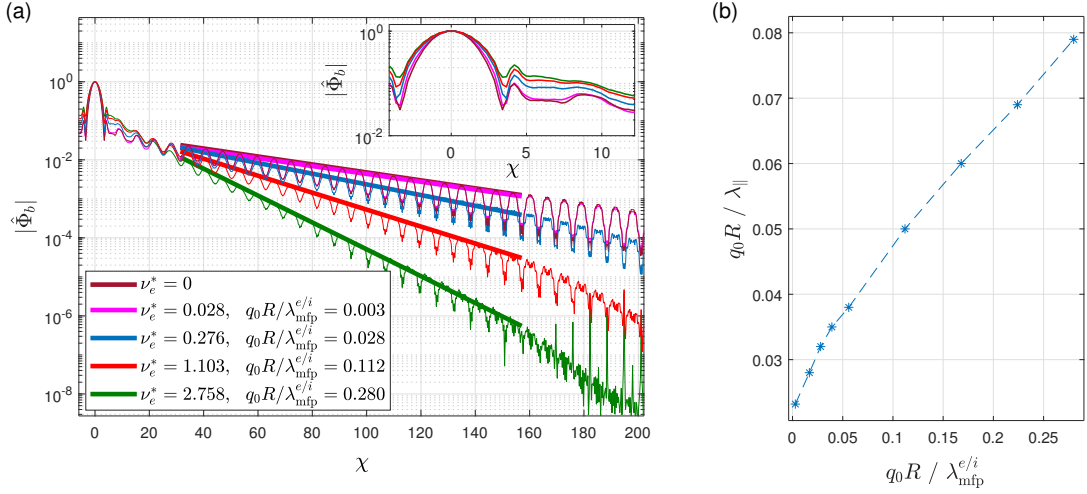


Figure 4.7: (a) Ballooning envelope $|\hat{\Phi}_b(\chi)|$ of the electrostatic potential Φ for the linear eigenmodes considered in figure 4.1, with collisionality $\nu_e^* = 0$ (brown), 0.028 (magenta), 0.276 (blue), 1.103 (red) and 2.758 (green). Thick lines indicate the respective best fits of the form $\mathcal{A}e^{-\chi/\Delta\chi}$. Zoom near $\chi = 0$ is shown in the subset. (b) Inverse of characteristic parallel scale length $\lambda_{||} = R q_0 \Delta\chi$ plotted as a function of the inverse of electron-ion mean free path $\lambda_{mfp,e}$, both normalised by $1/q_0 R$.

following, this statement is further justified by an analysis on the shearing rate associated to $E \times B$ zonal flows and a quasi-linear estimate on flux levels.

Shearing of turbulent eddies by zonal flows is a primary mechanism by which ITG driven turbulence saturates [Biglari et al., 1990, Rosenbluth and Hinton, 1998, Lin et al., 1998, Waltz et al., 1994]. The shearing rate associated to zonal flows for the considered nonlinear simulation scan on collisionality, is shown in figures 4.9(a-c). Following the analysis in section 3.3, three different estimates of the effective shearing rate ω_{eff} (defined in Eq 3.2) have been defined: (a) time and system average of total shearing rate $\text{RMS}_{x,t}(\omega_{\text{eff}}) = (\langle \omega_{\text{eff}}^2 \rangle_{x,t})^{1/2}$, (b) contribution from the stationary components, $\text{RMS}_x(\langle \omega_{\text{eff}} \rangle_t) = [\langle (\langle \omega_{\text{eff}} \rangle_t)^2 \rangle_x]^{1/2}$ and (c) contribution from fluctuating components $\text{SD}_{x,t}(\omega_{\text{eff}}) = [\langle (\omega_{\text{eff}} - \langle \omega_{\text{eff}} \rangle_t)^2 \rangle_{x,t}]^{1/2}$, all normalised by their corresponding maximum linear growth rates. One can also recollect the relation (3.6) between the three estimates. The plot of the shearing rate contribution from stationary structures for the case with kinetic electrons in figure 4.9(b) shows an increase of 19% as collisionality increase from $\nu_e^* = 0$ to 0.276, which then drops to an increase of only 13% between $\nu_e^* = 0$ and 2.758. The corresponding ion heat flux plot in figure 4.8, on the other hand shows a monotonic decrease over the full considered range of collisionality from $\nu_e^* = 0$ to 2.758. The fluctuating zonal flows, which also play an important role in the saturation mechanism (see the discussion on figure 3.8 in section 3.3), is found to show a negligible maximum change of only 6% in figure 4.9(c). The total shearing rate estimate in figure 4.9(a) also shows only a 5% maximum change over the considered range of collisionalities. These

Chapter 4. Effect of collisions and background shear flows on non-adiabatic passing electron dynamics

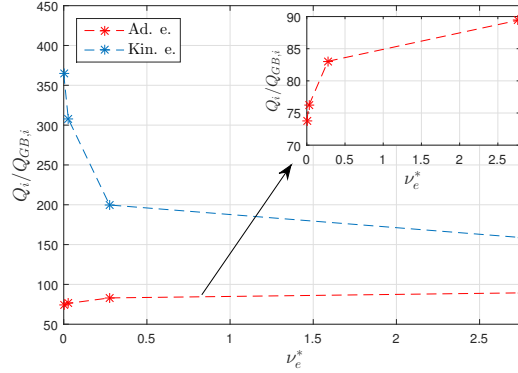


Figure 4.8: Time-averaged gyro-Bohm normalised ion heat flux $Q_i/Q_{GB,i}$ as a function of collisionality ν_e^* in simulations with kinetic (blue asterisks) and adiabatic (red asterisks) electrons.

results suggest that turbulence saturation via zonal flows is less likely to be the primary factor determining the steady state flux levels. The decrease in linear drive of turbulence with increasing collisionality is therefore more likely to be the reason for the observed decrease in turbulent fluxes.

To further verify that the decrease in linear growth rates with collisionality is indeed the primary cause for the decrease in nonlinear heat and particle fluxes in kinetic electron simulations, a rough quasi-linear estimate of the relative change in flux levels is performed. Following the quasi-linear model in [Fable et al., 2009, Lapillonne et al., 2011], one has the quasi-linear ion heat flux $Q_{QL,k_\perp} \simeq \mathcal{A}(\gamma/k_\perp)^\xi$ for each perpendicular wavenumber k_\perp ; \mathcal{A} is a constant, γ is the linear growth rate and $\xi = 2$ is a fitted parameter found from comparisons with nonlinear fluxes (Note that, in various other quasi-linear estimates [Jenko et al., 2005, Casati et al., 2009, Mariani et al., 2018], ξ typically ranges between 1 and 3. The following conclusions however still hold for $\xi \neq 2$). In the simplified estimate performed here, one only considers that $k_\perp \rho_i \sim k_y \rho_i \simeq 0.35$ where the growth rate $\gamma = \gamma_{\max}$, corresponding to the most unstable eigenmode, is observed (other choices of k_y and γ can be made for better quasi-linear estimates [Jenko et al., 2005, Casati et al., 2009]). Furthermore, one assumes that \mathcal{A} remains the same for different collisionalities. In our turbulence simulations, one finds that the relative decrease in ion heat flux from $\nu_e^* = 0$ to 0.276, *i.e.* $[Q_i(\nu_e^* = 0.276) - Q_i(\nu_e^* = 0)]/Q_i(\nu_e^* = 0) = -0.45$ is approximately the same as the corresponding decrease in the simplified quasi-linear estimate $[\gamma_{\max}^2(\nu_e^* = 0.276) - \gamma_{\max}^2(\nu_e^* = 0)]/\gamma_{\max}^2(\nu_e^* = 0) = -0.47$. One can therefore attribute the decrease in flux levels with increasing collisionality as a direct consequence of the decrease in linear growth rates.

In simulations with *adiabatic* electrons, ion heat flux increases with increasing collisionality as shown in figure 4.8. In this case, the relative increase in ion heat flux $[Q_i(\nu_e^* =$

4.1. Effect of collisions on non-adiabatic passing electron dynamics

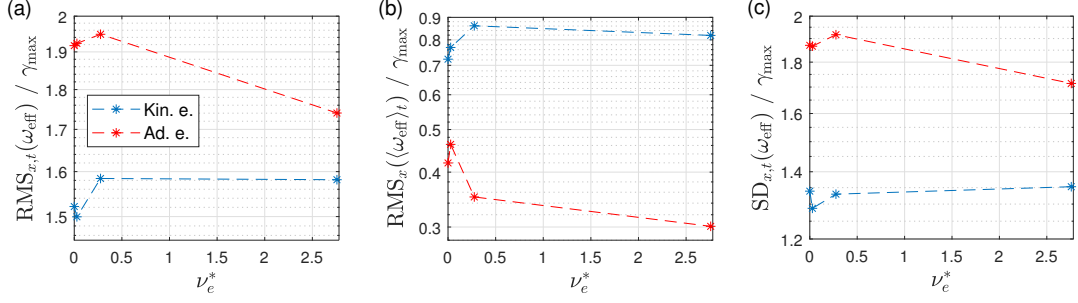


Figure 4.9: Effective shearing rate ω_{eff} associated to the zonal $E \times B$ flows, normalised to corresponding maximum linear growth rate γ_{max} , as a function of collisionality ν_e^* . Blue asterisks denote kinetic electron simulations and red asterisks denote adiabatic electron simulations. (a) Time and system average of total shearing rate estimated with $\text{RMS}_{x,t}(\omega_{\text{eff}}) = (\langle \omega_{\text{eff}}^2 \rangle_{x,t})^{1/2}$. (b) Contribution from the stationary component, $\text{RMS}_x(\langle \omega_{\text{eff}} \rangle_t) = [\langle (\langle \omega_{\text{eff}} \rangle_t)^2 \rangle_x]^{1/2}$. (c) Contribution from fluctuation component, $\text{SD}_{x,t}(\omega_{\text{eff}}) = [\langle (\omega_{\text{eff}} - \langle \omega_{\text{eff}} \rangle_t)^2 \rangle_{x,t}]^{1/2}$.

$0.276) - Q_i(\nu_e^* = 0)]/Q_i(\nu_e^* = 0) = 0.13$ is an order of magnitude higher than the corresponding increase in the quasi-linear estimate $[\gamma_{\text{max}}^2(\nu_e^* = 0.276) - \gamma_{\text{max}}^2(\nu_e^* = 0)]/\gamma_{\text{max}}^2(\nu_e^* = 0) = 0.02$. That is, the increase in the linear instability drive alone cannot account for the increase in ion heat flux in nonlinear simulations. In fact, such an increase in flux levels in nonlinear adiabatic electron simulations is attributed to an increased zonal flow damping by collisions [Hinton and Rosenbluth, 1999, Lin et al., 2000]. However, surprisingly, this expected monotonic decrease in zonal flow levels with increasing collisionality is not reflected clearly in any of the shearing rate estimates of ω_{eff} shown in figure 4.9. While the shearing rate estimates at $\nu_e^* = 2.758$ in figures 4.9(a and c) is approximately 10% smaller than that at $\nu_e^* = 0$, the intermediate values of collisionality have shearing rate values larger than that at $\nu_e^* = 0$. Given that stationary fine-structures are absent in adiabatic electron simulations, the non-zero shearing rates associated to the stationary zonal flows seen in figure 4.9(b) are essentially the result of statistical fluctuations, and will approach zero if the simulations are run for longer times.

4.1.2.2 Effect of collisions on radial width of fine-structures

The increase in the radial width of fine-structures on linear kinetic electron ITG microinstability eigenmodes with increasing collisionality have already been discussed in section 4.1.1.2. In this subsection, the effect of collisionality on the width of these structures in the turbulent steady state of nonlinear simulations is explored.

A broader tail of the ballooning representation of an eigenmode reflects a radially narrower fine structure in real space. It is therefore also possible to study the effect of collisionality on the width of fine-structures associated to an eigenmode in nonlinear simulation by

Chapter 4. Effect of collisions and background shear flows on non-adiabatic passing electron dynamics

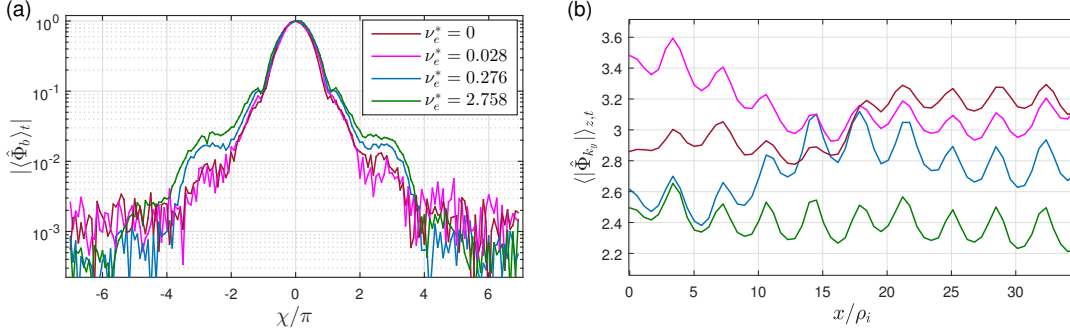


Figure 4.10: (a) Absolute value of the time-averaged ballooning structure of the electrostatic potential normalised by its value at $\chi = 0$, *i.e.* $|\langle \hat{\Phi}_b(\chi, t) / \hat{\Phi}_b(\chi_0 = 0, t) \rangle_t|$, for $k_{x0} = 0$ and $k_y \rho_i = 0.35$ in turbulence simulations with collisionalities $\nu_e^* = 0$ (brown), 0.028 (magenta), 0.276 (blue) and 2.758 (green). (b) Time and z averaged electrostatic potential $\langle |\hat{\Phi}_{k_y}| \rangle_{z,t}$ plotted as a function of the radial coordinate x , for the same set of simulations in sub-plot (a), and with the same colour labels.

comparing its ballooning representations across simulations with different collisionalities. In fact, this analysis is analogous to the study on the nonlinear broadening of eigenmodes, discussed in section 3.4.5. In figure 4.10(a), the absolute value of the time-averaged ballooning representation of the electrostatic potential for $k_{x0} = 0$ and $k_y \rho_i = 0.35$ (same as in figure 4.7), normalised by its value at $\chi = 0$, *i.e.* $|\langle \hat{\Phi}_b(\chi, t) / \hat{\Phi}_b(\chi_0 = 0, t) \rangle_t|$, is plotted for the four different values of collisionalities considered. Contrary to the linear result, a narrowing of the ballooning tails, corresponding to a radial broadening in real space, is not observed with increasing collisionality. In fact a slight decrease in the radial width is observed. This mismatch is a consequence of the linear coupling between $k_x = k_{x0} + p2\pi\hat{s}k_y, p \in \mathbb{Z}$, in an eigenmode being significantly disrupted and dominated by nonlinear couplings in a turbulent system for $|p| \geq 2$.

To understand this further, one can study how good the linear phase difference along the ballooning structure of an eigenmode is retained in a nonlinear simulation. Such an analysis had already been done in section 3.4.5, in particular in figure 3.13, where the quantity $\Delta\phi(\chi, t) = \delta\phi_{\text{nl}}(\chi, t) - \delta\phi_{\text{lin}}(\chi)$ measuring the deviation of the relative phase, at the extended ballooning space coordinate χ , between the nonlinear and linear simulations [see section 3.4.5 for the definition of $\delta\phi_{\text{nl}}(\chi, t)$ and $\delta\phi_{\text{lin}}(\chi)$], was plotted as a function of time for $\chi = 2\pi$ and 4π . In figure 4.11(a), similar plots are made for the eigenmode with $k_{x0} = 0$ and $k_y \rho_i = 0.35$ in two nonlinear simulations corresponding to the two extreme values of collisionalities considered here, *i.e.* $\nu_e^* = 0$ and $\nu_e^* = 2.758$. In this figure, one can observe that the relative phase along the ballooning structure remains nearer to its linear value in the case with $\nu_e^* = 2.758$ (as indicated by the corresponding plots more closely adhering to one of the horizontal dashed lines representing phase differences that are multiples of 2π), than in the case with no collisions. To quantitatively measure the extend to which the linear phase difference along the ballooning structure is retained

4.1. Effect of collisions on non-adiabatic passing electron dynamics

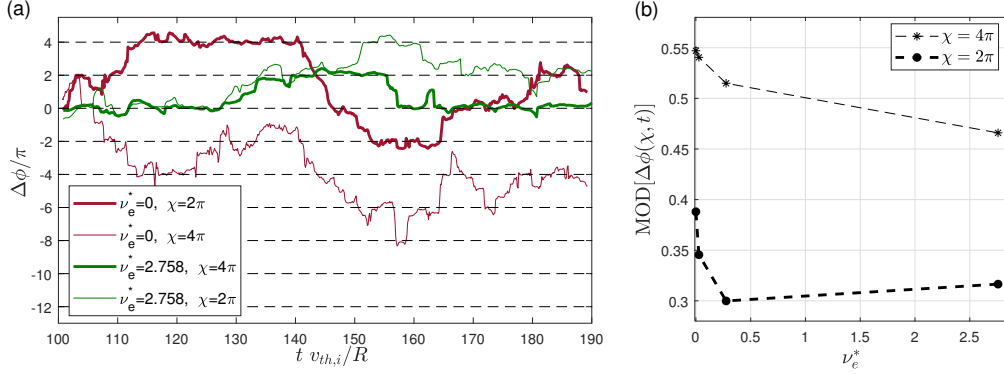


Figure 4.11: Phase difference $\Delta\phi(\chi, t) = (\phi[(\hat{\Phi}_{b,\text{nl}}(\chi, t)/\hat{\Phi}_{b,\text{nl}}(\chi_0 = 0, t))(\hat{\Phi}_{b,\text{lin}}(\chi_0 = 0)/\hat{\Phi}_{b,\text{lin}}(\chi))])$ plotted as a function of time. Here, $\hat{\Phi}_{b,\text{nl}}$ and $\hat{\Phi}_{b,\text{lin}}$ denote the ballooning representation of the electrostatic potential in non-linear and linear simulations respectively, for the eigenmode with $k_{x,0} = 0$ and $k_{y,\rho_i} = 0.35$. Brown and green colours represent simulations with collisionality $\nu_e^* = 0$ and 2.758 respectively, while thick and thin lines represent $\chi = 2\pi$ and 4π respectively. (b) $\text{MOD}(\Delta\phi(\chi, t))$ plotted as a function of collisionality ν_e^* . Thick and thin lines represent $\chi = 2\pi$ and 4π respectively.

in nonlinear simulations, one can use the quantity $\text{MOD}(\Delta\phi(\chi, t))$, defined in equation (3.16). To recall, smaller the value of $\text{MOD}(\Delta\phi(\chi, t))$, more strongly is the relative phase difference fixed by the linear couplings, and for uniform random values of $\Delta\Phi$ between $-\pi$ and π , one obtains $\text{MOD}(\Delta\phi(\chi, t)) = 0.58\pi$. In figure 4.11(b), $\text{MOD}(\Delta\phi(\chi, t))$ is plotted as a function of collisionality ν_e^* , for $\chi = 2\pi$ and 4π . From this figure, in general (with the exception of the $\nu_e^* = 2.758$ data point for the case with $\chi = 2\pi$), one could conclude that the linear relative phase difference along the ballooning structure of an eigenmode is more religiously maintained in turbulence simulations with larger collisionalities.

In figure 4.11(a and b) collisions have been shown to affect the nonlinear modification of the eigenmodes, in particular leading to a decrease in the width of the fine-structures with increasing collisionality. This can also be seen in figure 4.10(b), where the time and z averaged absolute value of the electrostatic potential $\langle |\hat{\Phi}_{k_y}| \rangle_{z,t}$ for $k_y \rho_i = 0.35$ [see equation (3.25) for the definition of $\hat{\Phi}_{k_y}$] is plotted as a function of x . Only a part of the radial domain is shown for better visualization. Each of the peaks is located at the radial positions of the corresponding MRSs. For the collisionless case, these fine-structures can be seen to be flatter, which then become more peaked as collisionality increases, indicating a (slight) narrowing of the fine-structures with collisions.

A slight decrease in the width of fine-structures with increasing collisionality can be further observed on the shearing rate associated to zonal flows, as seen in figure 4.12, where the effective shearing rate ω_{eff} is plotted as a function of the radial coordinate x for different collisionalities.

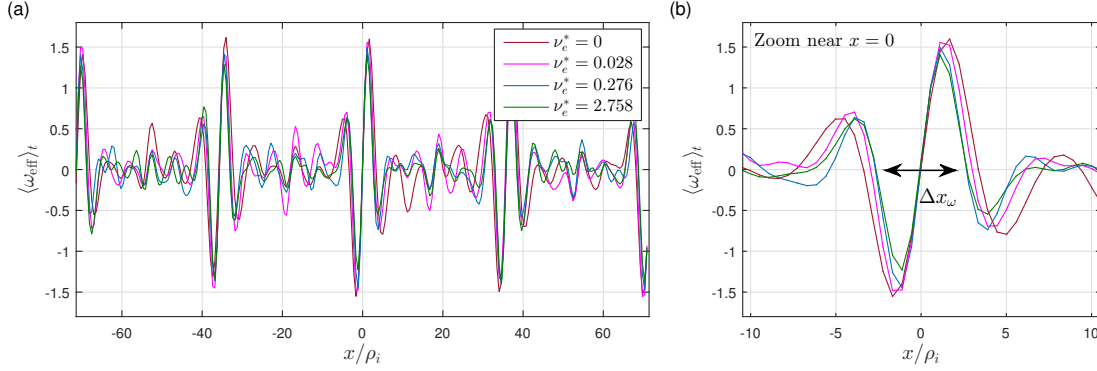


Figure 4.12: (a) Radial profile of the time-averaged effective shearing rate $\langle \omega_{\text{eff}} \rangle_t$ in simulations with collisionalities $\nu_e^* = 0$ (brown), 0.028 (magenta), 0.276 (blue) and 2.758 (green). (b) Zoom of the same plot near $x = 0$.

4.1.2.3 Effect of collisions on parallel correlation

In section 4.1.1.2, it was shown that the characteristic parallel length scale λ_{\parallel} associated to the ballooning representation in linear microinstability modes is predominantly determined by the electron-ion mean free path $\lambda_{\text{mfp}}^{e/i}$ [see figure 4.7(b)]. From figure 4.10 it is already clear that such a conclusion does not hold in turbulence simulations as nonlinear mode couplings dominate and deform the linear mode structure, in fact leading to a slight decrease in the exponential decay rate (increase in λ_{\parallel}) of the tails of the ballooning structure with increasing collisionality ν_e^* (decreasing $1/\lambda_{\text{mfp}}^{e/i}$). However it still remains to be explored if the parallel correlation length of turbulent eddies in nonlinear simulations, which is not necessarily measured by λ_{\parallel} , is set by the electron mean free path, *i.e.* collisionality. This is addressed in this subsection.

In reference [Ball et al., 2020] it was shown that turbulence feedback at low order MRSs (turbulent eddies 'biting their tails') can lead to greater correlation of turbulent eddies along the magnetic field line compared to radial locations away from low order MRSs. A two point correlation function C_{\parallel} measuring the degree of correlation between the parallel coordinates z_1 and z_2 on the same field line (*i.e.* for fixed x and y) was defined as

$$C_{\parallel}(x, y, z_1, z_2) = \frac{\langle \Phi_{\text{NZ}}(x, y, z_1, t) \Phi_{\text{NZ}}(x, y, z_2, t) \rangle_t}{\sqrt{\langle \Phi_{\text{NZ}}^2(x, y, z_1, t) \rangle_t \langle \Phi_{\text{NZ}}^2(x, y, z_2, t) \rangle_t}} \quad (4.1)$$

where the subscript NZ signifies the non-zonal component such that $\Phi_{\text{NZ}} = \Phi - \langle \Phi \rangle_{y,z}$. In figure 4.13(a), $\langle C_{\parallel}(x = 0, y, z_1 = 0, z_2) \rangle_y$ denoting the y-averaged correlation between the outboard midplane $z_1 = 0$ and z_2 , at the lowest order MRS $x = 0$, is plotted as a function of z_2 , for nonlinear simulations with different collisionalities. One can observe that the width of the correlation function along z decreases with increasing collisionality. To quantify this dependence, let Δz be the width along the parallel coordinate z defined such that $\langle C_{\parallel}(x = 0, y, z_1 = 0, z_2 = \Delta z) \rangle_y$ is 0.8 times its max value at $z_2 = 0$, approximately

4.1. Effect of collisions on non-adiabatic passing electron dynamics

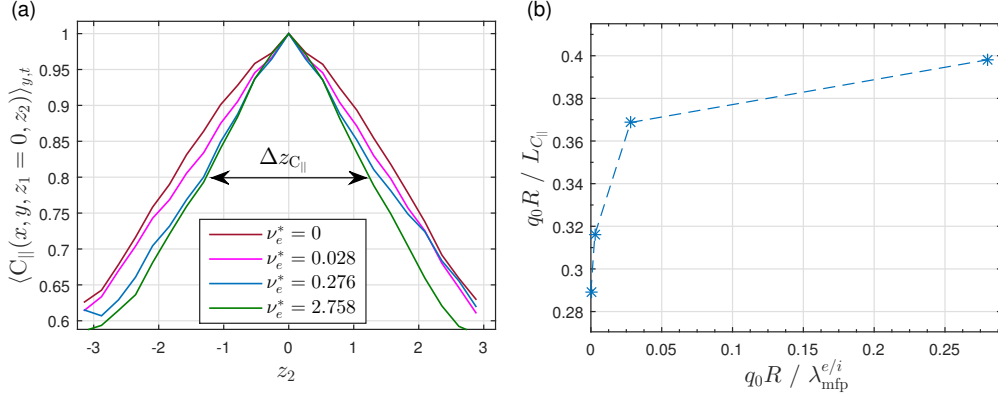


Figure 4.13: (a) y-averaged parallel correlation $\langle C_{||}(x=0, y, z_1=0, z_2) \rangle_y$ of turbulent eddies between the outboard midplane at $z_1 = 0$ and z_2 , as a function of z_2 , at the radial position $x = 0$ corresponding to lowest order MRS. Simulations with collisionalities $\nu_e^* = 0$ (brown), 0.028 (magenta), 0.276 (blue) and 2.758 (green) are shown. $\Delta z_{C_{||}}$ measures the width along z where $\langle C_{||}(x=0, y, z_1=0, z_2, t) \rangle_{y,t} = 0.8$. (b) Inverse of the parallel correlation length $L_{C_{||}} = q_0 R \Delta z_{C_{||}}$ plotted as a function of inverse of the electron-ion mean free path $\lambda_{mfp}^{e/i}$, both normalised by $q_0 R$.

measuring the full width at half maximum. To convert this angular width to a parallel length scale $L_{C_{||}}$, one can again (as in section 4.1.1.2) multiply it with $q_0 R$ to get $L_{C_{||}} = q_0 R \Delta z_{C_{||}}$. In figure 4.13(b), it is shown that $L_{C_{||}}$ does not scale linearly with the electron mean free path. In fact, it is found that $L_{C_{||}}$ scales weakly with $\lambda_{mfp}^{e/i}$, as $L_{C_{||}} \sim (\lambda_{mfp}^{e/i})^{0.05}$, implying that the parallel correlation length of turbulent eddies is not predominantly set by collisionality. The same conclusion holds for radial locations away from LMRSs as well.

4.1.2.4 Effect of collisions on self-interaction mechanism

In this subsection, the effects of collisions on the self-interaction mechanism in nonlinear simulations is explored using some of the diagnostics presented in chapter 3, namely the normalised self-interaction contribution to Reynolds stress, the bicoherence analysis and the correlation analysis between the various k_y contributions to Reynolds stress.

Recalling from section 3.4.5, $\partial^2 \hat{R}S_{k_y}^{si} / \partial x^2$ defined in equation (3.18), measures the self-interaction contribution to Reynolds stress from a given k_y . The time average of the self-interaction contribution to Reynolds stress normalised by the RMS over time of the total Reynolds stress contribution, *i.e.* $\langle \partial^2 \hat{R}S_{k_y}^{si} / \partial x^2 \rangle_t / \text{RMS}(\partial^2 \hat{R}S_{k_y} / \partial x^2)$, simultaneously measures the relative importance of the self-interaction drive of zonal flows with respect to the total contribution to Reynolds stress drive from the considered k_y , as well as how good its sign is fixed at each radial position over time, which is a characteristic feature of the self-interaction mechanism. In figure 4.14(a), $\mathcal{R} = \langle \partial^2 \hat{R}S_{k_y}^{si} / \partial x^2 \rangle_t / \text{RMS}(\partial^2 \hat{R}S_{k_y} / \partial x^2)$

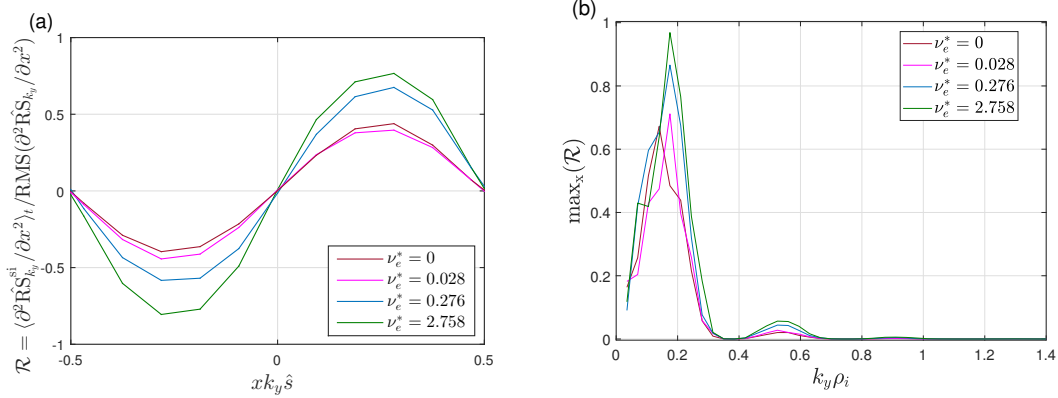


Figure 4.14: (a) Time-average of the self-interacting contribution to Reynolds stress normalised with respect to the RMS in time of the total contribution, *i.e.* $\mathcal{R} = \langle \partial^2 \hat{R}_{k_y}^{si} / \partial x^2 \rangle_t / \text{RMS}(\partial^2 \hat{R}_{k_y} / \partial x^2)$, plotted as a function of the radial coordinate x for $k_y \rho_i = 0.21$. (b) Maximum of \mathcal{R} along the radial coordinate x , plotted as a function of $k_y \rho_i$. Results in turbulence simulations with collisionalities $\nu_e^* = 0$ (brown), 0.028 (magenta), 0.276 (blue) and 2.758 (green) are shown.

for $k_y \rho_i = 0.21$ (related to a significant contribution to the electrostatic field energy $|\Phi|^2$ and ion heat flux k_y -spectra) in turbulence simulations with the different considered collisionalities is plotted as a function of the radial coordinate x over the distance $\Delta x_{\text{MRS}} = 1/k_y \hat{s}$ between MRSs, with $x = 0$ the position of a corresponding MRS. As already discussed in section 3.4.5, the nonlinear broadening mechanism radially widens these structures to essentially a sinusoid with a period Δx_{MRS} . It is found that the normalised measure \mathcal{R} becomes more significant with increasing collisionality, with the exception of the collisionless case, for the case of $k_y \rho_i = 0.21$ considered in figure 4.14(a). To study the dependence of \mathcal{R} on all k_y s, its maximum in x is plotted as a function of k_y in figure 4.14(b). The peak of these plots, measuring the maximum 'intensity' of self-interaction as measured by the normalised self-interaction contribution to Reynolds stress \mathcal{R} , is found to increase with increasing collisionality.

The bicoherence estimate $B_N(\mathbf{k}; \mathbf{k}')$ defined in equation (3.21) in section 3.4.6 measures the strength of the resonant interaction between any turbulence Fourier mode $\mathbf{k} = (k_x, k_y)$ with the zonal mode $\mathbf{k}' = (k'_x, 0)$ via the wave-vector matched daughter modes $\mathbf{k}'' = \mathbf{k} - \mathbf{k}'$ and $\mathbf{k}''' = \mathbf{k} + \mathbf{k}'$. In figure 4.15(a) and (b), $B_N(\mathbf{k}; \mathbf{k}')$ is plotted as a function of k_x and k_y , for the zonal mode $\mathbf{k}' = (k'_x \rho_i = 0.31, 0)$ [having a significant contribution to the k_x -spectra of effective zonal shearing rate ω_{eff}] in turbulence simulations with (a) no collisions and (b) collisionality $\nu_e^* = 2.758$. Clearly, with collisions, the bicoherence levels are higher. To quantify the increase in the bicoherence levels with collisions, the average of $B_N(\mathbf{k}; \mathbf{k}')$ over k_x and k_y , *i.e.* $\langle B_N(\mathbf{k}; \mathbf{k}') \rangle_{k_x, k_y}$ is plotted in figure 4.15(c) as a function of ν_e^* . Recollect from section 3.4.6 that higher bicoherence levels are characteristic of increased zonal flow drive from the modulational instability mechanism, while the

4.1. Effect of collisions on non-adiabatic passing electron dynamics

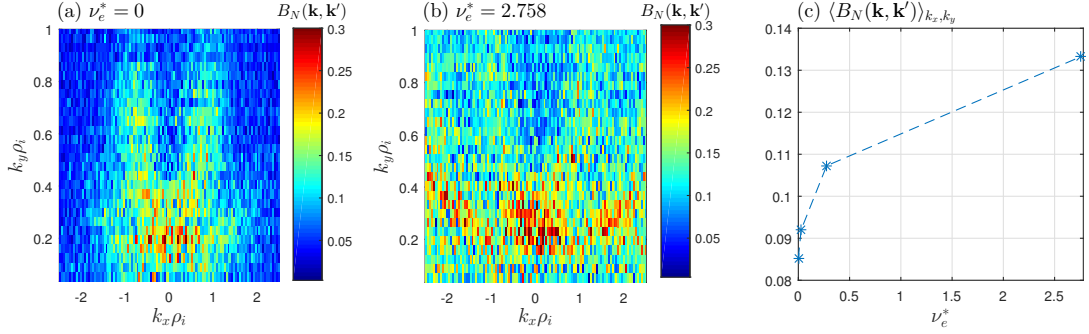


Figure 4.15: The bicoherence level $B_N(\mathbf{k} = (k_x, k_y), \mathbf{k}')$ plotted as a function of k_x and k_y , for the zonal mode $\mathbf{k}' = (k'_x, 0)$ with $k'_x \rho_i = 0.31$, in turbulence simulation with (a) no collisions and (b) collisionality $\nu_e^* = 2.758$. (c) Average bicoherence level $\langle B_N \rangle_{k_x, k_y}$ plotted as a function of collisionality ν_e^* .

self-interaction contribution to Reynolds stress from the different k_y s are uncorrelated with each other and random in time, leading to lower levels of bicoherence. Hence, the increase in $\langle B_N(\mathbf{k}; \mathbf{k}') \rangle_{k_x, k_y}$ with collisionality suggests that collisions weaken the self-interaction mechanism, contrary to the conclusion of the analysis based on the normalised self-interaction contribution to Reynolds stress discussed in the previous paragraph.

In figure 4.16(a), the normalised correlation $C_{RS}[\partial^2 RS / \partial x^2]$ between the k_y modes of Reynolds stress contributions as defined in equation (3.23) is plotted as a function of x for turbulence simulations with different collisionalities. And in figure 4.16(b), the corresponding radial average $\langle C_{RS}[\partial^2 RS / \partial x^2] \rangle_x$ is plotted as a function of ν_e^* . It is found that the normalised correlation between the k_y modes of Reynolds stress contributions, as measured by $C_{RS}[\partial^2 RS / \partial x^2]$, increases with increasing collisionality. This is consistent with the conclusion based on the bicoherence analysis, that collisions weaken the (incoherent) self-interaction drive mechanism and lead to a relative dominance of the (coherent) modulational instability mechanism.

Note that the diagnostic based on the normalised self-interaction contribution to Reynolds stress (in figure 4.14) estimates the relative self-interaction contribution independently for a single k_y . The analysis based on the time-averaged ballooning structure (in figure 4.10(a)) and the relative phase evolution (in figure 4.11) also provide insight related to key properties (see section 3.4.5) ensuring a strong self-interaction contribution independently for each k_y . The results from these three diagnostics (referred to as the first set) suggest that with increasing collisionality, the eigenmodes retain more of their linear characteristics in turbulence simulations. Given that higher RMS amplitudes of physical quantities ($|\Phi|^2$ for instance) in turbulence simulations is indicative of a system being more nonlinear, it is natural to expect simulations with higher collisionalities having less unstable linear eigenmodes, and therefore less RMS amplitudes of physical quantities, to be less nonlinear.

Chapter 4. Effect of collisions and background shear flows on non-adiabatic passing electron dynamics

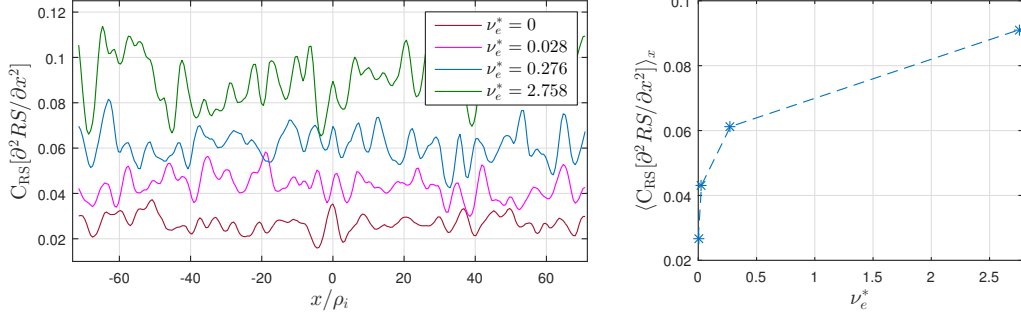


Figure 4.16: (a) Correlation C_{RS} between the k_y modes of Reynolds stress contributions $\partial^2 RS / \partial x^2$ as a function of x in turbulence simulations with collisionalities $\nu_e^* = 0$ (brown), 0.028 (magenta), 0.276 (blue) and 2.758 (green). (b) Radial average of the correlation $\langle C_{RS}[\partial^2 RS / \partial x^2] \rangle_x$ plotted as a function of collisionality ν_e^* .

The second set of diagnostics consisting of the bicoherence analysis (in figure 4.15) and the analysis based on the correlation between the different k_y contributions to Reynolds stress (in figure 4.16), measures the collective effect of self-interaction from multiple k_y s, *i.e.*, these diagnostics also account for how the different k_y s compete with each other to drive zonal flows via self-interaction.

A priori it may appear that there is a contradiction of results from these two sets of diagnostics with the first set of diagnostics suggesting that the effect of self-interaction from each k_y increases with increasing collisionality, while the second set of diagnostics suggesting that the total effect of self-interaction from the multiple k_y s decreases with increasing collisionality. However, it should be noted that the number of significant k_y modes participating in turbulence and how nonlinear the system is could also play a significant role in determining the total effect of self-interaction. This can be explained using the following thought experiment: As one increases collisionality, the linear eigenmodes become less unstable. Now, consider a nonlinear system with high enough collisionality such that effectively the microturbulence is driven by a single unstable eigenmode having a particular k_y . In such a system, the self-interaction contribution from this particular k_y is localised near its MRSs. Whereas in a more nonlinear system with a larger number of unstable k_y modes, the corresponding self-interaction contributions located at respective MRSs tend to be present all through the radial extent (since the MRSs of each k_y are mis-aligned in the radial coordinate) as shown in figures 3.4(a). One thus concludes that under conditions for which the system is less nonlinear, as is the case with high collisionality, the bicoherence analysis and the correlation between the various k_y contributions to Reynolds stress show a decrease in the total effect of self-interaction. To further substantiate this point, in the following subsection, a parallel is drawn between increasing collisionality and decreasing background drive gradient.

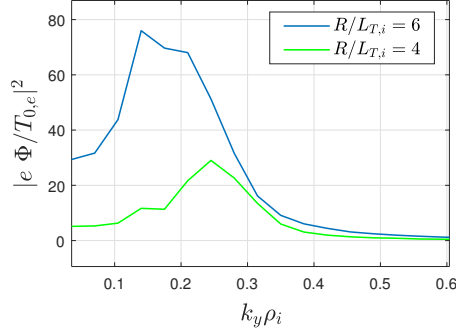


Figure 4.17: k_y spectra of $|\Phi|^2$ in simulations with $R/L_{T,i} = 6$ (blue) and 4 (green). Other parameters are the same as in table 3.1.

Parallel between increasing collisionality and decreasing $R/L_{T,i}$

The arguments presented in the previous paragraph can be verified by performing simulations close to marginal stability where a reduced number of unstable k_y modes contribute towards turbulence while also retaining more of their linear characteristics. In figure 4.17, the k_y spectra of $|\Phi|^2$ in simulations with $R/L_{T,i} = 6$ and 4 are shown with the latter being close to marginal stability. These are the same set of collisionless kinetic electron simulations presented in chapter 3 with parameters given in table 3.1. Indeed, for the case with $R/L_{T,i} = 4$, a reduced number of k_y s contribute significantly towards turbulence, with $k_y\rho_i = 0.245$ contributing a large fraction of the total fluctuation energy. Therefore, in the corresponding plot of zonal flow shearing rate $\omega_{E \times B, \text{ion}}$ shown in figure 4.18(b), one can see significant stationary structures at the corresponding MRSs separated by a distance $\Delta x_{\text{LMRS}} = 1/\hat{s}k_y = 5.10\rho_i$. Whereas in the case far from marginal stability, *i.e.* for $R/L_{T,i} = 6$, the stationary self-interaction contributions from the larger number of k_y s, being radially mis-aligned, tend to cancel each other out between lowest order MRSs.

The average bicoherence level $\langle B_N(\mathbf{k}; \mathbf{k}') \rangle_{k_x, k_y}$ in these simulations far and near from marginal stability are 0.113 and 0.160 respectively. The corresponding correlation levels $\langle C_{\text{RS}}[\partial^2 \text{RS}/\partial x^2] \rangle_x$ are 0.006 and 0.011 respectively. Both these diagnostics indicate that the total effect of self-interaction decreases as one moves closer to marginal stability. This provides a validation to the hypothesis that total self-interaction is weaker in a system with less number of significant k_y contributions despite the fact that the eigenmodes retain more of their linear characteristics.

4.1.3 Conclusions

The effect of collisions on the non-adiabatic passing electron dynamics has been studied in this work using both linear and nonlinear gyrokinetic simulations. In linear simulations,

Chapter 4. Effect of collisions and background shear flows on non-adiabatic passing electron dynamics

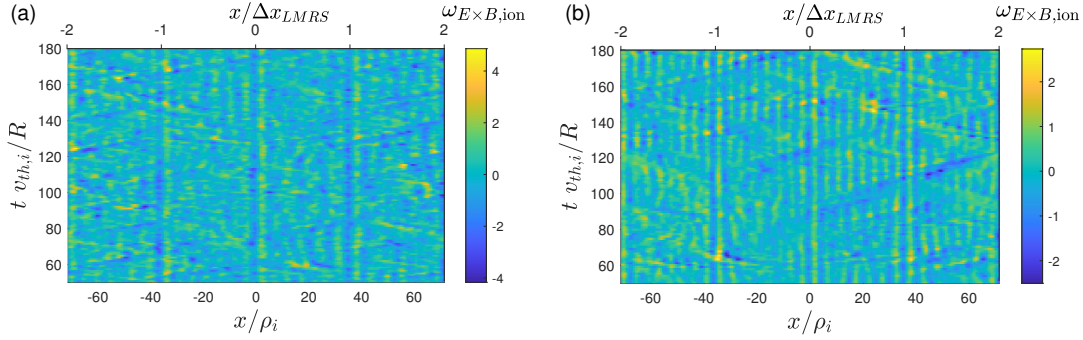


Figure 4.18: $\omega_{E \times B, ion}$ as a function of x and t in simulations with (a) $R/L_{T,i} = 6$ and (b) 4. Other parameters are the same as in table 3.1.

the weakening of the non-adiabatic electron drive of ITG microinstability with collisions, which has already been reported in [Mikkelsen and Dorland, 2008], has been shown to be a consequence of the increased adiabatic like response of electrons away from MRSs. In addition, it is found that the characteristic parallel length scale associated to the ballooning envelope tail of the eigenmodes is set primarily by the electron-ion mean free path. This in turn leads to an increase in the radial width of the fine-structures with increasing collisionality. The decrease in the linear drive of the microinstability with increasing collisions leads to a corresponding decrease in the heat and particle flux levels in nonlinear simulations. However the radial width of fine-structures in nonlinear simulations is not found to show any increase with increasing collisionality as the width of these structures are predominantly set by the nonlinear broadening mechanism. Furthermore, the parallel correlation length of the turbulent eddies is not found to be set by collisionality. Finally, the effect of collisions on the self-interaction mechanism is studied. The diagnostics measuring the total effect of self-interaction (and modulational instability) from the multiple k_y s simultaneously suggests that total self-interaction decreases with increasing collisionality. The final conclusion is that for physically relevant values of collisionality in the core, the effect of non-adiabatic passing electrons, in particular the self-interaction mechanism, remains significant.

4.2 Effect of background shear flow on non-adiabatic passing electron dynamics

Experimental measurements have shown that background $E \times B$ shear flows are essential to the formation of transport barriers in both the tokamak core and edge [Tresset et al., 2002], and significantly reduce turbulent transport levels [Burrell, 1997, Conway et al., 2000]. It is therefore crucial towards enabling H-mode confinement in tokamaks [Wagner, 2007]. Numerical studies have revealed that this transport suppression is caused by the perpendicular component (to the background magnetic field) of the flow shear while

4.2. Effect of background shear flow on non-adiabatic passing electron dynamics

the parallel component is known to drive the so-called parallel velocity gradient (PVG) instability [Waltz et al., 1998, Peeters and Angioni, 2005, Casson et al., 2009, Barnes et al., 2011].

Another effect of background flow shear on turbulence is the formation of soliton-like travelling structures. In presence of finite background shear flows, avalanche or burst-like structures drifting in a specific radial direction have been observed in gyrokinetic simulations [van Wyk et al., 2017, McMillan et al., 2018]. With strong enough background shear flows, the linear drive of turbulence from instabilities such as ITG can get suppressed. In such linearly stable systems, given a large enough perturbation, the plasma can be pushed into a subcritical state with non-zero turbulence levels [Casson et al., 2009, Roach et al., 2009, McMillan et al., 2009, van Wyk et al., 2016]. Recent studies have reported the presence of coherent travelling structures in these sub-critical states [Pringle et al., 2017, van Wyk et al., 2017, McMillan et al., 2018].

Background shear flow can therefore have significant effects on turbulence. However, since the interaction between the two involves multiple feedback loops, it is often not straightforward to predict these effects [Burrell, 1997]. Most of these studies on the effect of background flow shear on ion scale turbulence in tokamaks have been done using gyrokinetic simulations considering adiabatic electron response. In this section, a preliminary study on the effect of back-ground shear flow on non-adiabatic electron response, in particular on the associated fine-structures is carried out.

Simulation set-up: The simulation parameters are the same as those in table 4.1, with no collisions and kinetic electrons. A scan in the shearing rate S associated to the background flow is performed over a range $0 \leq SR/v_{th,i} \leq 1$. The background shearing rate S is defined as

$$S = -\frac{r_0}{q_0} \frac{\partial \Omega_{\text{tor}}}{\partial x}, \quad (4.2)$$

where $\partial \Omega_{\text{tor}}/\partial x$ is the radial derivative of the toroidal angular velocity. Note that the background flow is set to be purely toroidal [Told, 2012].

Effect on heat flux: In figure 4.19, the time-averaged gyro-Bohm normalised ion heat flux is plotted as a function of the background shearing rate S , showing a decrease with increasing value of S . This is in general consistent with the results in references [Barnes et al., 2011, McMillan et al., 2019] where a scan has been performed for a similar set of parameters, but with adiabatic electrons.

Effect on zonal fine-structures: The zonal fine structures, discussed in section 3.2, are found to persist even in presence of background shear flows. See figure 4.20, where the time-average of the shearing rate $\omega_{E \times B, \text{ion}}$ associated to the perturbed zonal flows [defined by equation (3.1)] are plotted with solid lines, as a function of the radial coordinate x .

Chapter 4. Effect of collisions and background shear flows on non-adiabatic passing electron dynamics

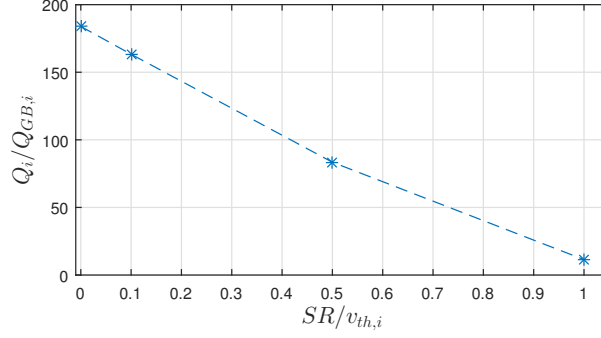


Figure 4.19: Time averaged and gyro-Bohm normalised ion heat flux Q_i plotted as a function of background flow shearing rate $SR/v_{th,i}$.

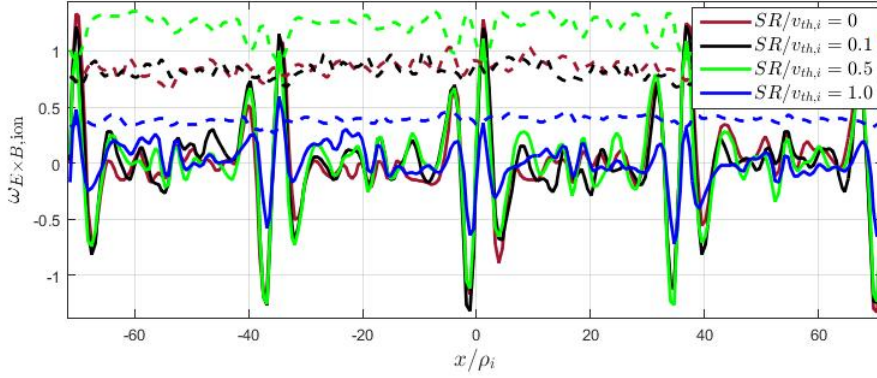


Figure 4.20: Solid lines indicate time averaged shearing rate $\omega_{E \times B, ion}$ associated with perturbed zonal flows as a function of the radial coordinate x . Simulations with four different values of background flow shearing rate $SR/v_{th,i} = 0$ (brown), 0.1 (black), 0.5 (green) and 1.0 (blue) are shown. Corresponding standard deviation of $\omega_{E \times B, ion}$ are also shown with dashed lines.

The amplitudes of the peaks at lowest order MRSs can be seen to decrease with increasing value of S . The standard deviation of $\omega_{E \times B, ion}$, measuring the fluctuating component of zonal flows, are also plotted in figure 4.20, denoted by dashed lines. Note that the ratio of the peak values of the time average with respect to the standard deviation remains approximately constant ($\simeq 1$) across the simulations being considered.

Avalanche-like structures on perturbed zonal flows: For a more qualitative study, the (x, t) profile of $\omega_{E \times B, ion}$ is plotted in figure 4.21, for each of the four values of background shear flow considered. In these plots, radially propagating fronts or avalanches, discussed in reference [McMillan et al., 2009], can be clearly observed. As S increases, these structures preferentially travel in a specific radial direction. The radial velocity (3.25, 3.20, 2.15 and 0.68, in units of $v_{th,i}\rho_i/R$) of these structures is also found to decrease with increasing values of background shear ($SR/v_{th,i} = 0, 0.1, 0.5$ and 1 respectively).

4.2. Effect of background shear flow on non-adiabatic passing electron dynamics

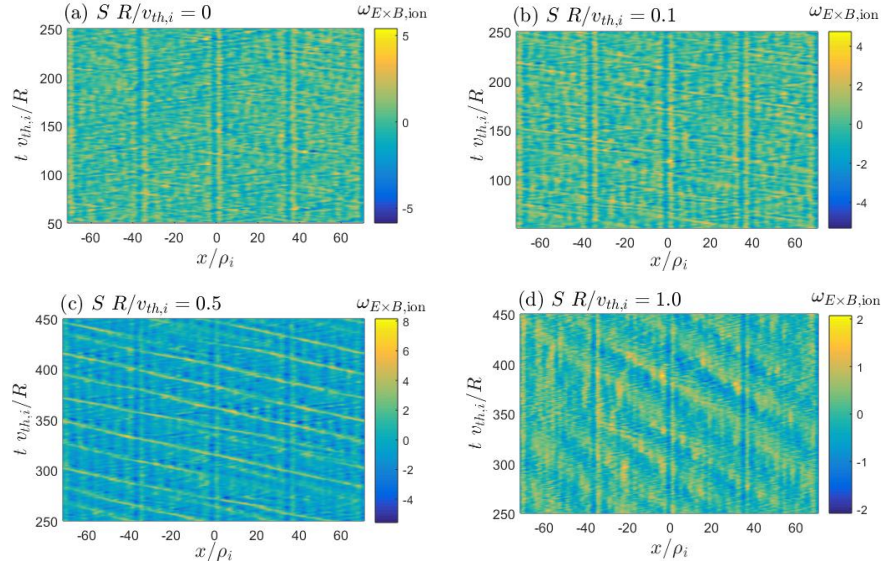


Figure 4.21: (x, t) color plot of the shearing rate $\omega_{E \times B, ion}$ associated with perturbed zonal flows in simulations with background flow shearing rate $SR/v_{th,i}$ of (a) 0, (b) 0.1, (c) 0.5 and (d) 1.0 .

Furthermore, compared to the cases with $SR/v_{th,i} = 0, 0.1$ and 0.5 , the radial width of the avalanche-like structures for the case with $SR/v_{th,i} = 1.0$ is found to be significantly larger.

Soliton like propagating density structures: The avalanche-like zonal structures also correspond to soliton-like radially drifting density perturbations. This can be seen in figures 4.22 and 4.23. In figure 4.22, the shearing rate $\omega_{E \times B, ion}$ for the case with $SR/v_{th,i} = 0.5$ is shown over a time window corresponding to the initial stage of turbulence evolution where only one prominent avalanche-like structure has been formed. In figure 4.23, the density perturbation at the outboard midplane $z = 0$ is shown for three different time snaps. In each of these density perturbation plots, structures having a specific periodicity in y (with $k_y \rho_i \simeq 0.3$) can be seen. The wavefronts of these structures correspond to the radial locations of the avalanche-like zonal structures seen in figure 4.22. These density structures appear to be very similar to the simple advecting structures reported in reference [McMillan et al., 2018].

In summary, the fine-structures associated to non-adiabatic passing electrons persist even in presence of finite background shear flow. The turbulent flux-levels decreases with increasing values of background shearing rate, and radially propagating structures are seen, similar to the results obtained with adiabatic electrons.

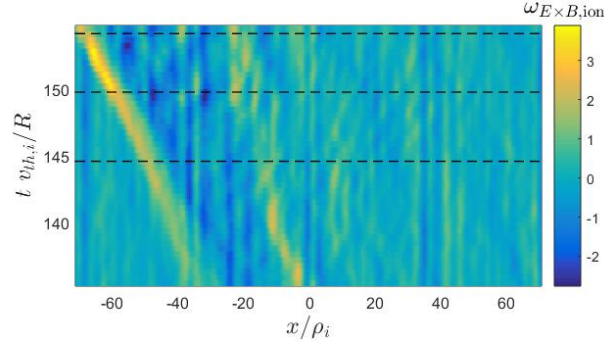


Figure 4.22: (x, t) color plot of the shearing rate $\omega_{E \times B, ion}$ associated with perturbed zonal flows in the simulation with background flow shearing rate $SR/v_{th,i} = 0.5$. The horizontal dashed lines denote the times $tv_{th,i}/R = 144.6, 149.8$ and 154.2 .

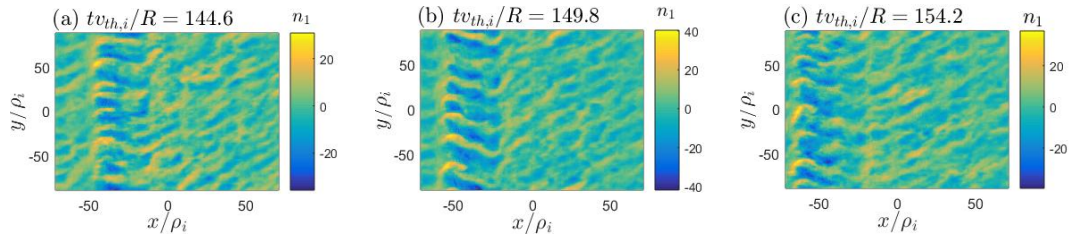


Figure 4.23: Electron density perturbation n_1 at the outboard midplane in the simulation with background flow shearing rate $SR/v_{th,i} = 0.5$, at times $tv_{th,i}/R$ (a) 144.6, (b) 149.8 and (c) 154.2.

5 Conclusions

5.1 Summary

In this thesis, the effect of non-adiabatic passing electrons on microturbulence in the tokamak core has been studied using the flux-tube version of the Eulerian gyrokinetic code GENE.

As a result of the non-adiabatic passing electron dynamics, linear ITG and TEM eigenmodes can become significantly extended along the magnetic field lines, generating fine radial structures at corresponding MRSs. These fine structures on the eigenmodes persist in turbulence simulations as well, and via non-linear coupling lead to stationary corrugations on the radial profiles of density, temperature and in particular $E \times B$ zonal shear flows, aligned with low order MRSs. Given that shearing and decorrelation of turbulent eddies by zonal flows is a primary mechanism by which turbulence saturates, the generation of these fine scale zonal flow structures, via a process called the self-interaction mechanism, was studied in detail.

Self-interaction essentially involves each individual microturbulence eigenmode interacting non-linearly with itself to produce a Reynolds stress contribution to the zonal flow drive, which is located around its corresponding MRSs. At low order MRSs, these self-interaction contributions to Reynolds stress from the different eigenmodes radially align and add up constructively to drive the stationary $E \times B$ zonal shear flows, whereas between the low order MRSs, these contributions to Reynolds stress related to the various microturbulence modes tend to be radially misaligned. These radially misaligned contributions to Reynolds stress drive zero stationary zonal shear flow but a non-zero fluctuating zonal shear flow component between low order MRSs. These fluctuating zonal flows are found to play a significant role in the zonal flow turbulence saturation mechanism.

An important finding of this thesis is that the self-interaction contributions to Reynolds stress act as random decorrelated kicks that can in some cases disrupt the zonal flow

Chapter 5. Conclusions

drive via modulational instability mechanism. Unlike self-interaction, it is a coherent process, leading to correlated contributions from the various microinstability modes to the Reynolds stress drive of zonal modes.

As a consequence of the decorrelated self-interaction contribution from the various microturbulence modes, the associated shearing rate of the fluctuating zonal flows is observed to decrease as more toroidal modes are resolved in the simulation. In flux-tube simulations accounting for the full toroidal domain, such an increase in the density of toroidal modes corresponds to an increase in the system size, leading to a finite system size effect that is distinct from the well-known profile shearing effect. The observed scaling of $E \times B$ shearing rate with the spectral density of toroidal modes has been explained based on simple statistical arguments.

For the practical purpose of running flux-tube simulations, it is also possible for one to view this system size effect resulting from self-interaction as a numerical convergence issue. In reference [Ball et al., 2020], a detailed analysis is presented on how to most efficiently remove the effects of self-interaction so as to achieve the true flux-tube limit of $k_{y,\min}\rho_i \rightarrow 0$. This may be done by increasing the simulation box size to span multiple poloidal turns instead of one.

How collisions and background shear flow may modify the effect of non-adiabatic passing electrons was also investigated in this thesis.

With collisions, linear growth rate of ITG microinstability was found to weaken as a consequence of the increased adiabatic-like response of electrons away from MRSs. Furthermore, the shortened electron mean free path in presence of collisions was shown to lead to a radial broadening of the fine-structures associated to ITG eigenmodes. The decrease in the linear drive of the microinstability with increasing collisions leads to a corresponding decrease in the heat and particle flux levels in nonlinear turbulence simulations. Furthermore, as a result of dominant nonlinear effects, a radial narrowing of the fine-structures is observed in turbulence simulations, along with an increase in the parallel correlation length of turbulent eddies.

In presence of finite background shear flow, the fine-structures associated with the non-adiabatic passing electron response were found to persist. The turbulent flux-levels decrease with increasing values of background shearing rate, and radially propagating soliton-like structures are seen, similar to the results obtained with adiabatic electrons in previous studies [Barnes et al., 2011, McMillan et al., 2019, van Wyk et al., 2017, Pringle et al., 2017, McMillan et al., 2018].

All these studies, including the investigations on the effect of collisions and background shear flow, show that self-interaction is a robust and ubiquitous feature of plasma turbulence in tokamaks. The results obtained as part of this work using simulations close to the Cyclon Base Case suggest that the effect of self-interaction in determining

the turbulent transport levels is significant only for small to medium size tokamaks ($\rho^* \gtrsim 1 \cdot 10^{-1}$). Whereas the stationary fine-structures associated with self-interaction at rational surfaces are found to persist even for large tokamaks ($\rho^* \lesssim 1 \cdot 10^{-1}$). Repeating these studies in more realistic geometries and in other turbulence regimes such as TEM, ETG, MTM, KBM etc. (as also discussed in the outlook below) can help one obtain a better understanding of the effect of self-interaction. In particular, checking for the effects of self-interaction in ITER/DEMO scenarios could also be insightful to the fusion community.

5.2 Outlook

In this thesis, the effects of non-adiabatic passing electrons have been studied with the help of flux-tube simulations. In particular, in chapter 3, the self-interaction mechanism associated with non-adiabatic passing electrons has been shown to lead to a system size effect. However, note that in flux-tube simulations the other finite ρ^* effects, such as profile shearing [Waltz et al., 1998, Waltz et al., 2002] and effect of finite radial extent of the unstable region [McMillan et al., 2010], are missing. Therefore, in order to study how self-interaction competes with other finite ρ^* effects, global simulations can be used (or local simulations that treat these other finite ρ^* effects explicitly such as in [Candy et al., 2020]). Using global simulations, a scan in ρ^* can be carried out and the results can be compared with the results from the $k_{y,\min}\rho_i$ scan obtained using flux-tube simulations in chapter 3. Since finding such system size effects and predicting the correct turbulent scaling laws are crucial towards designing future larger tokamaks such as ITER and DEMO, it is important to carry forward studies on the effect of non-adiabatic passing electron dynamics and the self-interaction mechanism.

While the effects of collisions and finite background shear on the fine structures related to non-adiabatic passing electrons have already been addressed in chapter 4, one can pursue this study for electromagnetic turbulence in finite β plasmas, or on electron scale turbulence. The presence of fine-structures at the MRSs of Kinetic Ballooning Modes (KBMs) and Microtearing Modes (MTMs) have already been reported in references [Falchetto et al., 2003] and [Doerk, 2012] respectively. One can pursue these studies to find the effect of self-interaction on electromagnetic turbulence. Many instances of the cross scale interactions between electron and ion scale turbulence have already been reported [Görler and Jenko, 2008, Maeyama et al., 2015, Howard et al., 2016]. Furthermore, studies such as [Maeyama et al., 2017] have shown that short wavelength zonal flows produced by non-adiabatic passing electron dynamics, can affect electron scale turbulence. Given that self-interaction generates the stationary $E \times B$ zonal shear layers with radial extents of the order of few ion Larmor radius at low order MRSs, it will be worthwhile to carry out electron-ion multiscale simulations to explore the associated cross-scale interactions further.

Chapter 5. Conclusions

Finally, these effects of non-adiabatic passing electrons found using gyrokinetic simulations should be verified by experimental measurements. In reference [Dif-Pradalier et al., 2015] for instance, a high-resolution fast-sweeping X-mode reflectometer has been used to measure the radial correlation length of fluctuations in the Tore Supra Tokamak. The minimas of these radial correlation lengths have then been identified as the radial positions of $E \times B$ staircases. An important pre-requirement in measuring the fine stationary zonal structures on density and temperature profiles at MRSs, which have a width of only a few Larmor radius, is that the measurement diagnostic should have sufficiently high radial resolutions. The Toroidal Phase Contrast Imaging (TPCI) and the Correlation Electron Cyclotron Emission (CECE) diagnostics available at the TCV tokamak, with radial resolutions of less than a mm, might be able to identify these structures.

A Local flattening of gradients between lowest order MRSs

In this appendix, the possibility of local flattening of effective gradients between Lowest order Mode Rational Surfaces (LMRSs) as a means to explain the increase in flux levels with decreasing $k_{y,\min}\rho_i$ observed for the kinetic electron runs (see figure 3.7), is explored.

The time-averaged gradient of density and temperature perturbations is found to present a net steepening of these gradients at the radial positions near LMRSs. For example, see the flux-surface and time averaged perturbed density gradient plots in figure A.1 for the reference ITG driven turbulence simulations presented in table 3.1, with $k_{y,\min}\rho_i = 0.035$ and 0.0175. Note that the gradient of background density dn_0/dx has a negative sign. Therefore, positive and negative values of the y-axis quantity $(d\delta n/dx)/(n_0/L_N)$ in figure A.1 represent respectively a flattening and steepening of the effective density profile $n = n_0 + \delta n$. Furthermore, a value of $(d\delta n/dx)/(n_0/L_N) = 1$ implies a fully flat effective density profile n . In figure A.1, one can indeed see that the x-average of the perturbed density gradient fine-structures near the LMRSs (*i.e.* averaged over the pink shaded region), is negative, representing a steepening of the gradients. Given that the total x-average of the quantity $(d\delta n/dx)/(n_0/L_N)$ over the entire L_x domain is zero, this implies a flattening of the total gradients between LMRSs (in the white region). In other words, one could say that the fine structures at LMRSs, including the intense shearing associated to zonal flows (see figure 3.5), constitute mini local transport barriers, which then sustain reduced effective gradients between LMRSs.

Assuming that the time and flux-surface averaged fine-structures at LMRSs of density and temperature gradients remain approximately the same in their amplitudes and radial widths across simulations with different $k_{y,\min}\rho_i$ s, the associated steepening of gradients near each LMRS also remains the same. However, as the radial density of LMRSs decreases with decreasing $k_{y,\min}\rho_i$, the net flattening of the gradients between LMRSs decreases. This is illustrated in figure A.2. Since the the fine-structures at LMRSs occupy an ever smaller fraction of the radial domain as $k_{y,\min}\rho_i$ and the density of LMRSs decreases, the dynamics between LMRSs will more dominantly determine the turbulence

Appendix A. Local flattening of gradients between lowest order MRSs

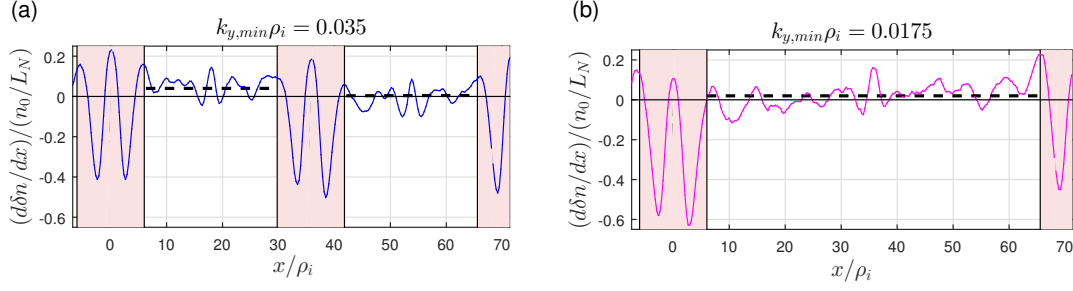


Figure A.1: Flux-surface and time-averaged relative density gradients $(d\delta n/dx)/(n_0/L_N)$ for cases with (a) $k_{y,min}\rho_i = 0.035$ and (b) $k_{y,min}\rho_i = 0.0175$. Horizontal dotted black lines indicate the average relative density gradient in the (white) region between the fine structures (pink) at LMRSs.

levels. Hence, as $k_{y,min}\rho_i$ decreases, the less flattened gradients between LMRSs can drive a larger turbulence flux. This could then potentially explain the observed increase in flux levels with decreasing $k_{y,min}\rho_i$. In the following, this hypothesis is tested.

In figure A.1, x-average of the flux-surface and time averaged perturbed density gradient [in units of the background gradient] in the region between LMRSs (white region) is indicated with horizontal dashed lines. For the case with $k_{y,min}\rho_i = 0.0175$, the flattening of the gradients between LMRSs is indeed lesser than that observed for the case with $k_{y,min}\rho_i = 0.035$. However, for all values of $k_{y,min}\rho_i \in \{0.0175, 0.035, 0.07, 0.07\}$ considered, it is found that the average change in the local perturbed density and temperature gradients between LMRSs (white region) is less than 10% and 1% of the background gradients of density and ion temperature respectively.

From figure A.3, which is the result of a linear simulation scan over density and temperature background gradients, one could see that the $\pm 10\%$ and $\pm 1\%$ change in the gradients as indicated by the vertical dotted lines lead only to less than $\pm 5\%$ change in growth rates of the most unstable ITG eigenmodes. Furthermore, from figure A.4, which is the result of a corresponding nonlinear scan, one could see that the $\pm 10\%$ and $\pm 1\%$ change in the gradients corresponds to only a $\pm 12\%$ and $\pm 5\%$ change in the ion heat flux, respectively. Therefore, the flattening of the effective profiles between LMRSs at most plays a minor role in explaining the $\sim 150\%$ increase in ion heat flux as $k_{y,min}\rho_i$ is decreased from 0.14 to 0.0175 (shown in figure 3.7). The fact that the nonlinear simulations with altered background gradients presented in figure A.4 themselves also contain fine structures at LMRSs and non-zero changes in effective local gradients between them is acknowledged. It is however not expected to lead to a different conclusion.

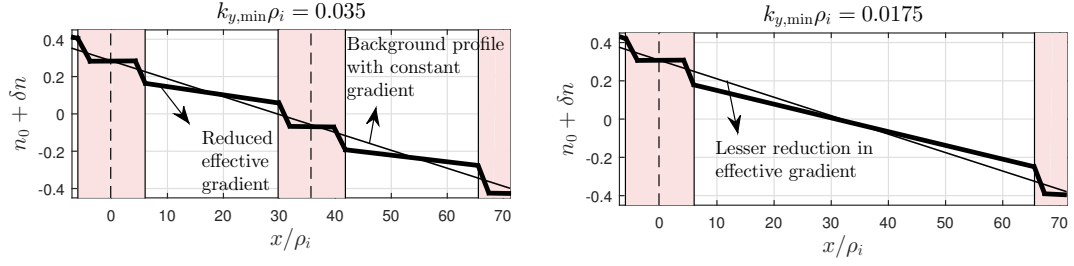


Figure A.2: Density profiles (thick black line) with exaggerated modifications resulting from mini-transport barriers at LMRs, for the same cases as in Fig. A.1. Dotted lines denote the position of LMRs and pink regions denote the extent of fine structures at LMRs. Thin black lines denote the background density. Note that there is lesser local flattening in the (white) region between fine structures at LMRs in the case with $k_{y,min}\rho_i = 0.0175$ than in the case with $k_{y,min}\rho_i = 0.035$.

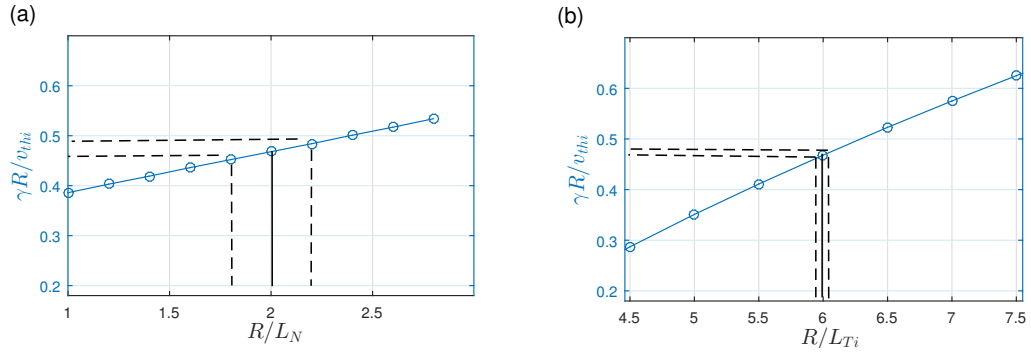


Figure A.3: Growth rate [cyan] versus logarithmic (a) density and (b) temperature background gradients for linear runs corresponding to the nonlinear runs considered. Vertical dotted lines indicate $\pm 10\%$ and $\pm 1\%$ change in the density and temperature gradients, respectively, while horizontal dotted lines indicate the corresponding changes in growth rates.

Appendix A. Local flattening of gradients between lowest order MRSs

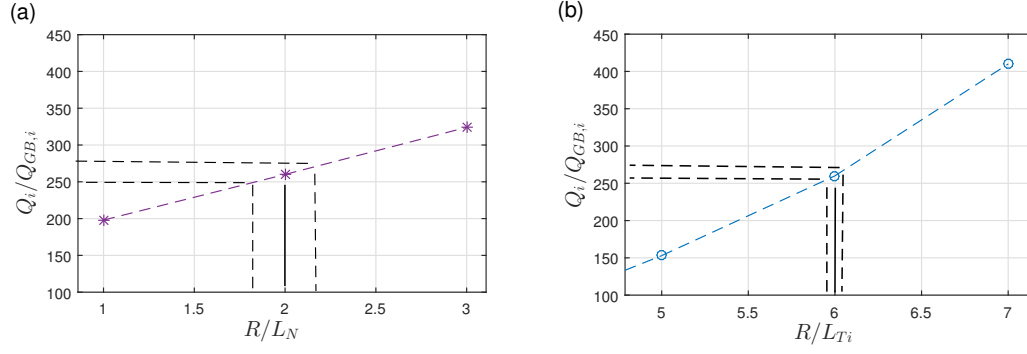


Figure A.4: Ion heat flux versus logarithmic (a) density and (b) temperature background gradients. Except for the changes in the background gradients, all parameters are kept the same as in Table 3.1. Vertical dotted lines indicate $\pm 10\%$ and $\pm 1\%$ changes in the density and temperature gradients respectively, while horizontal dotted lines indicate the corresponding change in heat fluxes.

B Flux-surface-averaged poloidal momentum conservation equation

Zonal flows are linearly stable and are driven by microinstability modes via the quadratic $E \times B$ non-linearity in the gyrokinetic equation [Diamond et al., 2005]. In order to identify and analyze the different possible mechanisms driving zonal flows and to study their statistical properties, it is useful to identify a physical quantity that can then be used as a proxy for estimating the zonal flow drive. In this appendix, justification is provided for considering the Reynolds stress, more specifically the off-diagonal component $\langle \tilde{V}_x \tilde{V}_\chi \rangle$ of the Reynolds stress tensor resulting from the combination of fluctuating $E \times B$ flow components in the radial and poloidal directions, as this proxy for the non-linear drive of zonal flows.

In subsection B.1, an approximate evolution equation for the shearing rate $\omega_{E \times B}$ associated to $E \times B$ zonal flows is derived so as to identify the nonlinear driving terms, in particular the Reynolds stress term. Before analysing the full nonlinear zonal flow evolution equation, it is first validated in the linear limit, on the output of a Rosenbluth-Hinton test. This is done in section B.2. Following which, in section B.3, the relative importance of the nonlinear terms are illustrated by analysing the evolution equation on the output of a full turbulence simulation.

B.1 Derivation in GENE flux-tube model

An approximate evolution equation for the shearing rate $\omega_{E \times B}$ associated to $E \times B$ zonal flows can be obtained from the radial conservation equation for the gyrocenter charge density, which in turn is obtained by taking the appropriate velocity moment and flux-surface average of the gyrokinetic equation [Abiteboul, 2012]. Note that, while a global "full-f" model is considered in reference [Abiteboul, 2012], here the derivation is done in the local (flux-tube) limit in "delta-f" representation as modelled in GENE. Further, this derivation is done in the electrostatic limit, invoking $m_i \gg m_e$, and making use of the quasi-neutrality equation in the long wave-length limit (correct to second order

Appendix B. Flux-surface-averaged poloidal momentum conservation equation

in $k_\perp \rho_i$).

One starts from the gyrokinetic equation for the perturbed distribution function given by equation (2.51). In the GENE field aligned (x, y, z) coordinates, in the electrostatic limit ($\beta \rightarrow 0$, $A_{1\parallel} \rightarrow 0$, and $B_{0\parallel}^* \rightarrow B_0$), it becomes [for more details, see the derivation leading up to equation (2.62) in reference [Lapillone, 2010]]:

$$\begin{aligned}
-\frac{\partial}{\partial t} f_{1j} = & \frac{1}{\mathcal{C}\gamma_1} \left[\underbrace{\gamma_2 \frac{\partial f_{0j}}{\partial z} \frac{\partial \bar{\Phi}_1}{\partial x}}_{=0; \text{ f.s. avg.}} - \underbrace{\gamma_1 \frac{\partial f_{0j}}{\partial x} \frac{\partial \bar{\Phi}_1}{\partial y}}_{=0; \text{ f.s. avg.}} + \underbrace{\gamma_3 \frac{\partial f_{0j}}{\partial z} \frac{\partial \bar{\Phi}_1}{\partial y}}_{=0; \text{ f.s. avg.}} \right. \\
& \left. - \frac{\mu}{m_j v_\parallel} \left(\underbrace{\gamma_2 \frac{\partial B_0}{\partial z} \frac{\partial \bar{\Phi}_1}{\partial x}}_{=0; \text{ f.s. avg.}} - \underbrace{\gamma_1 \frac{\partial B_0}{\partial x} \frac{\partial \bar{\Phi}_1}{\partial y}}_{=0; \text{ f.s. avg.}} + \underbrace{\gamma_3 \frac{\partial B_0}{\partial z} \frac{\partial \bar{\Phi}_1}{\partial y}}_{=0; \text{ f.s. avg.}} \right) \frac{\partial f_{0j}}{\partial v_\parallel} \right] + \underbrace{\frac{1}{\mathcal{C}} \left(\frac{\partial \bar{\Phi}_1}{\partial x} \Gamma_{y,j} - \frac{\partial \bar{\Phi}_1}{\partial y} \Gamma_{x,j} \right)}_{\text{non-linear terms}} \\
& + \frac{\mu B_0 + m_j v_\parallel^2}{m_j \Omega_j} \left(\mathcal{K}_x \Gamma_{x,j} + \underbrace{\mathcal{K}_y \Gamma_{y,j}}_{=0; \text{ f.s. avg.}} \right) + \underbrace{\frac{1}{\mathcal{C}} \frac{\mu_0 v_\parallel^2}{\Omega_j B_0} \frac{\partial P_0}{\partial x} \Gamma_{y,j}}_{=0; \text{ f.s. avg.}} \\
& + \underbrace{\frac{\mathcal{C} v_\parallel}{B_0 J^{xyz}} \Gamma_{z,j}}_{=0; \partial(\text{pert.})/\partial z \rightarrow 0} - \underbrace{\frac{\mathcal{C} \mu}{m_j B_0 J^{xyz}} \frac{\partial B_0}{\partial z} \frac{\partial f_{1j}}{\partial v_\parallel}}_{=0; \text{ vel. avg.}}, \tag{B.1}
\end{aligned}$$

where $\mathcal{C} = B_0/|\nabla x \times \nabla y|$, $\gamma_1 = g^{11}g^{22} - (g^{12})^2$, $\gamma_2 = g^{11}g^{23} - g^{12}g^{13}$, $\gamma_3 = g^{12}g^{23} - g^{22}g^{13}$,

$$\begin{aligned}
\Gamma_{\alpha,j} &= \frac{\partial f_{1j}}{\partial \alpha} - \frac{q_j}{m_j v_\parallel} \frac{\partial \bar{\Phi}_1}{\partial \alpha} \frac{\partial f_{0j}}{\partial v_\parallel}, \quad \alpha = x, y, z, \\
\mathcal{K}_x &= -\frac{1}{\mathcal{C}} \frac{\gamma_2}{\gamma_1} \frac{\partial B_0}{\partial z}, \\
\mathcal{K}_y &= \frac{1}{\mathcal{C}} \left(\frac{\partial B_0}{\partial x} - \frac{\gamma_3}{\gamma_1} \frac{\partial B_0}{\partial z} \right).
\end{aligned}$$

Here, $\bar{\mathcal{A}}$ denotes the gyro-average of any perturbed quantity \mathcal{A} .

The under-(square)bracketed terms in Eq. B.1 cancel out since the background distribution f_{0j} is considered to be a local Maxwellian of the form:

$$f_{0j}(x, z, v_\parallel, \mu) = \left(\frac{m_j}{2\pi T_{0j}(x)} \right)^{\frac{3}{2}} n_{0j}(x) \exp \left(-\frac{m_j v_\parallel^2/2 + \mu B_0}{T_{0j}(x)} \right), \tag{B.2}$$

B.1. Derivation in GENE flux-tube model

with

$$\begin{aligned}\frac{\partial f_{0j}}{\partial z} &= -\frac{\mu}{T_{0j}} \frac{\partial B_0}{\partial z} f_{0j}, \\ \frac{\partial f_{0j}}{\partial v_{\parallel}} &= -\frac{m_j v_{\parallel}}{T_{0j}} f_{0j}.\end{aligned}\tag{B.3}$$

The second last term in equation (B.1) can be neglected since microinstabilities tend to align with the magnetic field ($k_{\parallel} \ll k_{\perp}$), and hence $\partial/\partial z$ 'parallel' derivatives of perturbed quantities are ignored. To obtain the radially local gyrokinetic density conservation equation, we perform a velocity space integration, in which process the last term in equation (B.1) cancels out. Finally, we perform a flux-surface average, defined as $\langle \cdot \rangle_{\text{f.s.}} = \langle \cdot \rangle_{yz} = \int \cdot J^{xyz} dy dz / \int J^{xyz} dy dz$. A total of six linear terms average out to zero in this process, as indicated in Eq. B.1. Furthermore, a contribution to the non-linear term will also cancel in this process:

$$\begin{aligned}\frac{\partial \bar{\Phi}_1}{\partial x} \Gamma_{y,j} - \frac{\partial \bar{\Phi}_1}{\partial y} \Gamma_{x,j} &= \frac{\partial \bar{\Phi}_1}{\partial x} \frac{\partial f_{1j}}{\partial y} - \frac{\partial \bar{\Phi}_1}{\partial y} \frac{\partial f_{1j}}{\partial x} \\ &= -\frac{\partial}{\partial x} \left(\frac{\partial \bar{\Phi}_1}{\partial y} f_{1j} \right) + \underbrace{\frac{\partial}{\partial y} \left(\frac{\partial \bar{\Phi}_1}{\partial x} f_{1j} \right)}_{=0; \text{ f.s. avg.}}.\end{aligned}$$

With the perturbed gyrocenter density defined as

$$n_{1j} = 2\pi \int f_{1j} J_v dv_{\parallel} d\mu,\tag{B.4}$$

where $J_v = B_{0\parallel}^*/m_j$ is the phase space Jacobian from particle to guiding-center coordinates ($B_{0\parallel}^* \rightarrow B_0$ in the electrostatic limit considered here), we obtain:

$$\begin{aligned}\frac{\partial}{\partial t} \langle n_{1j} \rangle_{yz} &= \frac{2\pi}{\mathcal{C}} \frac{\partial}{\partial x} \left\langle \frac{B_0}{m_j} \int \frac{\partial \bar{\Phi}_1}{\partial y} f_{1j} dv_{\parallel} d\mu \right\rangle_{yz} \\ &\quad + \frac{2\pi}{\mathcal{C}} \frac{\partial}{\partial x} \left\langle \frac{\gamma_2}{\gamma_1} \frac{\partial B_0}{\partial z} \frac{B_0}{m_j} \int \frac{\mu B_0 + m_j v_{\parallel}^2}{m_j \Omega_j} \left(f_{1j} - \frac{q_j \bar{\Phi}_1}{m_j v_{\parallel}} \frac{\partial f_{0j}}{\partial v_{\parallel}} \right) dv_{\parallel} d\mu \right\rangle_{yz}.\end{aligned}\tag{B.5}$$

The perturbed gyrocenter charge density is defined as $\rho_{1j} = q_j n_{1j}$. Now, using equation (B.3), and the relation $\mathcal{C}\gamma_1 = B_0^2/\mathcal{C}$, Eq. B.5 can be written as:

$$\frac{\partial}{\partial t} \sum_j \langle \rho_{1j} \rangle_{yz} = \sum_j \frac{2\pi q_j}{\mathcal{C}} \frac{\partial}{\partial x} \left\langle \frac{B_0}{m_j} \int \frac{\partial \bar{\Phi}_1}{\partial y} f_{1j} dv_{\parallel} d\mu \right\rangle_{yz} - \frac{\partial}{\partial x} \mathcal{N},\tag{B.6}$$

Appendix B. Flux-surface-averaged poloidal momentum conservation equation

where the neo-classical contribution \mathcal{N} , related to curvature and ∇B drifts, is defined as:

$$\mathcal{N} = - \sum_j \frac{2\pi\mathcal{C}}{m_j} \left\langle \frac{\gamma_2}{B_0^2} \frac{\partial B_0}{\partial z} \int (\mu B_0 + m_j v_{\parallel}^2) \left(f_{1j} + \frac{q_j \bar{\Phi}_1}{T_{0j}} f_{0j} \right) dv_{\parallel} d\mu \right\rangle_{yz}.$$

Note that f_{0j} as appearing in the above equation is not a function of x in the flux-tube limit.

The perturbed gyrocenter charge density term on the LHS of equation (B.6) can be split into two parts as follows:

$$\sum_j \rho_{1j} = \sum_j 2\pi q_j \int \bar{f}_{1j} J_v dv_{\parallel} d\mu + \sum_j 2\pi q_j \int (f_{1j} - \bar{f}_{1j}) J_v dv_{\parallel} d\mu \quad (\text{B.7})$$

To find an appropriate expression for the first term in the RHS of equation (B.7), we make use of the quasi-neutrality equation:

$$\sum_j n_{1j} q_j = 0. \quad (\text{B.8})$$

Note that here n_{1j} is the perturbed particle density expressed in particle coordinates [not to be confused with the perturbed gyrocenter density n_{1j} defined in equation (B.4)]. The particle density can itself then be expressed in terms of gyrocenter variables [see equation (2.57)]:

$$n_{1j} = n_{1gj} + n_{1pj}, \quad (\text{B.9})$$

where n_{1gj} is the perturbed 'gyro-density' defined as

$$n_{1gj} = 2\pi \int \bar{f}_{1j} J_v dv_{\parallel} d\mu \quad (\text{B.10})$$

and n_{1pj} is the 'polarization density', which in the long wavelength limit (correct to second order in $k_{\perp} \rho_j$), can be approximated by the differential operator:

$$n_{1pj} \simeq \nabla_{\perp} \cdot \left(\frac{n_{0j} m_j}{q_j B_0^2} \nabla_{\perp} \Phi \right). \quad (\text{B.11})$$

Using equations (B.8)-(B.11), we obtain a useful expression for the first term on the RHS of equation (B.7):

$$\sum_j 2\pi q_j \int \bar{f}_{1j} J_v dv_{\parallel} d\mu = - \sum_j \nabla_{\perp} \cdot \left(\frac{n_{0j} m_j}{B_0^2} \nabla_{\perp} \Phi \right). \quad (\text{B.12})$$

In the long wavelength limit (correct to second order in $k_{\perp} \rho_j$), the gyro-averaging operator

B.1. Derivation in GENE flux-tube model

can be expressed as

$$\bar{\mathcal{A}} \simeq \left[1 + \frac{1}{2} \nabla_{\perp} \cdot \left(\frac{m_j \mu}{q_j^2 B_0} \nabla_{\perp} \right) \right] \mathcal{A}. \quad (\text{B.13})$$

Using this approximation, the second term in equation (B.7) can be expressed as:

$$\sum_j 2\pi q_j \int (f_{1j} - \bar{f}_{1j}) J_v dv_{\parallel} d\mu = - \sum_j \nabla_{\perp} \cdot \left(\frac{1}{2q_j} \frac{m_j}{B_0^2} \nabla_{\perp} P_{1\perp j} \right), \quad (\text{B.14})$$

where $P_{1\perp j} = 2\pi \int f_{1j} \mu B_0 dv_{\parallel} d\mu$ is the pressure perturbations perpendicular to \mathbf{B}_0 .

Now, using equations (B.7), (B.12) and (B.14), and the relation $\nabla_{\perp}^2 \simeq g^{xx} \partial^2 / \partial x^2 + 2g^{xy} \partial^2 / \partial x \partial y + g^{yy} \partial^2 / \partial y^2$, the LHS of equation (B.6) becomes:

$$\frac{\partial}{\partial t} \sum_j \langle \rho_{1j} \rangle_{yz} = - \sum_j \frac{\partial}{\partial t} \Omega_j - \sum_j \frac{\partial}{\partial t} \Pi_j, \quad (\text{B.15})$$

where

$$\Omega_j = n_{0j} m_j \frac{\partial^2}{\partial x^2} \left\langle \frac{g^{xx}}{B_0^2} \Phi_1 \right\rangle_{yz} \quad \text{and} \quad \Pi_j = \frac{m_j}{2q_j} \frac{\partial^2}{\partial x^2} \left\langle \frac{g^{xx}}{B_0^2} P_{1\perp j} \right\rangle_{yz}.$$

Ω_j (not to be confused with the larmor frequency) represents the vorticity associated to zonal flows and is closely related to the typical definition of zonal flow shearing rate $\omega_{E \times B} \simeq (1/B_0) \partial^2 \langle \Phi_1 \rangle_{yz} / \partial x^2$ [Dominski et al., 2015] (by approximating $g^{xx} \simeq 1$ and neglecting the z dependence of B_0 , we obtain $\omega_{E \times B} \simeq \Omega_j B_0 / (n_{0j} m_j)$). The term Π_j is a perpendicular pressure perturbation term related to lowest order finite larmor radius effects.

Following a similar procedure as for handling the LHS of equation (B.7), the first term in the RHS of Eq. B.6 can be split into two parts:

$$\begin{aligned} \sum_j \frac{2\pi q_j}{\mathcal{C}} \frac{\partial}{\partial x} \left\langle \frac{B_0}{m_j} \int \frac{\partial \bar{\Phi}_1}{\partial y} f_{1j} dv_{\parallel} d\mu \right\rangle_{yz} &= \sum_j \frac{2\pi q_j}{\mathcal{C}} \frac{\partial}{\partial x} \left\langle \frac{B_0}{m_j} \frac{\partial \Phi_1}{\partial y} \int \bar{f}_{1j} dv_{\parallel} d\mu \right\rangle_{yz} \\ &\quad + \sum_j \frac{2\pi q_j}{\mathcal{C}} \frac{\partial}{\partial x} \left\langle \frac{B_0}{m_j} \int \left(\frac{\partial \bar{\Phi}_1}{\partial y} f_{1j} - \frac{\partial \Phi_1}{\partial y} \bar{f}_{1j} \right) dv_{\parallel} d\mu \right\rangle_{yz}. \end{aligned} \quad (\text{B.16})$$

Using equation (B.12), and performing some algebraic manipulations, the first term on

Appendix B. Flux-surface-averaged poloidal momentum conservation equation

the RHS of equation (B.16) becomes:

$$\begin{aligned} \sum_j \frac{2\pi q_j}{\mathcal{C}} \frac{\partial}{\partial x} \left\langle \frac{B_0}{m_j} \frac{\partial \Phi_1}{\partial y} \int \bar{f}_{1j} dv_{\parallel} d\mu \right\rangle_{yz} &= - \sum_j \frac{n_{0j} m_j}{\mathcal{C}} \frac{\partial}{\partial x} \left\langle \frac{1}{B_0^2} \frac{\partial \Phi_1}{\partial y} \nabla_{\perp}^2 \Phi_1 \right\rangle_{yz} \\ &= - \sum_j \frac{\partial^2}{\partial x^2} \mathcal{R}_j \end{aligned} \quad (\text{B.17})$$

where $\mathcal{R}_j = (n_{0j} m_j / \mathcal{C}) \text{RS}$ and the Reynolds stress contribution RS is defined as

$$\text{RS} = \left\langle \frac{1}{B_0^2} \frac{\partial \Phi_1}{\partial y} \left(g^{xx} \frac{\partial \Phi_1}{\partial x} + g^{xy} \frac{\partial \Phi_1}{\partial y} \right) \right\rangle_{yz}.$$

Using the long wavelength approximation of the gyro-averaging operator given in equation (B.13), and performing some algebraic manipulations, the second term on the RHS of equation (B.16) becomes:

$$\begin{aligned} \sum_j \frac{2\pi q_j}{\mathcal{C}} \frac{\partial}{\partial x} \left\langle \frac{B_0}{m_j} \int \left(\frac{\partial \bar{\Phi}_1}{\partial y} f_{1j} - \frac{\partial \Phi_1}{\partial y} \bar{f}_{1j} \right) dv_{\parallel} d\mu \right\rangle_{yz} \\ = - \sum_j \frac{m_j}{2q_j \mathcal{C}} \frac{\partial}{\partial x} \left\langle \frac{1}{B_0^2} \left(\nabla_{\perp}^2 \Phi_1 \frac{\partial P_{1\perp j}}{\partial y} + \frac{\partial \Phi_1}{\partial y} \nabla_{\perp}^2 P_{1\perp j} \right) \right\rangle_{yz} \\ = - \sum_j \frac{\partial^2}{\partial x^2} \mathcal{P}_j \end{aligned} \quad (\text{B.18})$$

where \mathcal{P}_j is defined as

$$\mathcal{P}_j = \frac{m_j}{2q_j \mathcal{C}} \left\langle \frac{1}{B_0^2} \left(g^{xx} \frac{\partial \Phi_1}{\partial x} \frac{\partial P_{1\perp j}}{\partial y} + 2g^{xy} \frac{\partial \Phi_1}{\partial y} \frac{\partial P_{1\perp j}}{\partial y} + g^{xx} \frac{\partial \Phi_1}{\partial y} \frac{\partial P_{1\perp j}}{\partial x} \right) \right\rangle_{yz}.$$

\mathcal{P}_j can be identified as a finite larmor radius correction term to the Reynolds stress term.

Note that terms Ω_j , Π_j , \mathcal{R}_j and \mathcal{P}_j are proportional to m_j . Therefore, in the limit of $m_i \gg m_e$, and assuming that there is only one ion species denoted by index 'i', equation (B.6), using the results from equation (B.15) - (B.18), becomes:

$$\frac{\partial}{\partial t} (\Omega_i + \Pi_i) = \underbrace{\frac{\partial^2}{\partial x^2} (\mathcal{R}_i + \mathcal{P}_i)}_{\text{non-linear terms}} + \frac{\partial}{\partial x} \mathcal{N}. \quad (\text{B.19})$$

B.2 Testing validity in linear case: Rosenbluth-Hinton test

The Rosenbluth-Hinton test [Rosenbluth and Hinton, 1998] computes the linear evolution of a zonal mode. Using analytic calculations, starting from the gyrokinetic equation in the electrostatic and collisionless limit, an initial zonal perturbation can be shown to undergo Geodesic Acoustic Mode (GAM) [Winsor et al., 1968] oscillations, which get damped to a residual level, as:

$$\frac{\langle \Phi(t) \rangle}{\langle \Phi(0) \rangle} = (1 - A_R)e^{-\gamma_G t} \cos(\omega_G t) + A_R,$$

where $\langle \Phi(t) \rangle$ is the flux-surface averaged electrostatic potential measured at time t , ω_G and γ_G are the GAM frequency and damping rate respectively, and A_R is the residual, which for the circular geometry, takes the form

$$A_R = \frac{1}{1 + 1.6q_0^2/\sqrt{r/R}}, \quad (\text{B.20})$$

with q_0 , r and R being the local safety factor, local minor radius and the major radius respectively.

Here, the validity of the poloidal momentum conservation equation (B.19) is tested on the output of a Rosenbluth-Hinton test, considering adiabatic electrons. For this test, the electrostatic and collisionless limit is considered, and the evolution of a zonal mode ($k_x \rho_i = 0.05, k_y = 0$) is chosen so that the long wavelength approximation ($k_\perp \rho_i \ll 1$) under which equation (B.19) is derived, is valid. The ad-hoc circular geometry is considered, with $q_0 = 1.427$, $\epsilon = r/R = 0.18$, and $\hat{s} = 0.847$, along with numerical resolutions $N_z \times N_{v_\parallel} \times N_\mu = 32 \times 256 \times 32$. The resulting flux-surface averaged electrostatic potential normalised by its initial value, *i.e.* $\langle \Phi(t) \rangle / \langle \Phi(0) \rangle$, is plotted in figure B.1(a), where one can observe the initial GAM oscillations relaxing towards the residual $A_R = 0.12$. In figure B.1(b), the time evolution of the linear terms in the poloidal momentum conservation equation (B.19) are plotted, where a good match is obtained between the LHS and RHS, thereby justifying the validity of this equation in the linear limit. It is interesting to note that the contribution from the perpendicular gyrocenter pressure term $\partial \Pi_i / \partial t$ is negligible in this case.

B.3 Testing validity in non-linear case: Turbulence simulation

In this subsection, the validity of the poloidal momentum conservation equation (B.19) is checked for a full turbulence simulation. The output of the kinetic electron simulation with $R/L_{T,i} = 6$ and $k_{y,\min} \rho_i = 0.07$, considered in the $k_{y,\min} \rho_i$ scan in chapter 3 (whose other parameters are given in table 3.1), is considered here as well. In figure B.2, the

Appendix B. Flux-surface-averaged poloidal momentum conservation equation

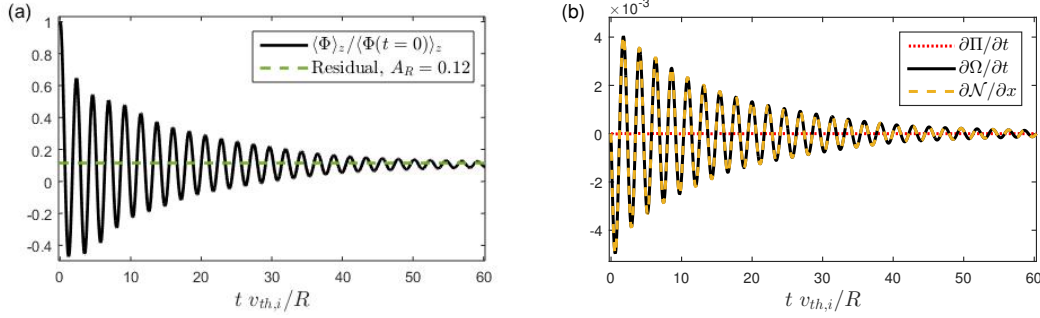


Figure B.1: Results of Rosenbluth-Hinton test. (a) Solid black line represents the flux-surface averaged electrostatic potential normalised by its initial value, *i.e.* $\langle \Phi(t) \rangle / \langle \Phi(0) \rangle$, plotted as a function of time. Dashed green line represents the residual, defined in equation (B.20). (b) Solid black line, yellow dashed line and dotted red line represent the terms $\partial \Omega / \partial t$, $\partial \Pi / \partial t$ and $\partial \mathcal{N} / \partial x$ terms respectively, plotted as a function of time.

various terms in equation (B.19) are plotted in the (x, t) plane, after filtering out the $k_x \rho_i > 0.5$ and $k_y \rho_i > 0.5$ contributions. This post-diagnostic filtering was done so as to only retain fluctuations verifying the long wavelength limit ($k_\perp \rho_i \ll 1$) under which equation (B.19) was derived. In these figures, a good match is obtained between the LHS and RHS of equation (B.19). Unlike in the Rosenbluth-Hinton test, the contribution from the $\partial \Pi / \partial t$ term is non-negligible, but is still lower than that of $\partial \Omega / \partial t$, approximately by a factor 1/3. The neoclassical term $\partial \mathcal{N} / \partial x$ is found to be a dominant contribution to the RHS. However, being a linear term, the neoclassical term only accounts for the damping of zonal flows. The zonal flows are in fact driven via the non-linear terms, the second radial derivatives of the Reynolds stress \mathcal{R} and the pressure term \mathcal{P} . The amplitudes of both these nonlinear terms are found to be comparable. An interesting observation is that there is a phase (sign) reversal between the neoclassical term and the Reynolds stress term. As mentioned in section 3.4.1, the positive correlation value [defined by equation (3.9)] of 0.37 between the shearing rate term Ω and the Reynolds stress term $\partial^2 \mathcal{R} / \partial x^2$ justifies considering the Reynolds stress term $\partial^2 \mathcal{R} / \partial x^2$ as a proxy for the drive of zonal flows. For corresponding adiabatic electron simulations (not shown here), the correlation is as high as 0.77.

B.3. Testing validity in non-linear case: Turbulence simulation

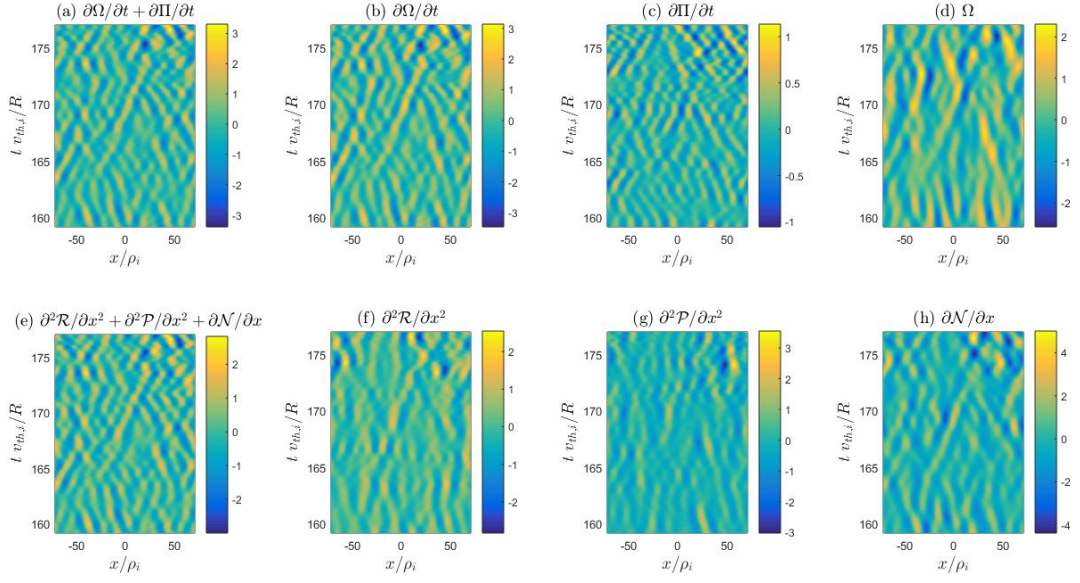


Figure B.2: Results of turbulence simulation, plotted in the (x, t) plane. (a) LHS of equation (B.19): $\partial\Omega/\partial t + \partial\Pi/\partial t$, (b) $\partial\Omega/\partial t$, (c) $\partial\Pi/\partial t$, (d) Ω , (e) RHS of equation (B.19): $\partial^2\mathcal{R}/\partial x^2 + \partial^2\mathcal{P}/\partial x^2 + \partial\mathcal{N}/\partial x$, (f) $\partial^2\mathcal{R}/\partial x^2$, (g) $\partial^2\mathcal{P}/\partial x^2$ and (h) $\partial\mathcal{N}/\partial x$.

C Local linear dispersion relation for analysing effect of collisions on ITG eigenmodes

In reference [Dominski et al., 2015], an analysis based on a local dispersion relation has been used to demonstrate the destabilising effect of non-adiabatic passing electron dynamics near MRSs and to estimate the radial size of the resulting fine-structures. In this appendix, the same analysis is extended to include collisional effects, with the aim of understanding the radial broadening of the fine-structures with collisions in ITG eigenmodes, observed in linear GENE flux-tube simulations with Landau collision operator as presented in section 4.1.1.2. A BGK-like collision operator [Bhatnagar et al., 1954] is chosen here to model collisions, following the approach presented in reference [Angus and Krasheninnikov, 2012]. In section C.1, first the validity of this simplified operator is tested for drift wave instability by comparing it with the full linearised Coulomb operator presented in reference [Jorge et al., 2018]. Section C.2 then addresses whether the resulting dispersion relation can be used to explain the radial broadening of the fine-structures with collisions.

C.1 Testing validity of the BGK-like collision operator

Similar to the analysis in reference [Angus and Krasheninnikov, 2012] based on slab geometry for drift wave modes, electrons are considered to be governed by the drift-kinetic equation with a BGK-like collisions operator:

$$\frac{\partial f_e}{\partial t} + \mathbf{v}_E \cdot \nabla f_e + v_{\parallel} \nabla_{\parallel} f_e + \frac{e}{m_e} \nabla_{\parallel} \Phi \frac{\partial f_e}{\partial v_{\parallel}} = -\nu(f_e - f_{M,e}), \quad (\text{C.1})$$

where f_e is the gyrophase independent electron distribution function and the Maxwellian distribution function is defined as $f_{M,e} = N_e \exp[-v^2/(2v_{Th,e}^2)]/(2\pi v_{Th,e}^2)^{3/2}$, with $v_{Th,e} = \sqrt{T_e/m_e}$. Note that $f_{M,e}$ is not a fixed stationary background distribution but a Maxwellian with density $n_e = n_{0,e} + n_{1,e}$ and temperature $T_e = T_{0,e} + T_{1,e}$ corresponding to the total values containing both the background and fluctuation contributions. The collision frequency ν is defined as $0.51/\tau_e$, where the electron collision

Appendix C. Local linear dispersion relation for analysing effect of collisions on ITG eigenmodes

time $\tau_e = 3\sqrt{m_e}T_{0,e}^{3/2}/4\sqrt{2}e^4n_{0,e}\ln\Lambda$ and $\ln\Lambda \simeq 10$ is the Coulomb logarithm [Braginskii, 1965]. The collision operator $-\nu(f - f_M)$ represents the loss of electron momentum $m_e \int v_{\parallel} f_e d\mathbf{v}$ to ions due to a difference in the electron and ion mean velocities. Since the electron-electron energy exchange rate is of the same order as electron-ion momentum exchange rate, this collision operator also approximates the collisional relaxation of electrons with themselves. The thermal energy exchange of electrons with ions is ignored since it is smaller than ν approximately by a factor m_e/m_i .

To obtain the perturbed form of the distribution function from equation (C.1), one can perform the analysis mentioned in section 2.5.1 leading up to equation (2.73), but in this case, for electrons, in the slab geometry ($1/L_B = 0$, $\omega_{D,e} = 0$), in the limit of drift kinetics ($k_{\perp}\rho_e \ll 1$), and with collisions. The resulting perturbed distribution function is:

$$\hat{f}_{1,e} = \frac{\frac{e\hat{\Phi}_1}{T_{0,e}}(k_{\parallel}v_{\parallel} - \omega_e^*)f_{0,M,e} - i\nu\hat{f}_{1,M,e}}{k_{\parallel}v_{\parallel} - \omega + i\nu}, \quad (\text{C.2})$$

where $\omega_e^* = \omega_{N,e}[1 + \eta_e T_{0,e}(\partial/\partial T_{0,e})]$, $\omega_{N,e} = k_y T_{0,e}/eB_0 L_N$, $\eta_e = L_N/L_{T,e}$, $f_{0,M,e}$ is the background Maxwellian and the linearised Maxwellian $\hat{f}_{1,M,e}$ is given by:

$$\hat{f}_{1,M,e} = \left[\frac{\hat{n}_{1,e}}{n_0} + \frac{1}{2} \left(\frac{v^2}{v_{th,e}^2} - 3 \right) \frac{\hat{T}_{1,e}}{T_{0,e}} \right] f_{0,M,e}. \quad (\text{C.3})$$

Now, the electron density perturbation $\hat{n}_{1,e}$ can be found in terms of the potential perturbations $\hat{\Phi}_1$ by taking the zeroth and second order velocity moments of equation (C.2) and carrying out some algebraic manipulations, similar to that given in the Appendix of reference [Angus and Krasheninnikov, 2012], to remove the temperature perturbations $\hat{T}_{1,e}$. Note that, while in reference [Angus and Krasheninnikov, 2012] only a background density gradient is considered, in this analysis, a gradient in the background temperature is also considered in order to model either ITG or TEM modes. One thus obtains:

$$\frac{\hat{n}_{1,e}}{n_0} = \frac{e\hat{\Phi}}{T_{0,e}} \left\{ \frac{\left[1 + \left(\alpha + \frac{\omega_{N,e}}{2\sqrt{2}v_{th,e}k_{\parallel}}\eta_e - \frac{\omega_e^*}{\sqrt{2}v_{th,e}k_{\parallel}} \right) Z(\alpha) \right] A + \frac{i\nu}{\sqrt{2}v_{th,e}k_{\parallel}} \left(\frac{\tilde{\omega}_e^* \alpha}{\sqrt{2}v_{th,e}k_{\parallel}} - \frac{1}{2} \right) B}{\left[1 + \left(\alpha - \frac{\omega}{\sqrt{2}v_{th,e}k_{\parallel}} \right) Z(\alpha) \right] A + \frac{i\nu}{\sqrt{2}v_{th,e}k_{\parallel}} \left(\frac{\omega \alpha}{\sqrt{2}v_{th,e}k_{\parallel}} - \frac{1}{2} \right) B} \right\}, \quad (\text{C.4})$$

where $Z(\alpha) = (1/\sqrt{\pi}) \int_{-\infty}^{\infty} \exp(-x^2)/(x - \alpha) dx$ is the plasma dispersion function, $\alpha = (\omega + i\nu)/(\sqrt{2}v_{th,e}k_{\parallel})$, $A = 3/2 + i\nu Z(\alpha)/\sqrt{2}v_{th,e}k_{\parallel}$, $\tilde{\omega}_e^* = \omega_{N,e}(1 + \eta_e/2)$ and $B = \alpha + (\alpha^2 - 1/2)Z(\alpha)$. Note that the $\partial/\partial T_{0,e}$ operator in ω_e^* acts only on $Z(\alpha)$.

For ions, the density response $\hat{n}_{1,i} = \int \hat{f}_{1,i} d^3v$ can be found using equation (2.73) for the slab geometry $\omega_{D,i} = 0$ [details on the derivation for a more general case can be seen in

C.1. Testing validity of the BGK-like collision operator

reference [Brunner, 2014], leading up to equation (1.18)]:

$$\frac{\hat{n}_{1,i}}{n_0} = -\frac{q_i \hat{\Phi}}{T_{0,i}} \left\{ 1 + \left(1 - \frac{\omega_i^*}{\omega} \right) \left[W \left(\frac{\omega}{k_{\parallel} v_{th,i}} \right) - 1 \right] e^{-(k_y \rho_i)^2} I_0(k_y^2 \rho_i^2) \right\}, \quad (\text{C.5})$$

where $W(x) = (x/\sqrt{2})Z(x/\sqrt{2}) + 1$ and I_0 is the modified Bessel function of first kind and of order 0. The finite ion Larmor radius effects are captured by the term $e^{-(k_y \rho_i)^2} I_0(k_y^2 \rho_i^2)$, which if needed to be neglected, can be replaced with 1 (limit of $k_y \rho_i \ll 1$, correct to zeroth order in $k_y \rho_i$).

A dispersion relation with the BGK-like collision operator can then be obtained from the quasi-neutrality equation $q_i \hat{n}_{1,i} + e \hat{n}_{1,e} = 0$, where the perturbed electron and ion density responses are given by equations (C.4) and (C.5) respectively, which can be solved for $\omega \in \mathbb{C}$ as a function of k_y and k_{\parallel} . In figure C.1, the growth rate $\gamma = \text{Imag}[\omega]$ is plotted as a function of k_y and k_{\parallel} for four different values of collisionality, with $T_{0,e}/T_{0,i} = 100$, $m_i/m_e = 1836$ and $\eta_{i,e} = 0$, considering the case of drift wave instability. The ion FLR effects are neglected by setting $e^{-(k_y \rho_i)^2} I_0(k_y^2 \rho_i^2) = 1$; in fact it is found to have a negligible effect on ω . The collision rate ν is normalised as $\nu_R = \nu L_N / c_s$, k_y is normalised as $k_y \rho_s$ and k_{\parallel} is normalised as $k_{\parallel} L_N$, so that a direct comparison can be made with figure 1 in reference [Jorge et al., 2018], which is obtained with the same set of parameters and reproduced here as figure C.2. In reference [Jorge et al., 2018] (and therefore in figure C.2), a drift-kinetic moment hierarchy model is considered with a full linearised Coulomb (\sim Landau) collision operator, which is then used to study the effect of collisions on the drift wave instability, having the parameters considered before, at arbitrary collisionalities.

Note that, unlike the full Coulomb collision operator, the BGK-like operator considered in this study is a very simple approximate collision operator. However, despite the many limitations of the considered BGK-like collision model, including that it does not account for ion-ion collisions, corresponding results (figure C.1) are found to match surprisingly well with the ones obtained with the full Coulomb collision operator (figure C.2). Two qualitative properties remain consistent across the results obtained with the two different collision operators: one, as collisionality ν increases, the maximum growth rate over all (k_{\parallel}, k_y) decreases, and two, as ν increases, the k_{\parallel} at which this maximum growth rate occurs increases. The growth rate γ as a function of k_{\parallel} for two different values of k_y is shown in figure C.3(a), for both collision operators, for the case with $\nu_R = 1$. Quantitatively, the growth rates between the two collision operators are found to differ by a maximum of $\sim 20\%$. This can also be seen in figure C.3(b), where the maximum of the growth rates over all k_y and k_{\parallel} are plotted as a function of collisionality. As collisionality decreases, the difference in the growth rate between the two collision operators becomes smaller, with both the cases correctly approaching the collisionless limit.

Appendix C. Local linear dispersion relation for analysing effect of collisions on ITG eigenmodes

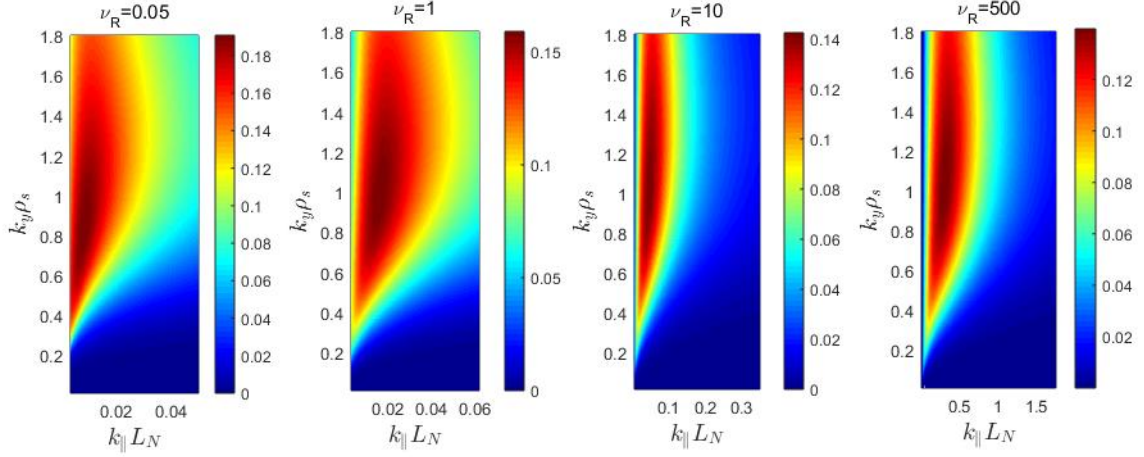


Figure C.1: Normalised growth rate $\gamma L_N / c_s$ of the drift wave instability as a function of $k_y \rho_s$ and $k_{\parallel} L_N$, obtained as solutions of the dispersion relation with the BGK-like collision operator, for four different values of collisionality $\nu_R = 0.05, 1, 10$ and 500 (from left to right) and with $T_{0,e}/T_{0,i} = 100$, $m_i/m_e = 1836$ and $\eta_{i,e} = 0$. The dispersion relation essentially results from the quasi-neutrality equation involving perturbed electron and ion density responses given in equations (C.4) and (C.5) respectively.

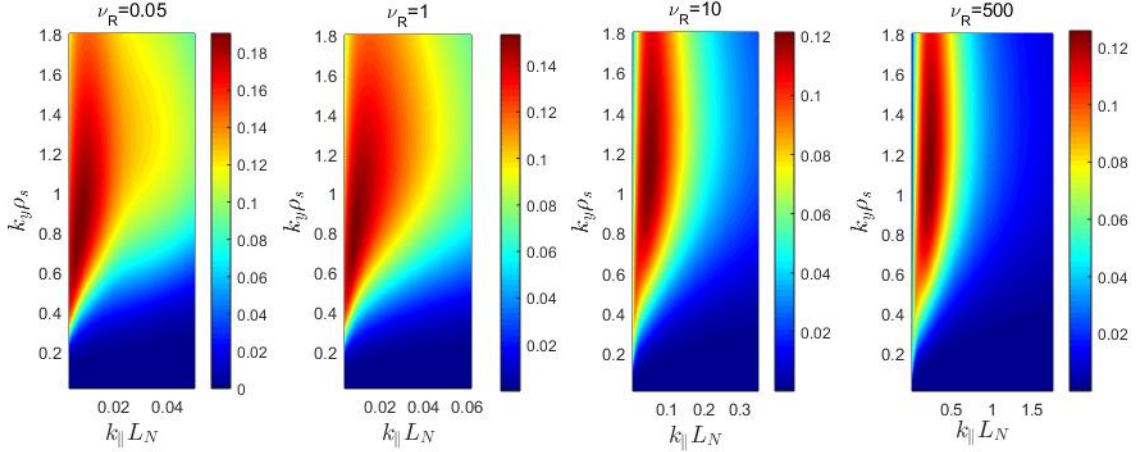


Figure C.2: Normalised growth rate $\gamma L_N / c_s$ of the drift wave instability as a function of $k_y \rho_s$ and $k_{\parallel} L_N$, obtained as solutions of the linearized moment hierarchy model with a full linearised Coulomb collision operator presented in reference [Jorge et al., 2018]. Four different values of collisionality are considered: $\nu_R = 0.05, 1, 10$ and 500 (from left to right), in the cold-ion limit with $m_i/m_e = 1836$. This figure is a replica of figure 1 in reference [Jorge et al., 2018].

C.2. Analysing the effect of collisions on the radial width of fine-structures

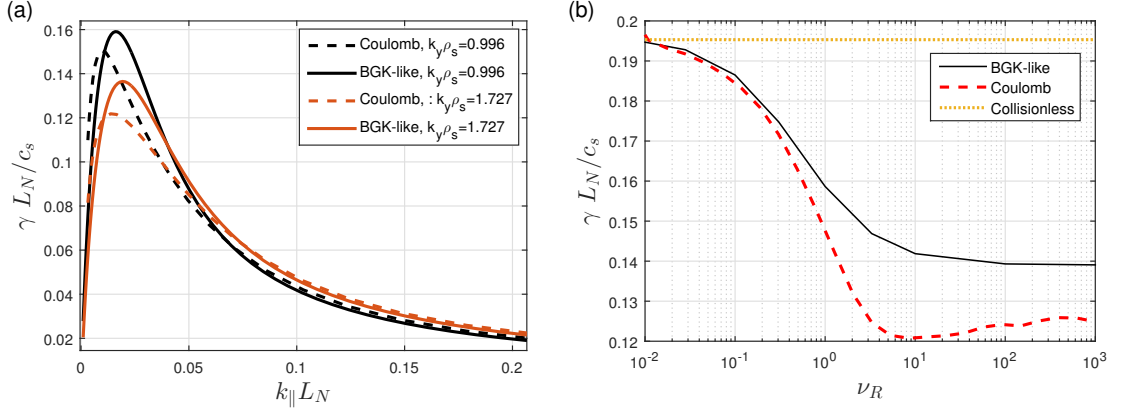


Figure C.3: (a) Solid lines represent normalised growth rate $\gamma L_N / c_s$ as a function of $k_{\parallel} L_N$, obtained as solutions of the dispersion relation with the BGK-like collision operator, with $\nu_R = 1$ and for $k_y \rho_s = 0.996$ (black colour) and 1.727 (orange colour). The plots are the $k_{\parallel} L_N$ traces in the $\nu_R = 1$ plot in figure C.1, at the respective k_y s. Dashed lines represent the same for the linearised moment hierarchy model with the full Coulomb collision operator, corresponding to $k_{\parallel} L_N$ traces in figure C.2. (b) Black line represents the maximum normalised growth rate $\gamma L_N / c_s$ over all k_y and k_{\parallel} , as a function of ν_R , obtained as solutions of the dispersion relation with the BGK-like collision operator. Dashed red line plots the same for the linearised moment hierarchy model with the full Coulomb collision operator. Dotted yellow line represents collisionless limit for reference.

C.2 Analysing the effect of collisions on the radial width of fine-structures

In reference [Dominski et al., 2015], an analysis based on a local dispersion relation has been used to estimate the radial width of fine-structures at MRSs related to non-adiabatic passing electron response, in a toroidal system. In this subsection, the same analysis is extended to include collisional effects, using the BGK-like collision operator discussed in the previous subsection.

Testing different electron models in the collisionless case

To begin with, the local dispersion relation in the collisionless case is considered. For both electrons and ions, the perturbed density response is given by

$$\delta \hat{n}_{1,j} = \int \hat{f}_{1,j} d^3v, \quad (\text{C.6})$$

Appendix C. Local linear dispersion relation for analysing effect of collisions on ITG eigenmodes

where $\hat{f}_{1,j}$ is the perturbed distribution function of species j obtained in equation (2.73). For ions, one thus obtains,

$$\frac{\hat{n}_{1,i}}{n_{0,i}} = -\frac{q_i \hat{\Phi}_1}{T_{0,i}} \left[1 - \int_{-\infty}^{\infty} d^3v J_0^2 \left(\frac{k_{\perp} v_{\perp}}{\Omega_i} \right) \frac{\omega - \omega_i^*}{\omega - k_{\parallel} v_{\parallel} - \omega_{D,i}} \frac{f_{0,i}}{n_{0,i}} \right]. \quad (\text{C.7})$$

Note that, unlike the slab case considered in the previous subsection, here the toroidal geometry is considered in view of studying the toroidal ITG instability relevant to the main studies in chapters 3 and 4. The effects of toroidicity manifests itself in the local dispersion relation as a finite contribution $\omega_{D,j} \neq 0$ from the grad-B and curvature drifts for any species j . The passing electron contribution can be separated out by considering appropriate limits for the velocity integrals in equation (C.6). For the passing contribution, the limits are $\int_{\text{pas}} d^3v = 2\pi \int_{-\infty}^{\infty} dv_{\parallel} \int_0^{v_{\perp,c}} dv_{\perp}$ where $v_{\perp,c} = v_{\parallel} / \tan \phi_v$ is the critical perpendicular velocity above which the electrons are trapped [see figure 1.2(a)]. Since the passing electrons are moving fast successively over the favorable and unfavorable sides of the poloidal plane with a transit frequency much higher than the typical ITG/TEM frequencies, one may average the passing electron density response over the poloidal coordinate so that the drift frequency $\omega_{D,e}$ gets averaged to 0. For the passing electrons, one thus obtains [see equation (3.8) in [Dominski, 2016]]:

$$\frac{\hat{n}_{1,e,\text{pass}}}{n_{0,e}} = (1 - \alpha_t) \frac{e \hat{\Phi}_1}{T_{0,e}} \left\{ 1 - \left(1 - \frac{\omega_e^*}{\omega} \right) \left[1 - \frac{W(\omega/k_{\parallel} v_{th,e}) - \alpha_t W(\omega/(k_{\parallel} v_{th,e} \alpha_t))}{1 - \alpha_t} \right] \right\}, \quad (\text{C.8})$$

where α_t is the average fraction of trapped particles. This passing slab-like electron response is labelled as *PassKinE*.

For the trapped electrons, one considers a bounce-averaged kinetic response mentioned in equation (2.79) and illustrated in detail in reference [Brunner, 1997]:

$$\frac{\hat{n}_{1,e,\text{trap}}}{n_{0,e}} = \alpha_t \frac{e \hat{\Phi}_1}{T_{0,e}} \left[1 + \left(1 - \frac{\omega_e^*}{\omega} \right) [z_{be}^2 W(z_{be})] \right], \quad (\text{C.9})$$

where $z_{be} = \text{sign}(\omega_{\varphi e}) \sqrt{2\omega/\omega_{\varphi e}}$, $\omega_{\varphi e} = n \langle \dot{\varphi} \rangle v_{th,e}^2 / \mathcal{E} \simeq 1$, $\mathcal{E} = (v_{\perp}^2 + v_{\parallel}^2)/2$ is the kinetic energy and $n \langle \dot{\varphi} \rangle$ is the toroidal precession drift frequency. This bounce averaged trapped kinetic electron response is labelled as *TrapKinE*.

The dispersion relation can be obtained from the quasi-neutrality equation:

$$q_i \frac{\delta \hat{n}_{1,i}}{n_{0,i}} - e \frac{\delta \hat{n}_{1,e,\text{pass}}}{n_{0,e}} - e \frac{\delta \hat{n}_{1,e,\text{trap}}}{n_{0,e}} = 0, \quad (\text{C.10})$$

which when solved gives $\omega \in \mathbb{C}$ as a function of k_{\parallel} and k_y . In figure C.4, the solid blue line, labelled as *PassKinE+TrapKinE*, represents the growth rate γ and real frequency ω_r

C.2. Analysing the effect of collisions on the radial width of fine-structures

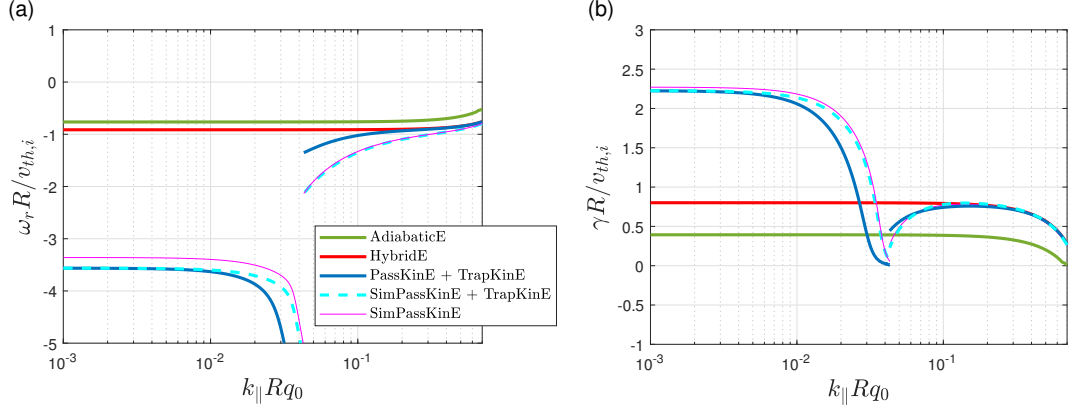


Figure C.4: (a) Normalised real frequency $\omega_r R/v_{th,i}$ and (b) growth rate $\gamma R/v_{th,i}$ as a function of $k_{||} R q_0$, obtained as solutions of the local dispersion relation in collisionless limit, considering different electron models. Green, red, solid dark blue, dashed light blue and magenta represent the adiabatic, hybrid, *PassKinE* + *TrapKinE*, *SimPassKinE* + *TrapKinE* and *SimPassKinE* electron models respectively. Physical parameters are the same as that given in table 3.1 and $k_y \rho_i = 0.3$.

obtained from the dispersion relation (C.10) for $k_y \rho_i = 0.3$, where the density responses are given by equations (C.7), (C.8) and (C.9). The physical parameters given in table 3.1 are considered, leading to a toroidal ITG type instability. For comparison, the results with adiabatic and hybrid electron response are also shown with green and red lines, labelled as *AdiabaticE* and *HybridE*, respectively. For the adiabatic electron case, one considers $\hat{n}_{1,e}/n_{0,e} = \hat{n}_{1,e,pass}/n_{0,e} + \hat{n}_{1,e,trap}/n_{0,e} = e\hat{\Phi}_1/T_{0,e}$ and for the hybrid case one considers adiabatic passing electron response $\hat{n}_{1,e,pass}/n_{0,e} = (1 - \alpha_t)e\hat{\Phi}_1/T_{0,e}$ along with the bounce averaged kinetic response of the trapped electrons given in equation (C.9). The plots corresponding to these three different electron models, shown in figure C.4, are the same as that in figure 6(a) of reference [Dominski et al., 2015].

The wave vector of a Fourier mode with poloidal and toroidal mode numbers m and n respectively is given by $\mathbf{k} = m\nabla\chi + n\nabla\varphi$. Its component parallel to the background magnetic field \mathbf{B}_0 is then given by

$$k_{||} = \mathbf{k} \cdot \frac{\mathbf{B}_0}{B_0} = \frac{\mathbf{B}_0 \cdot \nabla\chi}{B_0} [m + nq_s(x)] = \frac{\mathbf{B}_0 \nabla \cdot \varphi}{B_0 q_s} [m + nq_s(x)] \simeq \frac{1}{Rq_s} [m + nq_s(x)], \quad (\text{C.11})$$

having used $q_s = \mathbf{B}_0 \cdot \nabla\varphi / \mathbf{B}_0 \cdot \nabla\chi$. As one approaches the MRS where $q_0 = q_s(x_0) = -m/n$, the parallel wave number $k_{||} \rightarrow 0$ (and the condition $[\omega_r/k_{||} \ll v_{th,e}]$ for adiabatic electron response is clearly violated). Note that the growth rate corresponding to the *PassKinE*+*TrapKinE* case in figure C.4 is higher than those of the *HybridE* and *AdiabaticE* cases as $k_{||} \rightarrow 0$, which clearly illustrates the destabilising effect of non-adiabatic passing electron response near MRS.

Appendix C. Local linear dispersion relation for analysing effect of collisions on ITG eigenmodes

Since the passing electron kinetic response considered in equation (C.8) is essentially slab like after having set $\omega_{D,e} = 0$, one may further simplify it as a product of the passing electron fraction $(1 - \alpha_t)$ and the electron response in the slab limit, *i.e.*

$$\frac{\hat{n}_{1,e,\text{pass}}}{n_{0,e}} = (1 - \alpha_t) \frac{\hat{n}_{1,e,\text{slab}}}{n_{0,e}}. \quad (\text{C.12})$$

where the density response in the slab geometry, in the collisionless case, is given by,

$$\frac{\hat{n}_{1,e,\text{slab}}}{n_{0,e}} = \frac{e\Phi}{T_{0,e}} \left\{ 1 - \left(1 - \frac{\omega_e^*}{\omega} \right) \left[1 - W(\omega/k_{\parallel} v_{th,e}) \right] \right\}. \quad (\text{C.13})$$

Note that $\hat{n}_{1,e,\text{slab}}/n_{0,e}$ is the same as equation (C.4) in the limit of no collisions, *i.e.* $\nu = 0$. In figure C.4, the solution of the dispersion relation (C.10), where the density responses are given by equations (C.7), (C.12), (C.13) and (C.9), is shown using dashed light blue line and labelled as *SimPassKinE+TrapKinE*. The result matches well with the *PassKinE+TrapKinE* case, except for slight deviations in the intermediate values of $k_{\parallel} R_{q0}$ considered.

The dispersion relation can be simplified again for the case of ITG instability by considering the kinetic response of trapped electron to be passive [Dominski et al., 2015]. This is justified in figure C.4, where the solutions of the dispersion relation (C.10) with the density responses given in equations (C.7), (C.12) and (C.13), and with no trapped electron contribution ($\hat{n}_{1,e,\text{trap}}/n_{0,j} = 0$), is plotted. The result, shown with solid magenta line and labelled as *SimPassKinE*, matches well with the cases *SimPassKinE+TrapKinE* and *PassKinE+TrapKinE* where the kinetic trapped electron response is also considered.

Modelling the effect of collisions in local dispersion relation

Having justified the use of the simplified slab-like passing electron response *SimPassKinE* instead of the full kinetic electron response (*SimPassKinE+TrapKinE* and *PassKinE+TrapKinE*), one can now easily model the effect of collisions in the dispersion relation (C.10), by considering the electron response given in equation (C.12), but with $\hat{n}_{1,e,\text{slab}}/n_{0,e}$ given by equation (C.4) which models collisions with the BGK-like collision operator. For the ion density response, equation (C.7) is used and the trapped electron response is assumed to be passive. The resulting dispersion relation with the BGK-like collision operator can be considered to solve for $\omega \in \mathbb{C}$ as a function of k_y and k_{\parallel} . In figure C.5, the growth rates and real frequencies thus obtained are plotted as a function k_{\parallel} , for $k_y \rho_i = 0.3$, for a range of collisionalities [ν_c is the GENE collisionality defined in equation (2.99)]. The same physical parameters as those given in table 3.1 are considered. Even with finite collisionality, the maximum growth rate is still observed at $k_{\parallel} = 0$, similar to that observed in the case with no collisions. It is interesting to note that for lower values of collisionality considered, two different branches of eigenmodes are observed in the limit of $k_{\parallel} \rightarrow 0$ and $k_{\parallel} \gtrsim 0.04$, reflected by the discontinuity in the

C.2. Analysing the effect of collisions on the radial width of fine-structures

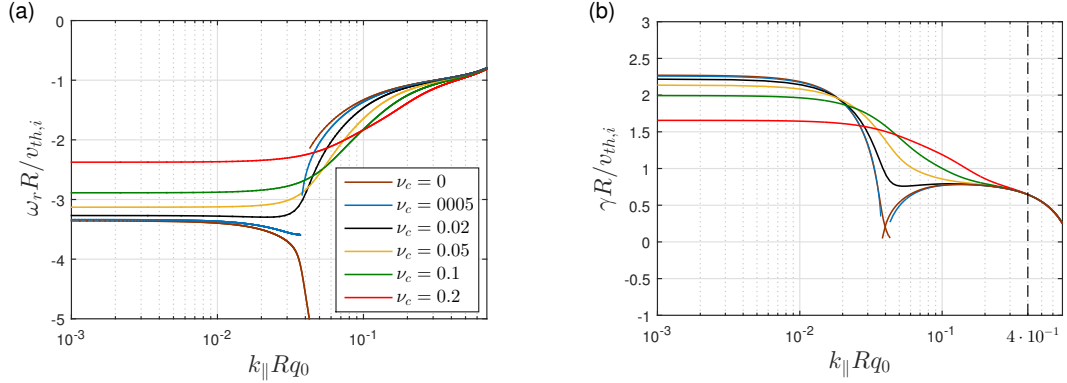


Figure C.5: (a) Normalised real frequency $\omega_r R / v_{th,i}$ and (b) growth rate $\gamma R / v_{th,i}$ as a function of $k_{\parallel} R q_0$, obtained as solutions of the dispersion relation with the BGK-like collision operator, considering the *SimPassKinE* electron model, for $k_y \rho_i = 0.3$, for different values of collisionality ν_c .

growth rate and real frequency at $k_{\parallel} R q_0 \simeq 0.04$, and that as collisionality is increased, these branches merge into one.

In figure C.6, the growth rate and real frequency are plotted as a function of collisionality ν_c , for the case with $k_{\parallel} R q_0 = 0.001$ (practical limit of $k_{\parallel} \rightarrow 0$). One observes a decrease in growth rates with increasing collisionality, similar to that observed in linear GENE simulations (see figure 4.1) for the same set of physical parameters. To be more quantitative, as ν_c increases from 0 to 0.01, the growth rate in GENE simulations drop by roughly 40%. Recollecting from section 4.1.1.1, this decrease in the growth rate in GENE simulations is a result of collisions leading to (de-)trapping of electrons and as a result, trapped electrons responding adiabatically. In the collisionless local dispersion relation results shown in figure C.4(b), this corresponds to the $\sim 50\%$ decrease in growth rate γ from the *HybridE* electron model result which considers non-adiabatic trapped electron response, to the fully *AdiabaticE* electron result.

However, in figure C.6(b) the corresponding drop is only approximately 1%. That is, the analysis based on the local dispersion relation, modelling collisions with the BGK-like collision operator, is not able to quantitatively predict the drop in growth rates with increasing collisionality.

Estimating the radial width of fine-structures

One now proceeds to find if the radial width of fine-structures can be predicted using the analysis based on the local dispersion relation, explained in the following.

Taylor expanding the relation for k_{\parallel} in equation (C.11), around x_0 to first order in the

Appendix C. Local linear dispersion relation for analysing effect of collisions on ITG eigenmodes

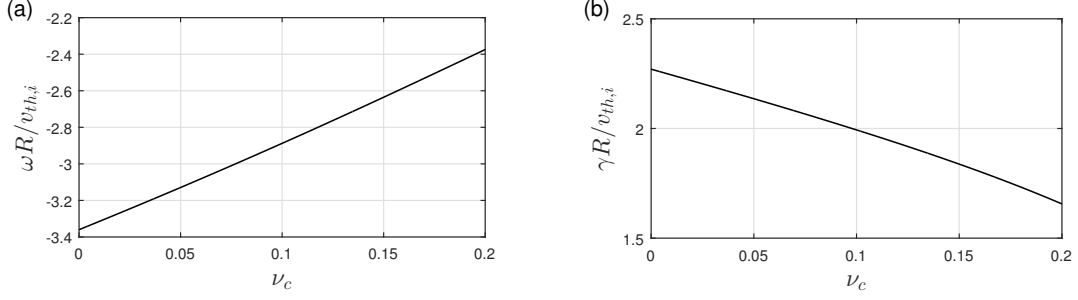


Figure C.6: (a) Normalised real frequency $\omega_r R/v_{th,i}$ and (b) growth rate $\gamma R/v_{th,i}$ as a function of collision frequency ν_c , obtained as solutions of the dispersion relation with the BGK-like collision operator, for $k_{\parallel} R q_0 = 0.001$, considering the *SimPassKinE* electron model. Physical parameters are the same as those given in table 3.1 and $k_y \rho_i = 0.3$.

small deviation $x = x - x_0$, one has

$$k_{\parallel}(x) \simeq \frac{\hat{s} k_y}{q_0 R} x, \quad (\text{C.14})$$

having used the linearised safety factor $q_s(x) \simeq q_0(1 + \hat{s}x/r_0)$, $k_y = -nq_0/r_0$ and $\mathbf{B}_0 \cdot \nabla \varphi \simeq B_0/R$. Using this definition of $k_{\parallel}(x)$, the width of the fine-structure (which is a result of non-adiabatic passing electron dynamics) can be approximated from figures C.4(a) and C.5(a) as that x where $|\omega_r/k_{\parallel}(x)v_{th,e}| = 1$, *i.e.* where the adiabatic electron approximation (valid in the limit $|\omega_r/k_{\parallel}(x)v_{th,e}| \ll 1$) breaks down. This approach is found to be valid in the collisionless limit [Dominski et al., 2015]. The same estimation for the radial size of the fine-structures is used in the case with collisions as well, and corresponding results are plotted in figure C.7 with green triangles. The actual radial width of fine-structures, estimated as the full width at half maximum of the z-averaged absolute value of the electrostatic potential $\langle |\Phi| \rangle_z$, in corresponding linear GENE simulations are also plotted as black crosses. While for the collisionless case ($\nu_c = 0$) there is a good agreement in the radial width between the local dispersion relation based estimate and the GENE result, they are seen to diverge as ν_c increases.

However, it should be noted that the condition for adiabatic electron response $|\omega_r/k_{\parallel}(x)v_{th,e}| \ll 1$ is true only in the collisionless limit. In the fluid description, assuming electrons to be isothermal on a magnetic surface, the linearised continuity and parallel force balance equation can be written as

$$\begin{aligned} \frac{\partial n_{1,e}}{\partial t} &= -n_{0,e} \nabla_{\parallel} v_{1,e} \\ m_e n_{0,e} \frac{\partial v_{e,1}}{\partial t} &= -T_{0,e} \nabla_{\parallel} n_{1,e} + e n_{0,e} \nabla_{\parallel} \Phi_1 - m_e n_{0,e} \nu (v_{1,e} - v_{1,i}), \end{aligned} \quad (\text{C.15})$$

where the friction force term $-m_e n_{0,e} \nu (v_{1,e} - v_{1,i})$ measures the rate of momentum loss from electrons to ions due to collisions. Identifying $\partial/\partial t \sim \omega_r$ and $\nabla_{\parallel} \sim k_{\parallel}$, under the

C.2. Analysing the effect of collisions on the radial width of fine-structures

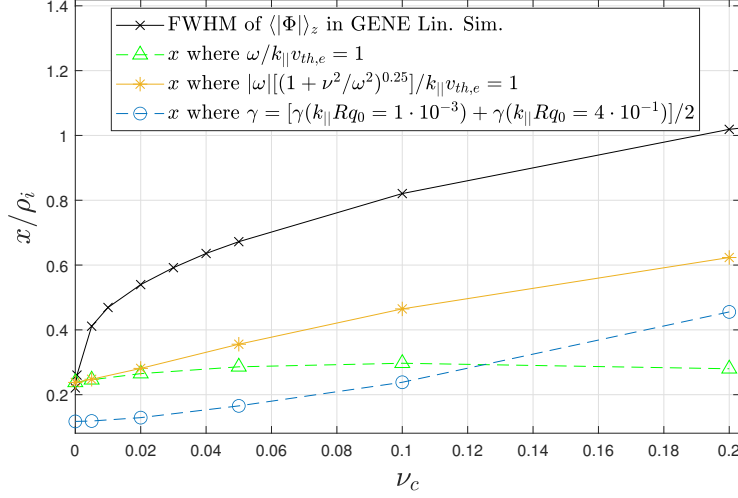


Figure C.7: Green triangles represent the radial width of the fine structures estimated as that x where $|\omega_r/k_||x)v_{th,e}| = 1$. Yellow asterisks represent the radial width of the fine structures estimated as that x where $|\omega|[(1 + \nu^2/\omega^2)^{0.25}]/k_||v_{th,e} = 1$. Blue circles represent the radial width of the fine structures estimated as that x where $\gamma = [\gamma(k_||Rq_0 = 1 \cdot 10^{-3}) + \gamma(k_||Rq_0 = 4 \cdot 10^{-1})]/2$. In all the above cases, x is related to $k_||x$ via the relation $x = k_||x)q_0R/k_y\hat{s}$. ω_r and γ are solutions of the dispersion relation with the BGK-like collision operator, considering the *SimPassKinE* electron response. Black crosses represent the full width at half maximum of the z -averaged absolute value of the electrostatic potential $\langle |\Phi| \rangle_z$ in linear GENE simulations. In all cases, physical parameters are the same as that given in table 3.1

condition $|\omega_r/k_||x)v_{th,e}| \ll 1$, the left hand side of equation (C.15) can be neglected. The solution of the resulting equation, in the collisionless limit $\nu \rightarrow 0$ indeed gives the adiabatic electron response $n_{e,1} = n_{0,e}(e\Phi_1/T_{0,e})$. Whereas in the case of finite collisionality $\nu \neq 0$, the condition $|\omega_r/k_||x)v_{th,e}| \ll 1$ no longer gives an adiabatic electron response. Therefore, estimating the width of the fine-structure as that x where $|\omega_r/k_||x)v_{th,e}| = 1$ may not be a good approach in presence of collisions.

In presence of collisions, the limit of adiabatic electron response is reached when the friction force term can also be neglected in equation (C.15), in addition to the LHS, *i.e.* when $|\omega|[(1 + \nu^2/\omega^2)^{0.25}]/k_||v_{th,e} \ll 1$. One can therefore approximate the radial width of the fine structures as that x where $|\omega|[(1 + \nu^2/\omega^2)^{0.25}]/k_||v_{th,e} = 1$. In figure C.7, this estimate of the radial width of fine structures is plotted with yellow asterisks. However there is still a quantitative mismatch with the GENE results.

In another approach, that $k_||x$ in figure C.5(b), where $\gamma = [\gamma(k_||Rq_0 = 1 \cdot 10^{-3}) + \gamma(k_||Rq_0 = 4 \cdot 10^{-1})]/2$ has been used to find the radial width of fine-structures, using the relation $x(k_||) = k_||q_0R/\hat{s}k_y$ from equation (C.14). The choice of $k_||Rq_0 = 4 \cdot 10^{-1}$ is made since at that value, the growth rates for all collisionalities considered are

Appendix C. Local linear dispersion relation for analysing effect of collisions on ITG eigenmodes

approximately the same. And the choice of $k_{\parallel} Rq_0 = 1 \cdot 10^{-3}$ is made since at that value, the growth rates have already converged and reflects the limit of $k_{\parallel} \rightarrow 0$. The estimate $[\gamma(k_{\parallel} Rq_0 = 1 \cdot 10^{-3}) + \gamma(k_{\parallel} Rq_0 = 4 \cdot 10^{-1})]/2$ is therefore the average growth rate between these two choices of k_{\parallel} s. The resulting width of fine-structures is plotted in figure C.7 using blue circles. An increase in the radial width of fine-structures is observed, however the values and the nature of the curve differ significantly from the corresponding full width at half maximum of the fine-structures seen in linear GENE simulations.

One therefore concludes that, while the local dispersion based estimation of the growth rates and the radial width of the fine structures with collisions has been useful to a certain degree to illustrate some of the qualitative results, it fails to produce results that match quantitatively with linear GENE simulations.

Bibliography

- [Abel et al., 2008] Abel, I. G., Barnes, M., Cowley, S. C., Dorland, W., and Schekochihin, A. A. (2008). Linearized model Fokker–Planck collision operators for gyrokinetic simulations. I. theory. *Physics of Plasmas*, 15(12):122509.
- [Abiteboul, 2012] Abiteboul, J. (2012). *Turbulent and neoclassical toroidal momentum transport in tokamak plasmas*. PhD thesis, Aix-Marseille Université.
- [Abiteboul et al., 2011] Abiteboul, J., Garbet, X., Grandgirard, V., Allfrey, S. J., Ghendrih, P., Latu, G., Sarazin, Y., and Strugarek, A. (2011). Conservation equations and calculation of mean flows in gyrokinetics. *Physics of Plasmas*, 18(8):082503.
- [Angelino et al., 2006] Angelino, P., Bottino, A., Hatzky, R., Joliet, S., Sauter, O., Tran, T. M., and Villard, L. (2006). On the definition of a kinetic equilibrium in global gyrokinetic simulations. *Physics of Plasmas*, 13(5):052304.
- [Angus and Krasheninnikov, 2012] Angus, J. R. and Krasheninnikov, S. I. (2012). Drift wave dispersion relation for arbitrarily collisional plasma. *Physics of Plasmas*, 19(5):052504.
- [Ball et al., 2020] Ball, J., Brunner, S., and C.J., Ajay (2020). Eliminating turbulent self-interaction through the parallel boundary condition in local gyrokinetic simulations. *Journal of Plasma Physics*, 86(2):905860207.
- [Ball et al., 2019] Ball, J., Brunner, S., and McMillan, B. F. (2019). The effect of background flow shear on gyrokinetic turbulence in the cold ion limit. *Plasma Physics and Controlled Fusion*, 61(6):064004.
- [Barnes et al., 2011] Barnes, M., Parra, F. I., Highcock, E. G., Schekochihin, A. A., Cowley, S. C., and Roach, C. M. (2011). Turbulent transport in tokamak plasmas with rotational shear. *Physical Review Letters*, 106:175004.
- [Beer et al., 1995] Beer, M. A., Cowley, S. C., and Hammett, G. W. (1995). Field-aligned coordinates for nonlinear simulations of tokamak turbulence. *Physics of Plasmas*, 2(7):2687–2700.

Bibliography

- [Bhatnagar et al., 1954] Bhatnagar, P. L., Gross, E. P., and Krook, M. (1954). A model for collision processes in gases. I. Small amplitude processes in charged and neutral one-component systems. *Physical Review*, 94:511–525.
- [Biglari et al., 1990] Biglari, H., Diamond, P. H., and Terry, P. W. (1990). Influence of sheared poloidal rotation on edge turbulence. *Physics of Fluids B: Plasma Physics*, 2(1):1–4.
- [Bosch and Hale, 1992] Bosch, H.-S. and Hale, G. (1992). Improved formulas for fusion cross-sections and thermal reactivities. *Nuclear Fusion*, 32(4):611–631.
- [Bourdelle et al., 2012] Bourdelle, C., Garbet, X., Singh, R., and Schmitz, L. (2012). New glance at resistive ballooning modes at the edge of tokamak plasmas. *Plasma Physics and Controlled Fusion*, 54(11):115003.
- [Braginskii, 1965] Braginskii, S. I. (1965). Transport Processes in a Plasma. *Reviews of Plasma Physics*, 1:205.
- [Brizard and Hahm, 2007] Brizard, A. J. and Hahm, T. S. (2007). Foundations of nonlinear gyrokinetic theory. *Reviews of Modern Physics*, 79:421–468.
- [Brunner, 1997] Brunner, S. (1997). *Global approach to the spectral problem of microinstabilities in tokamak plasmas using a gyrokinetic model*. PhD thesis, École Polytechnique Fédérale de Lausanne.
- [Brunner, 2014] Brunner, S. (2014). Waves and instabilities in inhomogeneous plasmas. *EPFL Doctoral School Lectures*.
- [Brunner et al., 2010] Brunner, S., Tran, T. M., and Hittinger, J. (2010). Review of the landau collision operator and (approximate) linearized forms for numerical implementation.
- [Burrell, 1997] Burrell, K. H. (1997). Effects of $E \times B$ velocity shear and magnetic shear on turbulence and transport in magnetic confinement devices. *Physics of Plasmas*, 4(5):1499–1518.
- [Camenen et al., 2007] Camenen, Y., Pochelon, A., Behn, R., Bottino, A., Bortolon, A., Coda, S., Karpushov, A., Sauter, O., Zhuang, G., and the TCV team (2007). Impact of plasma triangularity and collisionality on electron heat transport in TCV l-mode plasmas. *Nuclear Fusion*, 47(7):510–516.
- [Cameron, 1973] Cameron, A. G. W. (1973). Abundances of the elements in the solar system. *Space Science Reviews*, 15:121–146.
- [Candy et al., 2020] Candy, J., Belli, E. A., and Staebler, G. (2020). Spectral treatment of gyrokinetic profile curvature. *Plasma Physics and Controlled Fusion*, 62(4):042001.

- [Candy et al., 2006] Candy, J., Waltz, R. E., Parker, S. E., and Chen, Y. (2006). Relevance of the parallel nonlinearity in gyrokinetic simulations of tokamak plasmas. *Physics of Plasmas*, 13(7):074501.
- [Cary and Brizard, 2009] Cary, J. R. and Brizard, A. J. (2009). Hamiltonian theory of guiding-center motion. *Reviews of Modern Physics*, 81:693–738.
- [Casati et al., 2009] Casati, A., Bourdelle, C., Garbet, X., Imbeaux, F., Candy, J., Clairet, F., Dif-Pradalier, G., Falchetto, G., Gerbaud, T., Grandgirard, V., Gürcan, D., Hennequin, P., Kinsey, J., Ottaviani, M., Sabot, R., Sarazin, Y., Vermare, L., and Waltz, R. (2009). Validating a quasi-linear transport model versus nonlinear simulations. *Nuclear Fusion*, 49(8):085012.
- [Casson et al., 2009] Casson, F. J., Peeters, A. G., Camenen, Y., Hornsby, W. A., Snodin, A. P., Strintzi, D., and Szepesi, G. (2009). Anomalous parallel momentum transport due to $E \times B$ flow shear in a tokamak plasma. *Physics of Plasmas*, 16(9):092303.
- [Chen et al., 2000] Chen, L., Lin, Z., and White, R. (2000). Excitation of zonal flow by drift waves in toroidal plasmas. *Physics of Plasmas*, 7(8):3129–3132.
- [Chowdhury et al., 2008] Chowdhury, J., Ganesh, R., Angelino, P., Vaclavik, J., Villard, L., and Brunner, S. (2008). Role of non-adiabatic untrapped electrons in global electrostatic ion temperature gradient driven modes in a tokamak. *Physics of Plasmas*, 15(7):072117.
- [C.J.,Ajay et al., 2020] C.J.,Ajay, Brunner, S., McMillan, B., Ball, J., Dominski, J., and Merlo, G. (2020). How the self-interaction mechanism affects zonal flow drive and the convergence of turbulent transport in flux-tube simulations. *Accepted in Journal of Plasma Physics*.
- [Connor et al., 2006] Connor, J. W., Hastie, R. J., and Helander, P. (2006). Stability of the trapped electron mode in steep density and temperature gradients. *Plasma Physics and Controlled Fusion*, 48(6):885–900.
- [Connor et al., 1978] Connor, J. W., Hastie, R. J., and Taylor, J. B. (1978). Shear, periodicity, and plasma ballooning modes. *Physical Review Letters*, 40:396–399.
- [Conway et al., 2000] Conway, G. D., Borba, D. N., Alper, B., Bartlett, D. V., Gormezano, C., von Hellermann, M. G., Maas, A. C., Parail, V. V., Smeulders, P., and Zastrow, K.-D. (2000). Suppression of plasma turbulence during optimized shear configurations in JET. *Physical Review Letters*, 84:1463–1466.
- [Cowley et al., 1991] Cowley, S. C., Kulsrud, R. M., and Sudan, R. (1991). Considerations of ion-temperature-gradient-driven turbulence. *Physics of Fluids B: Plasma Physics*, 3(10):2767–2782.

Bibliography

- [Crandall, 2019] Crandall, P. (2019). *Collisional and Electromagnetic Physics in Gyrokinetic Models*. PhD thesis, UCLA.
- [Dannert, 2005] Dannert, T. (2005). *Gyrokinetische Simulation von Plasmaturbulenz mit gefangenen Teilchen und elektromagnetischen Effekten*. PhD thesis, Technische Universität München.
- [Diamond et al., 2005] Diamond, P. H., Itoh, S.-I., Itoh, K., and Hahm, T. S. (2005). Zonal flows in plasma - a review. *Plasma Physics and Controlled Fusion*, 47(12A):R35.
- [Dif-Pradalier et al., 2015] Dif-Pradalier, G., Hornung, G., Ghendrih, P., Sarazin, Y., Clairet, F., Vermare, L., Diamond, P. H., Abiteboul, J., Cartier-Michaud, T., Ehrlacher, C., Estève, D., Garbet, X., Grandgirard, V., Gürçan, O. D., Hennequin, P., Kosuga, Y., Latu, G., Maget, P., Morel, P., Norscini, C., Sabot, R., and Storelli, A. (2015). Finding the elusive $\mathbf{E} \times \mathbf{B}$ staircase in magnetized plasmas. *Physical Review Letters*, 114:085004.
- [Dimits et al., 2000] Dimits, A. M., Bateman, G., Beer, M. A., Cohen, B. I., Dorland, W., Hammett, G. W., Kim, C., Kinsey, J. E., Kotschenreuther, M., Kritz, A. H., Lao, L. L., Mandrekas, J., Nevins, W. M., Parker, S. E., Redd, A. J., Shumaker, D. E., Sydora, R., and Weiland, J. (2000). Comparisons and physics basis of tokamak transport models and turbulence simulations. *Physics of Plasmas*, 7(3):969–983.
- [Doerk, 2012] Doerk, H. (2012). *Gyrokinetic simulation of microtearing turbulence*. PhD thesis, Universität Ulm.
- [Doerk et al., 2011] Doerk, H., Jenko, F., Pueschel, M. J., and Hatch, D. R. (2011). Gyrokinetic microtearing turbulence. *Physical Review Letters*, 106:155003.
- [Dominski, 2016] Dominski, J. (2016). *Development and application of Eulerian and Particle-In-Cell gyrokinetic codes for studying the effect of non-adiabatic passing electron dynamics on microturbulence*. PhD thesis, École Polytechnique Fédérale de Lausanne.
- [Dominski et al., 2015] Dominski, J., Brunner, S., Görler, T., Jenko, F., Told, D., and Villard, L. (2015). How non-adiabatic passing electron layers of linear microinstabilities affect turbulent transport. *Physics of Plasmas*, 22(6):062303.
- [Dominski et al., 2017] Dominski, J., McMillan, B. F., Brunner, S., Merlo, G., Tran, T.-M., and Villard, L. (2017). An arbitrary wavelength solver for global gyrokinetic simulations. application to the study of fine radial structures on microturbulence due to non-adiabatic passing electron dynamics. *Physics of Plasmas*, 24(2):022308.
- [Dorland et al., 2000] Dorland, W., Jenko, F., Kotschenreuther, M., and Rogers, B. N. (2000). Electron temperature gradient turbulence. *Physical Review Letters*, 85:5579–5582.

-
- [Einstein, 1905] Einstein, A. (1905). Ist die trägheit eines körpers von seinem energieinhalt abhängig? *Annalen der Physik*, 323(13):639–641.
- [Faber et al., 2018] Faber, B. J., Pueschel, M. J., Terry, P. W., Hegna, C. C., and Roman, J. E. (2018). Stellarator microinstabilities and turbulence at low magnetic shear. *Journal of Plasma Physics*, 84(5):905840503.
- [Fable et al., 2009] Fable, E., Angioni, C., and Sauter, O. (2009). The role of ion and electron electrostatic turbulence in characterizing stationary particle transport in the core of tokamak plasmas. *Plasma Physics and Controlled Fusion*, 52(1):015007.
- [Falchetto et al., 2003] Falchetto, G. L., Vaclavik, J., and Villard, L. (2003). Global-gyrokinetic study of finite β effects on linear microinstabilities. *Physics of Plasmas*, 10(5):1424–1436.
- [Gallagher et al., 2012] Gallagher, S., Hnat, B., Connaughton, C., Nazarenko, S., and Rowlands, G. (2012). The modulational instability in the extended Hasegawa-Mima equation with a finite larmor radius. *Physics of Plasmas*, 19(12):122115.
- [Garbet and Waltz, 1996] Garbet, X. and Waltz, R. E. (1996). Action at distance and Bohm scaling of turbulence in tokamaks. *Physics of Plasmas*, 3(5):1898–1907.
- [Goerk, 2012] Goerk, H. (2012). *Gyrokinetic Simulations of microtearing turbulence*. PhD thesis, Universität Ulm.
- [Görler, 2009] Görler, T. (2009). *Multiscale effects in plasma microturbulence*. PhD thesis, Universität Ulm.
- [Görler and Jenko, 2008] Görler, T. and Jenko, F. (2008). Scale separation between electron and ion thermal transport. *Physical Review Letters*, 100(18):185002.
- [Görler et al., 2011] Görler, T., Lapillonne, X., Brunner, S., Dannert, T., Jenko, F., Merz, F., and Told, D. (2011). The global version of the gyrokinetic turbulence code gene. *Journal of Computational Physics*, 230(18):7053 – 7071.
- [Hager et al., 2016] Hager, R., Yoon, E., Ku, S., D’Azevedo, E., Worley, P., and Chang, C. (2016). A fully non-linear multi-species Fokker–Planck–Landau collision operator for simulation of fusion plasma. *Journal of Computational Physics*, 315:644 – 660.
- [Hahm et al., 1999] Hahm, T., Beer, M., Lin, Z., Hammett, G., Lee, W., and Tang, W. (1999). Shearing rate of time-dependent $E \times B$ flow. *Physics of Plasmas*, 6(2-3):922–926.
- [Hahm, 1988] Hahm, T. S. (1988). Nonlinear gyrokinetic equations for tokamak microturbulence. *The Physics of Fluids*, 31(9):2670–2673.
- [Hallatschek and Dorland, 2005] Hallatschek, K. and Dorland, W. (2005). Giant electron tails and passing electron pinch effects in tokamak-core turbulence. *Physical Review Letters*, 95:055002.

Bibliography

- [Hasegawa et al., 1979] Hasegawa, A., MacLennan, C. G., and Kodama, Y. (1979). Non-linear behavior and turbulence spectra of drift waves and rossby waves. *The Physics of Fluids*, 22(11):2122–2129.
- [Hasegawa and Mima, 1978] Hasegawa, A. and Mima, K. (1978). Pseudo-three-dimensional turbulence in magnetized nonuniform plasma. *The Physics of Fluids*, 21(1):87–92.
- [Hatch et al., 2011] Hatch, D. R., Terry, P. W., Jenko, F., Merz, F., and Nevins, W. M. (2011). Saturation of gyrokinetic turbulence through damped eigenmodes. *Physical Review Letters*, 106:115003.
- [Hazeltine and Waelbroeck, 1998] Hazeltine, R. and Waelbroeck, F. (1998). *The Framework of Plasma Physics*. Perseus Books.
- [Hazeltine and Newcomb, 1990] Hazeltine, R. D. and Newcomb, W. A. (1990). Inversion of the ballooning transformation. *Physics of Fluids B: Plasma Physics*, 2(1):7–10.
- [Helander and Sigmar, 2002] Helander, P. and Sigmar, D. (2002). *Collisional transport in Magnetized Plasmas*. Cambridge University Press.
- [Hinton and Hazeltine, 1976] Hinton, F. L. and Hazeltine, R. D. (1976). Theory of plasma transport in toroidal confinement systems. *Reviews of Modern Physics*, 48:239–308.
- [Hinton and Rosenbluth, 1999] Hinton, F. L. and Rosenbluth, M. N. (1999). Dynamics of axisymmetric and poloidal flows in tokamaks. *Plasma Physics and Controlled Fusion*, 41(3A):A653–A662.
- [Horton et al., 1981] Horton, W., Choi, D., and Tang, W. M. (1981). Toroidal drift modes driven by ion pressure gradients. *The Physics of Fluids*, 24(6):1077–1085.
- [Howard et al., 2016] Howard, N. T., Holland, C., White, A. E., Greenwald, M., and Candy, J. (2016). Multi-scale gyrokinetic simulation of tokamak plasmas: enhanced heat loss due to cross-scale coupling of plasma turbulence. *Nuclear Fusion*, 56:014004.
- [Idomura et al., 2007] Idomura, Y., Ida, M., Tokuda, S., and Villard, L. (2007). New conservative gyrokinetic full-f vlasov code and its comparison to gyrokinetic delta-f particle-in-cell code. *Journal of Computational Physics*, 226(1):244 – 262.
- [Idomura et al., 2000] Idomura, Y., Wakatani, M., and Tokuda, S. (2000). Stability of $\mathbf{e} \times \mathbf{b}$ zonal flow in electron temperature gradient driven turbulence. *Physics of Plasmas*, 7(9):3551–3566.
- [Jenko et al., 2005] Jenko, F., Dannert, T., and Angioni, C. (2005). Heat and particle transport in a tokamak: advances in nonlinear gyrokinetics. *Plasma Physics and Controlled Fusion*, 47(12B):B195–B206.

-
- [Jenko et al., 2000] Jenko, F., Dorland, W., Kotschenreuther, M., and Rogers, B. N. (2000). Electron temperature gradient driven turbulence. *Physics of Plasmas*, 7(5):1904–1910.
- [Jorge et al., 2018] Jorge, R., Ricci, P., and Loureiro, N. F. (2018). Theory of the drift-wave instability at arbitrary collisionality. *Physical Review Letters*, 121:165001.
- [Kane, 1987] Kane, K. (1987). *Introductory nuclear physics*. Wiley.
- [Kardashev, 1964] Kardashev, N. S. (1964). Transmission of Information by Extraterrestrial Civilizations. *Astronomicheskii Zhurnal*, 41:282.
- [Kauffmann et al., 2010] Kauffmann, K., Kleiber, R., and Hatzky, R. (2010). Collisional effects on global gyrokinetic particle-in-cell simulations of itg and tem instabilities in tokamaks. *McKenna, C.: 37th European Physical Society Conference on Plasma Physics. Contributed Papers, European Physical Society (2010)*, 1.
- [Krommes, 1999] Krommes, J. A. (1999). Thermostatted delta-f. *Physics of Plasmas*, 6(5):1477–1494.
- [Krommes and Kim, 2000] Krommes, J. A. and Kim, C.-B. (2000). Interactions of disparate scales in drift-wave turbulence. *Physical Review E*, 62:8508–8539.
- [Ku et al., 2009] Ku, S., Chang, C., and Diamond, P. (2009). Full-f gyrokinetic particle simulation of centrally heated global ITG turbulence from magnetic axis to edge pedestal top in a realistic tokamak geometry. *Nuclear Fusion*, 49(11):115021.
- [Lang et al., 2008] Lang, J., Parker, S. E., and Chen, Y. (2008). Nonlinear saturation of collisionless trapped electron mode turbulence: Zonal flows and zonal density. *Physics of Plasmas*, 15(5):055907.
- [Lapillone, 2010] Lapillone, X. (2010). *Local and Global Eulerian Gyrokinetic Simulations of Microturbulence in Realistic Geometry with Applications to the TCV Tokamak*. PhD thesis, École Polytechnique Fédérale de Lausanne.
- [Lapillonne et al., 2009] Lapillonne, X., Brunner, S., Dannert, T., Jolliet, S., Marinoni, A., Villard, L., Gorler, T., Jenko, F., and Merz, F. (2009). Clarifications to the limitations of the s-alpha equilibrium model for gyrokinetic computations of turbulence. *Physics of Plasmas*, 16(3):032308.
- [Lapillonne et al., 2011] Lapillonne, X., Brunner, S., Sauter, O., Villard, L., Fable, E., Görler, T., Jenko, F., and Merz, F. (2011). Non-linear gyrokinetic simulations of microturbulence in TCV electron internal transport barriers. *Plasma Physics and Controlled Fusion*, 53(5):054011.
- [Lawson, 1957] Lawson, J. D. (1957). Some criteria for a power producing thermonuclear reactor. *Proceedings of the Physical Society. Section B*, 70(1):6.

Bibliography

- [Lin et al., 2002] Lin, Z., Ethier, S., Hahm, T. S., and Tang, W. M. (2002). Size scaling of turbulent transport in magnetically confined plasmas. *Physical Review Letters*, 88:195004.
- [Lin et al., 1998] Lin, Z., Hahm, T. S., Lee, W. W., Tang, W. M., and White, R. B. (1998). Turbulent transport reduction by zonal flows: Massively parallel simulations. *Science*, 281(5384):1835–1837.
- [Lin et al., 2000] Lin, Z., Hahm, T. S., Lee, W. W., Tang, W. M., and White, R. B. (2000). Gyrokinetic simulations in general geometry and applications to collisional damping of zonal flows. *Physics of Plasmas*, 7(5):1857–1862.
- [Littlejohn, 1982] Littlejohn, R. G. (1982). Hamiltonian perturbation theory in non-canonical coordinates. *Journal of Mathematical Physics*, 23(5):742–747.
- [Lütjens et al., 1996] Lütjens, H., Bondeson, A., and Sauter, O. (1996). The CHEASE code for toroidal MHD equilibria. *Computer Physics Communications*, 97(3):219 – 260.
- [Maeyama et al., 2015] Maeyama, S., Idomura, Y., Watanabe, T.-H., Nakata, M., Yagi, M., Miyato, N., Ishizawa, A., and Nunami, M. (2015). Cross-scale interactions between electron and ion scale turbulence in a tokamak plasma. *Physical Review Letters*, 114:255002.
- [Maeyama et al., 2017] Maeyama, S., Watanabe, T.-H., Idomura, Y., Nakata, M., Ishizawa, A., and Nunami, M. (2017). Cross-scale interactions between turbulence driven by electron and ion temperature gradients via sub-ion-scale structures. *Nuclear Fusion*, 57(6):066036.
- [Mantica et al., 2009] Mantica, P., Strintzi, D., Tala, T., Giroud, C., Johnson, T., Leggate, H., Lerche, E., Loarer, T., Peeters, A. G., Salmi, A., Sharapov, S., Van Eester, D., de Vries, P. C., Zabeo, L., and Zastrow, K.-D. (2009). Experimental study of the ion critical-gradient length and stiffness level and the impact of rotation in the JET tokamak. *Physical Review Letters*, 102:175002.
- [Mariani et al., 2018] Mariani, A., Brunner, S., Dominski, J., Merle, A., Merlo, G., Sauter, O., Görler, T., Jenko, F., and Told, D. (2018). Identifying microturbulence regimes in a TCV discharge making use of physical constraints on particle and heat fluxes. *Physics of Plasmas*, 25(1):012313.
- [Mazzucato et al., 2008] Mazzucato, E., Smith, D. R., Bell, R. E., Kaye, S. M., Hosea, J. C., LeBlanc, B. P., Wilson, J. R., Ryan, P. M., Domier, C. W., Luhmann, N. C., Yuh, H., Lee, W., and Park, H. (2008). Short-scale turbulent fluctuations driven by the electron-temperature gradient in the national spherical torus experiment. *Physical Review Letters*, 101:075001.

- [McMillan et al., 2010] McMillan, B., Lapillonne, X., Brunner, S., Villard, L., Jolliet, S., Bottino, A., Goerler, T., and Jenko, F. (2010). System size effects on gyrokinetic turbulence. *Physical Review Letters*, 105:155001.
- [McMillan et al., 2019] McMillan, B. F., Ball, J., and Brunner, S. (2019). Simulating background shear flow in local gyrokinetic simulations. *Plasma Physics and Controlled Fusion*, 61(5):055006.
- [McMillan et al., 2009] McMillan, B. F., Jolliet, S., Tran, T. M., Villard, L., Bottino, A., and Angelino, P. (2009). Avalanchelike bursts in global gyrokinetic simulations. *Physics of Plasmas*, 16(2):022310.
- [McMillan et al., 2018] McMillan, B. F., Pringle, C. C. T., and Teaca, B. (2018). Simple advecting structures and the edge of chaos in subcritical tokamak plasmas. *Journal of Plasma Physics*, 84(6):905840611.
- [Merlo, 2016] Merlo, G. (2016). *Flux-tube and global grid-based gyrokinetic simulations of plasma microturbulence and comparisons with experimental TCV measurements*. PhD thesis, École Polytechnique Fédérale de Lausanne.
- [Merlo et al., 2016] Merlo, G., Sauter, O., Brunner, S., Burckel, A., Camenen, Y., Casson, F. J., Dorland, W., Fable, E., Görler, T., Jenko, F., Peeters, A. G., Told, D., and Villard, L. (2016). Linear multispecies gyrokinetic flux tube benchmarks in shaped tokamak plasmas. *Physics of Plasmas*, 23(3):032104.
- [Merz, 2008] Merz, F. (2008). *Gyrokinetic simulation of multimode plasma turbulence*. PhD thesis, Universität Münster.
- [Merz and Jenko, 2008] Merz, F. and Jenko, F. (2008). Nonlinear saturation of trapped electron modes via perpendicular particle diffusion. *Physical Review Letters*, 100:035005.
- [Mikkelsen and Dorland, 2008] Mikkelsen, D. and Dorland, W. (2008). Dimits shift in realistic gyrokinetic plasma-turbulence simulations. *Physical Review Letters*, 101:135003.
- [Parra and Catto, 2009] Parra, F. I. and Catto, P. J. (2009). Vorticity and intrinsic ambipolarity in turbulent tokamaks. *Plasma Physics and Controlled Fusion*, 51(9):095008.
- [Peeters and Angioni, 2005] Peeters, A. G. and Angioni, C. (2005). Linear gyrokinetic calculations of toroidal momentum transport in a tokamak due to the ion temperature gradient mode. *Physics of Plasmas*, 12(7):072515.
- [Petty et al., 1995] Petty, C. C., Luce, T. C., Pinsker, R. I., Burrell, K. H., Chiu, S. C., Gohil, P., James, R. A., and Wròblewski, D. (1995). Gyroradius scaling of electron and ion transport. *Physical Review Letters*, 74:1763–1766.

Bibliography

- [Pringle et al., 2017] Pringle, C. C. T., McMillan, B. F., and Teaca, B. (2017). A nonlinear approach to transition in subcritical plasmas with sheared flow. *Physics of Plasmas*, 24(12):122307.
- [Pueschel and Jenko, 2010] Pueschel, M. J. and Jenko, F. (2010). Transport properties of finite- β microturbulence. *Physics of Plasmas*, 17(6):062307.
- [Pueschel et al., 2013] Pueschel, M. J., Terry, P. W., Jenko, F., Hatch, D. R., Nevins, W. M., Görler, T., and Told, D. (2013). Extreme heat fluxes in gyrokinetic simulations: A new critical β . *Physical Review Letters*, 110:155005.
- [Püschel, 2009] Püschel, M. J. (2009). *Electromagnetic effects in gyrokinetic simulations of plasma turbulence*. PhD thesis, Universität Münster.
- [Rewoldt and Tang, 1990] Rewoldt, G. and Tang, W. M. (1990). Toroidal microinstability studies of high-temperature tokamaks. *Physics of Fluids B: Plasma Physics*, 2(2):318–323.
- [Roach et al., 2009] Roach, C. M., Abel, I. G., Akers, R. J., Arter, W., Barnes, M., Camenen, Y., Casson, F. J., Colyer, G., Connor, J. W., Cowley, S. C., Dickinson, D., Dorland, W., Field, A. R., Guttentfelder, W., Hammett, G. W., Hastie, R. J., Highcock, E., Loureiro, N. F., Peeters, A. G., Reshko, M., Saarelma, S., Schekochihin, A. A., Valovic, M., and Wilson, H. R. (2009). Gyrokinetic simulations of spherical tokamaks. *Plasma Physics and Controlled Fusion*, 51(12):124020.
- [Rogers et al., 2000] Rogers, B. N., Dorland, W., and Kotschenreuther, M. (2000). Generation and stability of zonal flows in ion-temperature-gradient mode turbulence. *Physical Review Letters*, 85:5336–5339.
- [Romanelli and Briguglio, 1990] Romanelli, F. and Briguglio, S. (1990). Toroidal semi-collisional microinstabilities and anomalous electron and ion transport. *Physics of Fluids B: Plasma Physics*, 2(4):754–763.
- [Rosenbluth and Hinton, 1998] Rosenbluth, M. N. and Hinton, F. L. (1998). Poloidal flow driven by ion-temperature-gradient turbulence in tokamaks. *Physical Review Letters*, 80:724–727.
- [Rosenbluth et al., 1957] Rosenbluth, M. N., MacDonald, W. M., and Judd, D. L. (1957). Fokker-Planck equation for an inverse-square force. *Physical Review*, 107:1–6.
- [Rubel, 2019] Rubel, M. (2019). Fusion neutrons: Tritium breeding and impact on wall materials and components of diagnostic systems. *Journal of Fusion Energy*, 38:315–329.
- [Ryter et al., 2005] Ryter, F., Angioni, C., Peeters, A. G., Leuterer, F., Fahrback, H.-U., and Suttrop, W. (2005). Experimental study of trapped-electron-mode properties in tokamaks: Threshold and stabilization by collisions. *Physical Review Letters*, 95:085001.

-
- [Schekochihin et al., 2008] Schekochihin, A. A., Cowley, S. C., Dorland, W., Hammett, G. W., Howes, G. G., Plunk, G. G., Quataert, E., and Tatsuno, T. (2008). Gyrokinetic turbulence: a nonlinear route to dissipation through phase space. *Plasma Physics and Controlled Fusion*, 50(12):124024.
- [Scott, 1998] Scott, B. (1998). Global consistency for thin flux tube treatments of toroidal geometry. *Physics of Plasmas*, 5(6):2334–2339.
- [Shirai et al., 1995] Shirai, H., Takizuka, T., Naito, O., Sato, M., Isei, N., Koide, Y., Hirayama, T., and Azumi, M. (1995). Nondimensional transport study of JT-60U plasmas. *Journal of the Physical Society of Japan*, 64(11):4209–4220.
- [Smith et al., 2009] Smith, D. R., Kaye, S. M., Lee, W., Mazzucato, E., Park, H. K., Bell, R. E., Domier, C. W., LeBlanc, B. P., Levinton, F. M., Luhmann, N. C., Menard, J. E., and Yuh, H. (2009). Observations of reduced electron gyroscale fluctuations in national spherical torus experiment H-Mode plasmas with large $E \times B$ flow shear. *Physical Review Letters*, 102:225005.
- [Sugama et al., 2009] Sugama, H., Watanabe, T.-H., and Nunami, M. (2009). Linearized model collision operators for multiple ion species plasmas and gyrokinetic entropy balance equations. *Physics of Plasmas*, 16(11):112503.
- [Tatsuno et al., 2009] Tatsuno, T., Dorland, W., Schekochihin, A. A., Plunk, G. G., Barnes, M., Cowley, S. C., and Howes, G. G. (2009). Nonlinear phase mixing and phase-space cascade of entropy in gyrokinetic plasma turbulence. *Physical Review Letters*, 103:015003.
- [Tetsuo, 2017] Tetsuo, T. (2017). *Tritium: Fuel of fusion reactors*. Springer.
- [Told, 2012] Told, D. (2012). *Gyrokinetic Microturbulence in Transport Barriers*. PhD thesis, Universität Ulm.
- [Tresset et al., 2002] Tresset, G., Litaudon, X., Moreau, D., Garbet, X., and to the EFDA-JET Work Programme, C. (2002). A dimensionless criterion for characterizing internal transport barriers in JET. *Nuclear Fusion*, 42(5):520–526.
- [van Wyk et al., 2017] van Wyk, F., Highcock, E. G., Field, A. R., Roach, C. M., Schekochihin, A. A., Parra, F. I., and Dorland, W. (2017). Ion-scale turbulence in MAST: anomalous transport, subcritical transitions, and comparison to BES measurements. *Plasma Physics and Controlled Fusion*, 59(11):114003.
- [van Wyk et al., 2016] van Wyk, F., Highcock, E. G., Schekochihin, A. A., Roach, C. M., Field, A. R., and Dorland, W. (2016). Transition to subcritical turbulence in a tokamak plasma. *Journal of Plasma Physics*, 82(6):905820609.
- [Vernay, 2013] Vernay, T. (2013). *Collisions in Global Gyrokinetic Simulations of Tokamak Plasmas using the Delta-f Particle-In-Cell Approach Neoclassical Physics and Turbulent Transport*. PhD thesis, École Polytechnique Fédérale de Lausanne.

Bibliography

- [Wagner, 2007] Wagner, F. (2007). A quarter-century of H-mode studies. *Plasma Physics and Controlled Fusion*, 49(12B):B1–B33.
- [Waltz, 2005] Waltz, R. E. (2005). Rho-star scaling and physically realistic gyrokinetic simulations of transport in DIII-D. *Fusion Science and Technology*, 48(2):1051–1059.
- [Waltz et al., 2006] Waltz, R. E., Austin, M. E., Burrell, K. H., and Candy, J. (2006). Gyrokinetic simulations of off-axis minimum-q profile corrugations. *Physics of Plasmas*, 13(5):052301.
- [Waltz et al., 2002] Waltz, R. E., Candy, J. M., and Rosenbluth, M. N. (2002). Gyrokinetic turbulence simulation of profile shear stabilization and broken gyroBohm scaling. *Physics of Plasmas*, 9(5):1938–1946.
- [Waltz et al., 1998] Waltz, R. E., Dewar, R. L., and Garbet, X. (1998). Theory and simulation of rotational shear stabilization of turbulence. *Physics of Plasmas*, 5(5):1784–1792.
- [Waltz et al., 1994] Waltz, R. E., Kerbel, G. D., and Milovich, J. (1994). Toroidal gyroLandau fluid model turbulence simulations in a nonlinear ballooning mode representation with radial modes. *Physics of Plasmas*, 1(7):2229–2244.
- [Watanabe and Sugama, 2004] Watanabe, T.-H. and Sugama, H. (2004). Kinetic simulation of steady states of ion temperature gradient driven turbulence with weak collisionality. *Physics of Plasmas*, 11(4):1476–1483.
- [Weikl et al., 2018] Weikl, A., Peeters, A. G., Rath, F., Seiferling, F., Buchholz, R., Grosshauser, S. R., and Strintzi, D. (2018). The occurrence of staircases in ITG turbulence with kinetic electrons and the zonal flow drive through self-interaction. *Physics of Plasmas*, 25(7):072305.
- [Winsor et al., 1968] Winsor, N., Johnson, J. L., and Dawson, J. M. (1968). Geodesic acoustic waves in hydromagnetic systems. *The Physics of Fluids*, 11(11):2448–2450.



Acknowledgements

I acknowledge everything leading up to this point.

Lausanne, 12 November 2020

Ajay C. J.

Simulations were carried out on Piz Daint, CSCS, Switzerland and Marconi, CINECA, Italy.

This work has been carried out within the framework of the EUROfusion Consortium and has received funding from the Euratom research and training programme 2014 - 2018 and 2019 - 2020 under grant agreement No 633053. The views and opinions expressed herein do not necessarily reflect those of the European Commission.

This work was supported in part by the Swiss National Science Foundation.

Curriculum Vitae

Ajay C. J.

Date of Birth: 30 October 1992

Nationality: Indian

Email: trax.42@hotmail.com

EDUCATION

EPFL, Swiss Plasma Center

Lausanne, Switzerland

Doctoral Assistant / PhD student in Plasma Physics

2016–2020

- Thesis: “Studying the effect of non-adiabatic passing electron dynamics on microturbulence self-interaction in fusion plasmas using gyrokinetic simulations”

UM - DAE - Center for Excellence in Basic Sciences

Mumbai, India

BSc and MSc in Physics

2011–2016

- Thesis: “Study of wave breaking and injection in density transition scheme in laser wakefield acceleration”

TEACHING

- **Teaching Assistant** at EPFL Spring 2017, Spring 2018 - Autumn 2019
Numerical Physics I/II
- **Teaching Assistant** at EPFL Autumn 2017
Mathematical Physics, Analysis III

PUBLICATIONS

- [1] Ajay C. J., S. Brunner, B. McMillan, J. Ball, J. Dominski, and G. Merlo, “How eigenmode self-interaction affects zonal flows and convergence of tokamak core turbulence with toroidal system size”, *Journal of Plasma Physics*, vol. 86, no. 5, p. 905 860 504, 2020.
- [2] J. Ball, S. Brunner, and Ajay C.J., “Eliminating turbulent self-interaction through the parallel boundary condition in local gyrokinetic simulations”, *Journal of Plasma Physics*, vol. 86, no. 2, p. 905 860 207, 2020.
- [3] M. Fontana, L. Porte, S. Coda, O. Sauter, S. Brunner, Ajay C.J., A. Fasoli, G. Merlo, and The TCV Team, “Effects of collisionality and T_e/T_i on fluctuations in positive and negative δ tokamak plasmas”, *Nuclear Fusion*, vol. 60, no. 1, p. 016 006, 2019.

CONFERENCE CONTRIBUTIONS

- | | |
|---|-----------------------|
| Joint Varenna Lausanne International Workshop | Lausanne, Switzerland |
| – “Effect of collisions and background shear flow on non-adiabatic passing electron dynamics” | October 2020 |
| | |
| European Fusion Theory Conference | Ghent, Belgium |
| – “Study of effect of non-adiabatic passing electron dynamics on turbulent transport in fusion plasmas using gyrokinetic simulations” | October 2019 |
| | |
| Joint Varenna Lausanne International Workshop | Varenna, Italy |
| – “Study of wavenumber resolution convergence and system size effect in turbulent transport simulations with kinetic electron dynamics” | August 2018 |
| | |
| European Fusion Theory Conference | Athens, Greece |
| – “How non-adiabatic passing electron dynamics and density of mode rational surfaces affect turbulent transport in magnetic fusion plasmas” | October 2017 |
| | |
| Joint Annual Meeting of the Swiss Physical Society (SPS) and the Austrian Physical Society (OPG) | Geneva, Switzerland |
| – “Studying the effect of non-adiabatic passing electron dynamics on turbulent transport in magnetic fusion plasmas” | August 2017 |